

# FOCUSING LIGHT THROUGH SPHERICAL INTERFACE FOR SUBSURFACE MICROSCOPY

THANH XUAN HOANG

(B.Eng.(Hons.)), NUS

A THESIS SUBMITTED  
FOR THE DEGREE OF  
DOCTOR OF PHILOSOPHY OF  
ENGINEERING

DEPARTMENT OF ELECTRICAL & COMPUTER  
ENGINEERING

NATIONAL UNIVERSITY OF SINGAPORE

2014

## Declaration

I hereby declare that the thesis is my original work and it has been written by me in its entirety. I have duly acknowledged all the sources of information which have been used in the thesis. This thesis has also not been submitted for any degree in any university previously.



---

Hoang Thanh Xuan  
28 January 2014

## Acknowledgements

First and foremost, I would like to express my heartfelt gratitude to Assoc. Prof. Chen Xudong for the very first lessons about research. From him, I learnt the invaluable lessons about self confidence and self reliance. His guidance and insightful comments have always made my work an enjoyable and fruitful experience. One of my former lecturers told me that I am lucky to be supervised by Assoc. Prof. Chen and I absolutely agree with him about that.

I would also like to send a special thank you to Prof. Colin J. R. Sheppard for his guidance as my co-supervisor, especially in the first two years when we had weekly discussion. Whenever I presented a result, he sent to me some related works. This has greatly motivated and inspired me throughout my PhD program. I have always been busy and happy with his ideas.

Additionally, I would like to thank Prof. Phang C.H Jacob for the collaboration between our group and SEMICAPS on the experiment. Two weeks before Prof. Phang passed away, in spite of his unwell condition, he still met and discussed with our group on our research progress. I am really impressed and inspired by his passion in work and his career.

I would like to take this chance to send many thanks to Dr. Chen Rui, Dr. Krishna, Dr. Yu Zhong, Dr. Chen Wen, and all of my friends for their helps and friendships. My special thanks are sent to Dr. Chen Rui and Dr. Krishna for their helps and discussions on my experiment.

To my parents and my sister, thank you so much for always loving me.

To Quynh Nhu, my special one, thank you for your love.

# Contents

<b>Contents</b>	<b>i</b>
<b>Summary</b>	<b>v</b>
<b>List of Figures</b>	<b>vi</b>
<b>List of Abbreviations</b>	<b>viii</b>
<b>List of Publications</b>	<b>xi</b>
<b>1 Introduction</b>	<b>1</b>
1.1 Perfect Imaging and Time Reversal Symmetry . . . . .	1
1.2 Light-matter Interactions in an Aplanatic System . . . . .	4
1.3 Angular Spectrum Representations and Multipole Theory for Optical Fields	5
1.4 Light Scattering by Particles in a Focused Beam . . . . .	8
1.5 Solid Immersion Microscopy . . . . .	11
1.6 Polarized Beams and Annular Filter . . . . .	13
<b>2 Multipole and Plane Wave Expansions of Diverging and Converging Fields</b>	<b>15</b>
2.1 Scalar Multipole Fields . . . . .	17
2.2 Electromagnetic Fields due to a Source and a Sink . . . . .	19
2.3 Angular Spectrum Representation of Electromagnetic Fields . . . . .	24
<b>3 Angular Spectrum Representation and Multipole Theory for the Focal</b>	

---

<b>Fields</b>		<b>26</b>
3.1	Aplanatic Lens Modeling . . . . .	26
3.2	Angular Spectrum Representation of Optical Fields . . . . .	30
3.3	Multipole Theory . . . . .	36
3.3.1	Multipole Strengths for the Focused Waves . . . . .	36
3.3.2	Direct Derivation for the Multipole Strengths . . . . .	37
3.4	Polarized Beams and Focal Fields . . . . .	42
3.4.1	Radial or Azimuthal Polarization with a Vortex . . . . .	43
3.4.1.1	Radially-polarized Beam with a Vortex of Charge $n$ . . . . .	43
3.4.1.2	Azimuthally-polarized Beam with a Vortex of Charge $n$ . . . . .	45
3.4.2	Generalized Linear Polarization . . . . .	46
3.5	Simulations . . . . .	47
3.5.1	Radial Polarization, $n = 0$ . . . . .	47
3.5.1.1	Axial Dipole Wave (ADW) . . . . .	48
3.5.1.2	Radial Polarization with Uniform Illumination (RU) . . . . .	54
3.5.2	Azimuthal Polarization, $n = 1$ . . . . .	55
3.5.3	Generalized Linear Polarization . . . . .	56
3.5.3.1	Mixed Dipole, $S(\alpha) = 0$ . . . . .	56
3.5.3.2	Electric Dipole . . . . .	57
3.5.3.3	Transverse Electric TE1 . . . . .	57
3.5.4	Focal Field Distributions . . . . .	58
<b>4</b>	<b>Interpretation of the Scattering Mechanism</b>	<b>60</b>
4.1	Incident Focused Field . . . . .	61
4.2	Scattering by a Hemispherical Solid Immersion Lens . . . . .	62
4.3	Scattering by a General Solid Immersion Lens . . . . .	64
4.3.1	Translational Addition Theorems . . . . .	64
4.3.2	Scattering Coefficients for the GSIL . . . . .	66
4.3.2.1	Translational Distance is less than the Radius: $d < R$ . . . . .	68
4.3.2.2	Translational Distance is greater than the Radius: $d > R$ . . . . .	69

---

4.4	Scattering by a Sphere . . . . .	71
4.4.1	The Distance between the Center of the Sphere and the Center of the GRS is less than the Radius $d < R$ . . . . .	72
4.4.2	The Distance between the Center of the Sphere and the Center of the GRS is greater than the Radius $d > R$ . . . . .	77
4.5	Debye Series . . . . .	78
4.5.1	Translation Distance is less than the Radius of the Scatterer $d < R$	78
4.5.2	Translation Distance is greater than the Radius of the Scatterer $d > R$ . . . . .	79
<b>5</b>	<b>Solid Immersion Microscopy</b>	<b>81</b>
5.1	Hemispherical Solid Immersion Lens . . . . .	83
5.1.1	Approximate Analytical Model for Evaluating the Focal Field of the HSIL . . . . .	84
5.1.2	Rigorous Analytical Model for Evaluating the Focal Field of the HSIL . . . . .	88
5.1.2.1	The Rigorous Model . . . . .	89
5.1.2.2	Approximate Model Reduced from the Rigorous Model .	90
5.2	General Solid Immersion Lens . . . . .	92
5.2.1	Approximate Analytical Model for Evaluating the Focal Field of the GSIL . . . . .	93
5.2.2	Rigorous Analytical Model for Evaluating the Focal Field of the GSIL . . . . .	95
5.3	Polarized Beams and Focal Fields of SIL . . . . .	96
5.3.1	Cylindrical Vector Beams . . . . .	97
5.3.1.1	Radially-polarized Beam with a Vortex of Charge $n$ . . .	97
5.3.1.2	Azimuthally-polarized Beam with a Vortex of Charge $n$ .	100
5.3.2	Generalized Linear Polarization . . . . .	101
5.4	Simulations . . . . .	104
5.4.1	Results for the Hemispherical Solid Immersion Lens . . . . .	105

---

5.4.2	Results for the General Solid Immersion Lens . . . . .	107
5.5	Experiment . . . . .	118
<b>6</b>	<b>Conclusions and Further Directions</b>	<b>126</b>
6.1	Summary . . . . .	126
6.2	Further Directions . . . . .	128
6.2.1	Theory . . . . .	128
6.2.2	Experiment . . . . .	129
	<b>References</b>	<b>132</b>
	<b>Appendix A</b>	<b>148</b>
	<b>Appendix B</b>	<b>153</b>
	<b>Appendix C</b>	<b>158</b>

## Summary

Focusing and directing lights have numerous applications in most of scientific and technological areas. The first part of this thesis reviews and develops an efficient method based on multipole expansions for studying the focused field of polarized light, including radially-polarized and other important cases. We compare and highlight the differences between our method with the well-known Debye-Wolf diffraction integrals for calculating the field in the focal region. We also decompose a focused beam into a converging beam and a diverging beam and discuss their implications in focusing beyond diffraction limit.

In the second part of this thesis, we give a novel interpretation of the scattering mechanism for particles in a focused beam. Light scattering by a spherical particle represents a classical topic. The generalized Lorenz-Mie theory (GLMT) has been well developed for analyzing the scattering effects. However, the GLMT is not able to account for the multiple reflections inside the scatterer. Through our interpretation, we derive a series for taking into account the multiple reflections in a simple and straightforward way. Our series not only explains the scattering mechanism well but also helps to solve the boundary conditions at a spherical interface rigorously.

Solid immersion microscopy (SIM) provides a high spatial resolution and optical collection efficiency, which are the most desirable properties of nearly all optical systems. The SIM has been developed and improved both theoretically and experimentally for the last 3 decades. Recently, it is becoming more and more important in identifying faulty locations in integrated circuits that, as predicted by the well-known Moore's law, are getting smaller and denser. In the third part of this thesis, we study the SIM both theoretically and experimentally. Theoretically, we form a rigorous analytical model for studying the focal field of the SIM and correct errors of the existing models. Experimentally, we manipulate binary masks and polarization of light to resolve gratings consisting of 120-nm-wide lines, spaced 120 nm apart, using 1342nm wavelength laser.

# List of Figures

1.1	SIL Configurations. . . . .	2
1.2	An aplanatic focusing system. . . . .	4
1.3	SIL Configurations. . . . .	10
1.4	Spherical Scatterer. . . . .	10
2.1	Integration contours. . . . .	18
3.1	Aplanatic Lens Modeling. . . . .	27
3.2	Multipole strengths for ADW and RU (ignoring the constant term $f e^{ikf}$ ). . . . .	48
3.3	Multipole strengths $ k p_{El}^0  =  k \times p_{El}^0 $ with $f = 100cm$ and $\lambda = 1.34\mu m$ . . . . .	49
3.4	Electric intensity modelings on GRS for ADW with $f = 10cm$ and $L = 400$ . . . . .	50
3.5	Electric intensity on spheres with different radius for ADW with $f = 10cm$ and $\alpha_m = 16^\circ$ . . . . .	51
3.6	Electric intensity on spheres with different radius for ADW with $f = 10cm$ and $\alpha_m = 16^\circ$ . . . . .	51
3.7	Contour plots of the electric energy density for the radial polarization (ADW) for $\alpha_m = 60^\circ$ . . . . .	52
3.8	Electric intensity modelings on the GRS for $a(\alpha) = \sin(3\alpha)$ , $f = 10cm$ , $\alpha_m = 60^\circ$ . . . . .	53
3.9	Electric intensity modelings on different spheres for $a(\alpha) = \sin(3\alpha)$ with $f = 10cm$ and $\alpha_m = 60^\circ$ . . . . .	53
3.10	The ratio $\frac{p_{E1}}{p_{E2}}$ and $\frac{p_{E1}}{p_{M1}}$ for different polarizations. . . . .	54

## LIST OF FIGURES

3.11	The ratio $\frac{p_{E1}}{p_{E2}}$ for ADW and RU polarizations for an annular lens with obscuration angle $\alpha_0$ . . . . .	55
3.12	Multipole strengths of MD, ED, and UTE1. . . . .	56
3.13	Electric focal intensity for ADW with $\alpha_m = 60^\circ$ . . . . .	59
4.1	Hemispherical SIL-based scatterer. . . . .	62
4.2	Scattering Coefficients for Hemispherical SIL. . . . .	67
4.3	Multipole strengths in $O'$ -coordinate system for $r' > d$ with $f = 100cm$ and $d = 1.75mm$ . . . . .	67
4.4	Multipole strengths in $O'$ -coordinate system for $r' < d$ with $f = 100cm$ , $d = 1.75mm$ , and $L = 600$ . . . . .	68
4.5	Scattering Coefficients for an ASIL with $R = 500\mu m$ , $\lambda = 1.34\mu m$ , and $d = 1.75mm$ . . . . .	69
4.6	Effective multipole strengths $c_{\nu} P_{E\nu}^0$ inside the ASIL with $R = 500\mu m$ , $\lambda = 1.34\mu m$ , $d = 1.75mm$ , and $L = 600$ . . . . .	71
4.7	Spherical scatterer. . . . .	72
4.8	Mie Scattering Coefficients for a silicon sphere in air with $R = 500\mu m$ and $\lambda = 1.34\mu m$ . . . . .	76
5.1	General SIL-based system. . . . .	82
5.2	An individual plane wave incident onto the spherical surface. . . . .	86
5.3	Electric intensity distributions with different radius of HSIL: $R_1 = 10\mu m$ , $R_2 = 50\mu m$ , $R_3 = 100\mu m$ , $R_4 = 500\mu m$ . . . . .	108
5.4	Electric intensity distributions with different radius of ASIL and $\alpha_m = 16^\circ$ . . . . .	110
5.5	Electric intensity at the spherical interface for ADW with $f = 10cm$ , $R = 500\mu m$ , and $\alpha_m = 16^\circ$ . . . . .	112
5.6	Electric intensity for ADW with $f = 10cm$ , $\alpha_m = 16^\circ$ , (a) $\alpha_0 = 8^\circ$ , and (b) $\alpha_0 = 10^\circ$ . . . . .	113
5.7	Electric intensity for ADW with $f = 10cm$ , $\alpha_m = 16^\circ$ , (a) $\alpha_0 = 12^\circ$ , and (b) $\alpha_0 = 15^\circ$ . . . . .	114

## LIST OF FIGURES

---

5.8	Electric intensity for ADW with $f = 10cm$ , $R = 500\mu m$ and $\alpha_m = 16^\circ$ . . .	116
5.9	$f = 10cm$ , $R = 500\mu m$ , $d_1 = 0$ (HSS), $d_2 = \frac{R}{2}$ , $d_3 = 2R$ , $d_4 = 3.5R$ (ASS). . .	117
5.10	Experimental Setup. . . . .	118
5.11	Imaging with linear polarization and an annular filter. . . . .	120
5.12	Image of the sample with pitch $240nm$ and line $120nm$ using different polarizations and no filter. . . . .	121
5.13	Imaging with linear polarization and different filters. . . . .	122
5.14	Imaging with circular polarization. . . . .	123
5.15	Imaging with radial polarization. . . . .	124
6.1	Annular solid immersion lens with radius $R$ , reflective index $n$ , and a blocking area $R_1$ . . . . .	130

---

## List of Abbreviations

- *GRS* Gaussian reference sphere
- *NA* Numerical aperture
- *FWHM* Full widths at half maximum
- *SIL* Solid immersion lens
- *HSIL* Hemispherical solid immersion lens
- *ASIL* Aplanatic solid immersion lens
- *HSS* Hemispherical SIL-based system
- *ASS* Aplanatic SIL-based system
- *GSS* General SIL-based system
- *LMT* Lorenz-Mie theory
- *GLMT* Generalized Lorenz-Mie theory
- *DS* Debye Series
- *DI* Diffraction integrals
- *MT* Multipole theory
- *GO* Geometrical optics
- *ADW* Axial dipole wave
- *RU* Radial polarization with uniform illumination
- *ED* Electric dipole
- *MD* Mixed dipole
- *UTE1* Uniform transversal electric TE1

## LIST OF ABBREVIATIONS

---

- $AV1$  Azimuthal polarization with a vortex  $n = 1$ .
- $f$  Focal length of aplanatic lens
- $R$  Radius of SIL
- $d$  Distance between the centres of lens and SIL
- $k$  Wavenumber outside SIL
- $\lambda$  Wavelength outside SIL
- $k_s$  Wavenumber inside SIL
- $\alpha_m$  Maximum illumination semi-angle
- $\alpha_o$  Blocking semi-angle

---

## List of Publications

### Journal Papers

1. **T. X. Hoang**, X. Chen, and C. J. R. Sheppard, “Multipole theory for tight focusing of polarized light, including radially polarized and other special cases,” *J. Opt. Soc. Am. A* **29**, 32–43 (2012).
2. **T. X. Hoang**, X. Chen, and C. J. R. Sheppard, “Interpretation of the scattering mechanism for particles in a focused beam,” *Phys. Rev. A* **86**, 033817–033817-6 (2012).
3. **T. X. Hoang**, X. Chen, and C. J. R. Sheppard, “Rigorous analytical modeling of high-aperture focusing through a spherical interface,” *J. Opt. Soc. Am. A* **30**, 1426–1440 (2013).
4. **T. X. Hoang**, X. Chen, and C. J. R. Sheppard, “Multipole and plane wave expansions of diverging and converging fields,” *Opt. Express* **22**, 8949–8961 (2014).

### Conference Papers

1. **T. X. Hoang**, X. Chen, and C. J. R. Sheppard, “Multipole expansion for tight focusing of polarized beams: A closer look into physical properties of the beams,” presented at Focus On Microscopy 2012, Singapore, April 1-4, 2012.
2. **T. X. Hoang**, X. Chen, and C. J. R. Sheppard, “Multipole theory for tight focusing of polarized light with arbitrary radiation pattern: Application to hemispherical solid immersion lens (SIL) for subsurface imaging,” presented at Advanced Electromagnetics Symposium, Paris, France, April 16-19, 2012.
3. **T. X. Hoang**, X. Chen, and C. J. R. Sheppard, “Rigorous analytical modeling of light scattering by particles and spherical surfaces in a focused beam,” presented at Focus On Microscopy 2013, Maastricht, The Netherlands, March 24-27, 2013.

## LIST OF PUBLICATIONS

---

4. **T. X. Hoang**, R. Chen, K. Agarwal, C. J. R. Sheppard, and X. Chen, “Imaging with annular focusing through a dielectric interface,” presented at Focus On Microscopy 2014, Sydney, Australia, April 13-16, 2014.
  
5. **T. X. Hoang** and X. Chen, “Focusing light for subsurface imaging,” accepted for presenting at 2014 IEEE International Symposium on Antennas and Propagation and USNC-URSI Radio Science Meeting, Memphis, Tennessee, United States of America, July 6-11, 2014.

# Chapter 1

## Introduction

Diffraction phenomena have been known since the time of Leonardo da Vinci [1]. And since the time of Abbe, diffraction has been believed to be the fundamental physical phenomenon which limits the resolution of a conventional microscope [1]. However, in the last several decades we have witnessed the invention of some methods to push the capacity of imaging of a microscope beyond the diffraction limit [2]. In this thesis, we will discuss the diffraction phenomena and their implications for sub-wavelength focusing and imaging capacity of an optical system.

### 1.1 Perfect Imaging and Time Reversal Symmetry

According to the definition in [1], for an ideal optical instrument, a source point  $P_0$  in the object space gives rise to a stigmatic image  $P_1$  in the image space. And if every curve  $C_0$ , produced by  $P_0$  in the object space, is geometrically similar to its conjugate curve in the image space, produced by its image, then the imaging between the two space is said to be perfect.

Feynman pointed out that both inward and outward spherical waves traveling to and from the origin are solutions of Maxwell's equations in free space [3]. In his lectures, he also briefly mentioned that only the outgoing (diverging) wave solution makes "physical sense" when describing the electromagnetic field radiated by a source. After the invention of laser, the concept of a converging wave has been mentioned more frequently, especially

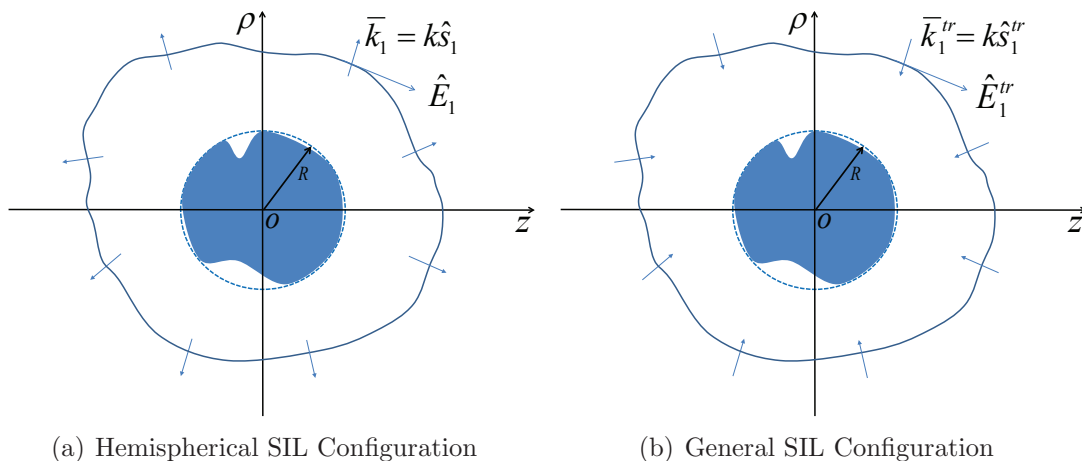


Figure 1.1: SIL Configurations.

in light focusing systems. Many lasers produce Gaussian beams that exhibit a Gaussian variation in the waist [4]. To describe the propagation of the Gaussian beam in free space, the complex-source-point theory has been developed. The central idea of this theory is to move the source an imaginary distance  $z_0$  from the origin so that there is no source in real space and the propagation of the beam still satisfies the Maxwell's equations. However, this complex-source-point theory results in a singularity in free space. Due to this singularity, a theory based on a source-sink pair has been proposed to avoid it ([4], and references therein). In the context of describing the propagation of the Gaussian beam, the source and the sink are purely-mathematical concepts. But the source and the sink in the context of time reversal symmetry have represented an active research topic for the last two decades and have been accepted widely as physical concepts. The sinks can be categorized into two types, i.e., passive sinks and active sinks, respectively. A passive sink absorbs energy and its physical mechanism has been explained in different contexts [5-7]. The physical mechanism of an active sink is to radiate a wave that destructively interferes completely with the resultant diverging wave of the converging wave. The active sink has been demonstrated in acoustic wave experiments, and has been exploited commercially in noise cancellation [8, 9].

The source shown in Fig. 1.1(a) radiates a wave propagating towards infinity. If the propagation direction of the radiated wave is reversed in all degrees of freedom - for example, by a process of phase conjugating the radiated field using a nonlinear material

[10], metamaterial, or graphene [11]- we will have a converging wave approaching back to the position of the source. Now, we consider the case in which the source is removed and hence the region around the origin is a source-free region. Due to energy flux conservation, there must be a diverging wave following the converging wave. And the total field in the source-free region is due to the interference of these two beams. It has been shown that the interference results in a focal spot which is subject to the diffraction limit [5, 12]. As a quantum mechanism, the nature of photons is the reason behind the diffraction limit that can be explained in terms of the Heisenberg uncertainty principle. The principle says that the spatial confinement of a photon, i.e. the focal spot, is inversely proportional to its momentum spread [11]. However, if the source is replaced by the time reversed source as shown in Fig. 1.1(b), which, in a more general context, is a sink, the converging wave will be absorbed completely. The energy of the converging wave is converted into two parts when approaching the sink: the energy of non-propagating field and the absorbed energy. The non-propagating field, or equivalently evanescent field, is associated with large or complex k-vectors [13], which are believed to be necessary for producing a sub-diffraction limit spot at the focus. In the particle-like manifestations of the electromagnetic field, the evanescent field is associated with a photon cloud around the sink in which corpuscular photons are imagined as being continually emitted and reabsorbed [13]. This evanescent field is also referred to as a localized field.

Due to the simplicity in explaining various phenomena relating to the light focusing, the time reversal symmetry has gained much attention from many researchers in recent years [14]. Under the guidance of time reversal symmetry, Quabis and colleagues predicted that using a radially polarized beam produces a tighter focal spot in comparison with a linearly polarized beam [15]. This prediction was later confirmed by Dorn et. al. [16]. Similarly, under the guidance, Mudry et. al. improved the performance of confocal microscopy to obtain a  $4\pi$  microscope with a combination of a spatial light modulator, a single microscope objective, and a mirror [17]. Light-matter interaction between a focused beam and a quantum target is also usually studied and explained in the context of time reversal symmetry [18, 19].

## 1.2 Light-matter Interactions in an Aplanatic System

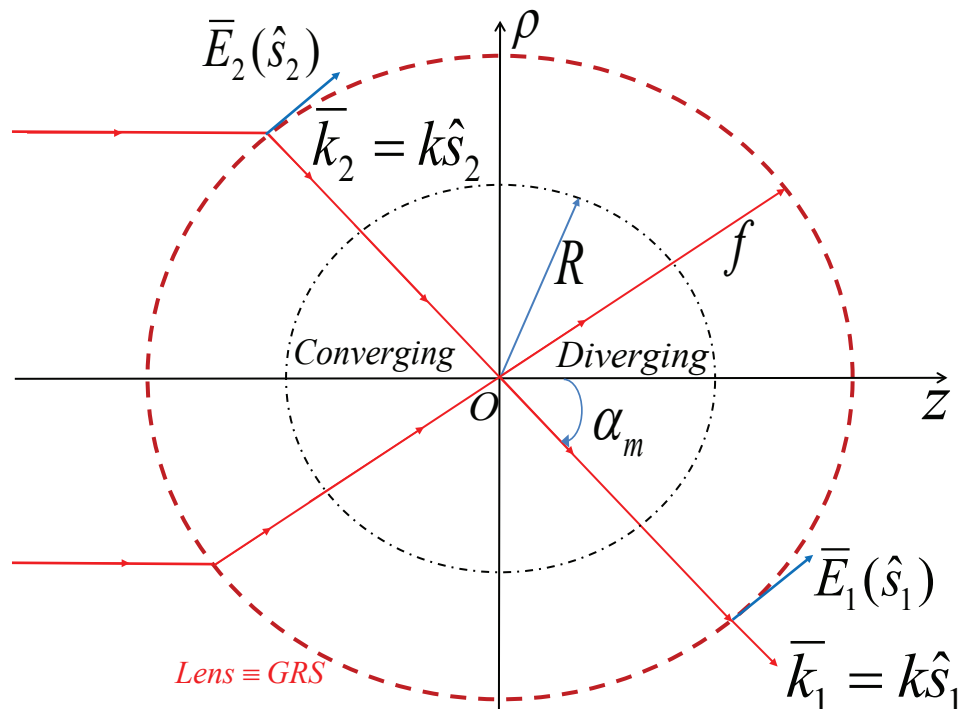


Figure 1.2: An aplanatic focusing system.

Figure 1.2 shows the model of an aplanatic lens, which is represented by the Gaussian reference sphere (GRS). The lens converts an incident collimated beam into a focused beam. The interaction between a focused beam and an atom, molecule, nano-particle, or a cluster of nano-particles is gaining much attention due to its potential in many applications in quantum mechanics and nanophotonics. The “atom” represents various kinds of quantum emitters and quantum targets [18]. In theory, under the guidance of time reversal symmetry Sondermann et. al. argued that a single atom will absorb a single photon with 100% efficiency if the radiation incident onto the atom resembles a dipole wave [19]. Zumofen et. al. showed that a focused dipole wave can be perfectly reflected by a single point-like oscillating dipole [20]. By matching the cross-section of plasmonic nanowires to the field structure of tightly focused beams, Normatov et. al. showed that the nanowires could absorb up to 65% of the total power of the incident beam [21]. Chen et. al. theoretically demonstrated that focused radially-polarized beams can

excite surface-plasmon-polaritons in metal nanowires and nanocones with efficiencies of the order of 90% [22]. Experimentally, some groups have investigated and demonstrated promising couplings though with low efficiencies [23–25]. These low efficiencies may be because of using a limited numerical aperture (NA), which consequently involve higher order multipoles [26]. To improve the performance of the setup, a mode converter was proposed [19]. The mode converter will convert an incident wave into a focused wave that resembles a dipole wave. More recently, with the fast development of nano-technology and many successful researches in plasmonics, a single atom integrated with an optical antenna was shown to radiate both dipole and higher order multipoles [27, 28]. By the time reversal symmetry, a focused field by a limited NA lens can be completely absorbed by a quantum target placing near the optical antenna. This opens the possibility of perfectly converting the incident focused beam into surface plasmon polaritons, which in turns can be manipulated using plasmonic devices [29, 30]. Moreover, using a spatial light modulator can control many thousands of spatial degrees of freedom of light and hence control the content of the multipole terms in the focused beam, i.e., the conversion efficiencies can be improved by using the spatial light modulator and the combination of an atom and an optical antenna. Hence, understanding the focusing using the aplanatic system is crucial, especially in the multipole theory. This thesis aims to provide a more complete understanding into the focused beam.

### 1.3 Angular Spectrum Representations and Multipole Theory for Optical Fields

The focal field of the aplanatic lens in Fig. (1.2) can be evaluated using different methods based on different bases of the solutions of Maxwell’s equations. The two most common bases in use are the plane waves and spherical harmonics. The two equivalent methods for evaluating the focal field are plane wave and multipole expansions, respectively. Many researchers have devoted time to develop and study the light diffraction phenomena based on the plane wave expansions, especially the angular spectrum representation of the elec-

tromagnetic field. In 1909, Debye derived an elegant formula for treating the diffraction caused by a small aperture, i.e., a scalar case. In 1959, Wolf generalized the formula by including the effect of vectorial nature of the field, and hence the diffraction integrals are sometimes referred to as Debye-Wolf diffraction integrals ([31], and references therein). Later, Richard and Wolf used the formula for estimating the focal field of an aplanatic lens [32]. Now, the diffraction integrals have been widely used for describing different focusing systems. Alternative to the angular spectrum representation of the electromagnetic field, the multipole theory for describing the focal field was recently developed [26]. In the paper, though we showed that the Debye-Wolf diffraction integrals and the multipole theory give a perfect agreement on the electric intensity around the focus, the two methods are in fact not equivalent due to the different approximations at the Gaussian reference sphere. This thesis will give more details about the difference between the two methods.

In his derivation, Debye showed that there is the peculiar behavior of the integrals on the optical axis at the far-region [33]. Later, Sommerfeld, in his lectures, argued that the behavior is similar to the Poisson spot occurring in the diffraction pattern of a circular disk [33]. In an asymptotic treatment of the diffraction problem, Van Kampen showed that there are three kinds of the critical points [34], which contribute to the diffraction field. The first kind consists of all points of diffraction aperture but not at the periphery of the aperture. The second kind consists all the points on the periphery but not at a corner, and the third kind consists of all the corners of the aperture. If we consider a circular aperture, there are only the first and second kinds of the critical points. The leading term of the first and second kinds of the critical points contributing to the asymptotic expansion are  $(kr)^{-1}$  and  $(kr)^{-3/2}$ , respectively [1, 34]. In the derivation of Debye-Wolf integrals, the authors used the method of stationary phase, i.e. they took into account only the first kind of critical points. Hence, the error introduced in using the asymptotic approximation is of the order  $(kr)^{-3/2}$  [31]. The second kind of the critical point was known to significantly contribute to the diffraction field around the optical axis and the boundary of the shadow region behind the aperture [33]. It is also well-known that in

general one can not separate the inhomogeneous and homogeneous plane waves in the angular-spectrum representations of waves due to a local source, even far from the source [35]. For a scalar dipole field, Carter showed that, a few wavelengths away from the source, the evanescent plane waves don't play any significant role in the total field [36]. However, for a more general case of a spherical scalar wave field, the contribution of the evanescent plane waves can be significant due to the interference among them, especially along the  $\mathbf{Z}$  axis and  $\mathbf{Z} = \mathbf{0}$  plane [37]. The Debye-Wolf diffraction integrals in fact describe the interference of the converging and diverging beams. Recently, we developed the multipole theory in which we decomposed the total field into the converging and diverging fields [26]. Then we explained the scattering mechanism using the converging beam as the incident beam [38]. Using our definition for the incident field, we later formed a rigorous model for focusing light through a spherical interface [39]. In fact, using the definition, in which the incident field is the interference field between the converging field and diverging field, will lead to some problems relating to the shadow region behind a scatterer [40, 41]. Brillouin investigated the scattering problem of a sphere illuminated by a plane wave and pointed out an error made by Stratton and Houghton due to the misinterpretation about some field components relating to the definition of the incident field [40, 42]. Brillouin then corrected the misinterpretation by taking into account a secondary field that compensated for the incident field in the shadow of the sphere. Later, Lock used similar idea to interpret the extinction in Gaussian-beam scattering in which the key point was that he decomposed the total field into the incoming and outgoing fields. And then he computed the interaction cross section in terms of the outgoing field only. However, Brillouin and Lock interpreted the scattering phenomenon based on the so-called compensating field accounting for the shadow of the sphere. Recently, we defined the incident field containing only the incoming field and hence presented a novel interpretation for the scattering mechanism [38]. We also derived the two infinite series of scattering coefficients that help us to avoid the ambiguity caused by using the compensating field in the shadow of a scatter. Using our definition also help to avoid the artifact caused by separating the inhomogeneous and homogenous waves. In this thesis,

we will discuss more about the scattering mechanism by considering a more general configuration for the scatterers, say off-axis scatterers.

## 1.4 Light Scattering by Particles in a Focused Beam

The scattering of light by a sphere in a focused laser beam has recently gained much attention due to its various applications in medicine, biology, and nanotechnology. Many researchers have analyzed scattering both theoretically [20, 43–47] and experimentally [24, 48–52]. The theoretical scattering study involves expressing the electric field of the focused beam in terms of the angular spectrum representation [31] or electric and magnetic multipole fields [26, 53]. The scattering effects are then taken into account using the generalized Lorenz-Mie theory (GLMT) in which the external ( $a_l^g, b_l^g$ ) and internal ( $c_l^g, d_l^g$ ) scattering coefficients play a central role. The GLMT was developed from Lorenz-Mie theory (LMT) [54–56]. LMT was proposed for studying the scattering of a linearly polarized plane wave by a homogenous sphere by several researchers, especially Lorenz [57] and Mie [58]. After the invention of the laser during the 1960s, much attention was paid to light scattering by a sphere in a shaped laser beam. Since the laser beam is usually treated as polarized, the study of light scattering eventually led to the establishment of GLMT. Both LMT and GLMT are convenient for scattering calculations. However, neither of them can explicitly explain the effect of multiple reflections inside the sphere on the scattering field distribution.

To understand and improve light-matter interaction for industrial and other applications, it is essential to analyze the physical mechanism responsible for the scattering. The Debye series (DSs) gives a deeper insight into the physical mechanism, in which the propagation of each partial wave can be traced and explained in terms of multiple reflections [59]. Since Debye constructed the series for a cylinder in 1908, a number of researchers studied the DSs for a number of different scatters, such as a homogeneous cylinder [59, 60], a multilayered cylinder [61–63], a homogeneous sphere [64–66], a multilayered sphere [67–70], a spheroid [71], and a non-spherical particle [72]. Through its

long history of development, the DSs not only help to match the LMT and GLMT but also to evaluate the validity of an approximate solution (such as geometrical optics) compared to the rigorous solution (GLMT) [65, 69, 73]. The DSs are also convenient to analyze various physical phenomena, such as rainbows [60, 61, 74, 75], glories [75–77], and coronas [75]. In derivation of the DSs, most authors used three steps as follows: Steps 1 and 2 are to derive the reflection and transmission coefficients for incoming  $(a_{l2}, b_{l2}, c_{l2}, d_{l2})$  and outgoing  $(a_{l1}, b_{l1}, c_{l1}, d_{l1})$  waves. Step 3 is to use some algebraic manipulations to express the Mie coefficients  $(a_l^g, b_l^g, c_l^g, d_l^g)$  in terms of the scattering coefficients of the incoming and outgoing waves [62, 65, 66, 71, 78]. The DSs are then used for investigation of the scattering mechanism and phenomena. This means that the authors firstly formed mathematical expressions and then explained the expressions by multiple reflections and transmissions. All the authors concluded that each term in the infinite summation of the expressions represents an interaction between the ray beam with the surface of the scatterers. In addition, they have derived the DSs in cases of a plane wave [59, 61, 62, 65, 67–70, 72, 75, 77, 78] and a shaped laser beam [63, 66, 71]. For a homogeneous sphere, Gouesbet used the above three steps to express the DSs in a GLMT framework which is now valid for an arbitrary shaped beam [66]. This thesis derives and explains a series accounting for the multiple scattering without using the above three steps.

As mentioned, the scattering of light by a sphere in a focused beam has been gaining much attention in both theory and experiment, and hence it is important to understand the physical mechanism of the scattering. This thesis aims to provide an insightful understanding to the scattering mechanisms by considering the two scattering systems as illustrated in Figs. 1.3 and 1.4. The first scattering system includes an aplanatic optical lens, which is represented by the Gaussian reference sphere (GRS) with a radius  $f$  much larger than the wavelengths  $\lambda$  of the focused beam, and the solid immersion lens (SIL) as shown in Fig. 1.3. The second system is a modification of the first system in which we replace the SIL with a complete sphere as shown in Fig. 1.4. Since the SIL has only one boundary on the left side, there is only one light-matter interaction at the boundary of the SIL. On the other hand, the sphere has a closed boundary, and hence there are

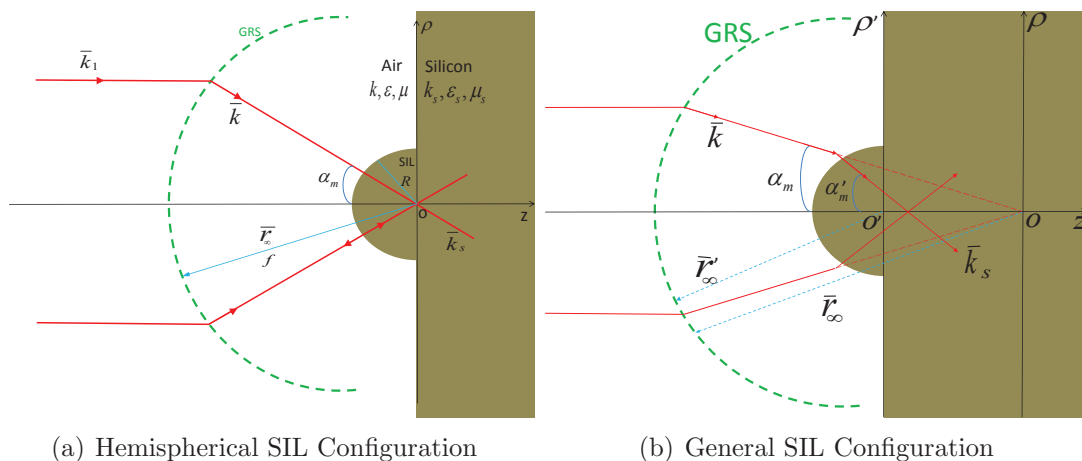


Figure 1.3: SIL Configurations.

an infinite number of light-matter interactions corresponding to internal reflections inside the sphere. For a scattering problem, the GLMT usually defines the incident focused beam as if it could propagate without any perturbation or without the presence of the scattering system [44–47]. This means the incident focused beam includes both incoming and outgoing waves, with reference to the focal point. However, this definition is not applicable to the calculation of the field inside the hemispherical solid immersion lens (HSIL) [79]. In other words, the GLMT should not be used for calculating the scattering of the HSIL. In fact, to calculate the field inside the SIL correctly, we must define the incident focused beam as containing only the incoming wave. In this thesis, we derive scattering coefficients for both of the scattering systems using our definition and give a clear explanation about the different series accounting for the multiple scattering. We

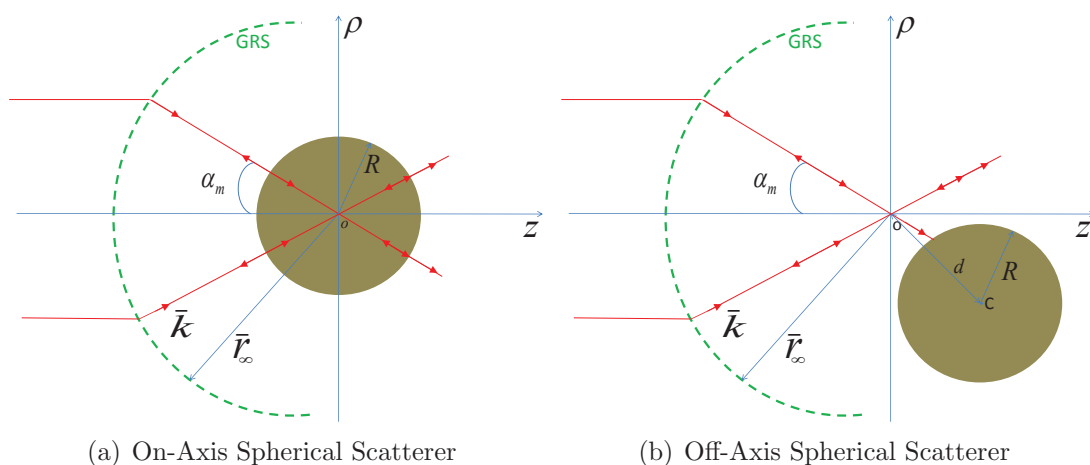


Figure 1.4: Spherical Scatterer.

also show that for the spherical scatterer, our definition results in the same total internal and external fields as the definition by the GLMT. Through our derivation of the total internal and external fields of the sphere, we demonstrate how to derive the DSs in a simple and straightforward way.

## 1.5 Solid Immersion Microscopy

High spatial resolution and optical collection efficiency are the most desirable properties of nearly all optical systems. The solid immersion technique is one of the optimal techniques that provide both of these important properties. Consequently, the technique has been extensively employed in microscopy [80–88], optical data storage [89–91], and photolithography [92]. The central component of the technique is a solid immersion lens (SIL). Optical systems using SILs normally involve focusing a high-aperture beam through a spherical interface. The performance of such systems has been analyzed in theory [86–89, 91, 93–100] and investigated by experiment [81, 82, 86, 89, 90, 92]. Figures 1.3(a) and 1.3(b) illustrate the main part of the systems. Most theoretical researchers analyzed the focusing systems using the angular spectrum representation of optical field developed by Richards and Wolf [32].

Ichimura *et al.* derived and analyzed the focal field of a SIL-based system, which is simplified and shown in Fig. 1.3(a). He applied electromagnetic boundary conditions at the spherical interface for the strength factors of the geometrical rays: in other words he matched the strength factors at the boundary. This application is not rigorous since the true boundary condition is that the tangential electric fields must be matched at the boundary, whereas the strength factors are not equivalent to the tangent electric fields. Consequently, Ichimura missed a phase change in the final expression of the focal field [89]. Some other researchers used similar approaches to Ichimura [88, 91, 95–97]. Recently, Ippolito *et al.* extended the Ichimura model by integrating a ray optics spherical aberration into Ichimura’s result [87]. Ippolito used the ray reference concept for calculating the spherical aberration. This ray reference concept was criticized by Sheppard and

Goh [101]. In their comment, Sheppard and Goh used a point reference concept. They took the Gaussian image point of the focusing system as the reference point. Sheppard and Goh's idea is in fact similar to Wolf's idea [31]. Nevertheless, there still exist some controversies on this fundamental concept [102]. This thesis will provide a clearer view on what happens at the SIL's boundary and solve the controversies.

Later, Vamivakas *et al.* proposed a model that directly solves the boundary conditions in the scope of the angular spectrum representation [103]. Vamivakas' idea is to express the electric field just outside the SIL as a superposition of an infinite number of individual plane waves. Then for each individual plane wave, he applied the boundary conditions as he had applied for a planar interface and derived the focal field by summing up an infinite number of the transmitted individual plane waves. Their idea is in fact similar to a rigorous analytical model proposed by Török *et al.* [104]. There are at least two similar models to the Vamivakas model [93, 94]. However, there exists doubt in the accuracy of extending the model of focusing light through a planar interface to form a model of focusing light through a spherical interface [86]. In fact, the treatment of the boundary conditions is not rigorously correct. This thesis will show how to solve the boundary conditions rigorously.

The angular spectrum representation developed from the angular spectrum method (ASM) expands the focal field into the superposition of an infinite number of individual plane waves. The angular spectrum representation is now widely used to study both the forward and inverse problems of focusing light using an aplanatic lens [105, 106]. However, the expansion presents a difficulty for solving the boundary conditions at the spherical interface. Recently, we expanded the focal field into vectorial spherical harmonics [26] that allows to solve the boundary conditions rigorously [38]. Using our expansion, we can also solve the inverse problem. This thesis uses the vectorial spherical harmonics for calculating the focal field rigorously.

---

## 1.6 Polarized Beams and Annular Filter

The study of electromagnetic fields around a focus of a high numerical aperture optical system is very topical in many areas of science such as microscopy [15, 107–110], particle trapping [111, 112], quantum electrodynamics [43], nonlinear optics [113], and near-field optics [90, 92]. Thus, it is of practical and scientific interest to derive and understand the nature of the fields in the focal region. It had been pointed out by Richards and Wolf [32] that the polarization of a focused beam has a decisive role on the size and shape of the focal point of a high numerical aperture (NA) aplanatic lens. Using theoretical analysis, they predicted that the focal-plane electric intensity produced by focusing a linearly-polarized beam with a high NA lens should be highly asymmetric. The theoretical prediction was later experimentally confirmed by Dorn *et al.* [114]. Serrels *et al.* exploited the asymmetric property of the focal spot to improve the resolution of solid immersion microscope [85]. However, it is also well-known that the radially-polarized beam (transversal magnetic beam) produces a tighter focal spot compared to the linearly-polarized beam [16]. Recently, the azimuthally-polarized beam combined with a phase plate has been theoretically proved to produce an even tighter spot compared to the radially-polarized beam [115]. In fact, the azimuthally-polarized beam after passing the phase plate becomes the azimuthally-polarized beam with a vortex. Manipulating phase and amplitude of the polarized beam to achieve a certain distribution of the focal field has always been active topics since long time ago. For example, the use of an annular filter to block the center part of incoming beam and produce the Bessel beam was shown by Rayleigh ([116], and references therein). Recently, using of many annuli to manipulate both the phase and the amplitude of a beam for sub-wavelength imaging has been studied extensively [117, 118]. The ability to obtain the sub-wavelength spot using an array of the annuli is related to a phenomenon known as super-oscillation which describes the fact that a band-limited function is able locally to oscillate arbitrarily quickly, faster than its highest Fourier component [118]. In terms of multipole expansions, this phenomenon is equivalent to the fact that by manipulating the phase and the amplitude of the incident beam, we can obtain a set of the multipole strengths which produce a sub-wavelength focal spot. In this thesis,

we study different polarizations and their impact on the focal field. We also show that an annular filter can improve the resolution of solid immersion microscope significantly.

## Chapter 2

### Multipole and Plane Wave

### Expansions of Diverging and

### Converging Fields

The nature of light has drawn attention of most of the greatest scientists like Christian Huyghen, James Clerk Maxwell, Max Planck, Einstein, just to name some. After a long history of debating on the nature of light, today light is known to exhibit both particle-like and wave-like properties. Among many great contributors to the development of the emission (or corpuscular) theory, Isaac Newton is considered to be the best known scientist, who devoted himself to the theory and made a major contribution to the theory. At the same time of the fast development of the emission theory, the wave theory of light also got developed and a firm foundation of the wave theory was formed during this time. Robert Hooke and Christian Huyghen can be considered as the first contributors to the development of the wave theory of light [1]. From the very beginning of the development, the researches in electricity and magnetism had developed almost independently of the light researches. After James Clerk Maxwell summed up and wrote the results in a system of equations to describe the behavior of electromagnetic field, he conjectured that the light waves were electromagnetic waves. The conjecture was later confirmed by Heinrich Hertz [1]. Now, almost of the optical researches are based on the Maxwell's equations. In

## 2. Multipole and Plane Wave Expansions of the Electromagnetic Field

his famous series of lectures on physics [3], Feynman describe the Maxwell's equations as the center of the universe of electromagnetism-the complete theory of electricity and magnetism, and of light. It is probably one of the greatest accomplishments of physics. For a convenient reference, we write down the Maxwell's equations and their solutions due to a charge-current distribution  $(\rho, \bar{J})$  as follows [3]:

### 1. Maxwell's equations:

$$\begin{aligned}\nabla \cdot \bar{E} &= \frac{\rho}{\varepsilon} & \nabla \cdot \bar{B} &= 0 \\ \nabla \times \bar{E} &= -\frac{\partial \bar{B}}{\partial t} & c^2 \nabla \times \bar{B} &= \frac{\bar{J}}{\varepsilon} + \frac{\partial \bar{E}}{\partial t}.\end{aligned}$$

### 2. Their solutions:

$$\begin{aligned}\bar{E} &= -\nabla\phi - \frac{\partial \bar{A}}{\partial t}, \\ \bar{B} &= \nabla \times \bar{A}, \\ \phi(\bar{r}_1, t) &= \int_{V_2} \frac{\rho(\bar{r}_2, t - \frac{r_{12}}{c})}{4\pi\varepsilon r_{12}} d^3\bar{r}_2, \\ \bar{A}(\bar{r}_1, t) &= \int_{V_2} \frac{\bar{J}(\bar{r}_2, t - \frac{r_{12}}{c})}{4\pi\varepsilon c^2 r_{12}} d^3\bar{r}_2,\end{aligned}$$

where the electromagnetic field is observed at  $(\bar{r}_1, t)$  due to the source at  $\bar{r}_2 \in V_2$ ,  $r_{12} = |\bar{r}_1 - \bar{r}_2|$ , and  $c$  is the velocity of light.

For a particular case, the Maxwell's equations and their solutions can be simplified much further. Throughout this thesis, we study a monochromatic field only and in our special case, the solutions of the Maxwell's equations are simplified to be summations of plane waves or multipole fields.

## 2.1 Scalar Multipole Fields

Erdélyi showed that [119]

$$\Lambda_{lm}(\bar{r}) = j_l(kr)Y_l^m(\theta, \phi) = C_l^m \left\{ \left[ \frac{1}{ik} \left( \frac{\partial}{\partial x} + i \frac{\partial}{\partial y} \right) \right]^m P_l^{(m)} \left( \frac{1}{ik} \frac{\partial}{\partial z} \right) \right\} \frac{\sin(kr)}{kr}, \quad (2.1)$$

$$\Pi_{lm}^{(1)}(\bar{r}) = h_l^{(1)}(kr)Y_l^m(\theta, \phi) = C_l^m \left\{ \left[ \frac{1}{ik} \left( \frac{\partial}{\partial x} + i \frac{\partial}{\partial y} \right) \right]^m P_l^{(m)} \left( \frac{1}{ik} \frac{\partial}{\partial z} \right) \right\} \frac{e^{ikr}}{ikr}, \quad (2.2)$$

$$\Pi_{lm}^{(2)}(\bar{r}) = h_l^{(2)}(kr)Y_l^m(\theta, \phi) = C_l^m \left\{ \left[ \frac{1}{ik} \left( \frac{\partial}{\partial x} + i \frac{\partial}{\partial y} \right) \right]^m P_l^{(m)} \left( \frac{1}{ik} \frac{\partial}{\partial z} \right) \right\} \frac{e^{-ikr}}{-ikr}, \quad (2.3)$$

we can easily realize the following relationship

$$\Pi_{lm}^{(1)}(\bar{r}) + \Pi_{lm}^{(2)}(\bar{r}) = 2\Lambda_{lm}(\bar{r}). \quad (2.4)$$

It can be verified that the scalar multipole fields  $\Pi_{lm}^{(1)}(\bar{r})$  and  $\Pi_{lm}^{(2)}(\bar{r})$  satisfy the Maxwell's equations in a free-source region except the origin of the coordinate system and the scalar multipole field  $\Lambda_{lm}(\bar{r})$  satisfies the equations in the free-source region including the origin. The scalar multipole field  $\Lambda_{lm}(\bar{r})$  is appropriate for a description of a source-free monochromatic scalar wave field [120]. On the other hand,  $\Pi_{lm}^{(1)}(\bar{r})$  and  $\Pi_{lm}^{(2)}(\bar{r})$  are appropriate for descriptions of a monochromatic scalar wave field in presence of a localized source distribution or a localized sink distribution, respectively. Whittaker expanded the multipole field  $\Lambda_{lm}(\bar{r})$  in terms of homogeneous plane waves as follows [120]:

$$\Lambda_{lm}(\bar{r}) = j_l(kr)Y_l^m(\theta, \phi) = (-i)^l \frac{1}{4\pi} \int_0^{2\pi} d\beta \int_0^\pi d\alpha \sin \alpha Y_l^m(\alpha, \beta) e^{i\bar{k} \cdot \bar{r}}. \quad (2.5)$$

Devaney and Wolf cited the article of Erdélyi and used the following definition for the scalar multipole field in Appendix A of their paper [53]:

$$\Pi_{lm}^{(1)}(\bar{r}) = C_l^m \left\{ \left[ \frac{1}{ik} \left( \frac{\partial}{\partial x} + i \frac{\partial}{\partial y} \right) \right]^m P_l^{(m)} \left( \frac{1}{ik} \frac{\partial}{\partial z} \right) \right\} \frac{e^{ikr}}{kr}, \quad (2.6)$$

Comparing Eqs. (2.2) and (2.6), we observe that Devaney and Wolf ignored a complex

## 2. Multipole and Plane Wave Expansions of the Electromagnetic Field

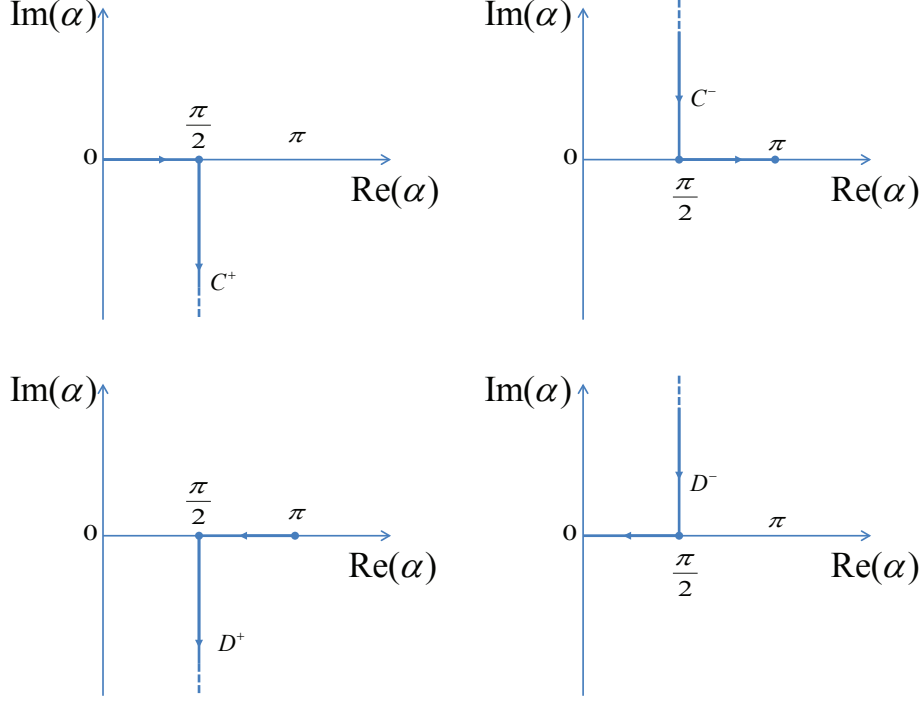


Figure 2.1: Integration contours.

unit  $i$  in the denominator of the outgoing spherical wave  $\frac{e^{ikr}}{ikr}$ . Consequently, they derived the following expression

$$\prod_{lm}^{(1)}(\vec{r}) = (-i)^l \frac{i}{2\pi} \int_0^{2\pi} d\beta \int_{C^\pm} d\alpha \sin \alpha Y_l^m(\alpha, \beta) e^{i\vec{k} \cdot \vec{r}}, \quad (2.7)$$

where the integral contours  $C^\pm$  are shown in Fig. 2.1.

If Devaney and Wolf used the correct form of Erdélyi's result for the multipole field  $\prod_{lm}^{(1)}(\vec{r})$ , then the following formula should be obtained

$$\prod_{lm}^{(1)}(\vec{r}) = (-i)^l \frac{1}{2\pi} \int_0^{2\pi} d\beta \int_{C^\pm} d\alpha \sin \alpha Y_l^m(\alpha, \beta) e^{i\vec{k} \cdot \vec{r}}. \quad (2.8)$$

Devaney and Wolf also compared the constant term outside the integrals in Eqs. (2.5) and (2.7), they found that the two terms are different by a fraction  $\frac{-i}{2}$ . Then, they explained the fraction as trivial due to the different integral domains on the right sides of Eqs. (2.5) and (2.7). In fact, the fraction is  $\frac{1}{2}$  and the fraction is nontrivial since it relates to the integral domains.

## 2. Multipole and Plane Wave Expansions of the Electromagnetic Field

---

In derivation of Eq. (2.8), we have substituted Weyl's formula [120]

$$\frac{e^{ikr}}{ikr} = \frac{1}{2\pi} \int_0^{2\pi} d\beta \int_{C^\pm} d\alpha \sin \alpha e^{i\bar{k}\cdot\bar{r}} \quad (2.9)$$

into Eq. (2.2). Similarly, we substitute the following expression for converging spherical wave [121]:

$$\frac{e^{-ikr}}{-ikr} = -\frac{1}{2\pi} \int_0^{2\pi} d\beta \int_{D^\pm} d\alpha \sin \alpha e^{i\bar{k}\cdot\bar{r}} \quad (2.10)$$

into Eq. (2.3), then we can derive

$$\prod_{lm}^{(2)}(\bar{r}) = -(-i)^l \frac{1}{2\pi} \int_0^{2\pi} d\beta \int_{D^\pm} d\alpha \sin \alpha Y_l^m(\alpha, \beta) e^{i\bar{k}\cdot\bar{r}}. \quad (2.11)$$

In Eqs. (2.7)-(2.11), we use the integral contour  $C^+$  and  $D^+$  ( $C^-$  and  $D^-$ ) for the region  $z > 0$  ( $z < 0$ ). It is noteworthy to list down some important observations here

- The expressions in Eqs. (2.5), (2.8), and (2.11) agree with the expression in Eq. (2.4) as expected.
- The integrations in Eqs. (2.8) and (2.11) over the imaginary parts of  $\alpha$  are correspondent to the evanescent parts of multipole fields. Moreover, the evanescent parts are out of phase and cancel each other completely when being added up.

## 2.2 Electromagnetic Fields due to a Source and a Sink

We consider a real, monochromatic, electromagnetic field [53]  $\bar{E}(\bar{r}, t) = \text{Re}\{\bar{E}(\bar{r})e^{-i\omega t}\}$  generated by a charge-current distribution

$$\rho(\bar{r}, t) = \text{Re}\{\rho(\bar{r})e^{-i\omega t}\}, \quad \bar{J}(\bar{r}, t) = \text{Re}\{\bar{J}(\bar{r})e^{-i\omega t}\}. \quad (2.12)$$

We assume that  $\rho(\bar{r})$  and  $\bar{J}(\bar{r})$  are continuous and continuously differentiable functions of position and vanish identically outside a sphere of radius  $R$  as shown in Fig. 1.1(a).

## 2. Multipole and Plane Wave Expansions of the Electromagnetic Field

From Maxwell's equations, we can show that  $\bar{E}(\bar{r})$  satisfies the equation

$$(\Delta^2 + k^2)\bar{E}(\bar{r}) = -4\pi \left[ i\frac{k}{c}\bar{J}(\bar{r}) - \nabla\rho(\bar{r}) \right]. \quad (2.13)$$

Here  $\bar{E}(\bar{r})$  represents a diverging field in the case that  $\rho(\bar{r})$  and  $\bar{J}(\bar{r})$  represent a source as shown in Fig. 1.1(a). If the charge-current distribution represents a sink,  $\bar{E}(\bar{r})$  represents a converging field.

To continue, we assume that  $\bar{J}_1(\bar{r})$  and  $\rho_1(\bar{r})$  play the role of a source which is radiating the electromagnetic field. And hence, the field  $\bar{E}_1(\bar{r})$  behaves at infinity as outgoing spherical wave. We use the Green function for outgoing wave and obtain the outgoing field

$$\bar{E}_1(\bar{r}) = \frac{ik}{2\pi} \int_0^{2\pi} d\beta_1 \int_{C^\pm} d\alpha_1 \sin\alpha_1 \hat{E}_1(\hat{s}_1) e^{i\bar{k}_1 \cdot \bar{r}}, \quad (2.14)$$

where the spectral amplitude vector  $\hat{E}_1(\hat{s})$  is given by

$$\hat{E}_1(\hat{s}) = \int_{|\bar{r}'| \leq R} \left[ i\frac{k}{c}\bar{J}_1(\bar{r}') - \nabla\rho_1(\bar{r}') \right] e^{-i\bar{k}_1 \cdot \bar{r}'} d^3\bar{r}'. \quad (2.15)$$

The outgoing wave is shown in Fig. 1.1(a). Equation (2.14) expands the electric field in terms of plane waves. Alternatively, we can expand the electric fields in terms of vectorial multipole fields. It is worth reminding that the vector spherical harmonics is

$$\begin{aligned} \mathbf{Y}_l^m(\alpha, \beta) &= L_s Y_l^m(\alpha, \beta) \\ &= -i \left( \hat{\beta} \frac{\partial}{\partial \alpha} Y_l^m(\alpha, \beta) - \hat{\alpha} \frac{1}{\sin \alpha} \frac{\partial}{\partial \beta} Y_l^m(\alpha, \beta) \right) \\ &= -i \left( \hat{\beta} \frac{\partial}{\partial \alpha} Y_l^m(\alpha, \beta) - \hat{\alpha} \frac{im}{\sin \alpha} Y_l^m(\alpha, \beta) \right). \end{aligned}$$

It is also known that  $\mathbf{Y}_l^m(\alpha, \beta)$  and  $\hat{\mathbf{s}} \times \mathbf{Y}_l^m(\alpha, \beta)$  form a complete orthogonal basis for all vectors perpendicular to  $\hat{\mathbf{s}}$ . Hence, we can express  $\hat{E}_1(\hat{s}_1)$  as follows

$$\hat{E}_1(\hat{s}_1) = \sum_{l=1}^{\infty} \sum_{m=-l}^l (-i)^{l+1} \{ g_{El}^m [\hat{s}_1 \times \mathbf{Y}_l^m(\alpha_1, \beta_1)] + g_{Ml}^m [\mathbf{Y}_l^m(\alpha_1, \beta_1)] \}. \quad (2.16)$$

## 2. Multipole and Plane Wave Expansions of the Electromagnetic Field

Applying orthogonality of the vector spherical harmonics to Eq. (2.16), we obtain

$$\begin{aligned} g_{El}^m &= \frac{i^{l+1}}{l(l+1)} \int_0^{2\pi} \int_0^\pi (\hat{E}_1(\hat{s}_1) \times \hat{s}_1) \cdot \mathbf{Y}_l^{m*}(\alpha_1, \beta_1) \sin \alpha_1 d\alpha_1 d\beta_1, \\ g_{Ml}^m &= \frac{i^{l+1}}{l(l+1)} \int_0^{2\pi} \int_0^\pi \hat{E}_1(\hat{s}_1) \cdot \mathbf{Y}_l^{m*}(\alpha_1, \beta_1) \sin \alpha_1 d\alpha_1 d\beta_1, \end{aligned} \quad (2.17)$$

Substituting Eq. (2.16) into Eq. (2.14), interchanging the order of the integration and summation, we obtain

$$\bar{E}_1(\bar{r}) = \sum_{l=1}^{\infty} \sum_{m=-l}^l [g_{El}^m \mathbf{N}_{lm}^{(1)}(\bar{r}) + g_{Ml}^m \mathbf{M}_{lm}^{(1)}(\bar{r})], \quad (2.18)$$

where

$$\mathbf{N}_{lm}^{(1)}(\bar{r}) = (-i)^l \frac{k}{2\pi} \int_0^{2\pi} d\beta_1 \int_{C^\pm} d\alpha_1 \sin \alpha_1 [\hat{s}_1 \times \mathbf{Y}_l^m(\alpha_1, \beta_1)] e^{i\bar{k}_1 \cdot \bar{r}}, \quad (2.19)$$

$$\mathbf{M}_{lm}^{(1)}(\bar{r}) = (-i)^l \frac{k}{2\pi} \int_0^{2\pi} d\beta_1 \int_{C^\pm} d\alpha_1 \sin \alpha_1 \mathbf{Y}_l^m(\alpha_1, \beta_1) e^{i\bar{k}_1 \cdot \bar{r}}. \quad (2.20)$$

We can prove that Eqs. (2.19) and (2.20) are exactly the electric and magnetic multipole fields as follows:

$$\mathbf{N}_{lm}^{(1)}(\bar{r}) = \nabla \times \nabla \times [\bar{r} \prod_{lm}^{(1)}(\bar{r})], \quad (2.21)$$

$$\mathbf{M}_{lm}^{(1)}(\bar{r}) = ik \nabla \times [\bar{r} \prod_{lm}^{(1)}(\bar{r})]. \quad (2.22)$$

We can obtain the time-reversed field  $\bar{E}_1^{tr}(\bar{r})$  of the radiated field  $\bar{E}_1(\bar{r})$  by applying the phase conjugation to the vectorial field in Eq. (2.18):

$$\bar{E}_1^{tr}(\bar{r}) = \sum_{l=1}^{\infty} \sum_{m=-l}^l [g_{El}^{m*} \mathbf{N}_{lm}^{(2)}(\bar{r}) - g_{Ml}^{m*} \mathbf{M}_{lm}^{(2)}(\bar{r})]. \quad (2.23)$$

For complete absorption of the time-reversed field, the sink, which is the time-reversed source, must comprise the charge-current distribution  $(\rho_1(\bar{r}, -t), \bar{J}_1(\bar{r}, -t))$  [122]. More details on the sink can be obtained in Refs. [5, 7, 123, 124].

For convenience, we denote the time-reversed field as  $\bar{E}_2(\bar{r})$  and the time-reversed

## 2. Multipole and Plane Wave Expansions of the Electromagnetic Field

source as  $\bar{J}_2(\bar{r})$  and  $\rho_2(\bar{r})$ . The electric field  $\bar{E}_2(\bar{r})$  behaves at infinity as ingoing spherical wave and we can show that [125]:

$$\bar{E}_2(\bar{r}) = -\frac{ik}{2\pi} \int_0^{2\pi} d\beta_2 \int_{D^\pm} d\alpha_2 \sin \alpha_2 \hat{E}_2(\hat{s}_2) e^{i\bar{k}_2 \cdot \bar{r}}, \quad (2.24)$$

where the spectral amplitude vector  $\hat{E}_2(\hat{s}_2)$  is given by

$$\hat{E}_2(\hat{s}_2) = \int_{|\bar{r}'| \leq R} \left[ i \frac{k}{c} \bar{J}_2(\bar{r}') - \nabla \rho_2(\bar{r}') \right] e^{-i\bar{k}_2 \cdot \bar{r}'} d^3\bar{r}'. \quad (2.25)$$

Figure 1.1(b) shows the ingoing wave, i.e. the wave is traveling from the infinity to the origin. Of course, in this case, the Sommerfeld's radiation condition is no longer satisfied. Alternative to the plane wave expansions in Eq. (2.24), we can expand the converging field in terms of vectorial multipole fields as follows:

$$\bar{E}_2(\bar{r}) = \sum_{l=1}^{\infty} \sum_{m=-l}^l [q_{El}^m \mathbf{N}_{lm}^{(2)}(\bar{r}) + q_{Ml}^m \mathbf{M}_{lm}^{(2)}(\bar{r})], \quad (2.26)$$

where

$$\mathbf{N}_{lm}^{(2)}(\bar{r}) = \nabla \times \nabla \times [\bar{r} \prod_{lm}^{(2)}(\bar{r})], \quad (2.27)$$

$$\mathbf{M}_{lm}^{(2)}(\bar{r}) = ik \nabla \times [\bar{r} \prod_{lm}^{(2)}(\bar{r})]. \quad (2.28)$$

The multipole strengths  $q_{El}^m$  and  $q_{Ml}^m$  can be evaluated using Eq. (2.17) in which  $\hat{E}_1$ ,  $\hat{s}_1$ ,  $\alpha_1$ , and  $\beta_1$  are replaced with  $\hat{E}_2$ ,  $\hat{s}_2$ ,  $\alpha_2$ , and  $\beta_2$ , respectively. Now, we consider the case in which the time-reversed field approaches the focus without a sink. Due to energy flux conservation, there must be a diverging wave from the focus following the converging wave [12]. This case is similar to the case of focusing by an aplanatic system as presented in Fig. 1.2. In the source-free region, we observe  $\hat{E}_1 = \hat{E}_2 = \hat{E}$  and  $\bar{k}_1 = \bar{k}_2 = \bar{k}$ . As a result, we have  $q_{El}^m = g_{El}^m = p_{El}^m$  and  $q_{Ml}^m = g_{Ml}^m = p_{Ml}^m$ . Hence without the sink, the total field will be the interference between the converging field  $\bar{E}_2$  and the diverging field  $\bar{E}_1$ .

## 2. Multipole and Plane Wave Expansions of the Electromagnetic Field

---

Adding Eq. (2.14) and Eq. (2.24) we obtain

$$\bar{E}(\bar{r}) = \frac{ik}{2\pi} \int_0^{2\pi} d\beta \int_0^\pi d\alpha \sin \alpha \hat{E}(\hat{s}) e^{i\bar{k} \cdot \bar{r}}, \quad (2.29)$$

Equivalently, we can express the total field in terms of multipole fields by adding Eq. (2.18) and Eq. (2.26):

$$\begin{aligned} \bar{E}(\bar{r}) &= \bar{E}_1(\bar{r}) + \bar{E}_2(\bar{r}) \\ &= 2 \sum_{l=1}^{\infty} \sum_{m=-l}^l [p_{El}^m \mathbf{N}_{lm}(\bar{r}) + p_{Ml}^m \mathbf{M}_{lm}(\bar{r})], \end{aligned} \quad (2.30)$$

where

$$\mathbf{N}_{lm}(\bar{r}) = \nabla \times \nabla \times [\bar{r} \bigwedge_{lm}(\bar{r})], \quad (2.31)$$

$$\mathbf{M}_{lm}(\bar{r}) = ik \nabla \times [\bar{r} \bigwedge_{lm}(\bar{r})]. \quad (2.32)$$

- We note that Eqs. (2.14), (2.24), and (2.29) describe outgoing, ingoing, and standing waves in terms of an infinite number of different plane waves.
- Whereas  $\bar{E}(\bar{r})$  is a subject to diffraction limit,  $\bar{E}_1(\bar{r})$  and  $\bar{E}_2(\bar{r})$  are not limited by the diffraction. We will discuss about these waves and their implication in next sections.

It is worth noting that Eq. (2.18) is related to Weyl's expansion and usually used to describe the field due to a source. Equation (2.30) is related to Whittaker's expansion and used to describe the total field in a source-free region. There are some time-space domains in which both are valid, such as the whole space, except the origin, after the source ceased to radiate [120].

## 2.3 Angular Spectrum Representation of Electromagnetic Fields

We can see that both the plane wave expansions (Eqs. (2.14), (2.24), (2.29)) and multipole expansions (Eqs. (2.18), (2.26), (2.30)) are mode expansions of the electromagnetic fields in the sense that each of the individual plane waves and multipole fields satisfy the same wave equation in the same validity domains as their corresponding total fields. However, only the multipole expansions are true mode expansions of the field outside the source region. Each expression has its own advantages and disadvantages. On one hand, plane wave expansions are convenient in solving some problems, such as forward diffraction, inverse diffraction, and focusing through a planar boundary. On the other hand, multipole expansions play a crucial role in scattering theory, optical trapping, optical nanomaterial design [126], and focusing through a spherical boundary [38, 39]. Moreover, the multipole expansions are particularly useful in calculating the orbital angular momentum and the spin angular momentum of the field which play an important role in the control of light-matter interactions [127–129]. It should be noted that the two expansions are equivalent and the field expressions can be expressed in terms of its angular spectrum by exploiting the transformation that maps angular variables  $\alpha$  and  $\beta$  to spatial frequency variables  $k_x$  and  $k_y$  [130] as follows

$$k_x = k \sin \alpha \cos \beta \text{ and } k_y = k \sin \alpha \sin \beta. \quad (2.33)$$

For example, substituting Eq. (2.33) into Eq (2.9), we can obtain the angular spectrum representation of the spherical wave

$$\frac{e^{ikr}}{r} = \frac{i}{2\pi} \int_{-\infty}^{+\infty} \int_{-\infty}^{+\infty} \frac{1}{k_z} e^{i(k_x x + k_y y + k_z |z|)} dk_x dk_y, \quad (2.34)$$

where  $k_z = \sqrt{k^2 - k_x^2 - k_y^2}$ . Borghi used the transformation in Eq. (2.33) for deriving the angular spectrum representation of multipole wave fields [130]. Alternative to Borghi's

## **2. Multipole and Plane Wave Expansions of the Electromagnetic Field**

---

method, Arnoldus derived another angular spectrum representation for the electromagnetic multipole fields and then he used the expression for solving the reflection problem due to the multipole fields approaching a perfect conductor [131]. Similarly, we can express the ingoing and outgoing beams in terms of its angular spectrum.

The angular spectrum representation of an optical field has been extensively developed and used in optical society, especially for topics related to a focusing system [31, 32, 132]. In next chapter, we will discuss the angular spectrum representation and multipole expansions of the focal field of an aplanatic lens.

# Chapter 3

## Angular Spectrum Representation and Multipole Theory for the Focal Fields

In chapter 2, we have derived both plane wave and multipole expansions for both incoming and outgoing electromagnetic fields. In this chapter, we will employ the expansions to study the focal field when a collimated polarized beam is focused by an aplanatic lens. We first review how an incident collimated beam approaching the aplanatic lens propagates through the lens. Then we study the propagation of the focused beam in the image space using the two expansions.

### 3.1 Aplanatic Lens Modeling

We consider a case of focusing a paraxial monochromatic polarized beam from medium 1 with the refractive index  $n_1$  into medium 2 with the refractive index  $n_2$  using an aplanatic lens as shown in Fig 3.1. Throughout this thesis, we consider the lens with a very large focal length  $f$  compared to the wavelength  $\lambda$  of the polarized beam and we also consider the polarized beam with very large wave-number only. The modeling of this lens was well explained and derived by Richards and Wolf [32]. The central idea is that we can replace the lens by a Gaussian reference sphere (GRS) as shown in Fig. 3.1. In other words,

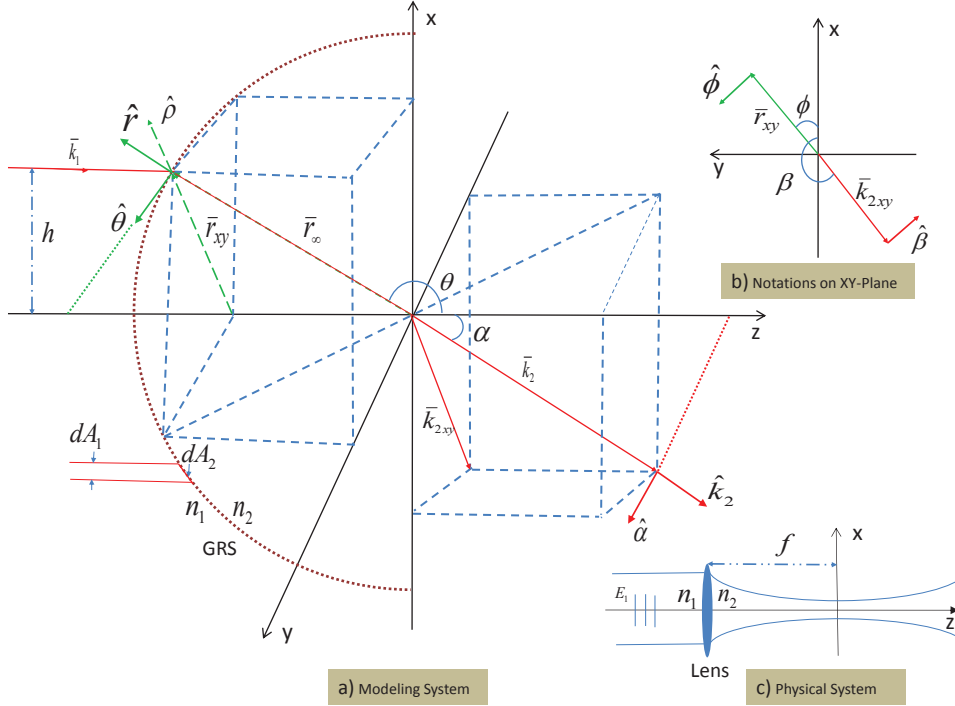


Figure 3.1: Aplanatic Lens Modeling.

the effects of the lens on the beam propagation can be described by the *sine condition* and the *intensity law*. Throughout this thesis, we use  $(r, \theta, \phi)$  and  $(k, \alpha, \beta)$  to represent an observation field point  $\bar{r}$  and a wave vector  $\bar{k}$ , respectively. All parameters with a hat above them are unit vectors representing their directions - for example-  $\hat{k}_2$  is an unit vector representing vector  $\bar{k}_2$ . The *sine condition* and the *intensity law* are described as follows [32, 103]:

- The *sine condition* states that each ray approaching the lens intersect its conjugate ray, which propagates toward the focus, at the surface of the GRS. In other words, we have  $h = f \sin \alpha$  with the notations shown in Fig. 3.1.
- The *intensity law* is in fact the fundamental law of energy conservation. We know that the power carried by a bundle of rays with an infinitesimal cross-section perpendicular to the ray propagation  $dA$  is  $P = \frac{1}{2} \frac{|\bar{E}|^2}{Z_{\mu\epsilon}} dA$  where  $Z_{\mu\epsilon}$  is the wave impedance. For the beam passing through the lens, we assume the bundle of rays passing the lens without loss due to absorption and reflection, the power should be conserved at the interface between the two mediums. Hence, at the GRS, we have  $P_1 = P_2 \Leftrightarrow \frac{|\bar{E}_1|^2}{Z_1} dA_1 = \frac{|\bar{E}_2|^2}{Z_2} dA_2$ , where  $dA_1 = dA_2 \cos \alpha$  and

$\frac{Z_2}{Z_1} = \sqrt{\frac{\mu_2 \varepsilon_1}{\mu_1 \varepsilon_2}} = \left( \sqrt{\frac{n_1}{n_2}} \sqrt{\frac{\mu_2}{\mu_1}} \right)^2$ . Consequently, we obtain

$$|\bar{E}_2| = |\bar{E}_1| \sqrt{\frac{n_1}{n_2}} \sqrt{\frac{\mu_2}{\mu_1}} \sqrt{\cos \alpha}. \quad (3.1)$$

For most mediums,  $\mu \simeq 1 \Rightarrow \frac{\mu_2}{\mu_1} \simeq 1$ , Eq. (3.1) is simplified to be

$$|\bar{E}_2| = |\bar{E}_1| \sqrt{\frac{n_1}{n_2}} \sqrt{\cos \alpha}. \quad (3.2)$$

In our case study, we also have  $n_1 = n_2 = 1$ . But in some special cases like liquid immersion microscope, we have  $n_1 \neq n_2$ .

Hence, given the amplitude of the electric field  $\bar{E}_1$  of the incident collimated beam, the amplitude of the electric field  $\bar{E}_2$  of the focused beam on the GRS can be evaluated using Eq. (3.2). Another property of the focused beam is that the polarization has not been known. To derive the polarization of the focused beam, we consider a meridional plane which is formed by the optical axis ( $z$ -axis) and the wave vector  $\bar{k}_2$ . It has been explained that the angle between the electric vector and the meridional plane can be considered to be unchanged during the propagation of a ray through the lens [32]. To derive the polarization of the focused field, we decompose the incident field into *p-polarization* and *s-polarization* components in which *p-polarization* and *s-polarization* are parallel and perpendicular to the meridional plane, respectively. For a convenient purpose, the incident electric field is expressed in the cylindrical coordinates  $(\hat{\rho}, \hat{\phi})$  as shown in Fig. 3.1. Similarly, the focused electric field is expressed in terms of  $\hat{\alpha}$  (*p-polarization*) and  $\hat{\beta}$  (*s-polarization*), where  $\alpha$  and  $\beta$  specify the direction of the propagation of the focused electric field. At the interface, we can approximate the interface to be locally-flat. Moreover, both media are isotropic, hence the *s-polarization* and *p-polarization* of the incident electric field are mapped into the *s-polarization* and *p-polarization* of the focused electric

### 3. Multipole Theory and Angular Spectrum Representation for the Focal Fields

---

field, respectively. Mathematically, we can express the fields as follows

$$\bar{E}_1 = \bar{E}_1^{(s)} + \bar{E}_1^{(p)} = E_{1\phi}\hat{\phi} + E_{1\rho}\hat{\rho}, \quad (3.3)$$

$$\bar{E}_2 = \bar{E}_2^{(s)} + \bar{E}_2^{(p)} = E_{2\beta}\hat{\beta} + E_{2\alpha}\hat{\alpha}. \quad (3.4)$$

Equation (3.2) applies for both *s-polarization* and *p-polarization* components, hence we have

$$E_{2\beta} = -E_{1\phi}\sqrt{\frac{n_1}{n_2}}\sqrt{\cos\alpha}, \quad (3.5)$$

$$E_{2\alpha} = -E_{1\rho}\sqrt{\frac{n_1}{n_2}}\sqrt{\cos\alpha}. \quad (3.6)$$

The minus sign in Eqs. (3.5) and (3.6) accounts for the fact that  $\hat{\beta}$  and  $\hat{\phi}$  are of opposite signs and so are  $\hat{\alpha}$  and  $\hat{\rho}$ . Substituting Eqs. (3.5) and (3.6) into Eq. (3.4), we obtain the focused electric field  $\bar{E}_2$

$$\bar{E}_2 = -[E_{1\phi}\hat{\beta} + E_{1\rho}\hat{\alpha}]\sqrt{\frac{n_1}{n_2}}\sqrt{\cos\alpha}. \quad (3.7)$$

We can express the focused electric field in the Cartesian coordinates by introducing the transformations  $\hat{\beta} = -\hat{x}\sin\beta + \hat{y}\cos\beta$ ,  $\hat{\alpha} = \hat{x}\cos\beta\cos\alpha + \hat{y}\sin\beta\cos\alpha - \hat{z}\sin\alpha$  into Eq. (3.7) to obtain

$$\bar{E}_2 = - \left[ E_{1\phi} \begin{pmatrix} -\sin\beta \\ \cos\beta \\ 0 \end{pmatrix} + E_{1\rho} \begin{pmatrix} \cos\beta\cos\alpha \\ \sin\beta\cos\alpha \\ -\sin\alpha \end{pmatrix} \right] \sqrt{\frac{n_1}{n_2}}\sqrt{\cos\alpha}. \quad (3.8)$$

In this section, we have derived the focused electric field on the GRS, given the incident electric field approaching the aplanatic lens. Using this focused field on the GRS as a far-field, we will derive the electromagnetic field in the whole image space using the plane wave expansions in next section.

## 3.2 Angular Spectrum Representation of Optical Fields

The previous section has derived the focused electric field on the GRS. However, how the focused field propagates in the image space is of interest. This section will model the propagation of the focused field based on the plane wave expansions. More accurately we use the angular spectrum representation of optical field for describing the propagation of the field, given the far-field on the GRS. For an example purpose, we consider the focusing of a linearly-polarized Gaussian beam using the aplanatic lens.

Bracewell [133, 134] has pointed out that physical possibility is a valid sufficient condition for the existence of a Fourier transform of a physical quantity. Hence, the electric field  $\bar{E}(x, y, z)$  at position  $(x, y, z)$  can be expressed in terms of an integral representation with respect to the variables  $k_x$ ,  $k_y$ , and  $k_z$ . In other words,  $\bar{E}(x, y, z)$  can be represented as follows

$$\begin{aligned}\bar{E}(x, y, z) &= \iiint_{-\infty}^{+\infty} \hat{\mathbf{E}}(k_x, k_y, k_z) e^{i(k_x x + k_y y + k_z z)} dk_x dk_y dk_z \\ &= \iint_{-\infty}^{+\infty} \left[ \int_{-\infty}^{+\infty} \hat{\mathbf{E}}(k_x, k_y, k_z) e^{ik_z z} dk_z \right] e^{i(k_x x + k_y y)} dk_x dk_y,\end{aligned}\quad (3.9)$$

where  $\hat{\mathbf{E}}(k_x, k_y, k_z)$  is the Fourier transform of the electric field  $\bar{E}(x, y, z)$ . Let's define  $\hat{\mathbf{E}}(k_x, k_y; z) = \int_{-\infty}^{+\infty} \hat{\mathbf{E}}(k_x, k_y, k_z) e^{ik_z z} dk_z$ , then  $\bar{E}(x, y, z)$  in Eq. (3.9) can be expressed in the following form

$$\bar{E}(x, y, z) = \iint_{-\infty}^{+\infty} \hat{\mathbf{E}}(k_x, k_y; z) e^{i(k_x x + k_y y)} dk_x dk_y.\quad (3.10)$$

In Eq. (3.10),  $\hat{\mathbf{E}}(k_x, k_y; z)$  is the angular spectrum of the field on a  $z = \text{const}$  plane. Now, we assume that the wave is traveling inside a homogeneous, isotropic, linear, and source-free medium,  $\bar{E}(x, y, z)$  satisfies the Helmholtz equation [134]:

$$(\nabla^2 + k^2)\bar{E}(x, y, z) = 0,\quad (3.11)$$

### 3. Multipole Theory and Angular Spectrum Representation for the Focal Fields

---

where  $k = n\frac{\omega}{c}$  with  $n = \sqrt{\mu\varepsilon}$  is the refractive index of the medium.

Substituting Eq. (3.10) into Eq. (3.11), we obtain

$$\frac{d^2\hat{\mathbf{E}}(k_x, k_y; z)}{dz^2} + (k^2 - k_x^2 - k_y^2)\hat{\mathbf{E}}(k_x, k_y; z) = 0 \quad (3.12)$$

Letting  $\nu^2 = k^2 - k_x^2 - k_y^2$ , the general solution of Eq. (3.12) is

$$\hat{\mathbf{E}}(k_x, k_y; z) = \mathbf{F}(k_x, k_y)e^{i\nu z} + \mathbf{G}(k_x, k_y)e^{-i\nu z}. \quad (3.13)$$

To evaluate the electromagnetic field  $\bar{\mathbf{E}}(x, y, z)$  in a specific case, we must correspondingly derive the functions  $\mathbf{F}(k_x, k_y)$  and  $\mathbf{G}(k_x, k_y)$  for the specific case. Now, we consider the case of focusing beam using the aplanatic lens. It is obvious that the focused wave, after passing through the focus of the lens, becomes a diverging beam and approaches the infinity in the half-space  $z > 0$ . We continue by assuming that our system obeys Sommerfeld's radiation condition in the half-space  $z > 0$ . In other words, at the infinity  $z = +\infty$ , there exists only the outgoing beam. This directly leads to  $\mathbf{G}(k_x, k_y) = 0$  and  $\mathbf{F}(k_x, k_y) = \hat{\mathbf{E}}(k_x, k_y; 0)$ . For a monochromatic field (constant  $k$ ) and for each set of  $(k_x, k_y)$ , there exists a unique value of  $k_z^2 = \nu^2 = k^2 - k_x^2 - k_y^2$ . Hence, Eq. (3.10) can be expressed as follows

$$\bar{\mathbf{E}}(x, y, z) = \iint_{-\infty}^{+\infty} \hat{\mathbf{E}}(k_x, k_y; 0)e^{i(k_x x + k_y y + k_z z)} dk_x dk_y. \quad (3.14)$$

If  $k_x^2 + k_y^2 > k^2$ ,  $k_z$  is pure imaginary, i.e., the corresponding wave is an evanescent wave which decays toward  $z = +\infty$ . On contrary, if  $k_x^2 + k_y^2 < k^2$ ,  $k_z$  is real. The associated wave is a homogeneous wave propagating toward  $z = +\infty$ . The case of  $k_x^2 + k_y^2 = k^2$  is associated with the transversal wave which travels in  $xy$ -plane. In our case, the focal field is of interest and the focus is far away from the aplanatic lens, hence we can ignore the wave associated with  $k_x^2 + k_y^2 > k^2$ . The focal field can be simplified from Eq. (3.14)

### 3. Multipole Theory and Angular Spectrum Representation for the Focal Fields

---

as follows

$$\bar{E}(x, y, z) = \iint_{k_x^2 + k_y^2 \leq k^2} \hat{\mathbf{E}}(k_x, k_y; 0) e^{i(k_x x + k_y y + k_z z)} dk_x dk_y. \quad (3.15)$$

For a diffraction problem, we usually know the incident field onto the scatterer. In our case, we know the incident field on the GRS. Since, the focal length of the aplanatic lens is much larger than the wavelength, we can approximate the incident field on the GRS to be the far-field. Our purpose is to evaluate the focal field in terms of the far-field. Appendix A derives the relation between the angular spectrum  $\hat{\mathbf{E}}(k_x, k_y; 0)$  and the far-field  $\bar{E}(k_x, k_y)$  and the result is

$$\hat{\mathbf{E}}(k_x, k_y; 0) = -\frac{ir_\infty e^{ikr_\infty}}{2\pi k_z} \bar{E}(k_x, k_y). \quad (3.16)$$

Substituting Eq. (3.16) into Eq. (3.14), we obtain the electric field in terms of its far field as follows

$$\bar{E}(x, y, z) = -\frac{i}{2\pi} \iint_{-\infty}^{+\infty} r_\infty e^{ikr_\infty} \bar{E}(k_x, k_y) e^{i(k_x x + k_y y + k_z z)} \frac{1}{k_z} dk_x dk_y \quad (3.17)$$

The focal field in Fig. (3.1) is evaluated by ignoring the evanescent field in Eq. (3.17) as follows

$$\bar{E}(x, y, z) = -\frac{i}{2\pi} \iint_{k_x^2 + k_y^2 \leq k^2} r_\infty e^{ikr_\infty} \bar{E}(k_x, k_y) e^{i(k_x x + k_y y + k_z z)} \frac{1}{k_z} dk_x dk_y \quad (3.18)$$

One should note that  $r_\infty$  is a function of  $k_x$  and  $k_y$  since it depends on the shape of the surface on which we apply the principle of stationary phase. One example is the case of light converging from the surface of an aplanatic solid immersion lens to its focus as presented in chapter 5. And hence it should be included in the double integrals. Equation (3.18) is extensively employed by many researchers. Here, we present an example of how to apply Eq. (3.18) to evaluate the focal field of focusing a linearly-polarized Gaussian beam using the aplanatic lens.

Since  $f \gg \lambda$ ,  $r_\infty = f$ , and the field  $\bar{E}_2$  in Eq. (3.8) is considered as the far field

### 3. Multipole Theory and Angular Spectrum Representation for the Focal Fields

---

in Eq. (3.18). We denote the wave-vector in the focal region by  $\bar{k}$ , it is obvious that  $k_x = k \sin \alpha \cos \beta$ ,  $k_y = k \sin \alpha \sin \beta$ ,  $k_z = k \cos \alpha$ , and  $dk_x dk_y = (k^2 \sin \alpha d\alpha d\beta) \cos \alpha$ . For a convenient purpose, we express the Cartesian coordinates  $(x, y, z)$  in terms of cylindrical coordinates  $(\rho, \phi, z)$ :  $x = \rho \cos \phi$ ,  $y = \rho \sin \phi \Rightarrow \rho = \sqrt{x^2 + y^2}$  and  $\phi = \arctan \frac{y}{x}$ . Hence, we have

$$\begin{aligned} k_x x + k_y y + k_z z &= (k \sin \alpha \cos \beta) \rho \cos \phi + (k \sin \alpha \sin \beta) \rho \sin \phi + (k \cos \alpha) z \\ &= k \rho \sin \alpha \cos(\beta - \phi) + k z \cos \alpha. \end{aligned} \quad (3.19)$$

We assume that the incident beam is linear polarized in  $x$ -direction, and hence the incident electric field approaching the aplanatic lens is

$$\bar{E}_1 = E_1(\alpha, \beta) \hat{x} \Rightarrow E_{1\phi} = -E_1(\alpha, \beta) \sin \beta \text{ and } E_{1\rho} = E_1(\alpha, \beta) \cos \beta. \quad (3.20)$$

From Eqs. (3.8) and (3.20), we have

$$\bar{E}_2 = E_1(\alpha, \beta) \begin{pmatrix} -\sin^2 \beta - \cos^2 \beta \cos \alpha \\ \sin \alpha \cos \beta (1 - \cos \alpha) \\ \sin \alpha \cos \beta \end{pmatrix} \sqrt{\frac{n_1}{n_2}} \sqrt{\cos \alpha}. \quad (3.21)$$

Substituting Eqs. (3.19), (3.21), and  $r_\infty = f$  into Eq. (3.18), we obtain

$$\begin{aligned} \bar{E}(\rho, \phi, z) &= -\frac{ikf e^{ikf}}{2\pi} \int_0^{\alpha_m} \sin \alpha d\alpha \int_0^{2\pi} d\beta E_1(\alpha, \beta) \begin{pmatrix} -\sin^2 \beta - \cos^2 \beta \cos \alpha \\ \sin \alpha \cos \beta (1 - \cos \alpha) \\ \sin \alpha \cos \beta \end{pmatrix} \\ &\quad \times \sqrt{\frac{n_1}{n_2}} \sqrt{\cos \alpha} e^{ik[\rho \sin \alpha \cos(\beta - \phi) + z \cos \alpha]}, \end{aligned} \quad (3.22)$$

where  $\alpha_m$  is the maximum angular semi-aperture of the aplanatic lens.

### 3. Multipole Theory and Angular Spectrum Representation for the Focal Fields

---

For the electric field whose intensity is Gaussian distribution in the lateral plane, we have

$$\begin{aligned} E_1(\alpha, \beta) &= E_0 e^{-(x^2+y^2)/w_0^2} = E_0 e^{-f^2 \sin^2 \alpha / w_0^2} \\ &= E_0 e^{-\sin^2 \alpha / (f_0 \sin \alpha_m)^2} = E_0 f_{w_0}(\alpha), \end{aligned} \quad (3.23)$$

where  $w_0$  is the half-width of the Gaussian beam,  $f_0 = w_0 / (f \sin \theta_m)$  is the filling factor, and  $f_{w_0}(\alpha)$  is the *apodization function* which describes the beam profile approaching the lens. The reason for investigating the Gaussian beam is that the Gaussian beam is produced by nearly all laser sources and it has been widely used in science and technology. In fact, we will use it for our experiment presented in chapter 5.

We can simplify Eq. (3.22) even more for the Gaussian beam by employing the following identities

$$\int_0^{2\pi} \cos n\beta e^{iu \cos(\beta-\phi)} d\beta = 2\pi i^n J_n(u) \cos(n\phi), \quad (3.24)$$

$$\int_0^{2\pi} \sin n\beta e^{iu \cos(\beta-\phi)} d\beta = 2\pi i^n J_n(u) \sin(n\phi), \quad (3.25)$$

$$\sin^2 \beta = \frac{1 - \cos 2\beta}{2}, \quad (3.26)$$

$$\cos^2 \beta = \frac{1 + \cos 2\beta}{2}, \quad (3.27)$$

$$\sin \beta \cos \beta = \frac{\sin 2\beta}{2}. \quad (3.28)$$

Here, we show how to simplify for  $E_x(\rho, \phi, z)$  only. For  $E_y(\rho, \phi, z)$  and  $E_z(\rho, \phi, z)$ , a similar procedure can be used. From Eqs. (3.22) and (3.23), we have

$$\begin{aligned} E_x(\rho, \phi, z) &= \frac{ikf e^{ikf}}{2\pi} \sqrt{\frac{n_1}{n_2}} E_0 \int_0^{\alpha_m} d\alpha f_{w_0}(\alpha) \sqrt{\cos \alpha} \sin \alpha \int_0^{2\pi} d\beta [\sin^2 \beta + \cos^2 \beta \cos \alpha] \\ &\quad \times e^{ik[\rho \sin \alpha \cos(\beta-\phi) + z \cos \alpha]} \\ &= \frac{ikf e^{ikf}}{2\pi} \sqrt{\frac{n_1}{n_2}} E_0 \int_0^{\alpha_m} d\alpha f_{w_0}(\alpha) \sqrt{\cos \alpha} \sin \alpha e^{ikz \cos \alpha} \\ &\quad \left[ \int_0^{2\pi} d\beta \sin^2 \beta e^{ik\rho \sin \alpha \cos(\beta-\phi)} + \cos \alpha \int_0^{2\pi} d\beta \cos^2 \beta e^{ik\rho \sin \alpha \cos(\beta-\phi)} \right] \end{aligned} \quad (3.29)$$

### 3. Multipole Theory and Angular Spectrum Representation for the Focal Fields

---

Using Eqs. (3.24) and (3.26), we have:

$$\int_0^{2\pi} d\beta [\sin^2 \beta e^{ik\rho \sin \alpha \cos(\beta-\phi)}] = \pi [J_0(k\rho \sin \alpha) + J_2(k\rho \sin \alpha) \cos 2\phi] \quad (3.30)$$

Using Eqs. (3.24) and (3.27), we have:

$$\int_0^{2\pi} d\beta [\cos^2 \beta e^{ik\rho \sin \alpha \cos(\beta-\phi)}] = \pi [J_0(k\rho \sin \alpha) - J_2(k\rho \sin \alpha) \cos 2\phi] \quad (3.31)$$

Substituting Eqs. (3.30) and (3.31) into Eq. (3.29), we obtain:

$$\begin{aligned} E_x(\rho, \phi, z) &= \frac{ikf e^{ikf}}{2\pi} \sqrt{\frac{n_1}{n_2}} E_0 \int_0^{\alpha_m} d\alpha f_{w_0}(\alpha) \sqrt{\cos \alpha} \sin \alpha e^{ikz \cos \alpha} [\pi \{J_0(k\rho \sin \alpha) \\ &\quad + J_2(k\rho \sin \alpha) \cos 2\phi\} + \pi \cos \alpha \{J_0(k\rho \sin \alpha) - J_2(k\rho \sin \alpha) \cos 2\phi\}] \\ &= \frac{ikf e^{ikf}}{2} \sqrt{\frac{n_1}{n_2}} E_0 \int_0^{\alpha_m} d\alpha f_{w_0}(\alpha) \sqrt{\cos \alpha} \sin \alpha e^{ikz \cos \alpha} \times \\ &\quad [(1 + \cos \alpha) J_0(k\rho \sin \alpha) + (1 - \cos \alpha) J_2(k\rho \sin \alpha) \cos 2\phi] \end{aligned} \quad (3.32)$$

Let  $I_0$  and  $I_2$  be

$$I_0 = \int_0^{\alpha_m} d\alpha E_0 f_{w_0}(\alpha) \sqrt{\cos \alpha} \sin \alpha J_0(k\rho \sin \alpha) e^{ikz \cos \alpha} (1 + \cos \alpha) \quad (3.33)$$

$$I_2 = \int_0^{\alpha_m} d\alpha E_0 f_{w_0}(\alpha) \sqrt{\cos \alpha} \sin \alpha J_2(k\rho \sin \alpha) e^{ikz \cos \alpha} (1 - \cos \alpha) \quad (3.34)$$

Substituting Eqs. (3.33) and (5.48) into Eq. (3.32), we obtain

$$E_x(\rho, \phi, z) = \frac{ikf e^{ikf}}{2} \sqrt{\frac{n_1}{n_2}} [I_0 + I_2 \cos 2\phi]. \quad (3.35)$$

Similarly,  $E_y(\rho, \phi, z)$  and  $E_z(\rho, \phi, z)$  can be obtained as follows:

$$E_y(\rho, \phi, z) = \frac{ikf e^{ikf}}{2} \sqrt{\frac{n_1}{n_2}} I_2 \sin 2\phi, \quad (3.36)$$

$$E_z(\rho, \phi, z) = \frac{ikf e^{ikf}}{2} \sqrt{\frac{n_1}{n_2}} [-2i I_1 \cos \phi], \quad (3.37)$$

where  $I_1 = \int_0^{\alpha_m} d\alpha E_0 f_{w_0}(\alpha) \sqrt{\cos \alpha} \sin \alpha J_1(k\rho \sin \alpha) e^{ikz \cos \alpha} \sin \alpha$ . In a compact form, the

focal field is written as follows

$$\bar{E}(\rho, \phi, z) = \frac{ikf e^{ikf}}{2} \sqrt{\frac{n_1}{n_2}} \begin{pmatrix} I_0 + I_2 \cos 2\phi \\ I_2 \sin 2\phi \\ -2iI_1 \cos \phi \end{pmatrix}. \quad (3.38)$$

This section has derived the angular spectrum representation of the optical field for evaluating the focal field of the aplanatic lens. In the next section, we are going to form another representation based on multipole theory.

### 3.3 Multipole Theory

The pivotal step in using the multipole expansion of the electromagnetic field is the evaluation of the multipole strengths. In general, we have derived the strengths in terms of the spectral amplitude vectors  $\hat{E}(\hat{s})$  and  $\hat{H}(\hat{s})$ . In this section, we apply the formulas derived in the previous chapter for formulating the focal field of an aplanatic lens.

#### 3.3.1 Multipole Strengths for the Focused Waves

At the far region, we have the following relationship between the far field and the spectral amplitude [53]:

$$\hat{E}(\hat{s}) = r_\infty e^{ikr_\infty} \bar{E}(\bar{r}_\infty). \quad (3.39)$$

It should be noted that the spectral amplitude is in fact equivalent to the concept of strength factor of a ray in Ref. [31]. For the aplanatic lens in Fig. 3.1, we can write  $\bar{E}(\bar{r}_\infty) = E_\alpha \hat{\alpha} + E_\beta \hat{\beta}$  and hence the spectral amplitude of the focused beam can be written as follows

$$\hat{E}(\hat{s}) = f e^{ikf} [E_\alpha \hat{\alpha} + E_\beta \hat{\beta}]. \quad (3.40)$$

### 3. Multipole Theory and Angular Spectrum Representation for the Focal Fields

Substituting Eq. (3.40) into Eq. (2.17), we obtain the multipole strengths of the focused beam as follows

$$\begin{aligned} p_{El}^m &= -\frac{i^l f e^{ikf}}{l(l+1)} c_{lm} \int_0^{2\pi} \int_0^\pi \left( \frac{dP_l^m(\cos \alpha)}{d\alpha} E_\alpha - im \frac{P_l^m(\cos \alpha)}{\sin \alpha} E_\beta \right) e^{-im\beta} \sin \alpha d\alpha d\beta, \\ p_{Ml}^m &= \frac{i^l f e^{ikf}}{l(l+1)} c_{lm} \int_0^{2\pi} \int_0^\pi \left( \frac{dP_l^m(\cos \alpha)}{d\alpha} E_\beta + im \frac{P_l^m(\cos \alpha)}{\sin \alpha} E_\alpha \right) e^{-im\beta} \sin \alpha d\alpha d\beta. \end{aligned} \quad (3.41)$$

It should be noted that the only approximation, which we made to derive the multipole strengths in Eq. (3.41), is that the electromagnetic field on the GRS can be approximated as the far field, i.e., the radial component of the field can be ignored. We will see the accuracy of the approximation in simulation section below.

#### 3.3.2 Direct Derivation for the Multipole Strengths

Multipole theory expresses the electromagnetic fields in terms of the vector electric  $\mathbf{N}_{lm}(\bar{r})$  and magnetic  $\mathbf{M}_{lm}(\bar{r})$  multipole fields as follows

$$\bar{\mathbf{E}}(\bar{r}) = \sum_{l=1}^{\infty} \sum_{m=-l}^l [p_{El}^m \mathbf{N}_{lm}(\bar{r}) + p_{Ml}^m \mathbf{M}_{lm}(\bar{r})], \quad (3.42)$$

where, for a converging beam, the multipole fields are

$$\begin{aligned} \mathbf{N}_{lm}^{(2)}(\bar{r}) &= \nabla \times \nabla \times [\bar{r} h_l^{(2)}(kr) Y_l^m(\theta, \phi)] \\ &= \hat{r} \frac{l(l+1)}{r} h_l^{(2)}(kr) Y_l^m(\theta, \phi) + \hat{\theta} \left[ \frac{1}{r} \frac{d}{dr} (r h_l^{(2)}(kr)) \frac{\partial}{\partial \theta} Y_l^m(\theta, \phi) \right] \\ &\quad + \hat{\phi} \frac{im}{\sin \theta} \frac{1}{r} \frac{d}{dr} (r h_l^{(2)}(kr)) Y_l^m(\theta, \phi), \end{aligned} \quad (3.43)$$

$$\begin{aligned} \mathbf{M}_{lm}^{(2)}(\bar{r}) &= ik \nabla \times [\bar{r} h_l^{(2)}(kr) Y_l^m(\theta, \phi)] \\ &= -k h_l^{(2)}(kr) \left[ \hat{\theta} \frac{m}{\sin \theta} Y_l^m(\theta, \phi) + i \hat{\phi} \frac{\partial}{\partial \theta} Y_l^m(\theta, \phi) \right]. \end{aligned} \quad (3.44)$$

To evaluate the multipole strengths, there exists several approaches like point-matching, focal plane matching, and far-field matching approaches [135]. In this section, we use the far-field matching approach to derive analytical expressions for the strengths. To avoid a possible confusion, we would like to remind that  $\hat{s} = \frac{\bar{k}}{k}$  is the unit vector of the propagation

### 3. Multipole Theory and Angular Spectrum Representation for the Focal Fields

direction.  $\hat{r}$  is the unit vector in the radial direction. The spherical angles  $(\alpha, \beta)$  and  $(\theta, \phi)$  specify the unit vector  $\hat{s}$  and  $\hat{r}$ , respectively. On the GRS shown in Fig. 3.1, we have  $\hat{s} = -\hat{r}$ ,  $\theta = \pi - \alpha$ ,  $\phi = \beta - \pi$ ,  $\hat{\theta} = \hat{\alpha}$ ,  $\hat{\phi} = -\hat{\beta}$ , and  $\bar{E} = E_\theta \hat{\theta} + E_\phi \hat{\phi} = E_\alpha \hat{\alpha} + E_\beta \hat{\beta}$ . Hence, we can easily observe that  $E_\theta = E_\alpha$  and  $E_\phi = -E_\beta$ . Using the following identities

$$P_l^m(\cos \theta) = P_l^m(-\cos \alpha) = (-1)^{l+m} P_l^m(\cos \alpha),$$

$$e^{im\phi} = e^{-im\pi} e^{im\beta} = (-1)^m e^{im\beta},$$

we can show that

$$Y_l^m(\theta, \phi) = c_{lm} P_l^m(\cos \theta) e^{im\phi} = (-1)^l c_{lm} P_l^m(\cos \alpha) e^{im\beta} = (-1)^l Y_l^m(\alpha, \beta), \quad (3.45)$$

where  $c_{lm} = (-1)^m \left[ \frac{2l+1}{4\pi} \frac{(l-m)!}{(l+m)!} \right]^{\frac{1}{2}}$ .

Using Eq. (3.45), we express Eq. (3.42) in terms of  $\alpha$  and  $\beta$  as follows

$$E_r = \sum_{l=1}^{\infty} \sum_{m=-l}^l (-1)^l \frac{p_{El}^m l(l+1)}{r} h_l^{(2)}(kr) Y_l^m(\alpha, \beta), \quad (3.46)$$

$$E_\alpha = \sum_{l=1}^{\infty} \sum_{m=-l}^l (-1)^{l+1} \left[ p_{El}^m \frac{1}{r} \frac{d}{dr} [r h_l^{(2)}(kr)] \frac{\partial}{\partial \alpha} Y_l^m(\alpha, \beta) + k m p_{Ml}^m h_l^{(2)}(kr) \frac{Y_l^m(\alpha, \beta)}{\sin \alpha} \right], \quad (3.47)$$

$$E_\beta = \sum_{l=1}^{\infty} \sum_{m=-l}^l (-1)^{l+1} \left[ i m p_{El}^m \frac{1}{r} \frac{d}{dr} [r h_l^{(2)}(kr)] \frac{Y_l^m(\alpha, \beta)}{\sin \alpha} + i k p_{Ml}^m h_l^{(2)}(kr) \frac{\partial}{\partial \alpha} Y_l^m(\alpha, \beta) \right]. \quad (3.48)$$

In limitation of  $kr_\infty \gg \frac{l(l+1)}{2}$ , we can approximate:

$$h_l^{(2)}(kr_\infty) \approx i^{l+1} \frac{e^{-ikr_\infty}}{kr_\infty}, \quad (3.49)$$

$$\frac{1}{r_\infty} \frac{d}{dr_\infty} [r_\infty h_l^{(2)}(kr_\infty)] \approx i^l \frac{e^{-ikr_\infty}}{r_\infty}. \quad (3.50)$$

### 3. Multipole Theory and Angular Spectrum Representation for the Focal Fields

---

Substituting Eqs. (3.49) and (3.50) into Eqs. (3.46), (3.47) and (3.48), we obtain

$$E_r \approx 0,$$

$$E_\alpha \approx -\frac{e^{-ikr_\infty}}{r_\infty} \sum_{l=1}^{\infty} \sum_{m=-l}^l (-i)^l c_{lm} \left[ p_{El}^m \frac{dP_l^m(\cos \alpha)}{d\alpha} + im p_{Ml}^m \frac{P_l^m(\cos \alpha)}{\sin \alpha} \right] e^{im\beta}, \quad (3.51)$$

$$E_\beta \approx -\frac{e^{-ikr_\infty}}{r_\infty} \sum_{l=1}^{\infty} \sum_{m=-l}^l (-i)^l c_{lm} \left[ im p_{El}^m \frac{P_l^m(\cos \alpha)}{\sin \alpha} - p_{Ml}^m \frac{dP_l^m(\cos \alpha)}{d\alpha} \right] e^{im\beta}. \quad (3.52)$$

Adding and subtracting Eq. (3.51) from Eq. (3.52), we have

$$E_\alpha + E_\beta = -\frac{e^{-ikr_\infty}}{r_\infty} \sum_{l=1}^{\infty} \sum_{m=-l}^l (-i)^l c_{lm} \left[ p_{El}^m \left( \frac{dP_l^m(\cos \alpha)}{d\alpha} + im \frac{P_l^m(\cos \alpha)}{\sin \alpha} \right) - p_{Ml}^m \left( \frac{dP_l^m(\cos \alpha)}{d\alpha} - im \frac{P_l^m(\cos \alpha)}{\sin \alpha} \right) \right] e^{im\beta}, \quad (3.53)$$

$$E_\alpha - E_\beta = -\frac{e^{-ikr_\infty}}{r_\infty} \sum_{l=1}^{\infty} \sum_{m=-l}^l (-i)^l c_{lm} \left[ p_{El}^m \left( \frac{dP_l^m(\cos \alpha)}{d\alpha} - im \frac{P_l^m(\cos \alpha)}{\sin \alpha} \right) + p_{Ml}^m \left( \frac{dP_l^m(\cos \alpha)}{d\alpha} + im \frac{P_l^m(\cos \alpha)}{\sin \alpha} \right) \right] e^{im\beta}. \quad (3.54)$$

From Eq. (3.53):

$$\begin{aligned} & \int_0^{2\pi} \int_0^\pi (E_\alpha + E_\beta) \left( \frac{dP_{l'}^{m'}(\cos \alpha)}{d\alpha} - im' \frac{P_{l'}^{m'}(\cos \alpha)}{\sin \alpha} \right) e^{-im'\beta} \sin \alpha d\alpha d\beta \\ &= -\frac{e^{-ikr_\infty}}{r_\infty} \int_0^{2\pi} \int_0^\pi \sum_{l=1}^{\infty} \sum_{m=-l}^l (-i)^l c_{lm} \left[ p_{El}^m \left( \frac{dP_l^m(\cos \alpha)}{d\alpha} + im \frac{P_l^m(\cos \alpha)}{\sin \alpha} \right) - p_{Ml}^m \left( \frac{dP_l^m(\cos \alpha)}{d\alpha} - im \frac{P_l^m(\cos \alpha)}{\sin \alpha} \right) \right] \left( \frac{dP_{l'}^{m'}(\cos \alpha)}{d\alpha} - im' \frac{P_{l'}^{m'}(\cos \alpha)}{\sin \alpha} \right) \\ & \quad \times e^{i(m-m')\beta} \sin \alpha d\alpha d\beta. \end{aligned} \quad (3.55)$$

Noting that  $\int_0^{2\pi} e^{i(m-m')\beta} d\beta = 2\pi \delta_{m-m'}^0$  where  $\delta_{m-m'}^0$  is a Kronecker tensor (also called

### 3. Multipole Theory and Angular Spectrum Representation for the Focal Fields

---

Kronecker delta) and using the following orthogonalizations

$$\begin{aligned}
 a_{lm} &= \int_0^\pi \left( \frac{dP_l^m(\cos \alpha)}{d\alpha} \pm im \frac{P_l^m(\cos \alpha)}{\sin \alpha} \right) \left( \frac{dP_{l'}^m(\cos \alpha)}{d\alpha} \mp im \frac{P_{l'}^m(\cos \alpha)}{\sin \alpha} \right) \sin \alpha d\alpha \\
 &= \int_0^\pi \left( \frac{dP_l^m(\cos \alpha)}{d\alpha} \frac{dP_{l'}^m(\cos \alpha)}{d\alpha} + m^2 \frac{P_l^m(\cos \alpha)}{\sin \alpha} \frac{P_{l'}^m(\cos \alpha)}{\sin \alpha} \right) \sin \alpha d\alpha \\
 &= \frac{2l(l+1)(l+m)!}{2l+1(l-m)!} \delta_{l-l'}^0, \tag{3.56}
 \end{aligned}$$

$$\begin{aligned}
 b_{lm} &= \int_0^\pi \left( \frac{dP_l^m(\cos \alpha)}{d\alpha} \pm im \frac{P_l^m(\cos \alpha)}{\sin \alpha} \right) \left( \frac{dP_{l'}^m(\cos \alpha)}{d\alpha} \pm im \frac{P_{l'}^m(\cos \alpha)}{\sin \alpha} \right) \sin \alpha d\alpha \\
 &= \int_0^\pi \left( \frac{dP_l^m(\cos \alpha)}{d\alpha} \frac{dP_{l'}^m(\cos \alpha)}{d\alpha} - m^2 \frac{P_l^m(\cos \alpha)}{\sin \alpha} \frac{P_{l'}^m(\cos \alpha)}{\sin \alpha} \right) \sin \alpha d\alpha \\
 &= \frac{2l(l+1) - 2m(2l+1)(l+m)!}{2l+1(l-m)!} \delta_{l-l'}^0, \tag{3.57}
 \end{aligned}$$

we can reduce Eq. (3.55) as follows

$$\begin{aligned}
 &\int_0^{2\pi} \int_0^\pi (E_\alpha + E_\beta) \left( \frac{dP_{l'}^{m'}(\cos \alpha)}{d\alpha} - im' \frac{P_{l'}^{m'}(\cos \alpha)}{\sin \alpha} \right) e^{-im'\beta} \sin \alpha d\alpha d\beta \\
 &= -\frac{e^{-ikr_\infty}}{r_\infty} \sum_{l=1}^{\infty} \sum_{m=-l}^l 2\pi (-i)^l c_{lm} [p_{El}^m a_{lm} - p_{Ml}^m b_{lm}] \delta_{m-m'}^0. \tag{3.58}
 \end{aligned}$$

Similarly, we obtain from Eq. (3.54)

$$\begin{aligned}
 &\int_0^{2\pi} \int_0^\pi (E_\alpha - E_\beta) \left( \frac{dP_{l'}^{m'}(\cos \alpha)}{d\alpha} + im' \frac{P_{l'}^{m'}(\cos \alpha)}{\sin \alpha} \right) e^{-im'\beta} \sin \alpha d\alpha d\beta \\
 &= -\frac{e^{-ikr_\infty}}{r_\infty} \sum_{l=1}^{\infty} \sum_{m=-l}^l 2\pi (-i)^l c_{lm} [p_{El}^m a_{lm} + p_{Ml}^m b_{lm}] \delta_{m-m'}^0. \tag{3.59}
 \end{aligned}$$

### 3. Multipole Theory and Angular Spectrum Representation for the Focal Fields

---

Adding Eqs. (3.58) and (3.59) together, we have:

$$\begin{aligned}
& \int_0^{2\pi} \int_0^\pi \left( \frac{dP_{l'}^{m'}(\cos \alpha)}{d\alpha} E_\alpha - im' \frac{P_{l'}^{m'}(\cos \alpha)}{\sin \alpha} E_\beta \right) e^{-im'\beta} \sin \alpha d\alpha d\beta \\
&= -\frac{e^{-ikr_\infty}}{r_\infty} \sum_{l=1}^{\infty} \sum_{m=-l}^l 2\pi (-i)^l c_{lm} p_{El}^m a_{lm} \delta_{m-m'}^0 \\
&= -\frac{e^{-ikr_\infty}}{r_\infty} \sum_{l=1}^{\infty} \sum_{m=-l}^l 2\pi (-i)^l c_{lm} p_{El}^m \frac{2l(l+1)}{2l+1} \frac{(l+m)!}{(l-m)!} \delta_{l-l'}^0 \delta_{m-m'}^0 \\
&= -\frac{e^{-ikr_\infty}}{r_\infty} \frac{l'(l'+1)}{i^{l'} c_{l'm'}} p_{El'}^{m'}. \tag{3.60}
\end{aligned}$$

Without loss of generalization, we can change  $(l', m')$  by  $(l, m)$  in Eq. (3.60), and obtain the electric multipole strength of the  $(l, m)$  multipole term in terms of the electric field on the GRS ( $r_\infty = f$ ) as follows

$$p_{El}^m = -\frac{i^l f e^{ikf}}{l(l+1)} c_{lm} \int_0^{2\pi} \int_0^\pi \left( \frac{dP_l^m(\cos \alpha)}{d\alpha} E_\alpha - im \frac{P_l^m(\cos \alpha)}{\sin \alpha} E_\beta \right) e^{-im\beta} \sin \alpha d\alpha d\beta. \tag{3.61}$$

The magnetic multipole strength of the  $(l, m)$  multipole term is

$$p_{Ml}^m = \frac{i^l f e^{ikf}}{l(l+1)} c_{lm} \int_0^{2\pi} \int_0^\pi \left( \frac{dP_l^m(\cos \alpha)}{d\alpha} E_\beta + im \frac{P_l^m(\cos \alpha)}{\sin \alpha} E_\alpha \right) e^{-im\beta} \sin \alpha d\alpha d\beta. \tag{3.62}$$

We can see that the Eqs. (3.61) and (3.62) are exactly the same as Eq. (3.41). Now, given the incident field approaching the aplanatic lens, we can evaluate the multipole strengths and equivalently the converging field using Eq. (3.42). If there is no source around the focus, there must be a beam diverging to the infinity as a consequence of the converging beam. The diverging field can be obtained from Eqs. (3.46), (3.47), and (3.48) by replacing  $h_l^{(2)}$  with  $h_l^{(1)}$ . Then, by summing up these two beams and using the following recurrence relationships for the spherical Bessel functions

$$\begin{aligned}
j_l(kr) &= \frac{kr}{2l+1} (j_{l-1}(kr) + j_{l+1}(kr)), \\
\frac{1}{r} \frac{d}{dr} [r j_l(kr)] &= \frac{k}{2l+1} [(l+1)j_{l-1}(kr) - l j_{l+1}(kr)],
\end{aligned}$$

we can derive the focal field as follows

$$\begin{aligned}
 E_r &= 2k \sum_{l=1}^{\infty} \sum_{m=-l}^l \frac{l(l+1)}{2l+1} c_{lm} (p_{El}^m [j_{l-1}(kr) + j_{l+1}(kr)] P_l^m(\cos \theta)) \exp(im\phi), \\
 E_\theta &= 2k \sum_{l=1}^{\infty} \sum_{m=-l}^l \frac{l(l+1)}{2l+1} c_{lm} \left( p_{El}^m \left[ \frac{j_{l-1}(kr)}{l} - \frac{j_{l+1}(kr)}{l+1} \right] \frac{dP_l^m(\cos \theta)}{d\theta} \right. \\
 &\quad \left. - m \frac{2l+1}{l(l+1)} p_{Ml}^m j_l(kr) \frac{P_l^m(\cos \theta)}{\sin \theta} \right) \exp(im\phi), \\
 E_\phi &= 2ik \sum_{l=1}^{\infty} \sum_{m=-l}^l \frac{l(l+1)}{2l+1} c_{lm} \left( m p_{El}^m \left[ \frac{j_{l-1}(kr)}{l} - \frac{j_{l+1}(kr)}{l+1} \right] \frac{P_l^m(\cos \theta)}{\sin \theta} \right. \\
 &\quad \left. - \frac{2l+1}{l(l+1)} p_{Ml}^m j_l(kr) \frac{dP_l^m(\cos \theta)}{d\theta} \right) \exp(im\phi). \quad (3.63)
 \end{aligned}$$

Alternative to the formula based on the angular spectrum representation, this section formed the formula based on multipole theory for evaluating the focal field of the aplanatic lens. In the next section, we use the formulas for various polarized beam including cylindrical beam and generalized linear polarized beam.

### 3.4 Polarized Beams and Focal Fields

Studying the focal field of the aplanatic lens has a long history since many years ago [31]. For a low NA beam, the focal field is well described by the scalar diffraction integrals and the vectorial nature of the beam can be ignored. However, for a high NA beam the polarization properties of the electromagnetic field play a dominant role. For example, for a linearly polarized beam, the energy density distribution of a longitudinally polarized component in the direction of propagation of the beam is not rotational symmetric. This primarily causes an asymmetric deformation of the focal spot. Using a circularly polarized beam produces a rotational symmetric energy density distribution around the longitudinal direction. Using a radially polarized beam with a high NA produces a strong symmetrical longitudinal electric field component in the vicinity of the focus [16]. The strong longitudinal component is sharply centered around the optical axis and leads to a smaller lateral focal spot size in comparison with the linear polarization. In contrast,

### 3. Multipole Theory and Angular Spectrum Representation for the Focal Fields

---

focusing an azimuthally polarized beam using a high NA lens generates a strong magnetic field on the optical axis, while the electric field is purely transverse and zero at the center due to a completely destructive interference between different parts of the electric field at the focus. To avoid the doughnut focal spot, one can encode the phase of the azimuthally polarized beam with a vortex  $0 - 2\pi$  phase plate which modifies the phase of the beam and hence leads to a constructive interference at the focus [115]. In this section, using Eqs. (3.18) and (3.63), we form different expressions to study the properties of different polarized beams.

#### 3.4.1 Radial or Azimuthal Polarization with a Vortex

Radially and azimuthally polarized beams are usually called cylindrical beam. Radially polarized beam has been the continuing topic of interest due to the strong longitudinal field which is produced at the focus of the aplanatic lens. Using the radially-polarized beam also produces a tighter focal spot on the transverse plane compared to linearly polarized beam [16]. Recently, cylindrical beam with a vortex has gained much attention due to its unique properties of angular momentum which find applications in optical trapping, spintronics, and quantum information. Focusing azimuthally-polarized beam produces a broader focal spot compared with the linearly and radially polarized beams, however azimuthally polarized beam with a vortex can give a tighter spot with a high numerical aperture lens [115]. One of the purposes of this thesis is to study and use different polarizations for improving performance of microscope. Hence, we formulate and study the focal fields using different polarizations in this section.

##### 3.4.1.1 Radially-polarized Beam with a Vortex of Charge $n$

The field on the GRS has the form of

$$\bar{E}(\hat{s}) = a(\alpha) \exp(in\beta) \hat{\alpha}. \quad (3.64)$$

### 3. Multipole Theory and Angular Spectrum Representation for the Focal Fields

By substituting Eq. (3.64) into Eq. (3.18), we obtain the focal field based on the angular spectrum representation as follows

$$\bar{E}(\rho, \phi, z) = -\frac{ikf e^{ikf}}{2} \begin{pmatrix} I_{n+1} + I_{n-1} \\ -i(I_{n+1} - I_{n-1}) \\ -2I_n \end{pmatrix}, \quad (3.65)$$

where

$$\begin{aligned} I_{n-1} &= i^{n-1} e^{i(n-1)\phi} \int_0^{\alpha_m} a(\alpha) \cos \alpha J_{n-1}(k\rho \sin \alpha) e^{ikz \cos \alpha} \sin \alpha d\alpha, \\ I_{n+1} &= i^{n+1} e^{i(n+1)\phi} \int_0^{\alpha_m} a(\alpha) \cos \alpha J_{n+1}(k\rho \sin \alpha) e^{ikz \cos \alpha} \sin \alpha d\alpha, \\ I_n &= i^n e^{in\phi} \int_0^{\alpha_m} a(\alpha) J_n(k\rho \sin \alpha) e^{ikz \cos \alpha} \sin^2 \alpha d\alpha. \end{aligned}$$

By substituting Eq. (3.64) into Eqs. (3.61) and (3.62), we obtain

$$\begin{aligned} p_{El}^m &= -\frac{2\pi i^l f e^{ikf}}{l(l+1)} c_{ln} \delta_{m-n}^0 \int_0^\pi a(\alpha) \frac{d}{d\alpha} P_l^n(\cos \alpha) \sin \alpha d\alpha, \\ p_{Ml}^m &= \frac{2\pi i^{l+1} f e^{ikf}}{l(l+1)} n c_{ln} \delta_{m-n}^0 \int_0^\pi a(\alpha) P_l^n(\cos \alpha) d\alpha. \end{aligned} \quad (3.66)$$

By substituting Eq. (3.66) into Eq. (3.63), we obtain the focal field based on the multipole theory as follows

$$\begin{aligned} E_r &= 2k \sum_{l=|n|}^{\infty} \frac{l(l+1)}{2l+1} c_{ln} (p_{El}^n [j_{l-1}(kr) + j_{l+1}(kr)] P_l^n(\cos \theta)) \exp(in\phi), \\ E_\theta &= 2k \sum_{l=|n|}^{\infty} \frac{l(l+1)}{2l+1} c_{ln} \left( p_{El}^n \left[ \frac{j_{l-1}(kr)}{l} - \frac{j_{l+1}(kr)}{l+1} \right] \frac{dP_l^n(\cos \theta)}{d\theta} \right. \\ &\quad \left. - n \frac{2l+1}{l(l+1)} p_{Ml}^n j_l(kr) \frac{P_l^n(\cos \theta)}{\sin \theta} \right) \exp(in\phi), \\ E_\phi &= 2ik \sum_{l=|n|}^{\infty} \frac{l(l+1)}{2l+1} c_{ln} \left( n p_{El}^n \left[ \frac{j_{l-1}(kr)}{l} - \frac{j_{l+1}(kr)}{l+1} \right] \frac{P_l^n(\cos \theta)}{\sin \theta} \right. \\ &\quad \left. - \frac{2l+1}{l(l+1)} p_{Ml}^n j_l(kr) \frac{dP_l^n(\cos \theta)}{d\theta} \right) \exp(in\phi). \end{aligned} \quad (3.67)$$

If  $n = 0$ , the summations start with 1 instead of 0.

### 3.4.1.2 Azimuthally-polarized Beam with a Vortex of Charge $n$

The field on the GRS has the form of

$$\bar{E}(\hat{\mathbf{s}}) = a(\alpha) \exp(in\beta) \hat{\beta}. \quad (3.68)$$

Substituting Eq. (3.68) into Eq. (3.18), we obtain the focal field based on the angular spectrum representation as follows

$$\bar{E}(\rho, \phi, z) = -\frac{ikf e^{ikf}}{2} \begin{pmatrix} i(F_{n+1} - F_{n-1}) \\ F_{n+1} + F_{n-1} \\ 0 \end{pmatrix}, \quad (3.69)$$

where

$$F_{n-1} = i^{n-1} e^{i(n-1)\phi} \int_0^{\alpha_m} a(\alpha) J_{n-1}(k\rho \sin \alpha) e^{ikz \cos \alpha} \sin \alpha \, d\alpha,$$

$$F_{n+1} = i^{n+1} e^{i(n+1)\phi} \int_0^{\alpha_m} a(\alpha) J_{n+1}(k\rho \sin \alpha) e^{ikz \cos \alpha} \sin \alpha \, d\alpha.$$

Substituting Eq. (3.68) into Eqs. (3.61) and (3.62), we obtain

$$p_{El}^m = \frac{2\pi i^{l+1} f e^{ikf}}{l(l+1)} n c_{ln} \delta_{m-n}^0 \int_0^\pi a(\alpha) P_l^n(\cos \alpha) \, d\alpha,$$

$$p_{Ml}^m = \frac{2\pi i^l f e^{ikf}}{l(l+1)} c_{ln} \delta_{m-n}^0 \int_0^\pi a(\alpha) \frac{d}{d\alpha} P_l^n(\cos \alpha) \sin \alpha \, d\alpha. \quad (3.70)$$

Substituting Eq. (3.70) into Eq. (3.63), we obtain exactly the same form as Eq. (3.67).

For a notice, we can write the multipole strengths of a cylindrical beam with a vortex in the following format

$$p_{El}^m = p_{El}^n \delta_m^n, \quad p_{Ml}^m = p_{Ml}^n \delta_m^n. \quad (3.71)$$

### 3.4.2 Generalized Linear Polarization

The field on the GRS has the form of [26]

$$\bar{E}(\hat{\mathbf{s}}) = a(\alpha) \cos^2 \frac{\alpha}{2} \{(1 - S(\alpha)) \cos \beta \hat{\alpha} - (1 + S(\alpha)) \sin \beta \hat{\beta}\}, \quad (3.72)$$

where  $S(\alpha)$  is a parameter that can be chosen to generate different polarizations and apodization distributions [136]. By substituting Eq. (3.72) into Eq. (3.18), we obtain the focal field based on the angular spectrum representation as follows

$$\bar{E}(\rho, \phi, z) = -\frac{ikf e^{ikf}}{2} \begin{pmatrix} H_0 + H_2 \cos 2\phi \\ H_2 \sin 2\phi \\ -2iH_1 \cos \phi \end{pmatrix}, \quad (3.73)$$

where

$$\begin{aligned} H_0 &= \int_0^{\alpha_m} a(\alpha) \cos^2\left(\frac{\alpha}{2}\right) [(1 + S(\alpha)) + (1 - S(\alpha)) \cos \alpha] J_0(k\rho \sin \alpha) e^{ikz \cos \alpha} \sin \alpha \, d\alpha, \\ H_1 &= \int_0^{\alpha_m} a(\alpha) \cos^2\left(\frac{\alpha}{2}\right) [1 - S(\alpha)] J_1(k\rho \sin \alpha) e^{ikz \cos \alpha} \sin^2 \alpha \, d\alpha, \\ H_2 &= \int_0^{\alpha_m} a(\alpha) \cos^2\left(\frac{\alpha}{2}\right) [(1 + S(\alpha)) - (1 - S(\alpha)) \cos \alpha] J_2(k\rho \sin \alpha) e^{ikz \cos \alpha} \sin \alpha \, d\alpha. \end{aligned}$$

By substituting Eq. (3.72) into Eqs. (3.61) and (3.62), we get the multipole strengths for the beam

$$\begin{aligned} p_{El}^m &= p_{El}^1 (\delta_m^1 - \delta_m^{-1}), \\ p_{Ml}^m &= p_{Ml}^1 (\delta_m^1 + \delta_m^{-1}), \end{aligned} \quad (3.74)$$

where

$$\begin{aligned}
 p_{El}^1 &= \frac{i^l f e^{ikf}}{2l(l+1)} \left[ \frac{\pi(2l+1)}{l(l+1)} \right]^{\frac{1}{2}} \int_0^{\alpha_m} a(\alpha) \cos^2 \frac{\alpha}{2} \left( [1 - S(\alpha)] \frac{d}{d\alpha} P_l^1(\cos \alpha) \right. \\
 &\quad \left. + [1 + S(\alpha)] \frac{1}{\sin \alpha} P_l^1(\cos \alpha) \right) \sin \alpha d\alpha, \\
 p_{Ml}^1 &= \frac{i^{l-1} f e^{ikf}}{2l(l+1)} \left[ \frac{\pi(2l+1)}{l(l+1)} \right]^{\frac{1}{2}} \int_0^{\alpha_m} a(\alpha) \cos^2 \frac{\alpha}{2} \left( [1 + S(\alpha)] \frac{d}{d\alpha} P_l^1(\cos \alpha) \right. \\
 &\quad \left. + [1 - S(\alpha)] \frac{1}{\sin \alpha} P_l^1(\cos \alpha) \right) \sin \alpha d\alpha. \tag{3.75}
 \end{aligned}$$

By substituting Eq. (3.75) into Eq. (3.63), we obtain the focal field based on the multipole theory as follows

$$\begin{aligned}
 E_r &= -\frac{k}{\sqrt{\pi}} \sum_{l=1}^{\infty} \sqrt{\frac{l(l+1)}{2l+1}} p_{El}^1 [j_{l-1}(kr) + j_{l+1}(kr)] P_l^1(\cos \theta) \cos \phi, \\
 E_\theta &= -\frac{k}{\sqrt{\pi}} \sum_{l=1}^{\infty} \sqrt{\frac{l(l+1)}{2l+1}} \left[ p_{El}^1 \left( \frac{j_{l-1}(kr)}{l} - \frac{j_{l+1}(kr)}{l+1} \right) \frac{d}{d\theta} P_l^1(\cos \theta) \right. \\
 &\quad \left. - \frac{2l+1}{l(l+1)} p_{Ml}^1 j_l(kr) \frac{P_l^1(\cos \theta)}{\sin \theta} \right] \cos \phi, \\
 E_\phi &= \frac{k}{\sqrt{\pi}} \sum_{l=1}^{\infty} \sqrt{\frac{l(l+1)}{2l+1}} \left[ p_{El}^1 \left( \frac{j_{l-1}(kr)}{l} - \frac{j_{l+1}(kr)}{l+1} \right) \frac{P_l^1(\cos \theta)}{\sin \theta} \right. \\
 &\quad \left. - \frac{2l+1}{l(l+1)} p_{Ml}^1 j_l(kr) \frac{d}{d\theta} P_l^1(\cos \theta) \right] \sin \phi. \tag{3.76}
 \end{aligned}$$

## 3.5 Simulations

Here, we present simulation results for some interesting polarized beams with specific polarizations and apodization distributions using both plane wave and multipole expansions.

### 3.5.1 Radial Polarization, $n = 0$

The far field of an electric multipole of strength  $p_{El}^0$ , order  $l$  ( $l \geq 1$ ), oriented along the axis, consists of a meridional electric field component only, and because it is circularly symmetrical, the variation on a sphere is obtained by putting the azimuthal mode number

### 3. Multipole Theory and Angular Spectrum Representation for the Focal Fields

$m = 0$  [137]. For the special case of radial polarization without a vortex  $n = 0$ , Eq. (3.66) reduces to

$$p_{El}^0 = -i^l f e^{ikf} \frac{[\pi(2l+1)]^{\frac{1}{2}}}{l(l+1)} \int_0^\pi a(\alpha) \frac{dP_l(\cos \alpha)}{d\alpha} \sin \alpha d\alpha, \quad (3.77)$$

and Eq. (3.67), after being normalized so that  $|E_r|^2 + |E_\theta|^2 + |E_\phi|^2 = |p_{E1}^0|^2$ , gives

$$E_r = \sum_{l=1}^{\infty} \left[ \frac{3}{2l+1} \right]^{\frac{1}{2}} \frac{p_{El}^0 l(l+1)}{2} [j_{l-1}(kr) + j_{l+1}(kr)] P_l(\cos \theta), \quad (3.78)$$

$$E_\theta = \sum_{l=1}^{\infty} \left[ \frac{3}{2l+1} \right]^{\frac{1}{2}} \frac{p_{El}^0 l(l+1)}{2} \left[ \frac{j_{l-1}(kr)}{l} - \frac{j_{l+1}(kr)}{l+1} \right] \frac{d}{d\theta} P_l(\cos \theta). \quad (3.79)$$

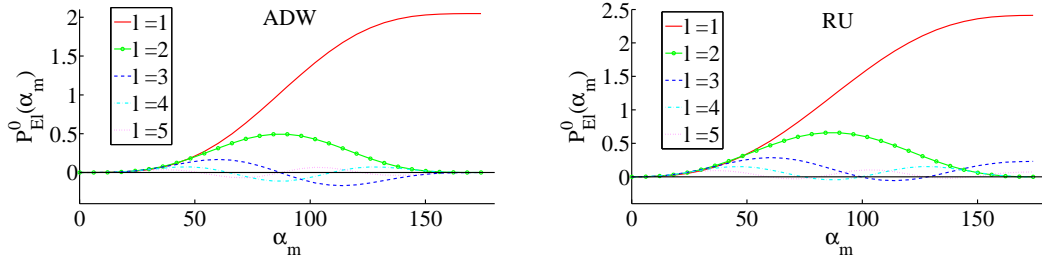
It is observed that at the focal point, the only contribution is from the electric dipole component.

#### 3.5.1.1 Axial Dipole Wave (ADW)

This approach can be used to investigate the behaviour of different illumination conditions. For radial polarization with no vortex, and for Eq. (3.64) with partial aperture

$$a(\alpha) = \sin \alpha \text{ for } \alpha < \alpha_m; a(\alpha) = 0 \text{ for } \alpha > \alpha_m$$

where  $\alpha_m$  is the angular semi-aperture of the lens, it results in a so-called axial dipole wave (ADW) [138]. This maximizes the electric energy density at the focal point for a given input power for a particular NA. For a complete spherical illumination,  $\alpha_m = \pi$ , the electric dipole term  $p_{E1}^0 = i f e^{ikf} \sqrt{\frac{4\pi}{3}}$ , and all higher order terms vanish. Since the term  $f e^{ikf}$  is constant, we can ignore it when plotting the multipole strengths. For a



(a) Axial Dipole Wave:  $a(\alpha) = \sin \alpha$

(b) Radial Polarization with  $a(\alpha) = 1$

Figure 3.2: Multipole strengths for ADW and RU (ignoring the constant term  $f e^{ikf}$ ).

### 3. Multipole Theory and Angular Spectrum Representation for the Focal Fields

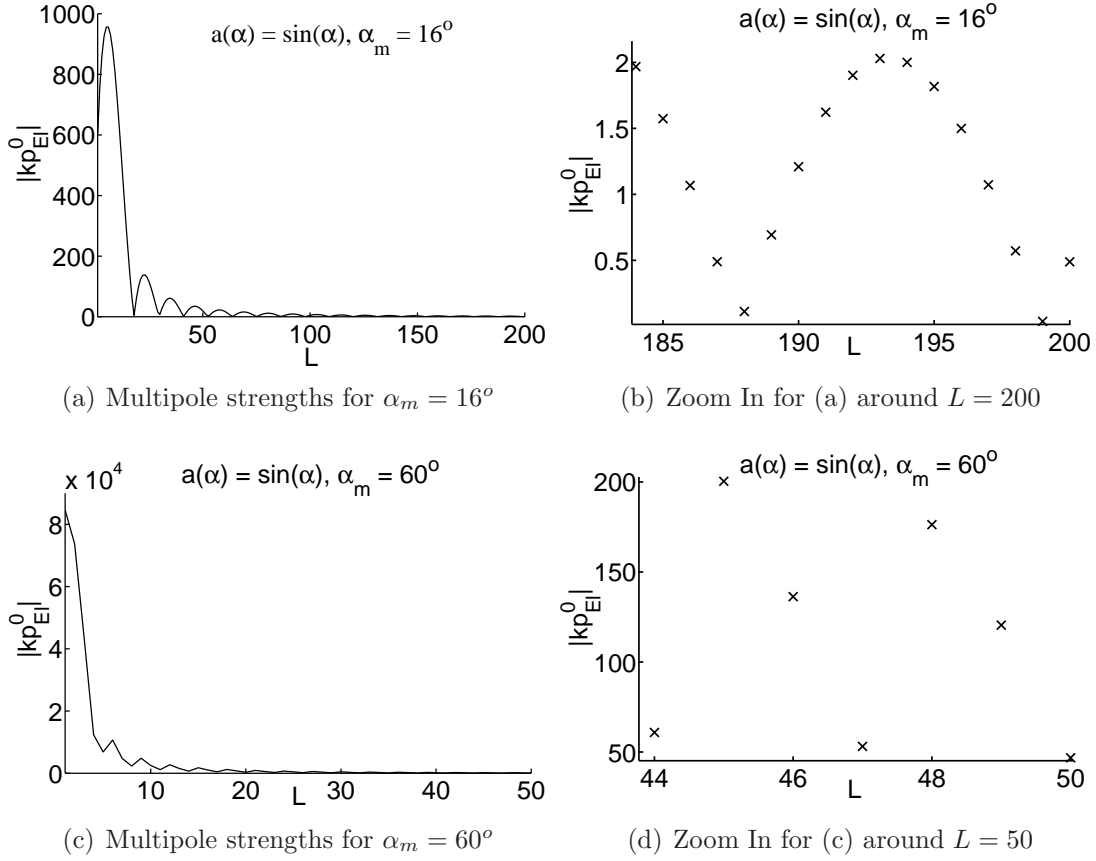


Figure 3.3: Multipole strengths  $|kp_{El}^0| = |k \times p_{El}^0|$  with  $f = 100\text{cm}$  and  $\lambda = 1.34\mu\text{m}$ .

system of limited aperture  $\alpha_m$ , the absolute strengths of the different orders is illustrated in Fig. 3.2(a). The first two terms are given by

$$p_{E1}^0 = i\sqrt{\frac{4\pi}{3}} \sin^4\left(\frac{\alpha_m}{2}\right) (2 + \cos \alpha_m), \quad p_{E2}^0 = -\frac{\sqrt{5\pi}}{8} \sin^4 \alpha_m.$$

Elsewhere the performance parameters to describe the focusing behavior of different systems have been introduced [109, 138, 139]. In particular, the parameter  $F$  is the electric energy density at the focus divided by the total input power, normalized to unity for a complete dipole wave. Then for this particular case,

$$F = \frac{2}{\sqrt{3\pi}} \frac{|p_{E1}^0|^2}{\int_0^{\alpha_m} |a(\alpha)|^2 \sin \alpha d\alpha} = |p_{E1}^0|.$$

Figure 3.3 plots the multipole strengths ( $k \times p_{El}^0$ ) in a unit of  $k$  for the two numerical apertures  $\alpha_m = 16^\circ$  and  $\alpha_m = 60^\circ$ . We can observe that with low NA lens  $\alpha_m = 16^\circ$ , the number of multipole terms with high relative strengths is larger compared to the high

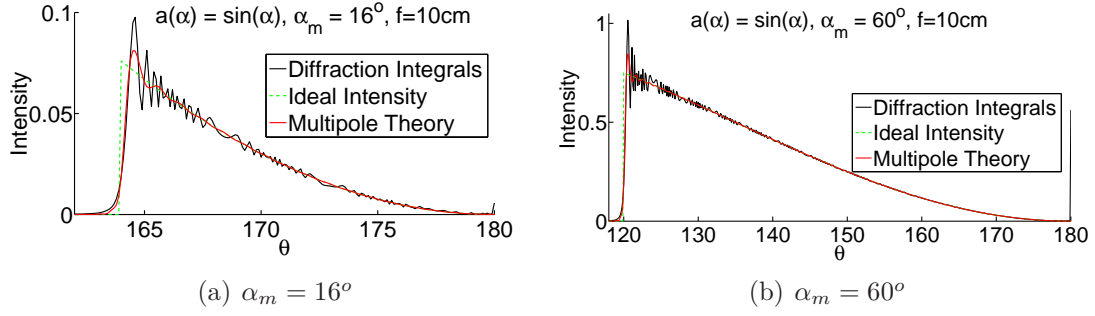


Figure 3.4: Electric intensity modelings on GRS for ADW with  $f = 10\text{cm}$  and  $L = 400$ .

NA lens  $\alpha_m = 60^\circ$ . It has been well-known that we need an infinite number of multipole terms to describe a plane wave  $\alpha_m = 0^\circ$ .

Figure 3.4 shows the electric intensity plots on the GRS. The ideal intensity is the assumption of the incident intensity. The Diffraction Integrals plot is plotted using Eq. (3.65). The Multipole Theory plot is plotted using Eq. (3.67) with  $j_l$  replaced by  $h_l^{(2)}$ . We observe the interesting phenomena that the diffraction integrals gives a strong oscillation around the hard-edge of the beam and also on the axial axis. This is due to the fact that the diffraction integrals ignore the contribution of the second kind of the critical points [34]. For the plot using the multipole theory, the oscillation around the hard-edge of the beam is due to the truncation of the multipole series which is similar to the phenomenon of modeling a hard-edge function using a finite Fourier series. Another interesting observation is that there is no anomalous behavior around the axial-axis ( $\alpha_m = 180^\circ$ ) when using the multipole theory for the model. This property is due to the fact that we have included the contribution of the second kind of the critical points in the modeling based on the multipole theory.

Figure 3.5 shows the plots of the electric intensity on different spheres whose centers are the focus. The plots using the ray optics is produced under the assumption that we can model the propagation of the beam using the geometrical optics. We will discuss further about the use of geometrical optics in this thesis in Chapter 5. It is observed that, while the wave approaches to the focus, there is a deviation between ray optics and other two approaches as shown in Figs. 3.5(a) and 3.5(b). When the wave travels away the aperture, the contribution of the second kind of the critical points reduces and hence the diffraction integrals and the multipole theory give better agreements in Figs. 3.5(a) and

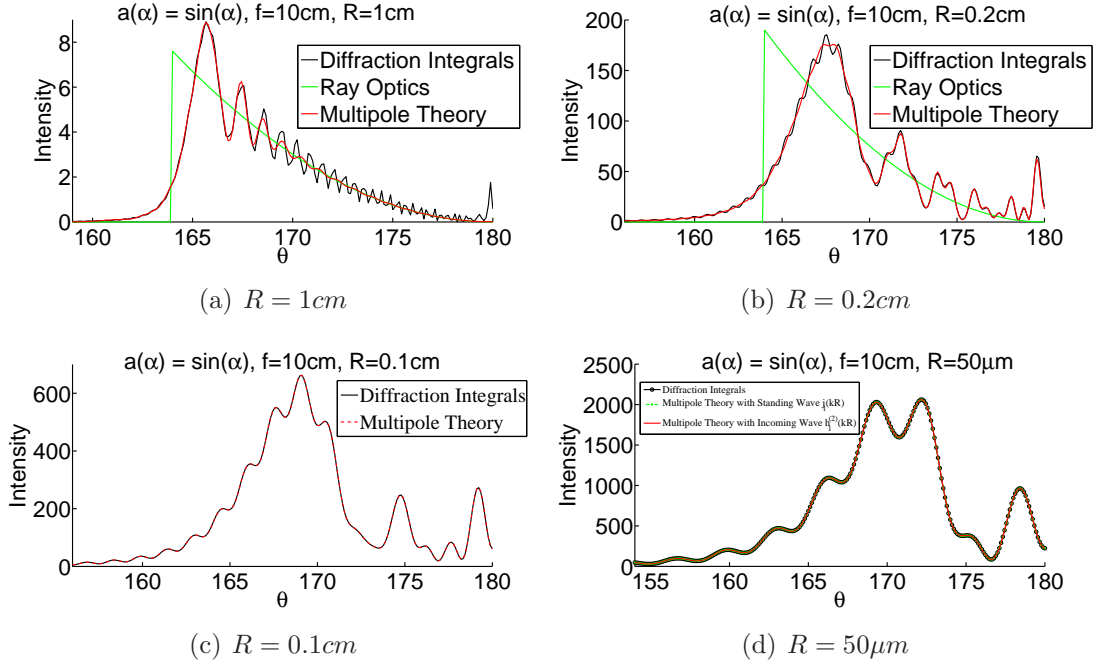


Figure 3.5: Electric intensity on spheres with different radius for ADW with  $f = 10\text{cm}$  and  $\alpha_m = 16^\circ$ .

3.5(b) and perfect agreements on Figs. 3.5(c) and 3.5(d). Since the outgoing wave, which is the consequence of the incoming wave after passing the focus, also contributes to the field around the focus, we also plot the electric intensity due to the interference between the incoming wave and the outgoing wave, i.e. the standing wave which is expressed in Eq. (3.67). Figure 3.5(d) shows that the outgoing wave does not contribute to the total field on the back surface ( $z < 0$ ) of the sphere with  $R = 50\mu\text{m}$ . However, when the wave approaches closer to the focus, the outgoing wave contribute more to the back surface. Hence, the incoming wave is different from the total field as shown in Fig. 3.6.

Figure 3.7 shows the contour plots of the electric energy density for the ADW. We can

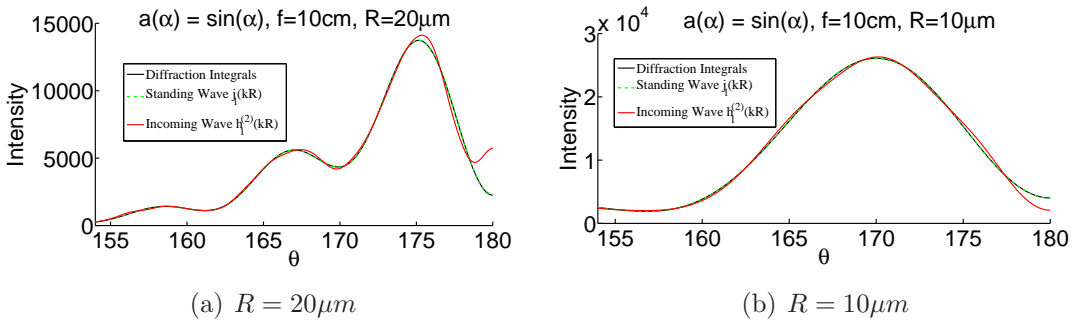


Figure 3.6: Electric intensity on spheres with different radius for ADW with  $f = 10\text{cm}$  and  $\alpha_m = 16^\circ$ .

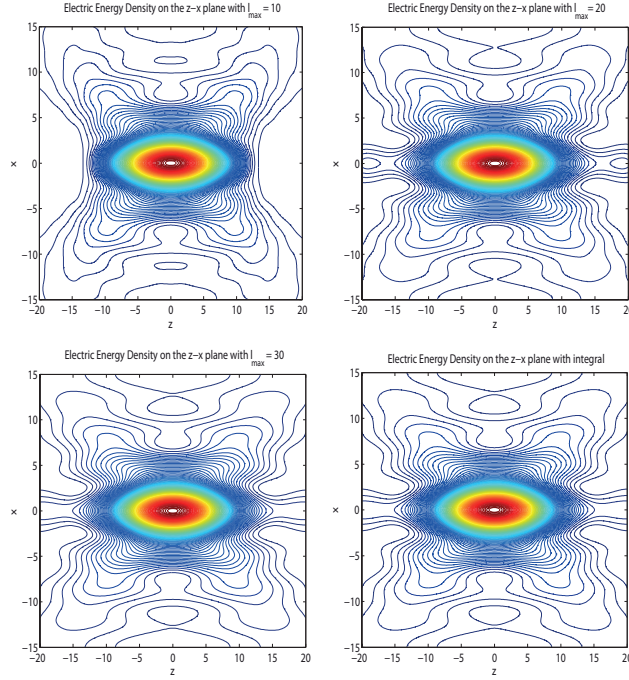


Figure 3.7: Contour plots of the electric energy density for the radial polarization (ADW) for  $\alpha_m = 60^\circ$ .

see that the summation in Eq. (3.67) can be terminated at  $L = 30$  to achieve the perfect agreement with the integral diffractions.

We have studied the ADW with a hard-edge aperture, i.e., we studied the cases  $\alpha_m = 16^\circ$  and  $\alpha_m = 60^\circ$ . To appreciate the effect of the hard-edge, we study an aperture without any hard-edge. We can choose  $a(\alpha) = \sin(3\alpha)$  and  $\alpha_m = 60^\circ$ . It can be seen that  $a(0^\circ) = 0$  and  $a(60^\circ) = 0$ , hence we can call the focused beam, a soft-edge beam. We plot the electric intensity of the assumed electric intensity and its modelings using the two approaches in Fig. 3.8. We observe that both modelings are perfect in this case due to the fact that there is no contribution of the second kind of the critical points [33, 34]. Figure 3.8 plots the electric intensity on the complete GRS, i.e., from  $\theta = 0^\circ$  to  $\theta = 180^\circ$ . We can see that the diffraction integrals in fact describe the total field, in other words, the diffraction integrals describe the summation of the incoming and the outgoing beams. On contrary, the multipole theory for the incoming beam describe, as its name means, the incoming beam only. Figure 3.9 plots the electric intensity distribution on different spheres. With the apodization function  $a(\alpha) = \sin(3\alpha)$  and  $\alpha_m = 60^\circ$ , we can observe that there is no difference between the results using Eqs. (3.65) and (3.67).

### 3. Multipole Theory and Angular Spectrum Representation for the Focal Fields

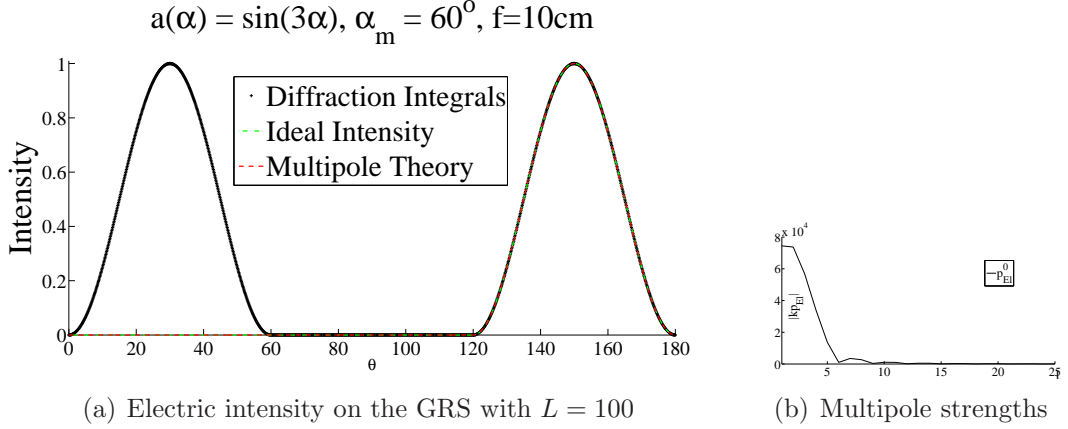


Figure 3.8: Electric intensity modelings on the GRS for  $a(\alpha) = \sin(3\alpha)$ ,  $f = 10\text{cm}$ ,  $\alpha_m = 60^\circ$ .

These equations describe the summation of the incoming and outgoing fields. We can observe that the outgoing field does not contribute to the total field at the back surface of the spheres with  $R > 10\mu\text{m}$  as shown in Fig. 3.9(c). The incoming field is different from the total field as shown in Fig. 3.9(d), which means the outgoing field contribute to everywhere on the sphere with  $R = 5\mu\text{m}$ .

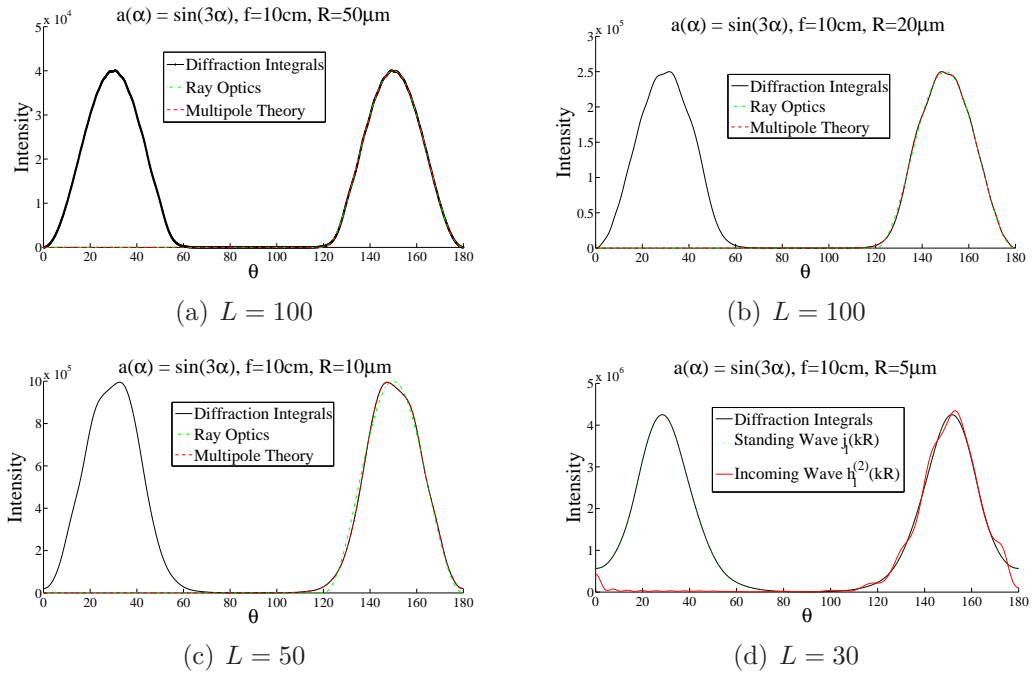


Figure 3.9: Electric intensity modelings on different spheres for  $a(\alpha) = \sin(3\alpha)$  with  $f = 10\text{cm}$  and  $\alpha_m = 60^\circ$ .

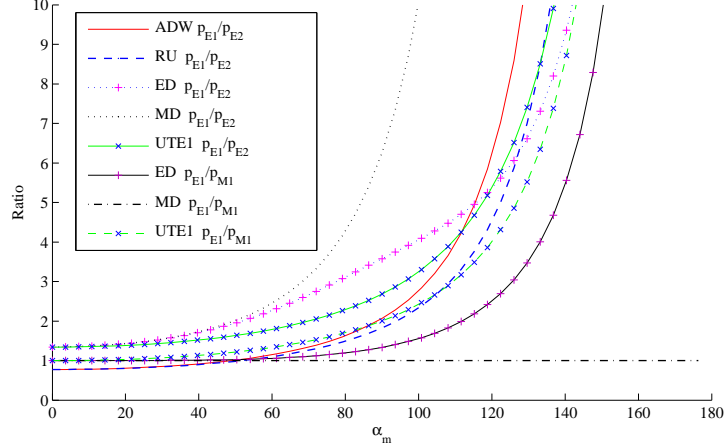


Figure 3.10: The ratio  $\frac{p_{E1}}{p_{E2}}$  and  $\frac{p_{E1}}{p_{M1}}$  for different polarizations.

#### 3.5.1.2 Radial Polarization with Uniform Illumination (RU)

Now, we consider a uniform illumination (RU), which means  $a(\alpha) = 1$ . For  $4\pi$  illumination, ignoring the constant term  $f e^{ikf}$ , we obtain  $p_{E1}^0 = i\frac{\pi\sqrt{3\pi}}{4}$ ,  $p_{E1}^0 = 0$ ,  $p_{E3}^0 = -i\frac{\pi\sqrt{7\pi}}{64}$ ,  $p_{E4}^0 = 0$ ,  $p_{E5}^0 = i\frac{\pi\sqrt{11\pi}}{256}$ . For a partial aperture, the first two terms are

$$p_{E1}^0 = i\frac{\sqrt{3\pi}}{4}(\alpha_m - \sin \alpha_m \cos \alpha_m), \quad p_{E2}^0 = -\frac{\sqrt{5\pi}}{6} \sin^3 \alpha_m,$$

and again the multipole strengths are plotted in Fig. 3.2(b). Note that although  $|p_{E1}^0|$  can be greater than the axial dipole wave case,  $F$  is lower as the input power is larger. The uniform illumination exhibits a singularity in amplitude at  $\alpha = 0$ : such a singularity can be generated experimentally (approximately) by using a polarization rotator (e.g. using a liquid crystal device) on a plane polarized beam. Quabis et al. reported that the focal spot was improved by using a high numerical aperture, and also by using an annular pupil [15]. Both these strategies increase the strength of the longitudinal field component related to the transverse field component, which is produced by higher order multipole terms. In the vicinity of the focus, the quadrupole term  $p_{E2}^0$  dominates the transverse field. The ratio  $\frac{|p_{E1}^0|}{|p_{E2}^0|}$  is thus an indication of the relative strength of the longitudinal field. The multipole approach thus benefits in providing a simple measure of the purity of the longitudinal field mode. The ratio  $\frac{|p_{E1}^0|}{|p_{E2}^0|}$  is illustrated in Fig. 3.10. We see that it increases with NA, and is higher for ADW than RU.

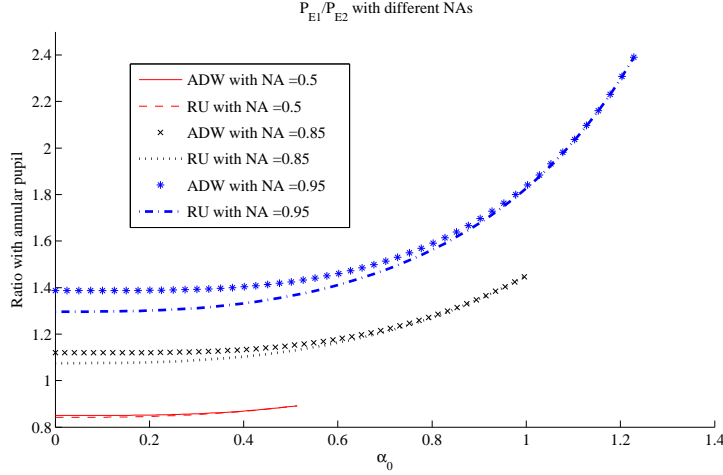


Figure 3.11: The ratio  $\frac{|p_{E1}^0|}{|p_{E2}^0|}$  for ADW and RU polarizations for an annular lens with obscuration angle  $\alpha_0$ .

The focal spot is also improved by using an annular pupil. In Fig. 3.11, the ratio  $\frac{|p_{E1}^0|}{|p_{E2}^0|}$  is shown for lenses of different  $NA$ , for annular pupils with different obscuration angles,  $\alpha_0$ . While the value of  $|p_{E1}^0|$  (and also  $F$ ) drops for an annular pupil, we see that  $\frac{|p_{E1}^0|}{|p_{E2}^0|}$  increases as the central obscuration increases. The annulus has a greater effect for higher  $NA$  and for the uniform illumination case.

### 3.5.2 Azimuthal Polarization, $n = 1$

Azimuthal polarization with  $n = 0$  gives, by symmetry, a focused field distribution with a zero in electric field at the focus, a type of doughnut beam [140]. For  $n = 1$ , Eq. (3.70) reduces to

$$\begin{aligned}
 p_{El}^1 &= \frac{i^{l-1} f e^{ikf}}{l(l+1)} \left[ \frac{\pi(2l+1)}{l(l+1)} \right]^{\frac{1}{2}} \int_0^\pi a(\alpha) P_l^1(\cos \alpha) d\alpha, \\
 p_{Ml}^1 &= -\frac{i^l f e^{ikf}}{l(l+1)} \left[ \frac{\pi(2l+1)}{l(l+1)} \right]^{\frac{1}{2}} \int_0^\pi a(\alpha) \frac{d}{d\alpha} P_l^1(\cos \alpha) \sin \alpha d\alpha.
 \end{aligned} \tag{3.80}$$

This corresponds to the vortex form of TE1, considered in Section 4. The resulting field distribution is rotating in time, and the electric field at the focal point is non-zero and circularly polarized [141]. The special case when  $a(\alpha) = 1$  for  $\alpha < \alpha_m$ ;  $a(\alpha) = 0$  for  $\alpha > \alpha_m$  is the vortex form of UTE1, which maximizes  $F$  for TE1.

### 3.5.3 Generalized Linear Polarization

#### 3.5.3.1 Mixed Dipole, $S(\alpha) = 0$

For  $S(\alpha) = 0$ , the polarization corresponds to the focusing of plane polarized light, and  $a(\alpha) = 1$  results in the mixed dipole field (MD), where the amplitude variation is chosen so that the energy density at focus for focusing of plane polarized light is maximized [110, 139]. Equation (3.72) becomes

$$\bar{E}(\hat{\mathbf{s}}) = \cos^2 \frac{\alpha}{2} (\cos \beta \hat{\alpha} - \sin \beta \hat{\beta}). \quad (3.81)$$

When  $S(\alpha) = 0$ , the components appear in electric and magnetic multipole pairs of equal strength:

$$p_{E1}^1 = ip_{M1}^1 = \frac{i^l f e^{ikf}}{2l(l+1)} \left[ \frac{\pi(2l+1)}{l(l+1)} \right]^{\frac{1}{2}} \int_0^{\alpha_m} \cos^2 \frac{\alpha}{2} \left( \frac{d}{d\alpha} P_l^1(\cos \alpha) + \frac{P_l^1(\cos \alpha)}{\sin \alpha} \right) \sin \alpha d\alpha. \quad (3.82)$$

The four lowest order terms are, ignoring the constant term  $f e^{ikf}$ , as follows

$$p_{E1}^1 = ip_{M1}^1 = \frac{i}{12} \sqrt{\frac{3\pi}{2}} \sin^2 \frac{\alpha_m}{2} (7 + 4 \cos \alpha_m + \cos^2 \alpha_m),$$

$$p_{E2}^1 = ip_{M2}^1 = -\frac{1}{4} \sqrt{\frac{5\pi}{6}} \sin^2 \alpha_m \cos^4 \frac{\alpha_m}{2}.$$

These are plotted in Fig. 3.12(a), and the ratio  $\frac{|p_{E1}^1|}{|p_{E2}^1|}$  is shown in Fig. 3.10.

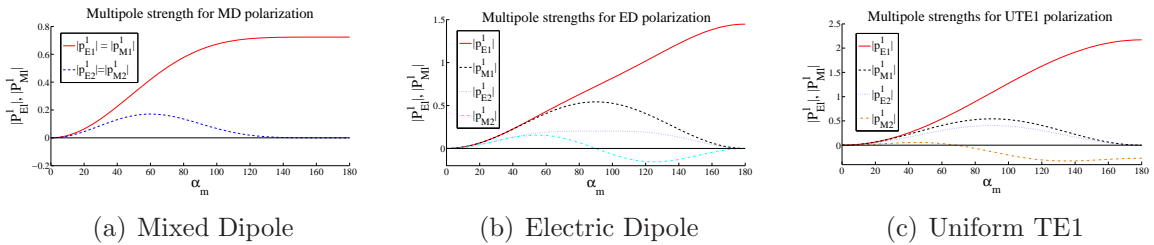


Figure 3.12: Multipole strengths of MD, ED, and UTE1.

### 3.5.3.2 Electric Dipole

It has been shown that modifying linear polarization so that it matches the polarization of a transverse-oriented electric dipole improves the focusing properties as compared with the linear polarized case [109, 136, 142, 143]. This can be useful for some applications, as the electric field at the focus is transverse, unlike when focusing radially-polarized light. The far-field is

$$\bar{E}(\hat{\mathbf{s}}) = a(\alpha)(\cos \alpha \cos \beta \hat{\alpha} - \sin \beta \hat{\beta}). \quad (3.83)$$

For the electric dipole polarization,  $S(\alpha) = \tan^2(\frac{\alpha}{2})$ , the multipole components are

$$\begin{aligned} p_{El}^1 &= \frac{i^l f e^{ikf}}{2l(l+1)} \left[ \frac{\pi(2l+1)}{l(l+1)} \right]^{\frac{1}{2}} \int_0^{\alpha_m} a(\alpha) \left( \cos \alpha \frac{d}{d\alpha} P_l^1(\cos \alpha) + \frac{1}{\sin \alpha} P_l^1(\cos \alpha) \right) \sin \alpha d\alpha, \\ p_{Ml}^1 &= \frac{i^{l-1} f e^{ikf}}{2l(l+1)} \left[ \frac{\pi(2l+1)}{l(l+1)} \right]^{\frac{1}{2}} \int_0^{\alpha_m} a(\alpha) \left( \frac{d}{d\alpha} P_l^1(\cos \alpha) + \cot \alpha P_l^1(\cos \alpha) \right) \sin \alpha d\alpha. \end{aligned} \quad (3.84)$$

The four lowest order terms are, ignoring the term  $f e^{ikf}$ , as follows

$$\begin{aligned} p_{E1}^1 &= \frac{i}{2} \sqrt{\frac{\pi}{6}} \sin^2 \frac{\alpha_m}{2} (4 + \cos \alpha_m + \cos^2 \alpha_m), \\ p_{M1}^1 &= \frac{1}{4} \sqrt{\frac{3\pi}{2}} \sin^2 \alpha_m, \\ p_{E2}^1 &= -\frac{1}{8} \sqrt{\frac{5\pi}{6}} \sin^2 \alpha_m (1 + \cos^2 \alpha_m), \\ p_{M2}^1 &= \frac{i}{4} \sqrt{\frac{5\pi}{6}} \sin^2 \alpha_m \cos \alpha_m. \end{aligned} \quad (3.85)$$

Again these are plotted in Fig. 3.12(b), and the ratio  $\frac{|p_{E1}^1|}{|p_{E2}^1|}$  is shown in Fig. 3.10.

### 3.5.3.3 Transverse Electric TE1

Another interesting case is for  $S(\alpha) = 1$ , which corresponds to the TE1 mode, which produces the smallest focal spot for any case where  $S(\alpha)$  is a constant. The value of  $F$  is then maximized when  $a(\alpha) \cos^2(\frac{\alpha}{2}) = 1$ , which we call uniform TE1 (UTE1) [136]. The

Eq. (3.72) becomes

$$\bar{E}(\hat{\mathbf{s}}) = -2 \sin \beta \hat{\beta}. \quad (3.86)$$

The multipole strengths are, ignoring the term  $f e^{ikf}$ , as follows

$$\begin{aligned} p_{El}^1 &= \frac{i^l f e^{ikf}}{l(l+1)} \left[ \frac{\pi(2l+1)}{l(l+1)} \right]^{\frac{1}{2}} \int_0^{\alpha_m} P_l^1(\cos \alpha) d\alpha, \\ p_{Ml}^1 &= \frac{i^{l-1} f e^{ikf}}{l(l+1)} \left[ \frac{\pi(2l+1)}{l(l+1)} \right]^{\frac{1}{2}} \int_0^{\alpha_m} \frac{d}{d\alpha} P_l^1(\cos \alpha) \sin \alpha d\alpha. \end{aligned} \quad (3.87)$$

The lowest order components are,

$$\begin{aligned} p_{E1}^1 &= i \sqrt{\frac{3\pi}{2}} \sin^2 \frac{\alpha_m}{2}, \\ p_{M1}^1 &= \frac{1}{4} \sqrt{\frac{3\pi}{2}} \sin^2 \alpha_m, \\ p_{E2}^1 &= -\frac{1}{4} \sqrt{\frac{5\pi}{6}} \sin^2 \alpha_m, \\ p_{M2}^1 &= \frac{i}{6} \sqrt{\frac{5\pi}{6}} \sin^2 \frac{\alpha_m}{2} (2 \cos^2 \alpha_m + 2 \cos \alpha_m - 1). \end{aligned} \quad (3.88)$$

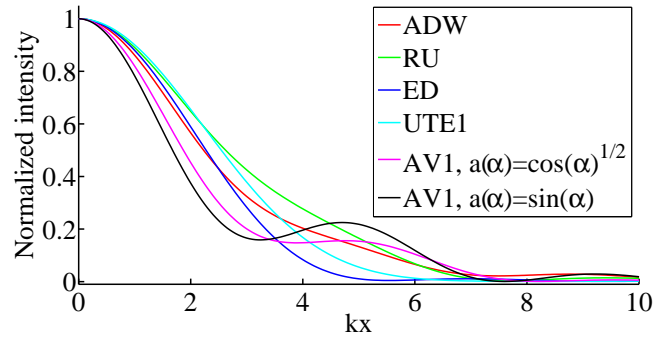
The strengths of the lowest order terms are shown in Fig. 3.12(c), and the ratios  $\frac{|p_{E1}^1|}{|p_{E2}^1|}$ ,  $\frac{|p_{E1}^1|}{|p_{M1}^1|}$  are shown in Fig. 3.10. For the generalized linear polarization cases, the ratio  $\frac{|p_{E1}^1|}{|p_{M1}^1|}$  of UTE1 has a higher value than that of ED and the ratio of MD has a lower value than that of ED. The ratio  $\frac{|p_{E1}^1|}{|p_{E2}^1|}$  is actually highest for MD, which suggests that for MD the focal spot is deteriorated mainly by the  $p_{M1}^1$  component.

### 3.5.4 Focal Field Distributions

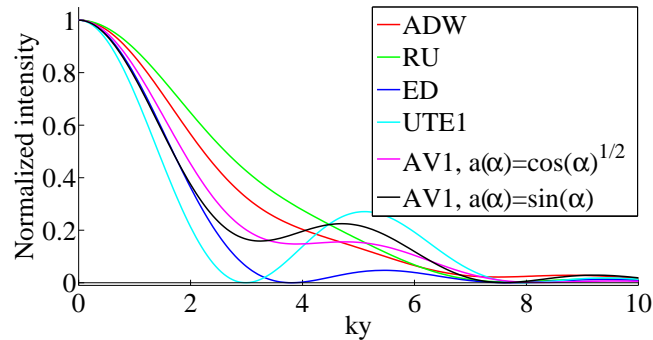
We have studied a variety of polarized beams, and here we show the best cases in terms of the smallest focal spots. The azimuthal polarization with a vortex  $n = 1$  is denoted by AV1. For the cylindrical beams ADW, RU, and AV1, we have the circular distribution on the transversal plane, i.e.  $x$ - distribution and  $y$ -distribution are the same. For the generalized linear polarized beams ED and UTE1, as expected, the distributions on the transversal plane are asymmetrical. It is obvious from Figs. 3.13(a) and 3.13(b) that the AV1 beams can produce the focal spots on the transversal plane with smaller full widths

### 3. Multipole Theory and Angular Spectrum Representation for the Focal Fields

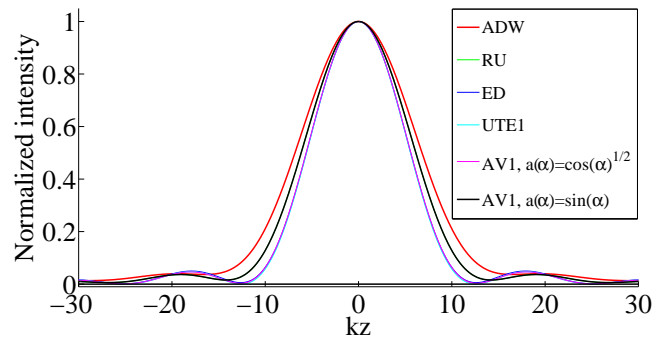
at half maximum (FWHM) compared to the radially polarized beams, ADW and RU. However, the side lobes produced by the AV1 beams are stronger than that of the radially polarized beams. A strong side lobe will deteriorates the performance of microscope by reducing the contrast and sometime the strong side lobe even causes artifacts in imaging applications. By employing pinholes, the side lobe can be reduced as shown in confocal scanning microscopy.



(a) Along  $x$ -axis



(b) Along  $y$ -axis



(c) Along  $z$ -axis

Figure 3.13: Electric focal intensity for ADW with  $\alpha_m = 60^\circ$ .

# Chapter 4

## Interpretation of the Scattering Mechanism

Light scattering occurs in nearly all aspects in our daily life and science. Probably, it is one of the most classical research topics which has been studied from the very beginning of our history. It may be excited by the curiousness about the nature phenomena like why we see a blue sky or how the rainbow appears after a rain. Understanding the scattering mechanism is hence always a topic of interest. This chapter is planned to present an interpretation of the scattering mechanism based on a novel definition of incident beams. The main objectives of this chapter are as follows: Firstly, we define the incident focused beam such that it contains only the incoming wave and hence is expressed in terms of the second kind of spherical Hankel function  $h_l^{(2)}(kr)$ . This definition is different from the definition by the GLMT which defines the incident focused beam such that it could propagate without any perturbation, and hence is expressed in terms of the spherical Bessel functions  $j_l(kr)$ . Using our definition, we show that we can calculate the internal and external electromagnetic fields of both the scatterers shown in Figs. 1.3 and 1.4. On contrary, the definition made by the GLMT is not applicable to the calculation of the total internal and external fields of the SIL. Secondly, for the spherical scatterer, though the two definitions are different, we show that both lead to the same results for the total internal and external fields of the sphere. We also derive the DSs in a straightforward

## 4. Interpretation of the Scattering Mechanism

---

manner. We use the concepts of incoming and outgoing waves to explain the scattering mechanism and accordingly form the mathematical formula. By doing these, we avoid a number of algebraic manipulations caused by other derivation approaches and give an insightful understanding of the scattering mechanism. The explanation of the scattering mechanism in this chapter will help us to solve the boundary conditions at a spherical interface rigorously as presented in chapter 5.

### 4.1 Incident Focused Field

Alternative to Eq. (3.42), the electromagnetic field can be expressed in terms of the Debye potentials (DPs)  $\Pi_e$  and  $\Pi_m$  [144]:

$$\begin{aligned} E_r &= \frac{i}{\omega\varepsilon} \left( \frac{\partial^2}{\partial r^2} r \Pi_e + k^2 r \Pi_e \right), \\ E_\theta &= \frac{i}{\omega\varepsilon} \frac{1}{r} \frac{\partial^2}{\partial r \partial \theta} r \Pi_e + \frac{1}{\sin \theta} \frac{\partial}{\partial \phi} \Pi_m, \\ E_\phi &= \frac{i}{\omega\varepsilon} \frac{1}{r \sin \theta} \frac{\partial^2}{\partial r \partial \phi} r \Pi_e - \frac{\partial}{\partial \theta} \Pi_m. \end{aligned} \quad (4.1)$$

For a converging beam, the incident focused field can be expressed in terms of the converging electric  $\Pi_e^{inc}$  and magnetic  $\Pi_m^{inc}$  DPs [79]:

$$\begin{aligned} \Pi_e^{inc} &= -i\omega\varepsilon \sum_{l=1}^{\infty} \sum_{m=-l}^l p_{El}^m h_l^{(2)}(kr) Y_l^m(\theta, \phi), \\ \Pi_m^{inc} &= ik \sum_{l=1}^{\infty} \sum_{m=-l}^l p_{Ml}^m h_l^{(2)}(kr) Y_l^m(\theta, \phi). \end{aligned} \quad (4.2)$$

The electric  $p_{El}^m$  and magnetic  $p_{Ml}^m$  multipole strengths (EMMSs), which are sometimes called the beam shape coefficients for a laser focused beam [66], are evaluated as shown in Eq. (3.41). We note that there exist other methods [55, 145–149], which are based on the radial components of the electric  $E_r^{inc}$  and magnetic  $H_r^{inc}$  fields, for evaluating the multipole strengths. In a paper about high-aperture beams, Sheppard categorized the beams into three types [4]. Whereas, our formula in Eq. (3.41) is suitable for type 1 beam in which the radial components of the field is ignorable, the other methods are

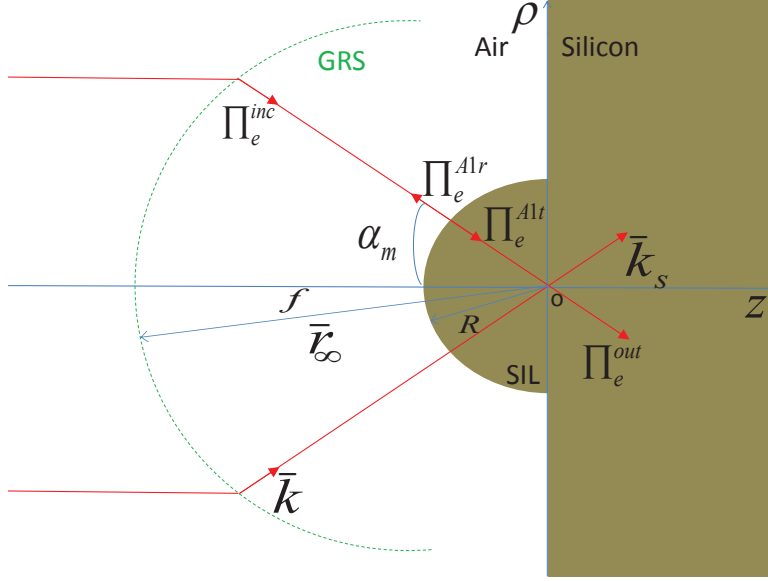


Figure 4.1: Hemispherical SIL-based scatterer.

suitable for the types 2 and 3 beams.

As we can observe, the DPs and the electromagnetic field are closely related and can be easily derived from each other. Hence, for a convenient purpose, we explain and derive results using the scalar DPs with the implication that our explanations and derivations are applied directly for the electromagnetic field. Since any result for the magnetic DP can be obtained from the result for the electric DP by applying the principle of duality, and vice versa, we derive the results only for the electric DP below.

## 4.2 Scattering by a Hemispherical Solid Immersion Lens

Firstly, we consider the case of the HSIL in Fig. 4.1. The incident DP  $\Pi_e^{inc}$  in Eq. (4.2) is partially reflected  $\Pi_e^{A1r}$  and partially transmitted  $\Pi_e^{A1t}$  and can be expressed as follows:

$$\Pi_e^{A1r} = -i\omega\varepsilon \sum_{l=1}^{\infty} \sum_{m=-l}^l a_{2l} p_{E1}^m h_l^{(1)}(kr) Y_l^m(\theta, \phi), \quad (4.3)$$

$$\Pi_e^{A1t} = -i\omega\varepsilon \sum_{l=1}^{\infty} \sum_{m=-l}^l c_{2l} p_{E1}^m h_l^{(2)}(k_s r) Y_l^m(\theta, \phi), \quad (4.4)$$

#### 4. Interpretation of the Scattering Mechanism

where  $a_{2l}$  and  $c_{2l}$  are the scattering coefficients. To derive the scattering coefficients, we apply the boundary conditions at the interface which require that the tangent electric ( $E_\theta, E_\phi$ ) and magnetic ( $H_\theta, H_\phi$ ) field components are continuous across the interface. By inspecting the expressions in Eq(4.1) and equivalent expressions for the magnetic field ( $H_\theta, H_\phi$  is obtained from Eq. (4.1) by exchanging the roles of  $\Pi_e$  with  $\Pi_m$  and  $\varepsilon$  with  $-\mu$ ) carefully, we see that the boundary conditions mean  $\Pi_e, \Pi_m, \frac{1}{\varepsilon} \frac{\partial}{\partial r}(r\Pi_e), \frac{1}{\mu} \frac{\partial}{\partial r}(r\Pi_m)$  are continuous across the interface. Applying the boundary conditions, we obtain the scattering coefficients as follows

$$\begin{aligned} a_{l2} &= \frac{\frac{\varepsilon}{\varepsilon_s} \frac{k_s}{k} \hat{H}_l^{(2)}(kR) \hat{H}_l^{(2)'}(k_s R) - \hat{H}_l^{(2)}(k_s R) \hat{H}_l^{(2)'}(kR)}{\hat{H}_l^{(1)'}(kR) \hat{H}_l^{(2)}(k_s R) - \frac{\varepsilon}{\varepsilon_s} \frac{k_s}{k} \hat{H}_l^{(1)}(kR) \hat{H}_l^{(2)'}(k_s R)}, \\ c_{l2} &= \frac{2i \frac{k_s}{k}}{\hat{H}_l^{(1)'}(kR) \hat{H}_l^{(2)}(k_s R) - \frac{\varepsilon}{\varepsilon_s} \frac{k_s}{k} \hat{H}_l^{(1)}(kR) \hat{H}_l^{(2)'}(k_s R)}, \end{aligned} \quad (4.5)$$

where  $\hat{H}_l^{(1)}(kr) = kr h_l^{(1)}(kr)$  and  $\hat{H}_l^{(2)}(kr) = kr h_l^{(2)}(kr)$  are Riccati-Bessel functions. Similarly, for the magnetic DP  $\Pi_m^{inc}$ , we can derive the reflection  $b_{l2}$  and transmission  $d_{l2}$  coefficients as follows

$$\begin{aligned} b_{l2} &= \frac{\frac{\mu}{\mu_s} \frac{k_s}{k} \hat{H}_l^{(2)}(kR) \hat{H}_l^{(2)'}(k_s R) - \hat{H}_l^{(2)}(k_s R) \hat{H}_l^{(2)'}(kR)}{\hat{H}_l^{(1)'}(kR) \hat{H}_l^{(2)}(k_s R) - \frac{\mu}{\mu_s} \frac{k_s}{k} \hat{H}_l^{(1)}(kR) \hat{H}_l^{(2)'}(k_s R)}, \\ d_{l2} &= \frac{2i \sqrt{\frac{\mu_s \varepsilon_s}{\mu \varepsilon}}}{\hat{H}_l^{(1)'}(kR) \hat{H}_l^{(2)}(k_s R) - \sqrt{\frac{\mu \varepsilon_s}{\mu_s \varepsilon}} \hat{H}_l^{(1)}(kR) \hat{H}_l^{(2)'}(k_s R)}. \end{aligned} \quad (4.6)$$

Figure 4.2 plots the scattering coefficients for a silicon HSIL with  $R = 500\mu m$  and the reflective index  $n_s = 3.5$ . We can observe that, for  $l > kR \simeq 2345$ , all coefficients  $c_{l2}$  and  $d_{l2}$  are almost zero.

The electric DP represented by Eq. (4.4) is the incident field approaching the focal region. Since there is no source in the focal region, there must be an outgoing field to remove the singularity caused by the incoming wave as visualized in Fig. 4.1. The DP representing this outgoing field can be obtained from Eq. (4.4) by replacing  $h_l^{(2)}(k_s r)$  by

$h_l^{(1)}(k_s r)$ :

$$\Pi_e^{out} = -i\omega\varepsilon \sum_{l=1}^{\infty} \sum_{m=-l}^l c_{l2} p_{El}^m h_l^{(1)}(k_s r) Y_l^m(\theta, \phi). \quad (4.7)$$

The total DP in the focal region are then the summation of  $\Pi_e^{A1t}$  in Eq. (4.4) and  $\Pi_e^{out}$  in Eq. (4.7):

$$\Pi_e^{tot1} = -2i\omega\varepsilon \sum_{l=1}^{\infty} \sum_{m=-l}^l c_{l2} p_{El}^m j_l(k_s r) Y_l^m(\theta, \phi). \quad (4.8)$$

The scattering coefficients and the DPs derived in this section will be used to evaluate the focal field of a HSIL in chapter 5.

### 4.3 Scattering by a General Solid Immersion Lens

In this section, we will derive the scattering coefficients for the scatterer shown in Fig. 1.3(b). As we can realize by comparing Figs. 1.3(a) and 1.3(b), there is a fundamental difference between the two configurations that is the distance between the center of the GRS and the center of the SIL. For the scatterer shown in Fig. 1.3(b), before we derive the scattering coefficients using the DPs, we have to represent the incident focusing field in the coordinates whose origin is the center of the SIL. This can be done by using the translational addition theorems.

#### 4.3.1 Translational Addition Theorems

Addition theorems translate electromagnetic field from one to another coordinate system. The theorems play a pivotal role in fast algorithms for solving integral equation used in a variety of applications [150–154]. There are two types of addition theorems involved with rotation and translation of a coordinate system, respectively. In this thesis, we discuss and use the translational addition theorem only. As we observed in Fig. 1.3(b), a translation of the electric field from  $O$  coordinate system to  $O'$  coordinate system is necessary for solving the boundary conditions. The translational addition theorem was derived firstly by Friedman and Russek for spherical scalar multipole fields [155]. Later, Stein [156] and Cruzan [157] derived the translational addition theorem for vector multipole fields.

#### 4. Interpretation of the Scattering Mechanism

---

After that, due to the usefulness of the addition theorem in solving problems relating to electromagnetic fields, the addition theorems have been active topics [158–162]. Basically, using the addition theorems involves calculating a translation matrix. The calculation of the translation matrix at first use Gaunt coefficients which are related to Wigner  $3j$  symbol. However, the evaluation of Wigner  $3j$  symbol involves a large number of factorials which makes the evaluation of the translation matrix extremely inefficient. Hence, better approaches naturally arise. For a translation along  $z$ -axis, Bruning and Lo derived recurrence relations for the Gaunt coefficients [158] and hence significantly reduced the computational cost. However, the computational complexity remains in the approach of Bruning and Lo. Chew derived recurrence relations for the translation coefficients for the scalar fields [163]. Chew and Wang presented two approaches for deriving the recurrence relations for the vector fields [164]. The first approach is to relate the elements of the vector case with that of scalar case. The second approach is to use a direct derivation of the recurrence relations. Alternative to Chew’s approach, Kim used angular-momentum operator for deriving his own recurrence relations and claimed that his approach could be more efficient [165]. The advantage of Kim’s approach is obtained by avoiding the calculation of extra elements in Chew’s approach. However, Kim formed the relations for more translation coefficients (5 and 6 compared to 4 of Chew’s relations). Hence, Kim’s approach is less efficient in some particular cases such as our case with a small number of the extra translation coefficients. Kim also discussed symmetrical properties of the translation coefficients for both scalar and vector fields [166]. Recently, Chew expressed the theorems in a more compact notation and derived a new expression which can be used to diagonalize the vector addition theorem [167]. In this thesis, we derive and use the addition theorems based on the results presented in Refs. [163, 164] to translate the electromagnetic field from the  $O$ -coordinate system to the  $O'$ -coordinate system. In fact, we use different definitions for the vector multipole fields, hence we derive the translational addition theorems for our definitions as presented in appendix B. Using the addition theorems, we can express the electromagnetic field in

## 4. Interpretation of the Scattering Mechanism

---

Eq. (4.2) in  $O'$ -coordinate system as follows

$$\mathbf{E}(\bar{r}') = \sum_{l'=1}^{\infty} \sum_{m'=-l'}^{l'} [p_{E'l'}^{m'} \mathbf{N}_{l'}^{m'}(\bar{r}') + p_{M'l'}^{m'} \mathbf{M}_{l'}^{m'}(\bar{r}')], \quad (4.9)$$

where

$$\begin{aligned} p_{E'l'}^{m'} &= \sum_{l=1}^{\infty} \sum_{m=-l}^l [A_{l'm'}^{lm} p_{El}^m + i B_{l'm'}^{lm} p_{Ml}^m], \\ p_{M'l'}^{m'} &= \sum_{l=1}^{\infty} \sum_{m=-l}^l [A_{l'm'}^{lm} p_{Ml}^m - i B_{l'm'}^{lm} p_{El}^m]. \end{aligned} \quad (4.10)$$

In Eq. (4.10), the translational coefficients  $A_{l'm'}^{lm}$  and  $B_{l'm'}^{lm}$  depend on the condition whether  $r' > d$  or  $r' < d$  as shown in appendix B. Figure 4.3 plots the multipole strengths of the axial dipole wave in the  $O'$  coordinate system with  $f = 100\text{cm}$ ,  $\lambda = 1.34\mu\text{m}$ , and  $d = 1.75\text{mm}$ . We observe the interesting result that is, for a higher NA beam in the  $O$  coordinate system, we need more multipole terms to describe it in the new coordinate system though we need a smaller number of the multipole terms to describe the higher NA beam in the original coordinate  $O$ . This seems to be contradictory but in fact it is not, due to the fact that in the new coordinate system the higher NA beam becomes lower NA beam since we consider the beam waist at the origin.

Figure 4.3 plots the electric multipole strengths for the case of  $r' > d$ . Figure 4.4 plots the multipole strength for the case of  $r' < d$ . Comparing Figs. 4.3(a) and 4.4, we see that the distributions of the multipole strengths are similar. The absolute values of the strengths in Fig. 4.4 are twice of those in Fig. 4.3(a) due to the initial values of the recurrence relations.

### 4.3.2 Scattering Coefficients for the GSIL

We have expressed the electric field in the  $O'$  coordinate system, and now it is straightforward to derive the scattering coefficients for the GSIL. We consider two cases depending on the translation distance and the radius of the SIL.

### Scattering Coefficients due to Incoming Beam

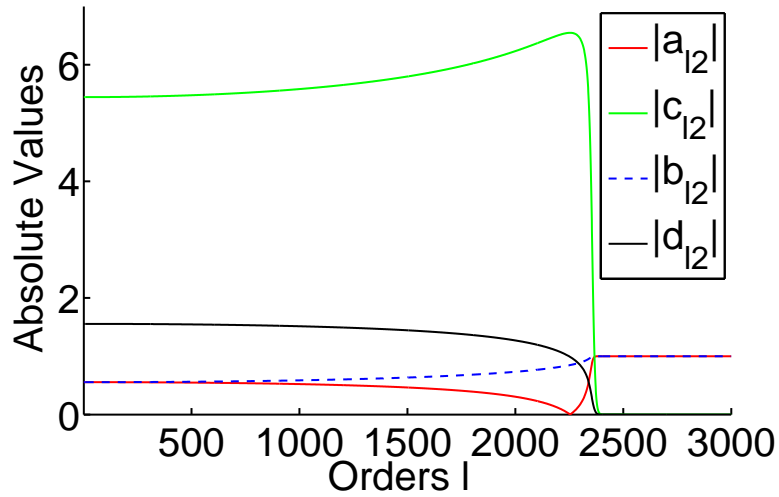


Figure 4.2: Scattering Coefficients for Hemispherical SIL.

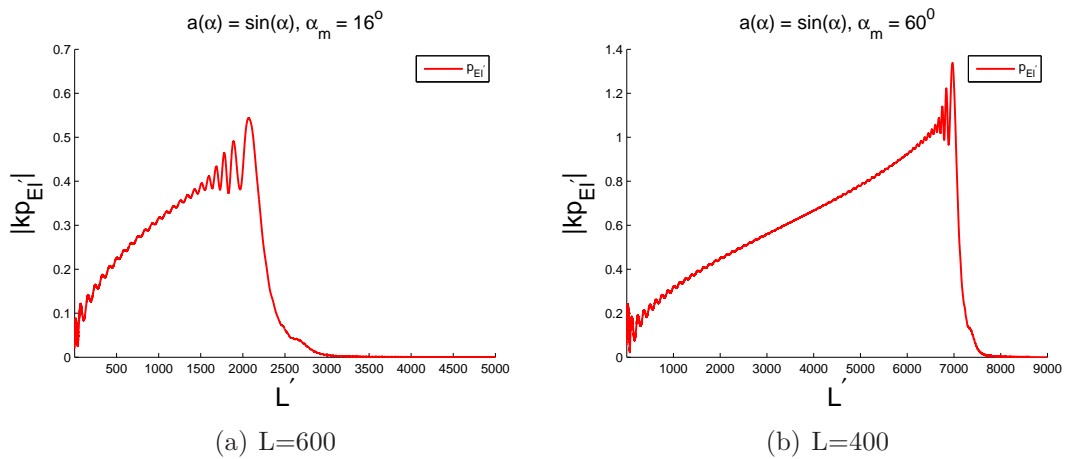


Figure 4.3: Multipole strengths in  $O'$ -coordinate system for  $r' > d$  with  $f = 100\text{cm}$  and  $d = 1.75\text{mm}$ .

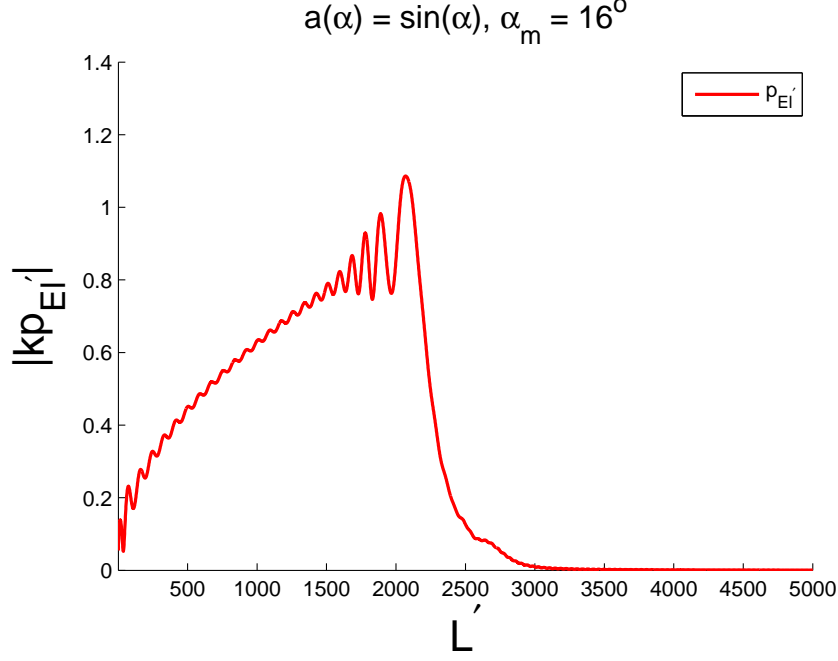


Figure 4.4: Multipole strengths in  $O'$ -coordinate system for  $r' < d$  with  $f = 100\text{cm}$ ,  $d = 1.75\text{mm}$ , and  $L = 600$ .

#### 4.3.2.1 Translational Distance is less than the Radius: $d < R$

From the translation theorems, we know that the spherical scalar multipole field  $\Psi_{l'}^{m'}(\vec{r}')$  for describing the incident beam is

$$\Psi_{l'}^{m'}(\vec{r}') = h_{l'}^{(2)}(kr')Y_{l'}^{m'}(\theta', \phi'),$$

hence, the incident DPs approaching the SIL are

$$\begin{aligned} \Pi_e^{inc} &= -i\omega\varepsilon \sum_{l'=1}^{\infty} \sum_{m'=-l'}^{l'} p_{E'l'}^{m'} h_{l'}^{(2)}(kr') Y_{l'}^{m'}(\theta', \phi'), \\ \Pi_m^{inc} &= ik \sum_{l'=1}^{\infty} \sum_{m'=-l'}^{l'} p_{M'l'}^{m'} h_{l'}^{(2)}(kr') Y_{l'}^{m'}(\theta', \phi'). \end{aligned} \quad (4.11)$$

We see that Eq. (4.11) is the same as Eq. (4.2) except being expressed in the different coordinate systems. Hence, applying the boundary conditions for the fields in the  $O'$  coordinate system, we get the same expressions for the scattering coefficients ( $a_{l'2}, b_{l'2}, c_{l'2}, d_{l'2}$ ) as we obtained in Eqs. (4.5) and (4.6) for the incident field in Eq. (4.2).

## 4. Interpretation of the Scattering Mechanism

### 4.3.2.2 Translational Distance is greater than the Radius: $d > R$

We know from the use of the addition theorems that the spherical scalar multipole field  $\Psi_{l'}^{m'}(\vec{r}')$  used for describing the incident field onto the GSIL is

$$\Psi_{l'}^{m'}(\vec{r}') = j_{l'}(kr')Y_{l'}^{m'}(\theta', \phi'),$$

hence, the incident DPs approaching the SIL are

$$\begin{aligned} \Pi_e^{inc} &= -i\omega\varepsilon \sum_{l'=1}^{\infty} \sum_{m'=-l'}^{l'} p_{El'}^{m'} j_{l'}(kr') Y_{l'}^{m'}(\theta', \phi'), \\ \Pi_m^{inc} &= ik \sum_{l'=1}^{\infty} \sum_{m'=-l'}^{l'} p_{Ml'}^{m'} j_{l'}(kr') Y_{l'}^{m'}(\theta', \phi'). \end{aligned} \quad (4.12)$$

We can observe from Eqs. (4.11) and (4.12) that Eq. (4.11) describes the incident beam as a converging beam but Eq. (4.12) describes the incident beam as a standing beam. This difference is due to the fact that the latter case describes the field, which is translated from the field due to the sink at the origin  $O$ , in the region excluding the sink.

The scattered field travels away from the origin and hence is expressed in terms of the

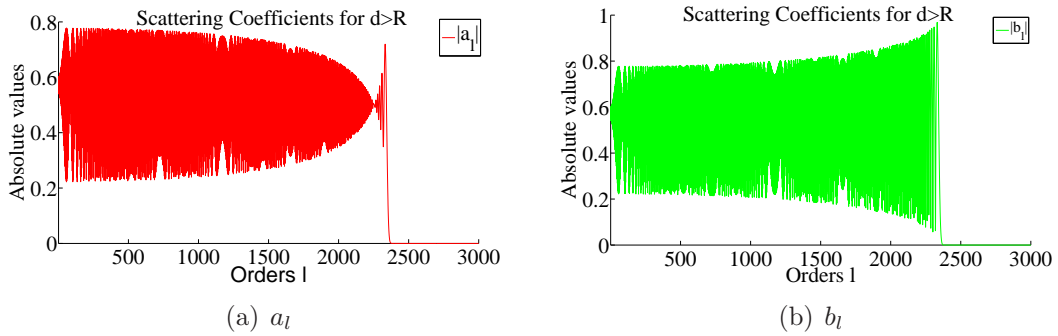


Figure 4.5: Scattering Coefficients for an ASIL with  $R = 500\mu m$ ,  $\lambda = 1.34\mu m$ , and  $d = 1.75mm$ .

## 4. Interpretation of the Scattering Mechanism

first kind of spherical Hankel functions

$$\begin{aligned}\Pi_e^{A1r} &= -i\omega\varepsilon \sum_{l'=1}^{\infty} \sum_{m'=-l'}^{l'} a_{l'} p_{E l'}^{m'} h_{l'}^{(1)}(kr') Y_{l'}^{m'}(\theta', \phi'), \\ \Pi_m^{A1r} &= ik \sum_{l'=1}^{\infty} \sum_{m'=-l'}^{l'} b_{l'} p_{M l'}^{m'} h_{l'}^{(1)}(kr') Y_{l'}^{m'}(\theta', \phi').\end{aligned}\quad (4.13)$$

The transmitted field travels toward the origin and hence is expressed in terms of the second kind of the spherical Hankel functions

$$\begin{aligned}\Pi_e^{A1t} &= -i\omega\varepsilon \sum_{l'=1}^{\infty} \sum_{m'=-l'}^{l'} c_{l'} p_{E l'}^{m'} h_{l'}^{(2)}(kr') Y_{l'}^{m'}(\theta', \phi'), \\ \Pi_m^{A1t} &= ik \sum_{l'=1}^{\infty} \sum_{m'=-l'}^{l'} d_{l'} p_{M l'}^{m'} h_{l'}^{(2)}(kr') Y_{l'}^{m'}(\theta', \phi').\end{aligned}\quad (4.14)$$

Applying the boundary conditions, we can derive the scattering coefficients as follows

$$\begin{aligned}a_{l'} &= \frac{\frac{\varepsilon}{\varepsilon_s} \frac{k_s}{k} \hat{J}_{l'}(kR) \hat{H}_{l'}^{(2)'}(k_s R) - \hat{H}_{l'}^{(2)}(k_s R) \hat{J}_{l'}(kR)}{\hat{H}_{l'}^{(1)'}(kR) \hat{H}_{l'}^{(2)}(k_s R) - \frac{\varepsilon}{\varepsilon_s} \frac{k_s}{k} \hat{H}_{l'}^{(1)}(kR) \hat{H}_{l'}^{(2)'}(k_s R)}, \\ b_{l'} &= \frac{\frac{\mu}{\mu_s} \frac{k_s}{k} \hat{J}_{l'}(kR) \hat{H}_{l'}^{(2)'}(k_s R) - \hat{H}_{l'}^{(2)}(k_s R) \hat{J}_{l'}(kR)}{\hat{H}_{l'}^{(1)'}(kR) \hat{H}_{l'}^{(2)}(k_s R) - \frac{\mu}{\mu_s} \frac{k_s}{k} \hat{H}_{l'}^{(1)}(kR) \hat{H}_{l'}^{(2)'}(k_s R)}, \\ c_{l'} &= \frac{i \sqrt{\frac{\mu_s \varepsilon_s}{\mu \varepsilon}}}{\hat{H}_{l'}^{(1)'}(kR) \hat{H}_{l'}^{(2)}(k_s R) - \sqrt{\frac{\mu_s \varepsilon}{\mu \varepsilon_s}} \hat{H}_{l'}^{(1)}(kR) \hat{H}_{l'}^{(2)'}(k_s R)}, \\ d_{l'} &= \frac{i \sqrt{\frac{\mu_s \varepsilon_s}{\mu \varepsilon}}}{\hat{H}_{l'}^{(1)'}(kR) \hat{H}_{l'}^{(2)}(k_s R) - \sqrt{\frac{\mu_s \varepsilon}{\mu_s \varepsilon}} \hat{H}_{l'}^{(1)}(kR) \hat{H}_{l'}^{(2)'}(k_s R)}.\end{aligned}\quad (4.15)$$

where  $\hat{J}_{l'}(kr') = kr' j_{l'}(kr')$  is also a Riccati-Hankel function.

We can observe  $c_{2l'} = 2c_{l'}$  and  $d_{2l'} = 2d_{l'}$ , and hence the plots for  $c_{l'}$  and  $c_{2l'}$  can be appreciated from Fig. 4.2. Figure 4.5 plots the absolute values of  $a_{l'}$  and  $b_{l'}$ . We can see the values of  $a_{l'}$  and  $b_{l'}$  are different from those of  $a_{2l'}$  and  $b_{2l'}$ . Compared to Eqs. (4.5) and (4.6), the scattering coefficients shown in Eq. (4.15) are different in the nominators in which the Riccati-Hankel function  $\hat{H}_{l'}^{(2)}(kr)$  is replaced by  $\hat{J}_{l'}(kr')$ . This difference is due to the different incident beams. We will discuss more about this difference and its

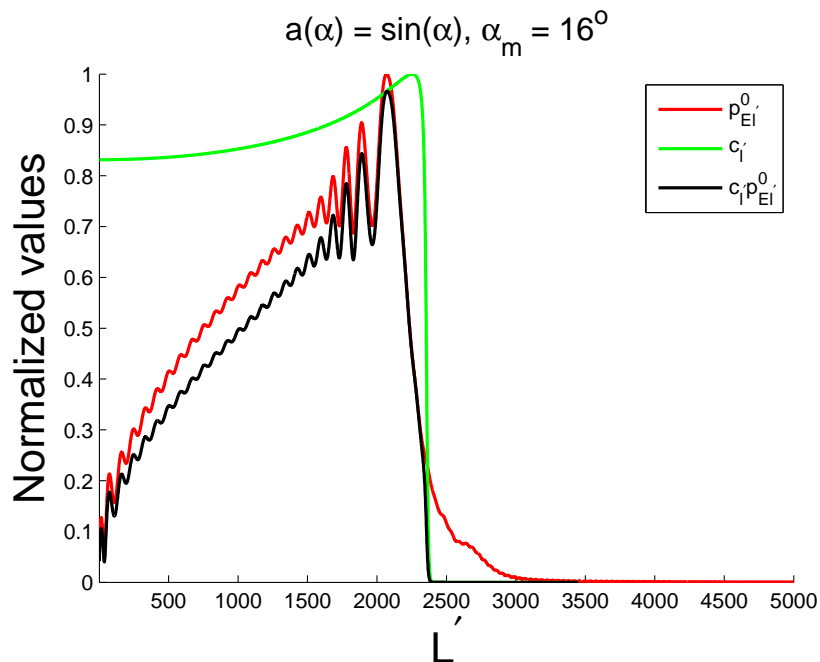


Figure 4.6: Effective multipole strengths  $c_l P_{E'l}^0$  inside the ASIL with  $R = 500\mu m$ ,  $\lambda = 1.34\mu m$ ,  $d = 1.75mm$ , and  $L = 600$ .

implication in explaining the scattering mechanism next section.

## 4.4 Scattering by a Sphere

We have considered and explained the scattering by the spherical interfaces shown in Fig. 1.3 which has an open boundary. Hence the scattering is one-time interaction only. The scattering mechanism is obviously different for a sphere in Fig. 1.4 due to the fact that the sphere has a closed boundary and consequently there is an infinite number of light-matter interactions at the boundary. In this section, we explain and derive the internal and external fields of the sphere. We consider the two cases of the incident beams approaching the scatterer which are represented by Eqs. (4.11) and (4.12). It should be noted that the expression in Eq. (4.2) is in fact the special case of Eq. (4.11) with  $d = 0$ .

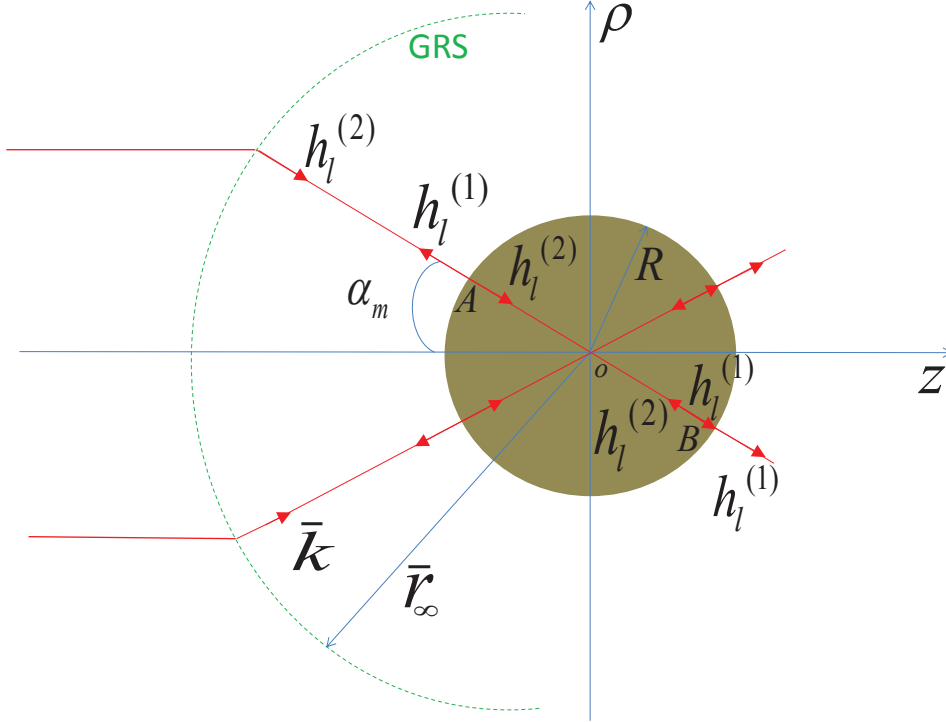


Figure 4.7: Spherical scatterer.

#### 4.4.1 The Distance between the Center of the Sphere and the Center of the GRS is less than the Radius $d < R$

Since Eqs. (4.2) and (4.11) have the same form, the following derivations are applicable to both cases. For convenience, we consider the case in Fig. 4.7 with the incident field expressed by Eq. (4.2). The outgoing DP in Eq. (4.4) now plays the role of incident DP  $\Pi_e^{B1i}$  on to the sphere's back surface. Equivalently, the geometrical ray, after penetrating into the sphere through point A, approaches point B in Fig. 4.7 and  $\Pi_e^{B1i}$  represents this ray:

$$\Pi_e^{B1i} = -i\omega\varepsilon \sum_{l=1}^{\infty} \sum_{m=-l}^l c_{l2} p_{El}^m h_l^{(1)}(k_s r) Y_l^m(\theta, \phi). \quad (4.16)$$

Then  $\Pi_e^{B1i}$  is partially reflected  $\Pi_e^{B1r}$  back to the interior region and partially transmitted  $\Pi_e^{B1t}$  into the external region:

$$\Pi_e^{B1r} = -i\omega\varepsilon \sum_{l=1}^{\infty} \sum_{m=-l}^l a_{l1} c_{l2} p_{El}^m h_l^{(2)}(k_s r) Y_l^m(\theta, \phi), \quad (4.17)$$

$$\Pi_e^{B1t} = -i\omega\varepsilon \sum_{l=1}^{\infty} \sum_{m=-l}^l c_{l1} c_{l2} p_{El}^m h_l^{(1)}(kr) Y_l^m(\theta, \phi), \quad (4.18)$$

#### 4. Interpretation of the Scattering Mechanism

where the scattering coefficients  $a_{l1}$  and  $c_{l1}$  of the outgoing wave can be derived as follows:

$$a_{l1} = \frac{\frac{\varepsilon}{\varepsilon_s} \frac{k_s}{k} \hat{H}_l^{(1)}(kR) \hat{H}_l^{(1)'}(k_s R) - \hat{H}_l^{(1)}(k_s R) \hat{H}_l^{(1)'}(kR)}{\hat{H}_l^{(1)'}(kR) \hat{H}_l^{(2)}(k_s R) - \frac{\varepsilon}{\varepsilon_s} \frac{k_s}{k} \hat{H}_l^{(1)}(kR) \hat{H}_l^{(2)'}(k_s R)},$$

$$c_{l1} = \frac{2i \frac{\varepsilon}{\varepsilon_s}}{\hat{H}_l^{(1)'}(kR) \hat{H}_l^{(2)}(k_s R) - \frac{\varepsilon}{\varepsilon_s} \frac{k_s}{k} \hat{H}_l^{(1)}(kR) \hat{H}_l^{(2)'}(k_s R)}.$$

The reflected part  $\Pi_e^{B1r}$  travels back through the origin and becomes an outgoing wave  $\Pi_e^{A2i}$  which is obtained from  $\Pi_e^{B1r}$  by replacing  $h_l^{(2)}(k_s r)$  by  $h_l^{(1)}(k_s r)$ :

$$\Pi_e^{A2i} = -i\omega\varepsilon \sum_{l=1}^{\infty} \sum_{m=-l}^l a_{l1} c_{l2} p_{El}^m h_l^{(1)}(k_s r) Y_l^m(\theta, \phi). \quad (4.19)$$

Again  $\Pi_e^{A2i}$  will be partially reflected  $\Pi_e^{A2r}$  back to the interior region and partially transmitted  $\Pi_e^{A2t}$  into the external region:

$$\Pi_e^{A2r} = -i\omega\varepsilon \sum_{l=1}^{\infty} \sum_{m=-l}^l a_{l1}^2 c_{l2} p_{El}^m h_l^{(2)}(k_s r) Y_l^m(\theta, \phi), \quad (4.20)$$

$$\Pi_e^{A2t} = -i\omega\varepsilon \sum_{l=1}^{\infty} \sum_{m=-l}^l c_{l1} a_{l1} c_{l2} p_{El}^m h_l^{(1)}(kr) Y_l^m(\theta, \phi). \quad (4.21)$$

The reflected part  $\Pi_e^{A2r}$  travels back through the origin and becomes an outgoing DP  $\Pi_e^{B2i}$  which is obtained from  $\Pi_e^{A2r}$  by replacing  $h_l^{(2)}(k_s r)$  by  $h_l^{(1)}(k_s r)$ :

$$\Pi_e^{B2i} = -i\omega\varepsilon \sum_{l=1}^{\infty} \sum_{m=-l}^l a_{l1}^2 c_{l2} p_{El}^m h_l^{(1)}(k_s r) Y_l^m(\theta, \phi), \quad (4.22)$$

Again the reflected  $\Pi_e^{B2r}$  and transmitted  $\Pi_e^{B2t}$  parts due to  $\Pi_e^{B2i}$  can be expressed as follows:

$$\Pi_e^{B2r} = -i\omega\varepsilon \sum_{l=1}^{\infty} \sum_{m=-l}^l a_{l1}^3 c_{l2} p_{El}^m h_l^{(2)}(k_s r) Y_l^m(\theta, \phi), \quad (4.23)$$

$$\Pi_e^{B2t} = -i\omega\varepsilon \sum_{l=1}^{\infty} \sum_{m=-l}^l c_{l1} a_{l1}^2 c_{l2} p_{El}^m h_l^{(1)}(kr) Y_l^m(\theta, \phi). \quad (4.24)$$

#### 4. Interpretation of the Scattering Mechanism

Repeatedly, at the  $N$ th time of reflection inside the sphere, the incident  $\Pi_e^{Ni}$ , reflected  $\Pi_e^{Nr}$ , and transmitted  $\Pi_e^{Nt}$  DPs are expressed as follows:

$$\Pi_e^{Ni} = -i\omega\varepsilon \sum_{l=1}^{\infty} \sum_{m=-l}^l a_{l1}^{n-1} c_{l2} p_{El}^m h_l^{(1)}(k_s r) Y_l^m(\theta, \phi), \quad (4.25)$$

$$\Pi_e^{Nr} = -i\omega\varepsilon \sum_{l=1}^{\infty} \sum_{m=-l}^l a_{l1}^n c_{l2} p_{El}^m h_l^{(2)}(k_s r) Y_l^m(\theta, \phi), \quad (4.26)$$

$$\Pi_e^{Nt} = -i\omega\varepsilon \sum_{l=1}^{\infty} \sum_{m=-l}^l c_{l1} a_{l1}^{n-1} c_{l2} p_{El}^m h_l^{(1)}(kr) Y_l^m(\theta, \phi), \quad (4.27)$$

where odd  $N$  is responsible for the ray approaching the point  $B$  and even  $N$  is responsible for the ray approaching the point  $A$ . From Eqs. (4.3), (4.18), (4.21), (4.24), and (4.27), we can express the total scattered Debye potential as follows:

$$\begin{aligned} \Pi_e^s &= -i\omega\varepsilon \sum_{l=1}^{\infty} \sum_{m=-l}^l [a_{l2} + c_{l1}c_{l2} + c_{l1}a_{l1}c_{l2} + \dots + c_{l1}a_{l1}^{n-1}c_{l2} + \dots] p_{El}^m h_l^{(1)}(kr) Y_l^m(\theta, \phi) \\ &= -i\omega\varepsilon \sum_{l=1}^{\infty} \sum_{m=-l}^l \left[ a_{l2} + \frac{c_{l1}c_{l2}}{1 - a_{l1}} \right] p_{El}^m h_l^{(1)}(kr) Y_l^m(\theta, \phi) \\ &= -i\omega\varepsilon \sum_{l=1}^{\infty} \sum_{m=-l}^l a_{l2}^e p_{El}^m h_l^{(1)}(kr) Y_l^m(\theta, \phi), \end{aligned} \quad (4.28)$$

where the effective scattering coefficient  $a_{l2}^e$  is

$$\begin{aligned} a_{l2}^e &= a_{l2} + \frac{c_{l1}c_{l2}}{1 - a_{l1}} \\ &= 2 \frac{\frac{\varepsilon}{\varepsilon_s} \frac{k_s}{k} \hat{J}_l(kR) \hat{J}'_l(k_s R) - \hat{J}'_l(kR) \hat{J}_l(k_s R)}{\hat{H}_l^{(1)'}(kR) \hat{J}_l(k_s R) - \frac{\varepsilon}{\varepsilon_s} \frac{k_s}{k} \hat{H}_l^{(1)}(kR) \hat{J}'_l(k_s R)} + 1 \\ &= 2a_l^g + 1, \end{aligned} \quad (4.29)$$

and  $a_l^g$  is the scattering coefficient used in the GLMT method.

After some mathematical manipulations, we express the total Debye potential inside the

## 4. Interpretation of the Scattering Mechanism

sphere as follows:

$$\begin{aligned}
\Pi_e^{in} &= -i\omega\varepsilon \sum_{l=1}^{\infty} \sum_{m=-l}^l p_{El}^m \left[ c_{l2} [h_l^{(2)}(k_s r) + h_l^{(1)}(k_s r)] + a_{l1} c_{l2} [h_l^{(2)}(k_s r) + h_l^{(1)}(k_s r)] \right. \\
&\quad \left. + a_{l1}^2 c_{l2} [h_l^{(2)}(k_s r) + h_l^{(1)}(k_s r)] + a_{l1}^{n-1} c_{l2} [h_l^{(2)}(k_s r) + h_l^{(1)}(k_s r)] + \dots \right] Y_l^m(\theta, \phi) \\
&= -2i\omega\varepsilon \sum_{l=1}^{\infty} \sum_{m=-l}^l \frac{c_{l2}}{1 - a_{l1}} p_{El}^m j_l(k_s r) Y_l^m(\theta, \phi) \\
&= -2i\omega\varepsilon \sum_{l=1}^{\infty} \sum_{m=-l}^l c_{l2}^e p_{El}^m j_l(k_s r) Y_l^m(\theta, \phi), \tag{4.30}
\end{aligned}$$

where the effective scattering coefficient  $c_{l2}^e$  is

$$\begin{aligned}
c_{l2}^e &= \frac{c_{l2}}{1 - a_{l1}} \\
&= \frac{i \frac{k_s}{k}}{\hat{H}_l^{(1)'}(kR) \hat{J}_l(k_s R) - \frac{\varepsilon}{\varepsilon_s} \frac{k_s}{k} \hat{H}_l^{(1)}(kR) \hat{J}_l'(k_s R)} \\
&= c_l^g, \tag{4.31}
\end{aligned}$$

and  $c_l^g$  is the scattering coefficient used in the GLMT method.

Using the principle of duality, the expression for the scattering coefficients  $b_l$  and  $d_l$  due to  $\Pi_m^{inc}$  can be obtained from the expressions in Eqs. (4.29) and (4.31), respectively, by replacing  $\frac{\varepsilon}{\varepsilon_s}$  with  $\frac{\mu}{\mu_s}$ . Equations (4.2), (4.28), and (4.29) give us the total Debye potential outside the sphere:

$$\begin{aligned}
\Pi_e^{tot2} &= \Pi_e^{inc} + \Pi_e^s \\
&= -i\omega\varepsilon \sum_{l=1}^{\infty} \sum_{m=-l}^l p_{El}^m h_l^{(2)}(kr) Y_l^m(\theta, \phi) - i\omega\varepsilon \sum_{l=1}^{\infty} \sum_{m=-l}^l (2a_l^g + 1) p_{El}^m h_l^{(1)}(kr) Y_l^m(\theta, \phi) \\
&= -2i\omega\varepsilon \sum_{l=1}^{\infty} \sum_{m=-l}^l p_{El}^m j_l(kr) Y_l^m(\theta, \phi) - 2i\omega\varepsilon \sum_{l=1}^{\infty} \sum_{m=-l}^l a_l^g p_{El}^m h_l^{(1)}(kr) Y_l^m(\theta, \phi). \tag{4.32}
\end{aligned}$$

Most researchers have used the GLMT to analyze light scattering by a sphere in a focused polarized beam. The GLMT expresses the incident  $\Pi_e^{Ginc}$ , scattered  $\Pi_e^{Gs}$ , and internal

## 4. Interpretation of the Scattering Mechanism

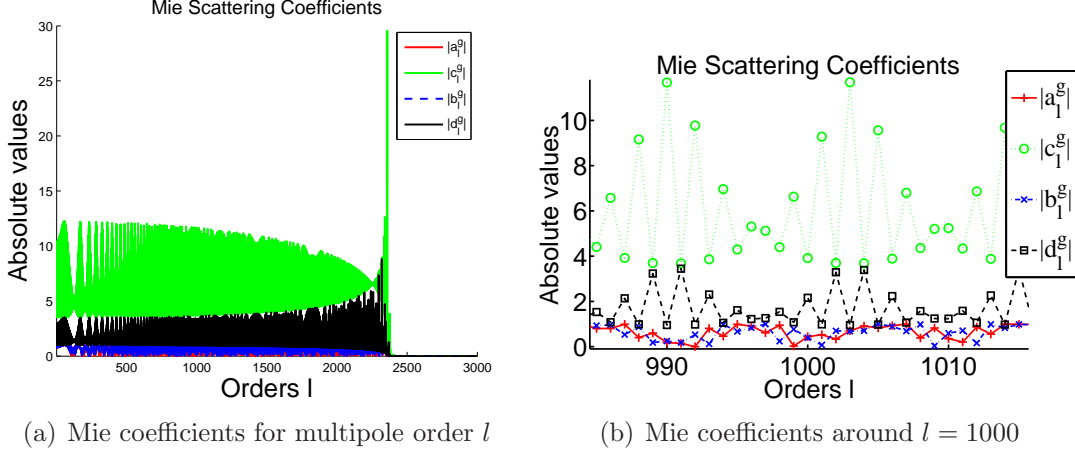


Figure 4.8: Mie Scattering Coefficients for a silicon sphere in air with  $R = 500\mu m$  and  $\lambda = 1.34\mu m$

$\Pi_e^{Gin}$  DPs as follows [44–47]:

$$\Pi_e^{Ginc} = -2i\omega\varepsilon \sum_{l=1}^{\infty} \sum_{m=-l}^l p_{El}^m j_l(kr) Y_l^m(\theta, \phi), \quad (4.33)$$

$$\Pi_e^{Gs} = -2i\omega\varepsilon \sum_{l=1}^{\infty} \sum_{m=-l}^l a_l^g p_{El}^m h_l^{(1)}(kr) Y_l^m(\theta, \phi), \quad (4.34)$$

$$\Pi_e^{Gin} = -2i\omega\varepsilon \sum_{l=1}^{\infty} \sum_{m=-l}^l c_l^g p_{El}^m j_l(k_s r) Y_l^m(\theta, \phi), \quad (4.35)$$

where the Mie scattering coefficients  $a_l^g$ ,  $b_l^g$ ,  $c_l^g$ , and  $d_l^g$  are plotted in Fig. 4.8.

We now compare the results obtained by the two approaches. Firstly, Eqs. (4.30), (4.31), and (4.35) show that the internal fields are the same for both our derivation and the GLMT. Secondly, we compare the total external fields. We see that the incident and scattered DPs in Eqs. (4.33) and (4.34) are exactly the first and second terms on the right side of Eq. (4.32), respectively. This means our derivation and the GLMT give the same total external fields regardless of the different definitions. This fact is due to the fact that the outgoing part of  $\Pi_e^{Ginc}$  is a part of the scattered field  $\Pi_e^s$ . This part of the scattered field

$$-i\omega\varepsilon \sum_{l=1}^{\infty} \sum_{m=-l}^l p_{El}^m h_l^{(1)}(kr) Y_l^m(\theta, \phi)$$

is independent of the composition of the sphere and hence can be considered as the diffraction part of the scattered field [168].

### 4.4.2 The Distance between the Center of the Sphere and the Center of the GRS is greater than the Radius $d > R$

In section 4.3.2.2, we have derived the scattering for the first interaction between the incident beam and the front spherical interface. In the case of a sphere, the transmitted DPs  $\Pi_e^{A1t}$  and  $\Pi_m^{A1t}$  in Eq. (4.14), after passing the focus, become the incident DPs approaching the back spherical interface between the sphere and the outside space. The scattering mechanism is exactly the same as the case explained in section 4.4.1. We ignore the prime of the parameters for convenience. We can derive and express the incident field, scattered field, and internal field as follows:

$$\Pi_e^{inc} = -i\omega\varepsilon \sum_{l=1}^{\infty} \sum_{m=-l}^l p_{El}^m j_l(kr) Y_l^m(\theta, \phi), \quad (4.36)$$

$$\begin{aligned} \Pi_e^s &= -i\omega\varepsilon \sum_{l=1}^{\infty} \sum_{m=-l}^l [a_l + c_{l1}c_l + c_{l1}a_{l1}c_l + \dots + c_{l1}a_{l1}^{n-1}c_l + \dots] p_{El}^m h_l^{(1)}(kr) Y_l^m(\theta, \phi) \\ &= -i\omega\varepsilon \sum_{l=1}^{\infty} \sum_{m=-l}^l \left[ a_l + \frac{c_{l1}c_l}{1 - a_{l1}} \right] p_{El}^m h_l^{(1)}(kr) Y_l^m(\theta, \phi) \\ &= -i\omega\varepsilon \sum_{l=1}^{\infty} \sum_{m=-l}^l a_l^e p_{El}^m h_l^{(1)}(kr) Y_l^m(\theta, \phi), \end{aligned} \quad (4.37)$$

$$\begin{aligned} \Pi_e^{in} &= -i\omega\varepsilon \sum_{l=1}^{\infty} \sum_{m=-l}^l p_{El}^m \left[ c_l [h_l^{(2)}(k_s r) + h_l^{(1)}(k_s r)] + a_{l1} c_l [h_l^{(2)}(k_s r) + h_l^{(1)}(k_s r)] \right. \\ &\quad \left. + a_{l1}^2 c_l [h_l^{(2)}(k_s r) + h_l^{(1)}(k_s r)] + a_{l1}^{n-1} c_l [h_l^{(2)}(k_s r) + h_l^{(1)}(k_s r)] + \dots \right] Y_l^m(\theta, \phi) \\ &= -i\omega\varepsilon \sum_{l=1}^{\infty} \sum_{m=-l}^l \frac{2c_l}{1 - a_{l1}} p_{El}^m j_l(k_s r) Y_l^m(\theta, \phi) \\ &= -i\omega\varepsilon \sum_{l=1}^{\infty} \sum_{m=-l}^l c_l^e p_{El}^m j_l(k_s r) Y_l^m(\theta, \phi), \end{aligned} \quad (4.38)$$

## 4. Interpretation of the Scattering Mechanism

---

where the effective scattering coefficients  $a_l^e$  and  $c_l^e$  are as follows:

$$\begin{aligned}
 a_l^e &= a_l + \frac{c_{l1}c_l}{1 - a_{l1}} \\
 &= \frac{\frac{\varepsilon}{\varepsilon_s} \frac{k_s}{k} \hat{J}_l(kR) \hat{J}'_l(k_s R) - \hat{J}'_l(kR) \hat{J}_l(k_s R)}{\hat{H}_l^{(1)'}(kR) \hat{J}_l(k_s R) - \frac{\varepsilon}{\varepsilon_s} \frac{k_s}{k} \hat{H}_l^{(1)}(kR) \hat{J}'_l(k_s R)} \\
 &= a_l^g,
 \end{aligned} \tag{4.39}$$

$$\begin{aligned}
 c_l^e &= \frac{2c_l}{1 - a_{l1}} \\
 &= \frac{i \frac{k_s}{k}}{\hat{H}_l^{(1)'}(kR) \hat{J}_l(k_s R) - \frac{\varepsilon}{\varepsilon_s} \frac{k_s}{k} \hat{H}_l^{(1)}(kR) \hat{J}'_l(k_s R)} \\
 &= c_l^g.
 \end{aligned} \tag{4.40}$$

Equations (4.39) and (4.40) prove that the scattered field and the internal field of the sphere are exactly the same as the results derived using the GLMT, and of course, the total internal and external fields are also the same for the two approaches.

## 4.5 Debye Series

In this section, we will discuss how the series representing the multiple interaction between the polarized beams and the scatterers are explained using our derivations and the Debye series formed by many researchers.

### 4.5.1 Translation Distance is less than the Radius of the Scatterer $d < R$

Eqs. (4.28) and (4.30) not only present the scattered and internal fields of the sphere in terms of the summations of the multiple scattering fields but also present the DSs for the

## 4. Interpretation of the Scattering Mechanism

---

scattering coefficients  $a_{l2}^e$  and  $c_{l2}^e$  without the need for any algebraic manipulation:

$$\begin{aligned} a_{l2}^e &= a_{l2} + c_{l1}c_{l2} + c_{l1}a_{l1}c_{l2} + \dots + c_{l1}a_{l1}^{n-1}c_{l2} + \dots \\ &= a_{l2} + c_{l1}c_{l2} \sum_{n=0}^{\infty} a_{l1}^n, \end{aligned} \quad (4.41)$$

$$\begin{aligned} c_{l2}^e &= c_{l2} + a_{l1}c_{l2} + a_{l1}^2c_{l2} + \dots + a_{l1}^{n-1}c_{l2} + \dots \\ &= c_{l2} \sum_{n=0}^{\infty} a_{l1}^n. \end{aligned} \quad (4.42)$$

The first coefficients  $a_{l2}$  and  $c_{l2}$  in Eqs. (4.41) and (4.42) are responsible for the first time scattering at the left boundary of the sphere from the incident DP  $\Pi_e^{inc}$ , and hence are the scattering coefficients for the case of HSIL due to the fact that there is no longer any scattering inside the HSIL. In the case of a sphere, the field directly transmitted into the sphere from the incident field is scattered an infinite number of times at the internal boundaries of the sphere, and each internal scattering will partially contribute to both the total scattered and internal fields. The effects of the multiple scatterings are represented by the DSs in Eqs. (4.41) and (4.42).

In fact, the scattered field is usually used in the GLMT and is expressed in Eq. (4.34) with the DS for  $a_l^g$  as follows [66, 78]:

$$a_l^g = \frac{1}{2} \left[ a_{l2} + c_{l1}c_{l2} \sum_{n=0}^{\infty} a_{l1}^n \right] - \frac{1}{2}. \quad (4.43)$$

### 4.5.2 Translation Distance is greater than the Radius of the Scatterer $d > R$

In section 4.4.2, we have showed that the incident field, the total scattered field, and the total internal field are the same for the approaches using our derivation and the GLMT. However, the meanings of the DSs for the effective scattering coefficients  $a_l^g$  and  $a_l^e$  are different. Whereas the DS of  $a_l^g$  is expressed in Eq. (4.43), we can obtain the DS for  $a_l^e$  from Eq. (4.37) as follows:

$$a_l^e = a_l + c_{l1}c_l \sum_{n=0}^{\infty} a_{l1}^n. \quad (4.44)$$

#### 4. Interpretation of the Scattering Mechanism

---

We know  $c_l = \frac{1}{2}c_{l2}$  and  $a_l = \frac{1}{2}(a_{l2} - 1)$ , hence Eqs. (4.43) and (4.44) are mathematically equivalent. However, the term  $-\frac{1}{2}$  in Eq. (4.43) is usually explained as a diffraction term but in Eq. (4.44), the term is included in the direct scattering coefficient  $a_l$ . In other words, the physical meanings of Eqs. (4.43) and (4.44) are different.

# Chapter 5

## Solid Immersion Microscopy

In previous chapter 3, we established the analytical expressions for the focusing of the polarized beams using an aplanatic lens. In chapter 4, we rigorously solved the boundary conditions for the polarized beams approaching the spherical interface. In this chapter, we use the results in the previous chapters for modeling wave propagation in the focal region and evaluating the focal field of a solid immersion microscope. Firstly, we form an approximate model using the angular spectrum method. Then we form a rigorous model using multipole theory.

The following notations are used in this chapter:  $R$  is the radius of the SIL;  $d$  is the distance between the centers of the SIL and the GRS;  $k$  and  $k_s$  are, respectively, the wave-numbers outside and inside the SIL. SIL-based systems can be categorized into two types, the hemispherical SIL-based system (HSS) and the general SIL-based system (GSS). Figure 5.1 represents an HSS for which  $d = 0$ . Figure 5.1 represents a GSS for which we have  $d \neq 0$ . When the condition  $d = \frac{k_s}{k}R$  is satisfied, the GSS is referred to an aplanatic SIL-based system (ASS). An ASS has both advantages and disadvantages compared to an HSS. An ASS has a lateral magnification of  $n^2 = \frac{k_s^2}{k^2}$ , and it increases the numerical aperture ( $NA$ ) of an incident beam by a factor of  $n^2$ , compared to  $n$  of an HSS. However, the maximum achievable  $NA$  of the two systems is the same and is equal to  $n$ . This is because the maximum achievable illumination angle  $\alpha_m$  of an ASS ( $\sin \alpha_m \leq \frac{1}{n}$ ) is smaller than that of an HSS ( $\sin \alpha_m \leq 1$ ). Because of this property, an ASS is superior

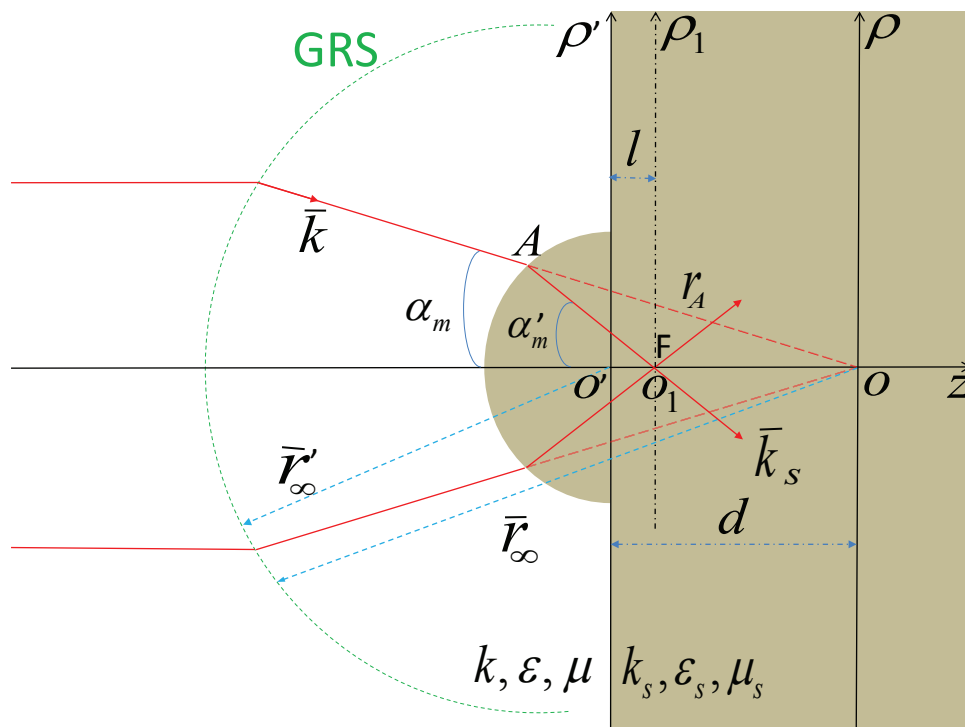


Figure 5.1: General SIL-based system.

for a low  $NA$  incident beam. The disadvantage of an ASS is that it suffers a serious chromatic aberration, whereas an HSS is almost free of chromatic aberration [82]. In addition, an HSS is better in term of degree of tolerance when the depth of the image point is changed. These properties make an HSS superior for a high  $NA$  incident beam. For the sake of a better visualization, we divide the wave propagation in Fig. 5.1 into four stages as follows: First stage: an incident collimated beam approaching the GRS is refracted and becomes a focused beam. This stage can be modeled using the intensity law, the sine condition, and transmission coefficients [32, 89, 103]. Second stage: the focused beam propagates a distance between the GRS and the SIL. Third stage: the focused beam is scattered at the surface of the SIL and produces a partially transmitted beam and a partially reflected beam. Fourth stage: the transmitted beam converges to the focal region before diverging to the infinity.

Before we discuss how different models take the four stages into account, we summarize the angular spectrum representation (ASR) of an image field in a linear, homogeneous, and isotropic medium [31] and show how to combine geometrical optics and Fourier optics for approximating the image field inside a SIL. For the development of the ASR,

we recommend the paper of Wolf [31] and the book of Born and Wolf [1]. In this thesis, we discuss the representation based on Wolf's paper [31] and Richards and Wolf's paper [32]. For an aplanatic lens represented by the GRS in Fig. 3.1, Wolf derived the representation for the image field as follows [31]:

$$\bar{E}(x, y, z) = -\frac{i}{2\pi} \iint_{\Omega} \frac{\mathbf{a}(k_x, k_y)}{k_z} e^{i(k_x x + k_y y + k_z z)} dk_x dk_y, \quad (5.1)$$

where  $\mathbf{a}(k_x, k_y)$  is the strength factor of the ray that is related to the electric field at far region  $\bar{E}(k_x, k_y) = \bar{E}(\bar{r}_\infty)$  as follows:

$$\mathbf{a}(k_x, k_y) = r_\infty e^{ikr_\infty} \bar{E}(k_x, k_y). \quad (5.2)$$

A comparison between Eq. (3.39) and Eq. (5.2), we can conclude that the strength factor is equivalent to the spectral amplitude vector of the field. Substituting Eq. (5.2) into Eq. (5.1), we obtain an equivalent expression as follows:

$$\bar{E}(x, y, z) = -\frac{i}{2\pi} \iint_{\Omega} \frac{r e^{ikr} \bar{E}(k_x, k_y)}{k_z} e^{i(k_x x + k_y y + k_z z)} dk_x dk_y, \quad (5.3)$$

To derive Eq. (5.1), Wolf used the principle of stationary phase that requires at the far region the condition

$$\hat{k} = -\hat{r} \quad (5.4)$$

must be satisfied. Physically, this condition means that all the rays must ideally converge to a point or a small region around a point. Mathematically, this condition is only satisfied when the origin of the coordinate system is chosen at the Gaussian image point and at the same time all the rays must converge to the origin.

## 5.1 Hemispherical Solid Immersion Lens

This section first forms an approximate model based on angular spectrum representation of the optical field for evaluating the focal field of the HSIL and discusses different models

existing in the literature. Then we form a rigorous model based on the multipole theory.

### 5.1.1 Approximate Analytical Model for Evaluating the Focal Field of the HSIL

Now, we combine geometrical optics and Fourier optics for approximating the image field, i.e. we first apply Eq. (5.2) for deriving the strength factor of the ray transmitting through the spherical interface, and then we apply Eq. (5.1) for evaluating the image field. For simplicity, we consider an HSS first and then the case of a GSS can be straightforwardly generalized. It is reasonable to assume that the electric field on the GRS is  $\bar{E}(k_x, k_y) = E_\alpha \hat{\alpha} + E_\beta \hat{\beta}$ , and then applying Eq. (5.2) we obtain the strength factor of a ray outside the SIL

$$\mathbf{a}(k_x, k_y) = f e^{ikf} [E_\alpha \hat{\alpha} + E_\beta \hat{\beta}].$$

Since the strength factor of the ray is independent of the position along the ray, we apply Eq. (5.2) to derive the electric field just outside the SIL:

$$\begin{aligned} \bar{E}^{out}(k_x, k_y) &= \frac{f e^{ikf} [E_\alpha \hat{\alpha} + E_\beta \hat{\beta}]}{e^{ikR} R} \\ &= \frac{f}{R} e^{ik(f-R)} [E_\alpha \hat{\alpha} + E_\beta \hat{\beta}]. \end{aligned} \quad (5.5)$$

Next, we apply the local plane-wave approximation and obtain the electric field just inside the SIL:

$$\bar{E}^{in}(k_{sx}, k_{sy}) = \frac{f}{R} e^{ik(f-R)} [t_p E_\alpha \hat{\alpha} + t_s E_\beta \hat{\beta}].$$

We apply Eq. (5.2) again, noting that now the ray is traveling inside the SIL with a different wave-number  $k_s$ . We obtain the strength factor of the transmitted ray as follows:

$$\begin{aligned} \mathbf{a}^{in}(k_x, k_y) &= R e^{ik_s R} \bar{E}^{in}(k_{sx}, k_{sy}), \\ &= f e^{ikf} e^{i(k_s - k)R} [t_p E_\alpha \hat{\alpha} + t_s E_\beta \hat{\beta}]. \end{aligned} \quad (5.6)$$

With the notice that the wave is now traveling inside the SIL, we approximate the focal field by substituting Eq (5.6) into Eq. (5.1). The focal field is expressed in terms of cylindrical coordinates  $(\rho, \phi, z)$  as follows:

$$\bar{E}^s(x, y, z) = -\frac{ik_s f e^{ikf}}{2\pi} \int_0^{\alpha_m} \sin \alpha d\alpha \int_0^{2\pi} d\beta \left[ t_p E_\alpha \begin{pmatrix} \cos \beta \cos \alpha \\ \sin \beta \cos \alpha \\ -\sin \alpha \end{pmatrix} + t_s E_\beta \begin{pmatrix} -\sin \beta \\ \cos \beta \\ 0 \end{pmatrix} \right] e^{i(k_s - k)R} e^{ik_s[\rho \sin \alpha \cos(\beta - \phi) + z \cos \alpha]}. \quad (5.7)$$

We will call the model, based on geometrical optics and Fourier optics, i.e. using Eq. (5.7), the approximate model.

Now, we discuss how the different models, which are also based on the ASR, differ from our derivation. The Ichimura model applied Eq. (5.1) [89]. In fact, Ichimura and many other researchers used Eq. (5.1) but they never mentioned the validity of using it, i.e. the validity of the condition  $\hat{k} = -\hat{r}$  was never mentioned. For an HSS, the condition is satisfied and hence Eq. (5.1) is applicable. Ichimura's approach is that he first approximates the strength factors of the rays inside the SIL. And then Eq. (5.1) is applied for evaluating the focal field. Ichimura applied the boundary conditions for the strength factor: in other words he matched the strength factors at the boundary. This application is not rigorous, since the boundary condition is that the tangential electric fields must be matched at the boundary, whereas the strength factors are not equivalent to the tangential electric fields, as observed in Eq. (5.2). Ichimura applied the boundary conditions for the strength factor  $\mathbf{a}(s_x, s_y) = f e^{ikf} [E_\alpha \hat{\alpha} + E_\beta \hat{\beta}]$ , and hence he obtained

$$\mathbf{a}^{in}(s_x, s_y) = f e^{ikf} [t_p E_\alpha \hat{\alpha} + t_s E_\beta \hat{\beta}]. \quad (5.8)$$

A comparison between Eqs. (5.6) and (5.8) shows that Ichimura ignored the constant phase term  $e^{i(k_s - k)R}$ , and subsequently Ichimura model misses the phase term compared

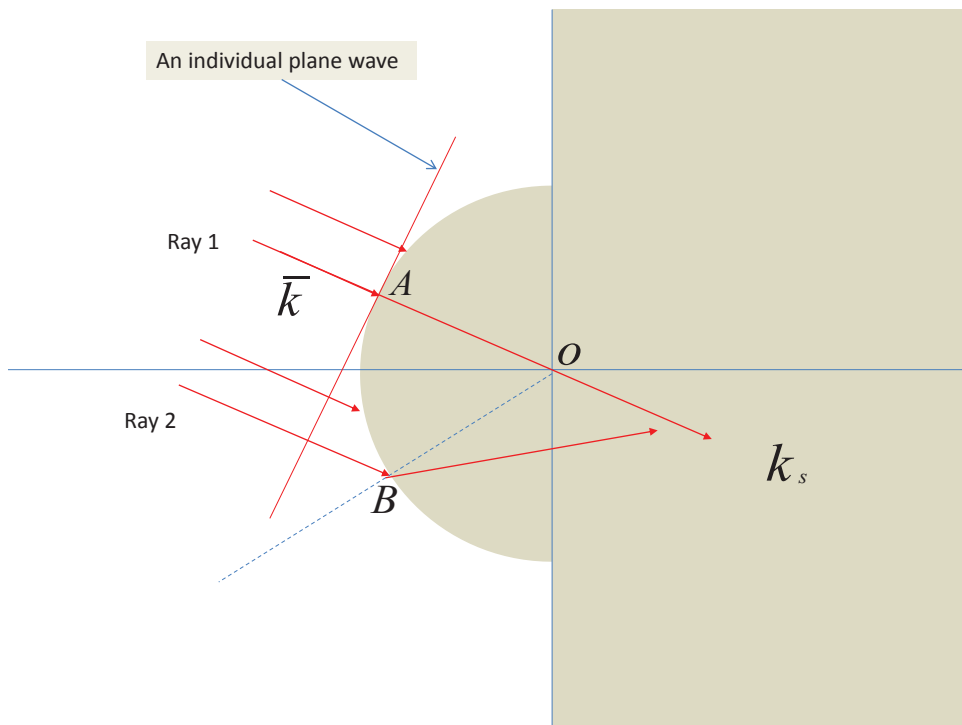


Figure 5.2: An individual plane wave incident onto the spherical surface.

to our approximate model. Since Ichimura also combined geometrical optics and Fourier optics as we did, we can consider the approximate model as a corrected version of the Ichimura model. Vamivakas also ignored this constant term but for a different reason that is discussed later. The Ichimura model and its corrected version described the 2nd and 3rd stages of the wave propagation by geometrical optics, and the 4th stage by Fourier optics.

Next, we discuss the Vamivakas model, which attempted to solve the 2nd, 3rd, and 4th stages within the scope of Fourier optics. Vamivakas began with Eq. (5.3) by expressing the electric field outside the SIL as follows:

$$\bar{E}(x, y, z) = -\frac{if e^{ikf}}{2\pi} \iint_{\Omega} \bar{E}^{GRS}(k_x, k_y) e^{i(k_x x + k_y y + k_z z)} \frac{1}{k_z} dk_x dk_y. \quad (5.9)$$

Equation (5.9) expresses the electric field as a superimposition of an infinite number of individual plane waves. Each individual plane wave with a wave-number  $(k_x, k_y, k_z)$  is

expressed as follows:

$$\begin{aligned}\bar{E}(k_x, k_y) &= -\frac{if e^{ikf} dk_x dk_y}{2\pi k_z} \bar{E}^{GRS}(k_x, k_y) e^{i(k_x x + k_y y + k_z z)} \\ &= -\frac{if e^{ikf} dk_x dk_y}{2\pi k_z} [E_\alpha \hat{\alpha} + E_\beta \hat{\beta}] e^{i\bar{k} \cdot \bar{r}}.\end{aligned}\quad (5.10)$$

This individual plane wave approaches the SIL as shown in Fig. 5.2. Vamivakas considered two effects caused by the spherical interface, the transmission amplitude coefficient and the phase change. Vamivakas explained that the convergent rays are normally incident on the hemispherical surface of the SIL, and the hemispherical surface is an equiphase surface. Hence, he used only one transmission amplitude coefficient  $t^\perp = t_s = t_p$  and the wave-number  $\bar{k}$  can be changed to  $\bar{k}_s$ . Consequently, the transmitted plane wave is

$$\bar{E}^{in}(k_x, k_y) = -\frac{if e^{ikf} dk_x dk_y}{2\pi k_z} t^\perp [E_\alpha \hat{\alpha} + E_\beta \hat{\beta}] e^{i\bar{k}_s \cdot \bar{r}}.\quad (5.11)$$

The focal field is then estimated by summing up all individual transmitted plane waves. For a planar surface, the method of solving the boundary conditions in the scope of the angular spectrum method is correct but for a spherical surface the concept poses a difficulty. As we observe in Fig. 5.2, the plane wave approaching the surface comprises an infinite number of geometrical rays that make varying angles with the normal of the surface. Hence, the rays 1 and 2 in Fig. 5.2 approaching points  $A$  and  $B$  are refracted at angles as predicted by Snell's law. Because of the different incident angles, the electric fields associated with these transmitted rays are different, as predicted by the Fresnel equations. Vamivakas used only  $t^\perp$  for all the incident rays though it is only correct for the ray approaching point  $A$  in Fig. 5.2, and hence he obtained the electric field of the individual plane wave presented in Eq.(5.11). Because of this improper treatment, Vamivakas formed an incorrect expression shown in Eq. (5.11). Consequently, the Vamivakas model leads to an incorrect constant term outside the integration of Eq. (5.7), that is  $\frac{ikf e^{ikf}}{2\pi}$  instead of  $\frac{ik_s f e^{ikf}}{2\pi}$ . Vamivakas also reasoned that the surface of a hemispherical SIL is equiphase, and hence the constant phase term  $e^{i(k_s - k)R}$  is also missed in his model.

In summary, although the reasons making the models based on the ASR invalid or inaccurate differ in detail from each other, the main cause is the improper treatment of the boundary conditions. We corrected the Ichimura model to obtain the approximate model. Compared to the approximate model, both the Ichimura model and the Vamivakas model ignored the exponential term  $e^{i(k_s - k)R}$ . The Vamivakas model also leads to an incorrect constant term outside the integration of Eq. (5.7). On the other hand, we should note that the approximate model is limited only to an HSS or an ASS based on a large-radius SIL. For a wavelength-scaled SIL [169–171] geometrical optics is invalid for describing the field near the surface, and consequently the combination between geometrical optics and Fourier optics is invalid. In addition, Eq. (5.1) is not strictly applicable to a GSS except for a ASS because the condition  $\hat{k} = -\hat{r}$  is not strictly satisfied for the GSS.

In this thesis, we propose a rigorous model based on multipole theory method (MTM) that is applicable to both large-radius SILs and wavelength-scaled SILs. In fact, MTM has been extensively used for computing diffracted fields, especially in the scattering by a full sphere. However, when the scattering surface is only a portion of a spherical surface, it is rather complicated and delicate. The light-matter interaction at the spherical interface is no longer trivial, and consequently the standard MTM cannot be applied to this case. We recently presented an approach, based on MTM, for solving the interaction rigorously [39]. Our proposed model in this section employs the rigorous approach for solving the boundary conditions, and hence a rigorous model for evaluating the focal field of optical SIL-based systems is formed. We also show that the approximate model is an approximation to our rigorous model. Through a detail analysis in this section, an insightful understanding of the wave propagation through the systems should be gained.

### 5.1.2 Rigorous Analytical Model for Evaluating the Focal Field of the HSIL

For the configuration of a HSIL, the center of GRS coincides with the center of the SIL. Hence, the scattering coefficients in section 4.2 are used for evaluating the focal field of the HSIL. This section will first form a rigorous model based on the scattering coefficients

in section 4.2, and then shows that, the approximate model presented in section 5.1.1 is an approximation of the rigorous model.

### 5.1.2.1 The Rigorous Model

We showed in section 4.2 that the total electric Debye potential is as follows:

$$\Pi_e = -2i\omega\varepsilon \sum_{l=1}^{\infty} \sum_{m=-l}^l c_{l2} p_{El}^m j_l(k_s r) Y_l^m(\theta, \phi). \quad (5.12)$$

Similarly, we can show that the total magnetic Debye potential is

$$\Pi_m = 2ik \sum_{l=1}^{\infty} \sum_{m=-l}^l d_{l2} p_{El}^m j_l(k_s r) Y_l^m(\theta, \phi). \quad (5.13)$$

By substituting Eqs. (5.12) and (5.13) into Eq. (4.1), we can evaluate rigorously the focal field inside the HSIL as follows:

$$\begin{aligned} E_r &= 2k_s \sum_{l=1}^{\infty} \sum_{m=-l}^l \frac{l(l+1)}{2l+1} c_{lm} \left( \frac{\varepsilon}{\varepsilon_s} c_{l2} p_{El}^m [j_{l-1}(k_s r) + j_{l+1}(k_s r)] P_l^m(\cos \theta) \right) \exp(im\phi), \\ E_\theta &= 2k_s \sum_{l=1}^{\infty} \sum_{m=-l}^l \frac{l(l+1)}{2l+1} c_{lm} \left( \frac{\varepsilon}{\varepsilon_s} c_{l2} p_{El}^m \left[ \frac{j_{l-1}(k_s r)}{l} - \frac{j_{l+1}(k_s r)}{l+1} \right] \frac{dP_l^m(\cos \theta)}{d\theta} \right. \\ &\quad \left. - m \frac{2l+1}{l(l+1)} \frac{k}{k_s} d_{l2} p_{Ml}^m j_l(k_s r) \frac{P_l^m(\cos \theta)}{\sin \theta} \right) \exp(im\phi), \\ E_\phi &= 2ik_s \sum_{l=1}^{\infty} \sum_{m=-l}^l \frac{l(l+1)}{2l+1} c_{lm} \left( m \frac{\varepsilon}{\varepsilon_s} c_{l2} p_{El}^m \left[ \frac{j_{l-1}(k_s r)}{l} - \frac{j_{l+1}(k_s r)}{l+1} \right] \frac{P_l^m(\cos \theta)}{\sin \theta} \right. \\ &\quad \left. - \frac{2l+1}{l(l+1)} \frac{k}{k_s} d_{l2} p_{Ml}^m j_l(k_s r) \frac{dP_l^m(\cos \theta)}{d\theta} \right) \exp(im\phi). \end{aligned} \quad (5.14)$$

## 5.1.2.2 Approximate Model Reduced from the Rigorous Model

Equations (4.1) and (4.2) describe a converging beam outside the SIL. For the convenience of making approximations, we express the converging field as follows:

$$\begin{aligned}
 E_r &= k \sum_{l=1}^{\infty} \sum_{m=-l}^l \frac{l(l+1)}{2l+1} c_{lm} \left( p_{El}^m [h_{l-1}^{(2)}(kr) + h_{l+1}^{(2)}(kr)] P_l^m(\cos \theta) \right) \exp(im\phi), \\
 E_\theta &= k \sum_{l=1}^{\infty} \sum_{m=-l}^l \frac{l(l+1)}{2l+1} c_{lm} \left( p_{El}^m \left[ \frac{h_{l-1}^{(2)}(kr)}{l} - \frac{h_{l+1}^{(2)}(kr)}{l+1} \right] \frac{dP_l^m(\cos \theta)}{d\theta} \right. \\
 &\quad \left. - m \frac{2l+1}{l(l+1)} p_{Ml}^m h_l^{(2)}(kr) \frac{P_l^m(\cos \theta)}{\sin \theta} \right) \exp(im\phi), \\
 E_\phi &= ik \sum_{l=1}^{\infty} \sum_{m=-l}^l \frac{l(l+1)}{2l+1} c_{lm} \left( m p_{El}^m \left[ \frac{h_{l-1}^{(2)}(kr)}{l} - \frac{h_{l+1}^{(1)}(kr)}{l+1} \right] \frac{P_l^m(\cos \theta)}{\sin \theta} \right. \\
 &\quad \left. - \frac{2l+1}{l(l+1)} p_{Ml}^m h_l^{(2)}(kr) \frac{dP_l^m(\cos \theta)}{d\theta} \right) \exp(im\phi). \quad (5.15)
 \end{aligned}$$

For  $kr_\infty \gg \frac{l(l+1)}{2}$ , we have

$$h_l^{(2)}(kr_\infty) \approx i^{l+1} \frac{e^{-ikr_\infty}}{kr_\infty}. \quad (5.16)$$

Substituting Eq. (5.16) into Eq. (5.15), and noting that  $\theta = \pi - \alpha$  and  $\phi = \pi + \beta$ , the electric field is approximated as follows:

$$\begin{aligned}
 E_r(r_\infty, \alpha, \beta) &\approx 0, \\
 E_\alpha(r_\infty, \alpha, \beta) &\approx -\frac{e^{-ikr_\infty}}{r_\infty} \sum_{l=1}^{\infty} \sum_{m=-l}^l (-i)^l c_{lm} \left[ p_{El}^m \frac{dP_l^m(\cos \alpha)}{d\alpha} + imp_{Ml}^m \frac{P_l^m(\cos \alpha)}{\sin \alpha} \right] e^{im\beta}, \\
 E_\beta(r_\infty, \alpha, \beta) &\approx -\frac{e^{-ikr_\infty}}{r_\infty} \sum_{l=1}^{\infty} \sum_{m=-l}^l (-i)^l c_{lm} \left[ imp_{El}^m \frac{P_l^m(\cos \alpha)}{\sin \alpha} - p_{Ml}^m \frac{dP_l^m(\cos \alpha)}{d\alpha} \right] e^{im\beta}. \quad (5.17)
 \end{aligned}$$

We see that the double summations in Eq. (5.17) are functions of the direction, or angles  $\alpha$  and  $\beta$ , and are independent of the distance  $r$ . Hence in the far region, the electric field can be considered as a spherical wave. This means we can treat the electric field outside the SIL as a bundle of geometrical rays converging to the focus. The electric field in Eq. (5.17) is associated with a ray traveling in the direction  $(\alpha, \beta)$ . Using Eq. (5.17), we

express the electric field just outside the SIL in terms of the field on the GRS:

$$\bar{E}(\bar{R}) \approx \frac{f}{R} e^{ik(f-R)} [E_\alpha \hat{\alpha} + E_\beta \hat{\beta}]. \quad (5.18)$$

The reflected electric field is derived rigorously to be

$$\begin{aligned} E_r^r &= k \sum_{l=1}^{\infty} \sum_{m=-l}^l \frac{l(l+1)}{2l+1} c_{lm} \left( a_{l2} p_{El}^m [h_{l-1}^{(1)}(kr) + h_{l+1}^{(1)}(kr)] P_l^m(\cos \theta) \right) \exp(im\phi), \\ E_\theta^r &= k \sum_{l=1}^{\infty} \sum_{m=-l}^l \frac{l(l+1)}{2l+1} c_{lm} \left( a_{l2} p_{El}^m \left[ \frac{h_{l-1}^{(1)}(kr)}{l} - \frac{h_{l+1}^{(1)}(kr)}{l+1} \right] \frac{dP_l^m(\cos \theta)}{d\theta} \right. \\ &\quad \left. - m \frac{2l+1}{l(l+1)} b_{l2} p_{Ml}^m h_l^{(1)}(kr) \frac{P_l^m(\cos \theta)}{\sin \theta} \right) \exp(im\phi), \\ E_\phi^r &= ik \sum_{l=1}^{\infty} \sum_{m=-l}^l \frac{l(l+1)}{2l+1} c_{lm} \left( m a_{l2} p_{El}^m \left[ \frac{h_{l-1}^{(1)}(kr)}{l} - \frac{h_{l+1}^{(1)}(kr)}{l+1} \right] \frac{P_l^m(\cos \theta)}{\sin \theta} \right. \\ &\quad \left. - \frac{2l+1}{l(l+1)} b_{l2} p_{Ml}^m h_l^{(1)}(kr) \frac{dP_l^m(\cos \theta)}{d\theta} \right) \exp(im\phi). \end{aligned} \quad (5.19)$$

Using the following approximations:

$$a_{l2} \approx (-1)^l e^{-2ikR} \frac{\frac{\varepsilon k_s}{\varepsilon_s k} - 1}{\frac{\varepsilon k_s}{\varepsilon_s k} + 1}, \quad b_{l2} \approx (-1)^l e^{-2ikR} \frac{\frac{\mu k_s}{\mu_s k} - 1}{\frac{\mu k_s}{\mu_s k} + 1}, \quad h_l^{(1)}(kR) \approx (-i)^{l+1} \frac{e^{ikR}}{kR},$$

we approximate Eq. (5.19) to be

$$\begin{aligned} E_r^r &\approx 0, \\ E_\alpha^r &\approx -\frac{\frac{\varepsilon k_s}{\varepsilon_s k} - 1}{\frac{\varepsilon k_s}{\varepsilon_s k} + 1} \frac{e^{-ikR}}{R} \sum_{l=1}^{\infty} \sum_{m=-l}^l (-i)^l c_{lm} \left[ p_{El}^m \frac{dP_l^m(\cos \alpha)}{d\alpha} + i m p_{Ml}^m \frac{P_l^m(\cos \alpha)}{\sin \alpha} \right] e^{im\beta}, \\ E_\beta^r &\approx -\frac{\frac{\varepsilon k_s}{\varepsilon_s k} - 1}{\frac{\varepsilon k_s}{\varepsilon_s k} + 1} \frac{e^{-ikR}}{R} \sum_{l=1}^{\infty} \sum_{m=-l}^l (-i)^l c_{lm} \left[ i m p_{El}^m \frac{P_l^m(\cos \alpha)}{\sin \alpha} - p_{Ml}^m \frac{dP_l^m(\cos \alpha)}{d\alpha} \right] e^{im\beta}. \end{aligned} \quad (5.20)$$

In terms of the electric field on the GRS:

$$\bar{E}^r(\bar{R}) \approx \frac{\frac{\varepsilon k_s}{\varepsilon_s k} - 1}{\frac{\varepsilon k_s}{\varepsilon_s k} + 1} \frac{f}{R} e^{ik(f-R)} [E_\alpha \hat{\alpha} + E_\beta \hat{\beta}]. \quad (5.21)$$

The transmitted electric field inside the SIL is obtained from Eq. (5.19) by replacing  $k$ ,  $a_{l2}$ ,  $b_{l2}$ , and  $h^{(1)}$  with  $k_s$ ,  $\frac{\varepsilon}{\varepsilon_s}c_{l2}$ ,  $\frac{k}{k_s}d_{l2}$ , and  $h^{(2)}$ , respectively. Using the following approximations,

$$c_{l2} \approx \frac{2k_s}{k + \frac{\varepsilon}{\varepsilon_s}k_s} e^{i(k_s - k)R}, \quad d_{l2} \approx \frac{2k_s}{k + \frac{\mu}{\mu_s}k_s} e^{i(k_s - k)R}, \quad h_l^{(2)}(kR) \approx i^{l+1} \frac{e^{-ikR}}{kR},$$

we approximate the transmitted electric field just inside the SIL's surface to be

$$\bar{E}^t(\bar{R}) \approx \frac{2\frac{\varepsilon}{\varepsilon_s}\frac{k_s}{k}}{\frac{\varepsilon}{\varepsilon_s}\frac{k_s}{k} + 1} \frac{f}{R} e^{ik(f-R)} [E_\alpha \hat{\alpha} + E_\beta \hat{\beta}]. \quad (5.22)$$

It is obvious from Eqs. (5.18), (5.21), and (5.22) that

$$\bar{E}(\bar{R}) + \bar{E}^r(\bar{R}) = \bar{E}^t(\bar{R}). \quad (5.23)$$

Note that for an electromagnetic wave normally incident onto a planar interface, the Fresnel reflection ( $r_p, r_s$ ) and transmission ( $t_p, t_s$ ) coefficients are

$$r_p = r_s = \frac{\frac{\varepsilon}{\varepsilon_s}\frac{k_s}{k} - 1}{\frac{\varepsilon}{\varepsilon_s}\frac{k_s}{k} + 1}, \quad t_p = t_s = \frac{2\frac{\varepsilon}{\varepsilon_s}\frac{k_s}{k}}{\frac{\varepsilon}{\varepsilon_s}\frac{k_s}{k} + 1}.$$

Hence Eq. (5.23) represents the well-known locally-plane approximation that is valid only for a large-radius SIL. In fact, the approximation in Eq. (5.17) is equivalent to the approximation in Eq. (5.2) and this approximated electric field can be considered to be equivalent to a ray traveling between the GRS and the SIL. In section 5.1.1, we used the locally-plane approximation to derive the electric field just inside the SIL. In this section, the locally-plane approximation was proven, and expressed in Eq. (5.23). In other words, the approximate model is an approximation of our rigorous model.

## 5.2 General Solid Immersion Lens

In this section, we discuss and form an approximate model and a rigorous model for evaluating the focal field of a general solid immersion lens.

### 5.2.1 Approximate Analytical Model for Evaluating the Focal Field of the GSIL

Similarly to Eq. (5.18), for a large SIL, the electric field just outside the SIL at point  $A$  in Fig. 5.1 can be approximated:

$$\bar{E}(\bar{r}_A) = \frac{f}{r_A} e^{ik(f-r_A)} [E_\alpha \hat{\alpha}' + E_\beta \hat{\beta}]. \quad (5.24)$$

Applying the local plane-wave approximation, the electric field just inside the SIL at point  $A$  is

$$\bar{E}^t(\bar{r}_A) = \frac{f}{r_A} e^{ik(f-r_A)} [t_p(\alpha) E_\alpha \hat{\alpha}' + t_s(\alpha) E_\beta \hat{\beta}], \quad (5.25)$$

where the Fresnel transmission coefficient for  $P$ -polarization component  $t_p(\alpha)$  and  $S$ -polarization component  $t_s(\alpha)$  are as follows:

$$t_p(\alpha) = \frac{2k \sqrt{1 - \left(\frac{d}{R} \sin \alpha\right)^2}}{k \sqrt{1 - \left(\frac{k}{k_s} \frac{d}{R} \sin \alpha\right)^2} + k_s \sqrt{1 - \left(\frac{d}{R} \sin \alpha\right)^2}},$$

$$t_s(\alpha) = \frac{2k \sqrt{1 - \left(\frac{d}{R} \sin \alpha\right)^2}}{k \sqrt{1 - \left(\frac{d}{R} \sin \alpha\right)^2} + k_s \sqrt{1 - \left(\frac{k}{k_s} \frac{d}{R} \sin \alpha\right)^2}}.$$

In fact, Eq. (5.25) is the electric field just inside the SIL of a GSS. i.e. the electric field at the far region. However, for the GSS, rays approaching the spherical surface with different angles are refracted with different angles predicted by Snell's law. These refracted rays do not converge to the same point, except for the ASS, and hence the condition  $\hat{k} = -\hat{r}$  is not satisfied in general. Consequently, Eq. (5.3) is not applicable strictly to the GSS except for the ASS. However, there are some cases that all of the rays converge into a small region around a Gaussian image point, i.e. the condition  $\hat{k} = -\hat{r}$  is nearly satisfied. An example is the case of focusing into a point near either of the aplanatic points. In such a case, we can approximate the focal field by following the procedure that was presented in section 5.1.1. This procedure leads to exactly the same expression of the spherical aberration presented in Ref. [101]. For the ASS, the condition

## 5. Solid Immersion Microscopy

$\hat{k} = -\hat{r}$  is satisfied and hence the focal field can be approximated. For the GSS, we denote the coordinates  $(x_1, y_1, z_1)$  of which the origin  $O_1$  is where the optical ray corresponding to the maximum incident angle  $\alpha_m$  intersects with the optical axis of the SIL. For the special case of ASS, the origin  $O_1$  is also the aplanatic point. The angular spectrum corresponding to the far-field in Eq. (5.25) is

$$\begin{aligned}\hat{\mathbf{E}}(k_{sx_1}, k_{sy_1}; 0) &= -\frac{iAF e^{ik_s AF}}{2\pi} \frac{1}{k_{sz_1}} \bar{E}^t(\bar{r}_A), \\ &= -\frac{if e^{ikf}}{2\pi} \frac{1}{k_{sz_1}} \frac{\sin \alpha}{\sin \alpha'} [t_p(\alpha) E_\alpha \hat{\alpha}' + t_s(\alpha) E_\beta \hat{\beta}]\end{aligned}$$

where  $AF = r_A \frac{\sin \alpha}{\sin \alpha'} = r_A \frac{k}{k_s}$  is the distance between points  $A$  and  $F$  indicated in Fig. 5.1. It should be noted that  $r_A$  (and hence  $AF$ ) is a function of  $\alpha$  and  $\beta$  (and equivalent  $k_x$  and  $k_y$ ) in this case of an ASS. Consequently, the electric field inside the ASIL is derived as follow:

$$\begin{aligned}\bar{E}^s(x_1, y_1, z_1) &= \iint_{k_{sx_1}^2 + k_{sy_1}^2 \leq k_s^2} \hat{\mathbf{E}}(k_{sx_1}, k_{sy_1}; 0) e^{i(k_{sx_1} x_1 + k_{sy_1} y_1 + k_{sz_1} z_1)} dk_{sx_1} dk_{sy_1} \\ &= -\frac{ik_s f e^{ikf}}{2\pi} \int_0^{\alpha'_m} \sin \alpha' d\alpha' \int_0^{2\pi} d\beta \frac{\sin \alpha}{\sin \alpha'} \left[ t_p(\alpha) E_\alpha \begin{pmatrix} \cos \beta \cos \alpha' \\ \sin \beta \cos \alpha' \\ -\sin \alpha' \end{pmatrix} \right. \\ &\quad \left. + t_s(\alpha) E_\beta \begin{pmatrix} -\sin \beta \\ \cos \beta \\ 0 \end{pmatrix} \right] e^{ik_s [\rho_1 \sin \alpha' \cos(\beta - \phi_1) + z_1 \cos \alpha']}. \quad (5.26)\end{aligned}$$

We know that  $\alpha' = \arcsin(\frac{k_s}{k} \sin \alpha)$  and  $d\alpha' = \frac{\frac{k_s}{k} \cos \alpha}{\cos \alpha'} d\alpha$ . Then Eq. (5.26) becomes

$$\begin{aligned}
 \bar{E}^s(x_1, y_1, z_1) &= -\frac{ik_s f e^{ikf}}{2\pi} \int_0^{\alpha_m} \sin \alpha' \frac{\frac{k_s}{k} \cos \alpha}{\cos \alpha'} d\alpha \int_0^{2\pi} d\beta \frac{k}{k_s} \left[ t_p(\alpha) E_\alpha \begin{pmatrix} \cos \beta \cos \alpha' \\ \sin \beta \cos \alpha' \\ -\sin \alpha' \end{pmatrix} \right. \\
 &\quad \left. + t_s(\alpha) E_\beta \begin{pmatrix} -\sin \beta \\ \cos \beta \\ 0 \end{pmatrix} \right] e^{ik_s[\rho_1 \sin \alpha' \cos(\beta-\phi_1) + z_1 \cos \alpha']} \\
 &= -\frac{ik_s f e^{ikf}}{2\pi} \int_0^{\alpha_m} \tan \alpha' \cos \alpha d\alpha \int_0^{2\pi} d\beta \left[ t_p(\alpha) E_\alpha \begin{pmatrix} \cos \beta \cos \alpha' \\ \sin \beta \cos \alpha' \\ -\sin \alpha' \end{pmatrix} \right. \\
 &\quad \left. + t_s(\alpha) E_\beta \begin{pmatrix} -\sin \beta \\ \cos \beta \\ 0 \end{pmatrix} \right] e^{ik_s[\rho_1 \sin \alpha' \cos(\beta-\phi_1) + z_1 \cos \alpha']}. \quad (5.27)
 \end{aligned}$$

Based on this approximate model for the ASS, the complete theoretical model of subsurface microscopy system based on aplanatic solid immersion lens has been proposed in Refs. [100, 172]. Recently, this complete model was experimentally verified in Ref. [173].

### 5.2.2 Rigorous Analytical Model for Evaluating the Focal Field of the GSIL

In section 4.3, we solved the boundary conditions and derived the scattering coefficients for polarized beams approaching the surface of the GSIL. In this section, we will form a model for evaluating the focal field of the GSIL using the scattering coefficients. Since the scattering coefficients depend on the distance between the centers of the GSIL and the GRS, our model also depends on the distance.

For  $d < R$ , the focal field is evaluated rigorously as follows:

$$\begin{aligned}
 E_{r'} &= 2k_s \sum_{l'=1}^{\infty} \sum_{m'=-l'}^{l'} \frac{l'(l'+1)}{2l'+1} c_{l'm'} \left( \frac{\varepsilon}{\varepsilon_s} c_{l'2} p_{E'l'}^{m'} [j_{l'-1}(k_s r') + j_{l'+1}(k_s r')] P_{l'}^{m'}(\cos \theta') \right) \exp(im' \phi'), \\
 E_{\theta'} &= 2k_s \sum_{l'=1}^{\infty} \sum_{m'=-l'}^{l'} \frac{l'(l'+1)}{2l'+1} c_{l'm'} \left( \frac{\varepsilon}{\varepsilon_s} c_{l'2} p_{E'l'}^{m'} \left[ \frac{j_{l'-1}(k_s r')}{l'} - \frac{j_{l'+1}(k_s r')}{l'+1} \right] \frac{dP_{l'}^{m'}(\cos \theta')}{d\theta'} \right. \\
 &\quad \left. - m' \frac{2l'+1}{l'(l'+1)} \frac{k}{k_s} d_{l'2} p_{M'l'}^{m'} j_{l'}(k_s r') \frac{P_{l'}^{m'}(\cos \theta')}{\sin \theta'} \right) \exp(im' \phi'), \\
 E_{\phi'} &= 2ik_s \sum_{l'=1}^{\infty} \sum_{m'=-l'}^{l'} \frac{l'(l'+1)}{2l'+1} c_{l'm'} \left( m' \frac{\varepsilon}{\varepsilon_s} c_{l'2} p_{E'l'}^{m'} \left[ \frac{j_{l'-1}(k_s r')}{l'} - \frac{j_{l'+1}(k_s r')}{l'+1} \right] \frac{P_{l'}^{m'}(\cos \theta')}{\sin \theta'} \right. \\
 &\quad \left. - \frac{2l'+1}{l'(l'+1)} \frac{k}{k_s} d_{l'2} p_{M'l'}^{m'} j_{l'}(k_s r') \frac{dP_{l'}^{m'}(\cos \theta')}{d\theta'} \right) \exp(im' \phi').
 \end{aligned} \tag{5.28}$$

For  $d > R$ , the focal field is evaluated rigorously as follows:

$$\begin{aligned}
 E_{r'} &= 2k_s \sum_{l'=1}^{\infty} \sum_{m'=-l'}^{l'} \frac{l'(l'+1)}{2l'+1} c_{l'm'} \left( \frac{\varepsilon}{\varepsilon_s} c_{l'2} p_{E'l'}^{m'} [j_{l'-1}(k_s r') + j_{l'+1}(k_s r')] P_{l'}^{m'}(\cos \theta') \right) \exp(im' \phi'), \\
 E_{\theta'} &= 2k_s \sum_{l'=1}^{\infty} \sum_{m'=-l'}^{l'} \frac{l'(l'+1)}{2l'+1} c_{l'm'} \left( \frac{\varepsilon}{\varepsilon_s} c_{l'2} p_{E'l'}^{m'} \left[ \frac{j_{l'-1}(k_s r')}{l'} - \frac{j_{l'+1}(k_s r')}{l'+1} \right] \frac{dP_{l'}^{m'}(\cos \theta')}{d\theta'} \right. \\
 &\quad \left. - m' \frac{2l'+1}{l'(l'+1)} \frac{k}{k_s} d_{l'2} p_{M'l'}^{m'} j_{l'}(k_s r') \frac{P_{l'}^{m'}(\cos \theta')}{\sin \theta'} \right) \exp(im' \phi'), \\
 E_{\phi'} &= 2ik_s \sum_{l'=1}^{\infty} \sum_{m'=-l'}^{l'} \frac{l'(l'+1)}{2l'+1} c_{l'm'} \left( m' \frac{\varepsilon}{\varepsilon_s} c_{l'2} p_{E'l'}^{m'} \left[ \frac{j_{l'-1}(k_s r')}{l'} - \frac{j_{l'+1}(k_s r')}{l'+1} \right] \frac{P_{l'}^{m'}(\cos \theta')}{\sin \theta'} \right. \\
 &\quad \left. - \frac{2l'+1}{l'(l'+1)} \frac{k}{k_s} d_{l'2} p_{M'l'}^{m'} j_{l'}(k_s r') \frac{dP_{l'}^{m'}(\cos \theta')}{d\theta'} \right) \exp(im' \phi').
 \end{aligned} \tag{5.29}$$

It should be noted that the differences between Eqs. (5.28) and (5.29) are the scattering coefficients and the multipole strengths which have been derived in chapter 4.

### 5.3 Polarized Beams and Focal Fields of SIL

In this section, we apply the general results presented in sections 5.1 and 5.2 for specific polarized beams, including cylindrical and linearly-polarized beams.

### 5.3.1 Cylindrical Vector Beams

We study the radially-polarized beam with a vortex and the azimuthally-polarized beam with a vortex presented in chapter 3.

#### 5.3.1.1 Radially-polarized Beam with a Vortex of Charge $n$

The incident focusing field on the GRS is shown in Eq. (3.64).

##### 1. Hemispherical Solid Immersion Lens

Substituting Eq. (3.64) into Eq. (5.7), after some trivial mathematical manipulations, we obtain the focal field using the approximate model as follows:

$$\bar{E}(\rho, \phi, z) = -\frac{ik_s f e^{ikf}}{2} e^{i(k_s - k)R} \begin{pmatrix} I_{n+1}^s + I_{n-1}^s \\ -i(I_{n+1}^s - I_{n-1}^s) \\ -2I_n^s \end{pmatrix}, \quad (5.30)$$

where

$$\begin{aligned} I_{n-1}^s &= i^{n-1} e^{i(n-1)\phi} \int_0^{\alpha_m} t_p a(\alpha) \cos \alpha J_{n-1}(k_s \rho \sin \alpha) e^{ik_s z \cos \alpha} \sin \alpha d\alpha, \\ I_{n+1}^s &= i^{n+1} e^{i(n+1)\phi} \int_0^{\alpha_m} t_p a(\alpha) \cos \alpha J_{n+1}(k_s \rho \sin \alpha) e^{ik_s z \cos \alpha} \sin \alpha d\alpha, \\ I_n^s &= i^n e^{in\phi} \int_0^{\alpha_m} t_p a(\alpha) \sin \alpha J_n(k_s \rho \sin \alpha) e^{k_s z \cos \alpha} \sin \alpha d\alpha. \end{aligned}$$

Equation (5.30) is used to evaluate the focal field approximately. We can evaluate the focal field rigorously using the rigorous model presented in section 5.1.2.1. Substituting Eq. (3.66) into Eq. (5.14), we obtain the formula for evaluating the focal

field of the HSIL using the multipole theory:

$$\begin{aligned}
 E_r &= 2k_s \sum_{l=|n|}^{\infty} \frac{l(l+1)}{2l+1} c_{ln} \left( \frac{\varepsilon}{\varepsilon_s} c_l p_{El}^n [j_{l-1}(k_s r) + j_{l+1}(k_s r)] P_l^n(\cos \theta) \right) \exp(in\phi), \\
 E_\theta &= 2k_s \sum_{l=|n|}^{\infty} \frac{l(l+1)}{2l+1} c_{ln} \left( \frac{\varepsilon}{\varepsilon_s} c_l p_{El}^n \left[ \frac{j_{l-1}(k_s r)}{l} - \frac{j_{l+1}(k_s r)}{l+1} \right] \frac{dP_l^m(\cos \theta)}{d\theta} \right. \\
 &\quad \left. - n \frac{2l+1}{l(l+1)} \frac{k}{k_s} d_l p_{Ml}^n j_l(kr) \frac{P_l^n(\cos \theta)}{\sin \theta} \right) \exp(in\phi), \\
 E_\phi &= 2ik_s \sum_{l=|n|}^{\infty} \frac{l(l+1)}{2l+1} c_{ln} \left( n \frac{\varepsilon}{\varepsilon_s} c_l p_{El}^n \left[ \frac{j_{l-1}(k_s r)}{l} - \frac{j_{l+1}(k_s r)}{l+1} \right] \frac{P_l^n(\cos \theta)}{\sin \theta} \right. \\
 &\quad \left. - \frac{2l+1}{l(l+1)} \frac{k}{k_s} p_{Ml}^n j_l(k_s r) \frac{dP_l^n(\cos \theta)}{d\theta} \right) \exp(in\phi). \quad (5.31)
 \end{aligned}$$

If  $n = 0$ , the summations in Eq. (5.31) start with  $l = 1$ , instead of  $l = 0$ .

## 2. General Solid Immersion Lens

We have shown in section 5.2.1 that the approximate model represented by Eq. (5.27) is not valid strictly for the GSIL except ASIL configuration. Hence, we consider here only the ASIL configuration. Substituting Eq. (3.64) into Eq. (5.27), after some trivial mathematical manipulations, we obtain the focal field for the ASIL as follows:

$$\bar{E}(\rho_1, \phi_1, z_1) = -\frac{ik_s f e^{ik_s f}}{2} \begin{pmatrix} I_{n+1}^s + I_{n-1}^s \\ -i(I_{n+1}^s - I_{n-1}^s) \\ -2I_n^s \end{pmatrix}, \quad (5.32)$$

where

$$\begin{aligned}
 I_{n-1}^s &= i^{n-1} e^{i(n-1)\phi_1} \int_0^{\alpha_m} t_p(\alpha) a(\alpha) \cos \alpha' J_{n-1}(k_s \rho_1 \sin \alpha') e^{ik_s z_1 \cos \alpha'} \tan \alpha' \cos \alpha \, d\alpha, \\
 I_{n+1}^s &= i^{n+1} e^{i(n+1)\phi_1} \int_0^{\alpha_m} t_p(\alpha) a(\alpha) \cos \alpha' J_{n+1}(k_s \rho_1 \sin \alpha') e^{ik_s z_1 \cos \alpha'} \tan \alpha' \cos \alpha \, d\alpha, \\
 I_n^s &= i^n e^{in\phi_1} \int_0^{\alpha_m} t_p(\alpha) a(\alpha) \sin \alpha' J_n(k_s \rho_1 \sin \alpha') e^{ik_s z_1 \cos \alpha'} \tan \alpha' \cos \alpha \, d\alpha.
 \end{aligned}$$

Equation (5.32) is derived from the approximate model and it is valid strictly for

the ASIL only. We can use the rigorous model to evaluate not only the focal field of the ASIL but also the focal field of a GSIL as follows:

- **Translational distance is less than the radius  $d < R$**

Substituting Eq. (3.66) into Eq. (4.10), we obtain the multipole strengths of the focal field of the GSIL as follows:

$$\begin{aligned} p_{E'l'}^{m'} &= \delta_{m'}^n \sum_{l=|n|}^{\infty} [A_{l'n}^{ln} p_{El}^n + iB_{l'n}^{ln} p_{Ml}^n], \\ p_{M'l'}^{m'} &= \delta_{m'}^n \sum_{l=|n|}^{\infty} [A_{l'n}^{ln} p_{Ml}^n - iB_{l'n}^{ln} p_{El}^n]. \end{aligned} \quad (5.33)$$

Substituting Eq. (5.33) into Eq. (5.28), we can evaluate the focal field using the rigorous model as follows:

$$\begin{aligned} E_{r'} &= 2k_s \sum_{l'=|n|}^{\infty} \frac{l'(l'+1)}{2l'+1} c_{l'n} \left( \frac{\varepsilon}{\varepsilon_s} c_{l'2} p_{E'l'}^n [j_{l'-1}(k_s r') + j_{l'+1}(k_s r')] P_{l'}^n(\cos \theta') \right) e^{in\phi'}, \\ E_{\theta'} &= 2k_s \sum_{l'=|n|}^{\infty} \frac{l'(l'+1)}{2l'+1} c_{l'n} \left( \frac{\varepsilon}{\varepsilon_s} c_{l'2} p_{E'l'}^n \left[ \frac{j_{l'-1}(k_s r')}{l'} - \frac{j_{l'+1}(k_s r')}{l'+1} \right] \frac{dP_l^n(\cos \theta')}{d\theta'} \right. \\ &\quad \left. - n \frac{2l'+1}{l'(l'+1)} \frac{k}{k_s} d_{l'2} p_{M'l'}^n j_{l'}(k_s r') \frac{P_{l'}^n(\cos \theta')}{\sin \theta'} \right) e^{in\phi'}, \\ E_{\phi'} &= 2ik_s \sum_{l'=|n|}^{\infty} \frac{l'(l'+1)}{2l'+1} c_{l'n} \left( n \frac{\varepsilon}{\varepsilon_s} c_{l'2} p_{E'l'}^n \left[ \frac{j_{l'-1}(k_s r')}{l'} - \frac{j_{l'+1}(k_s r')}{l'+1} \right] \frac{P_{l'}^n(\cos \theta')}{\sin \theta'} \right. \\ &\quad \left. - \frac{2l'+1}{l'(l'+1)} \frac{k}{k_s} d_{l'2} p_{M'l'}^n j_{l'}(k_s r') \frac{dP_{l'}^n(\cos \theta')}{d\theta'} \right) e^{in\phi'}. \end{aligned} \quad (5.34)$$

- **Translational distance is less than the radius  $d > R$**

The multipole strengths can be evaluated by a formula similar to the formula shown in Eq. (5.33) but with different translation coefficients presented in section 4.3.1. Then using Eq. (5.29), we can evaluate the focal field of the

GSIL as follows:

$$\begin{aligned}
 E_{r'} &= 2k_s \sum_{l'=|n|}^{\infty} \frac{l'(l'+1)}{2l'+1} c_{l'n} \left( \frac{\varepsilon}{\varepsilon_s} c_{l'} p_{E l'}^n [j_{l'-1}(k_s r') + j_{l'+1}(k_s r')] P_{l'}^n(\cos \theta') \right) e^{in\phi'}, \\
 E_{\theta'} &= 2k_s \sum_{l'=|n|}^{\infty} \frac{l'(l'+1)}{2l'+1} c_{l'n} \left( \frac{\varepsilon}{\varepsilon_s} c_{l'} p_{E l'}^n \left[ \frac{j_{l'-1}(k_s r')}{l'} - \frac{j_{l'+1}(k_s r')}{l'+1} \right] \frac{dP_{l'}^n(\cos \theta')}{d\theta'} \right. \\
 &\quad \left. - n \frac{2l'+1}{l'(l'+1)} \frac{k}{k_s} d_{l'} p_{M l'}^n j_{l'}(k_s r') \frac{P_{l'}^n(\cos \theta')}{\sin \theta'} \right) e^{in\phi'}, \\
 E_{\phi'} &= 2ik_s \sum_{l'=|n|}^{\infty} \frac{l'(l'+1)}{2l'+1} c_{l'n} \left( n \frac{\varepsilon}{\varepsilon_s} c_{l'} p_{E l'}^n \left[ \frac{j_{l'-1}(k_s r')}{l'} - \frac{j_{l'+1}(k_s r')}{l'+1} \right] \frac{P_{l'}^n(\cos \theta')}{\sin \theta'} \right. \\
 &\quad \left. - \frac{2l'+1}{l'(l'+1)} \frac{k}{k_s} d_{l'} p_{M l'}^n j_{l'}(k_s r') \frac{dP_{l'}^n(\cos \theta')}{d\theta'} \right) e^{in\phi'}. \quad (5.35)
 \end{aligned}$$

It is worth highlighting that the difference between Eqs. (5.34) and (5.35) is the values of the translation coefficients and the scattering coefficients as shown in Chapter 4.

### 5.3.1.2 Azimuthally-polarized Beam with a Vortex of Charge $n$

The incident focusing field on the GRS is shown in Eq. (3.68).

#### 1. Hemispherical Solid Immersion Lens

Substituting Eq. (3.68) into Eq. (5.7), we obtain the focal field:

$$\bar{E}(\rho, \phi, z) = -\frac{ik_s f e^{ik_s f}}{2} e^{i(k_s - k)R} \begin{pmatrix} i(F_{n+1}^s - F_{n-1}^s) \\ F_{n+1}^s + F_{n-1}^s \\ 0 \end{pmatrix}, \quad (5.36)$$

where

$$\begin{aligned}
 F_{n-1}^s &= i^{n-1} e^{i(n-1)\phi} \int_0^{\alpha_m} t_s a(\alpha) J_{n-1}(k_s \rho \sin \alpha) e^{ik_s z \cos \alpha} \sin \alpha d\alpha, \\
 F_{n+1}^s &= i^{n+1} e^{i(n+1)\phi} \int_0^{\alpha_m} t_s a(\alpha) J_{n+1}(k_s \rho \sin \alpha) e^{ik_s z \cos \alpha} \sin \alpha d\alpha.
 \end{aligned}$$

We can also use the rigorous model based on the multipole theory for an HSIL to evaluate the focal field for the focused azimuthally-polarized beam. The formula is exactly the same as Eq. (5.31) except that the multipole strengths are evaluated

using Eq. (3.70).

## 2. General Solid Immersion Lens

Substituting Eq. (3.68) into Eq. (5.27), we obtain the focal field of the ASIL as follows:

$$\bar{E}(\rho_1, \phi_1, z_1) = -\frac{ik_s f e^{ikf}}{2} \begin{pmatrix} i(F_{n+1}^s - F_{n-1}^s) \\ F_{n+1}^s + F_{n-1}^s \\ 0 \end{pmatrix}, \quad (5.37)$$

where

$$F_{n-1}^s = i^{n-1} e^{i(n-1)\phi_1} \int_0^{\alpha_m} t_s(\alpha) a(\alpha) J_{n-1}(k_s \rho_1 \sin \alpha') e^{ik_s z_1 \cos \alpha'} \tan \alpha' \cos \alpha \, d\alpha,$$

$$F_{n+1}^s = i^{n+1} e^{i(n+1)\phi_1} \int_0^{\alpha_m} t_s(\alpha) a(\alpha) J_{n+1}(k_s \rho_1 \sin \alpha') e^{ik_s z_1 \cos \alpha'} \tan \alpha' \cos \alpha \, d\alpha.$$

Equation (5.37) is derived using the approximate model based on the angular spectrum method. We can also evaluate the focal field using the rigorous model presented in section 5.2.2 for the GSIL. The formulas using the rigorous model for the incident azimuthally-polarized beam are exactly the same as Eqs. (5.34) and (5.35) except the values of the multipole strengths.

### 5.3.2 Generalized Linear Polarization

The incident focusing field on the GRS is shown in Eq. (3.72).

#### 1. Hemispherical Solid Immersion Lens

Substituting Eq. (3.72) into Eq. (5.7), we obtain the focal field of the HSIL as follows:

$$\bar{E}(\rho, \phi, z) = -\frac{ik_s f e^{ikf}}{2} e^{i(k_s - k)R} \begin{pmatrix} H_0^s + H_2^s \cos 2\phi \\ H_2^s \sin 2\phi \\ -2iH_1^s \cos \phi \end{pmatrix}, \quad (5.38)$$

where

$$\begin{aligned}
 H_0^s &= \int_0^{\alpha_m} a(\alpha) \cos^2\left(\frac{\alpha}{2}\right) \{t_s[1 + S(\alpha)] + t_p[1 - S(\alpha)] \cos \alpha\} J_0(k_s \rho \sin \alpha) e^{ik_s z \cos \alpha} \sin \alpha \, d\alpha, \\
 H_1^s &= \int_0^{\alpha_m} t_p a(\alpha) \cos^2\left(\frac{\alpha}{2}\right) \{1 - S(\alpha)\} \sin \alpha J_1(k_s \rho \sin \alpha) e^{ik_s z \cos \alpha} \sin \alpha \, d\alpha, \\
 H_2^s &= \int_0^{\alpha_m} a(\alpha) \cos^2\left(\frac{\alpha}{2}\right) \{t_s[1 + S(\alpha)] - t_p[1 - S(\alpha)] \cos \alpha\} J_2(k_s \rho \sin \alpha) e^{ik_s z \cos \alpha} \sin \alpha \, d\alpha.
 \end{aligned}$$

Using the rigorous model that is presented in section 5.2.2, we can evaluate the focal field more accurate. Substituting Eq. (3.74) into Eq. (5.14), we obtain the focal field based on the rigorous model:

$$\begin{aligned}
 E_r &= -\frac{k_s}{\sqrt{\pi}} \sum_{l=1}^{\infty} \sqrt{\frac{l(l+1)}{2l+1}} \frac{\varepsilon}{\varepsilon_s} c_{l2} p_{El}^1 [j_{l-1}(k_s r) + j_{l+1}(k_s r)] P_l^1(\cos \theta) \cos \phi \\
 E_\theta &= -\frac{k_s}{\sqrt{\pi}} \sum_{l=1}^{\infty} \sqrt{\frac{l(l+1)}{2l+1}} \left[ \frac{\varepsilon}{\varepsilon_s} c_{l2} p_{El}^1 \left( \frac{j_{l-1}(k_s r)}{l} - \frac{j_{l+1}(k_s r)}{l+1} \right) \frac{d}{d\theta} P_l^1(\cos \theta) \right. \\
 &\quad \left. - \frac{2l+1}{l(l+1)} \frac{k}{k_s} d_{l2} p_{Ml}^1 j_l(k_s r) \frac{P_l^1(\cos \theta)}{\sin \theta} \right] \cos \phi, \\
 E_\phi &= \frac{k_s}{\sqrt{\pi}} \sum_{l=1}^{\infty} \sqrt{\frac{l(l+1)}{2l+1}} \left[ \frac{\varepsilon}{\varepsilon_s} c_{l2} p_{El}^1 \left( \frac{j_{l-1}(k_s r)}{l} - \frac{j_{l+1}(k_s r)}{l+1} \right) \frac{P_l^1(\cos \theta)}{\sin \theta} \right. \\
 &\quad \left. - \frac{2l+1}{l(l+1)} \frac{k}{k_s} d_{l2} p_{Ml}^1 j_l(k_s r) \frac{d}{d\theta} P_l^1(\cos \theta) \right] \sin \phi. \tag{5.39}
 \end{aligned}$$

## 2. General Solid Immersion Lens

Substituting Eq. (3.72) into Eq. (5.27), we obtain the focal field of the ASIL:

$$\bar{E}(\rho_1, \phi_1, z_1) = -\frac{ik_s f e^{ikf}}{2} \begin{pmatrix} H_0^s + H_2^s \cos 2\phi_1 \\ H_2^s \sin 2\phi_1 \\ -2iH_1^s \cos \phi_1 \end{pmatrix}, \tag{5.40}$$

where

$$\begin{aligned}
 H_0^s &= \int_0^{\alpha_m} a(\alpha) \cos^2\left(\frac{\alpha}{2}\right) \{t_s(\alpha)[1 + S(\alpha)] + t_p(\alpha)[1 - S(\alpha)] \cos \alpha'\} \times \\
 &\quad \times J_0(k_s \rho_1 \sin \alpha') e^{ik_s z_1 \cos \alpha'} \tan \alpha' \cos \alpha \, d\alpha, \\
 H_1^s &= \int_0^{\alpha_m} t_p(\alpha) a(\alpha) \cos^2\left(\frac{\alpha}{2}\right) [1 - S(\alpha)] \sin \alpha' J_1(k_s \rho_1 \sin \alpha') e^{ik_s z_1 \cos \alpha'} \tan \alpha' \cos \alpha \, d\alpha, \\
 H_2^s &= \int_0^{\alpha_m} a(\alpha) \cos^2\left(\frac{\alpha}{2}\right) \{t_s(\alpha)[1 + S(\alpha)] - t_p(\alpha)[1 - S(\alpha)] \cos \alpha'\} \times \\
 &\quad \times J_2(k_s \rho_1 \sin \alpha') e^{ik_s z_1 \cos \alpha'} \tan \alpha' \cos \alpha \, d\alpha.
 \end{aligned}$$

Equation (5.39) is valid only for the ASIL configuration. For a general configuration, we should use the rigorous model presented in section 5.2.2. Firstly, we must evaluate the multipole strengths in the  $O'$  coordinate system by substituting Eq. (3.74) into Eq. (4.10), we obtain the multipole strengths as follows:

$$\begin{aligned}
 p_{EV'}^{m'} &= p_{EV'}^1 (\delta_{m'}^1 - \delta_{m'}^{-1}), \\
 p_{MV'}^{m'} &= p_{MV'}^1 (\delta_{m'}^1 + \delta_{m'}^{-1}),
 \end{aligned} \tag{5.41}$$

where

$$\begin{aligned}
 p_{EV'}^1 &= \sum_{l=1}^{\infty} [A_{V'1}^{l1} p_{El}^1 + iB_{V'1}^{l1} p_{Ml}^1], \\
 p_{MV'}^1 &= \sum_{l=1}^{\infty} [A_{V'1}^{l1} p_{Ml}^1 - iB_{V'1}^{l1} p_{El}^1].
 \end{aligned} \tag{5.42}$$

It should be noted that the translation coefficients in Eq. (5.42) are dependent on whether  $d > R$  or  $d < R$  as presented in section 4.3.1.

- **Translational distance is less than the radius  $d < R$**

We substitute Eq. (5.41) into Eq. (5.28), we obtain the focal field for the GSIL:

$$\begin{aligned}
 E_{r'} &= -\frac{k_s}{\sqrt{\pi}} \sum_{l'=1}^{\infty} \sqrt{\frac{l'(l'+1)}{2l'+1}} \frac{\varepsilon}{\varepsilon_s} c_{l'} p_{E l'}^1 [j_{l'-1}(k_s r') + j_{l'+1}(k_s r')] P_{l'}^1(\cos \theta') \cos \phi', \\
 E_{\theta'} &= -\frac{k_s}{\sqrt{\pi}} \sum_{l'=1}^{\infty} \sqrt{\frac{l'(l'+1)}{2l'+1}} \left[ \frac{\varepsilon}{\varepsilon_s} c_{l'} p_{E l'}^1 \left( \frac{j_{l'-1}(k_s r')}{l'} - \frac{j_{l'+1}(k_s r')}{l'+1} \right) \frac{d}{d\theta'} P_{l'}^1(\cos \theta') \right. \\
 &\quad \left. - \frac{2l'+1}{l'(l'+1)} \frac{k}{k_s} d_{l'} p_{M l'}^1 j_{l'}(k_s r') \frac{P_{l'}^1(\cos \theta')}{\sin \theta'} \right] \cos \phi', \\
 E_{\phi'} &= \frac{k_s}{\sqrt{\pi}} \sum_{l'=1}^{\infty} \sqrt{\frac{l'(l'+1)}{2l'+1}} \left[ \frac{\varepsilon}{\varepsilon_s} c_{l'} p_{E l'}^1 \left( \frac{j_{l'-1}(k_s r')}{l'} - \frac{j_{l'+1}(k_s r')}{l'+1} \right) \frac{P_{l'}^1(\cos \theta')}{\sin \theta'} \right. \\
 &\quad \left. - \frac{2l'+1}{l'(l'+1)} \frac{k}{k_s} d_{l'} p_{M l'}^1 j_{l'}(k_s r') \frac{d}{d\theta'} P_{l'}^1(\cos \theta') \right] \sin \phi'. \tag{5.43}
 \end{aligned}$$

- **Translational distance is greater than the radius  $d > R$**

We substitute Eq. (5.41) into Eq. (5.29), we obtain the focal field for the GSIL:

$$\begin{aligned}
 E_{r'} &= -\frac{k_s}{\sqrt{\pi}} \sum_{l'=1}^{\infty} \sqrt{\frac{l'(l'+1)}{2l'+1}} \frac{\varepsilon}{\varepsilon_s} c_{l'} p_{E l'}^1 [j_{l'-1}(k_s r') + j_{l'+1}(k_s r')] P_{l'}^1(\cos \theta') \cos \phi', \\
 E_{\theta'} &= -\frac{k_s}{\sqrt{\pi}} \sum_{l'=1}^{\infty} \sqrt{\frac{l'(l'+1)}{2l'+1}} \left[ \frac{\varepsilon}{\varepsilon_s} c_{l'} p_{E l'}^1 \left( \frac{j_{l'-1}(k_s r')}{l'} - \frac{j_{l'+1}(k_s r')}{l'+1} \right) \frac{d}{d\theta'} P_{l'}^1(\cos \theta') \right. \\
 &\quad \left. - \frac{2l'+1}{l'(l'+1)} \frac{k}{k_s} d_{l'} p_{M l'}^1 j_{l'}(k_s r') \frac{P_{l'}^1(\cos \theta')}{\sin \theta'} \right] \cos \phi', \\
 E_{\phi'} &= \frac{k_s}{\sqrt{\pi}} \sum_{l'=1}^{\infty} \sqrt{\frac{l'(l'+1)}{2l'+1}} \left[ \frac{\varepsilon}{\varepsilon_s} c_{l'} p_{E l'}^1 \left( \frac{j_{l'-1}(k_s r')}{l'} - \frac{j_{l'+1}(k_s r')}{l'+1} \right) \frac{P_{l'}^1(\cos \theta')}{\sin \theta'} \right. \\
 &\quad \left. - \frac{2l'+1}{l'(l'+1)} \frac{k}{k_s} d_{l'} p_{M l'}^1 j_{l'}(k_s r') \frac{d}{d\theta'} P_{l'}^1(\cos \theta') \right] \sin \phi'. \tag{5.44}
 \end{aligned}$$

The difference between Eqs. (5.43) and (5.44) is the values of the multipole strengths and the scattering coefficients.

## 5.4 Simulations

We run simulations for the axial dipole wave being presented in Chapter 3 using the formulas derived in section 5.3.

### 5.4.1 Results for the Hemispherical Solid Immersion Lens

As an example, we investigate the axial dipole wave which is mentioned in section 3.5.1.1. It is important because it is known to produce a smaller focal spot than linearly polarized light. We remind here for convenience that the electric field on the GRS of the ADW is

$$\bar{E}(\hat{s}) = a(\alpha)\hat{\alpha}, \quad (5.45)$$

where

$$a(\alpha) = \sin \alpha \text{ for } \alpha \leq \alpha_m; \text{ and } a(\alpha) = 0 \text{ for } \alpha > \alpha_m,$$

and the *EMMS* of the beam are estimated by Eq. (3.77):

$$p_{El}^m = -\frac{i^l f e^{ikf} [\pi(2l+1)]^{\frac{1}{2}}}{l(l+1)} \delta_m^0 \int_0^{\alpha_m} a(\alpha) \frac{dP_l(\cos \alpha)}{d\alpha} \sin \alpha d\alpha, \quad p_{Ml}^m = 0. \quad (5.46)$$

Now, the focal field of the HSS is estimated rigorously using our rigorous model as follows:

$$\begin{aligned} E_r &= \frac{k_s}{\sqrt{\pi}} \sum_{l=1}^{\infty} \frac{l(l+1)}{\sqrt{2l+1}} \frac{\varepsilon}{\varepsilon_s} c_{l2} p_{El}^0 [j_{l-1}(k_s r) + j_{l+1}(k_s r)] P_l(\cos \theta), \\ E_\theta &= \frac{k_s}{\sqrt{\pi}} \sum_{l=1}^{\infty} \frac{l(l+1)}{\sqrt{2l+1}} \frac{\varepsilon}{\varepsilon_s} c_{l2} p_{El}^0 \left[ \frac{j_{l-1}(k_s r)}{l} - \frac{j_{l+1}(k_s r)}{l+1} \right] \frac{dP_l(\cos \theta)}{d\theta}, \\ E_\phi &= 0. \end{aligned} \quad (5.47)$$

Equation (5.47) rigorously evaluates the focal field. For comparison, we also present the result using the approximate model by substituting Eq. (5.45) into Eq. (5.7):

$$\bar{E}(x, y, z) = k_s f e^{ikf} e^{i(k_s - k)R} \begin{pmatrix} I_1 \cos \phi \\ I_1 \sin \phi \\ iI_0 \end{pmatrix}, \quad (5.48)$$

where

$$I_0 = \int_0^{\alpha_m} t_p \sin \alpha J_0(k_s \rho \sin \alpha) e^{ik_s z \cos \alpha} \sin^2 \alpha d\alpha,$$

$$I_1 = \int_0^{\alpha_m} t_p \cos \alpha J_1(k_s \rho \sin \alpha) e^{ik_s z \cos \alpha} \sin^2 \alpha d\alpha,$$

are called diffraction integrals. We note that Eq. (5.48) is an approximation of Eq. (5.47) and is valid only for a large SIL. In contrast, Eq. (5.47) is valid even for a small SIL as long as the presence of the planar interface in Fig. 1.3(a) is still ignorable. Here we also present the results of the Ichimura and the Vamivakas models for the sake of comparison. The Ichimura model gives the following result:

$$\bar{E}(x, y, z) = k_s f e^{ikf} \begin{pmatrix} I_1 \cos \phi \\ I_1 \sin \phi \\ iI_0 \end{pmatrix}. \quad (5.49)$$

The Vamivakas model expresses the focal field as follows:

$$\bar{E}(x, y, z) = k f e^{ikf} \begin{pmatrix} I_1 \cos \phi \\ I_1 \sin \phi \\ iI_0 \end{pmatrix}. \quad (5.50)$$

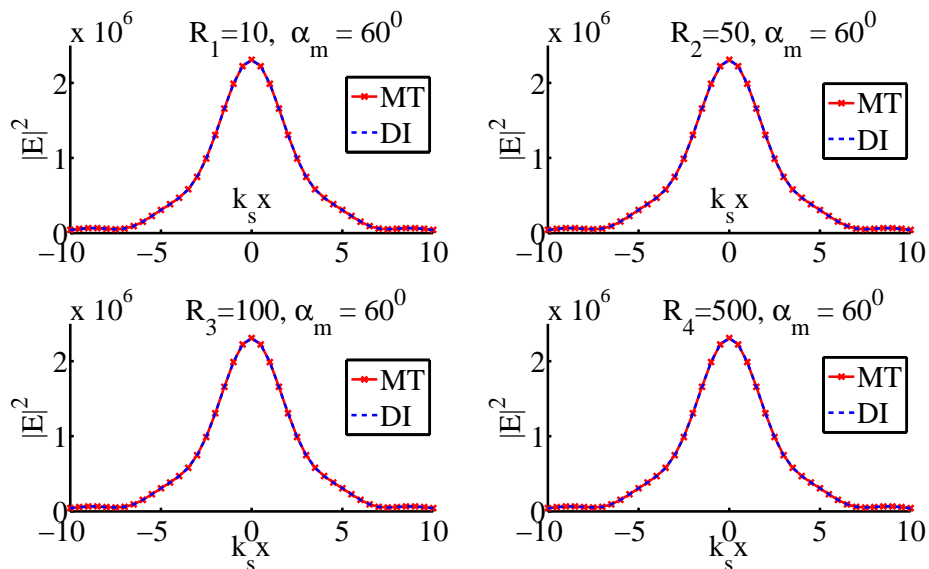
We observe from Eqs. (5.48) and (5.49) that the Ichimura model ignores the constant phase term  $e^{i(k_s - k)R}$ , and hence gives the same intensity as the approximate model, but a different phase. From Eqs. (5.48) and (5.50), we see that the Vamivakas model not only ignores the constant phase term, but also gives a different electric amplitude. Fortunately, the three models give the same normalized electric intensities, and the fact is that most researchers analyzed experimental results using the normalized electric intensities [82, 89]. Hence, the conclusions in the published experimental articles hold for our approximate model.

Since it is obvious to appreciate the difference among simulation results using the Ichimura, the approximate, and the Vamivakas models, we plot the simulation result using the approximate model only. For the case of  $f = 10^3$  and  $\alpha_m = 60^\circ$ , we use Eqs. (5.47) and (5.48) to obtain the simulation results in Fig 5.4, where MT represents our rigorous model based on the MTM and DI represents the approximate model based on the diffraction integrals. Figure 5.3(a) plots the transverse variation in electric intensity for four different radii of HSIL, which shows perfect agreement between the approximate model and our rigorous model. All of the four plots look similar, i.e. the focal spots are independent of radius, which can be reduced to several wavelengths. Correspondingly, Fig. 5.3(b) shows plots of the longitudinal variation in electric intensity. For the small radius HSIL,  $R_1 = 10$ , though the two models have perfect agreement for the transverse distribution, these models exhibit a small difference for the longitudinal distribution. This small difference is mathematically explained by the fact that higher orders of multipole are needed for evaluating correctly the longitudinal distribution (30 compared to 6 for the case of transversal distribution). Hence, the assumption  $kR \gg \frac{l(l+1)}{2}$  is not well satisfied for evaluating the longitudinal electric intensity, i.e. equation (5.17) is not an accurate approximation and thus the approximate model gives the small difference from the rigorous model. Another important observation is that the maximum longitudinal electric intensity for the rigorous model is not at the geometrical focus for the small radius. The difference proves that the models, based on the ASR, are invalid for evaluating the focal field of a small HSIL.

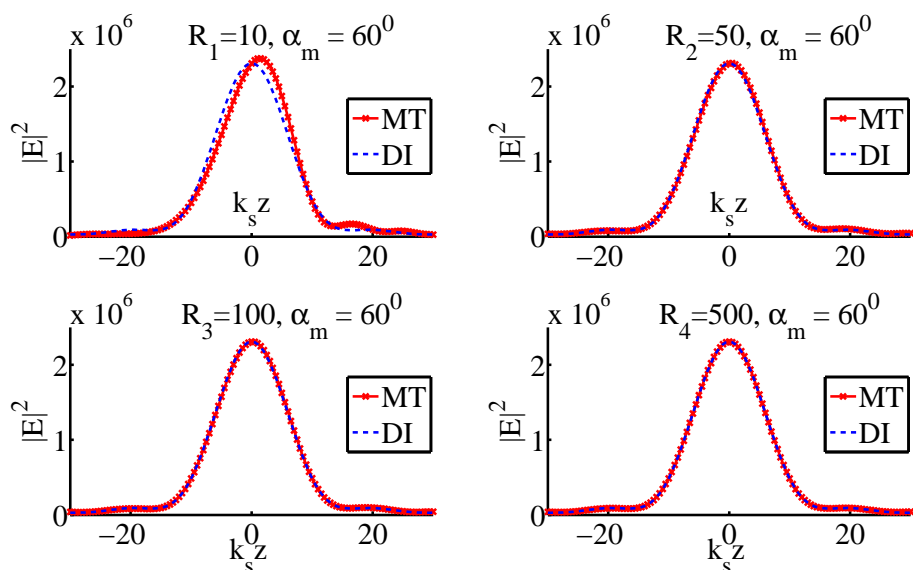
### 5.4.2 Results for the General Solid Immersion Lens

We first derive the focal field of a GSS for the incident ADW using our rigorous model. Substituting Eq. (5.46) into Eq. (5.33), we obtain the EMMS of the ADW in the  $O'$ -coordinates:

$$p_{E'l'}^{m'} = \delta_{m'}^0 \sum_{l=1}^{\infty} A_{l'0}^{l0} p_{El}^0, \quad p_{M'l'}^{m'} = 0. \quad (5.51)$$



(a) Transversal distributions



(b) Longitudinal distributions

Figure 5.3: Electric intensity distributions with different radius of HSIL:  $R_1 = 10\mu m$ ,  $R_2 = 50\mu m$ ,  $R_3 = 100\mu m$ ,  $R_4 = 500\mu m$ .

The focal field is then rigorously evaluated as follows: For  $d < R$ , Eq. (5.28) is used:

$$\begin{aligned}
 E_{r'} &= \frac{k_s}{\sqrt{\pi}} \sum_{l'=1}^{\infty} \frac{l'(l'+1)}{\sqrt{2l'+1}} \frac{\varepsilon}{\varepsilon_s} c_{l'} p_{El'}^0 [j_{l'-1}(k_s r') + j_{l'+1}(k_s r')] P_{l'}(\cos \theta'), \\
 E_{\theta'} &= \frac{k_s}{\sqrt{\pi}} \sum_{l'=1}^{\infty} \frac{l'(l'+1)}{\sqrt{2l'+1}} \frac{\varepsilon}{\varepsilon_s} c_{l'} p_{El'}^0 \left[ \frac{j_{l'-1}(k_s r')}{l'} - \frac{j_{l'+1}(k_s r')}{l'+1} \right] \frac{dP_{l'}(\cos \theta')}{d\theta'}, \\
 E_{\phi'} &= 0.
 \end{aligned} \tag{5.52}$$

For  $d > R$ , Eq. (5.29) is used:

$$\begin{aligned}
 E_{r'} &= \frac{k_s}{\sqrt{\pi}} \sum_{l'=1}^{\infty} \frac{l'(l'+1)}{\sqrt{2l'+1}} \frac{\varepsilon}{\varepsilon_s} c_{l'} p_{El'}^0 [j_{l'-1}(k_s r') + j_{l'+1}(k_s r')] P_{l'}(\cos \theta'), \\
 E_{\theta'} &= \frac{k_s}{\sqrt{\pi}} \sum_{l'=1}^{\infty} \frac{l'(l'+1)}{\sqrt{2l'+1}} \frac{\varepsilon}{\varepsilon_s} c_{l'} p_{El'}^0 \left[ \frac{j_{l'-1}(k_s r')}{l'} - \frac{j_{l'+1}(k_s r')}{l'+1} \right] \frac{dP_{l'}(\cos \theta')}{d\theta'}, \\
 E_{\phi'} &= 0.
 \end{aligned} \tag{5.53}$$

Equations (5.52) and (5.53) are applicable for any value of  $d$ .

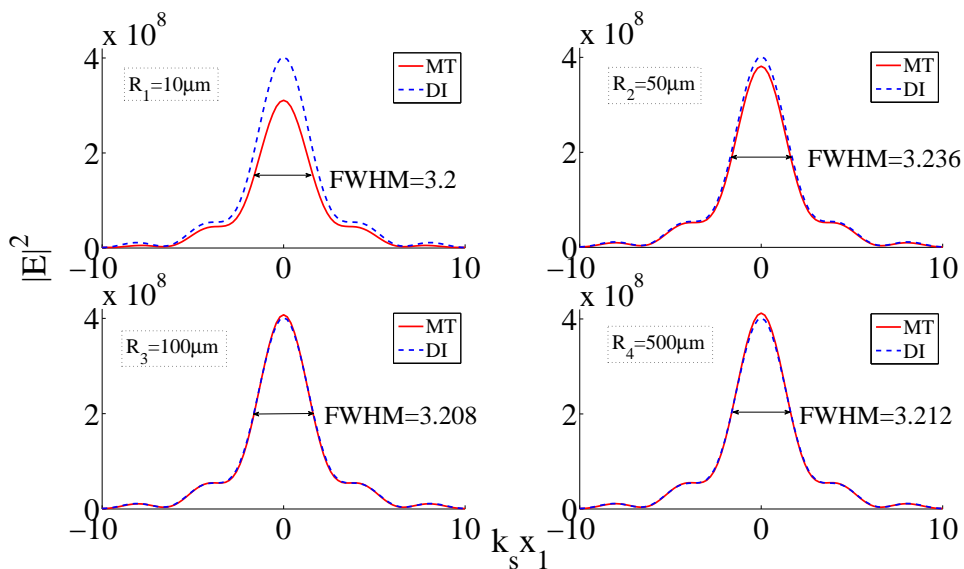
For an ASS, the focal field can be approximated by using Eq. (5.27) as follows

$$\bar{E}(x_1, y_1, z_1) = k_s f e^{ikf} \begin{pmatrix} I_1 \cos \phi_1 \\ I_1 \sin \phi_1 \\ iI_0 \end{pmatrix}, \tag{5.54}$$

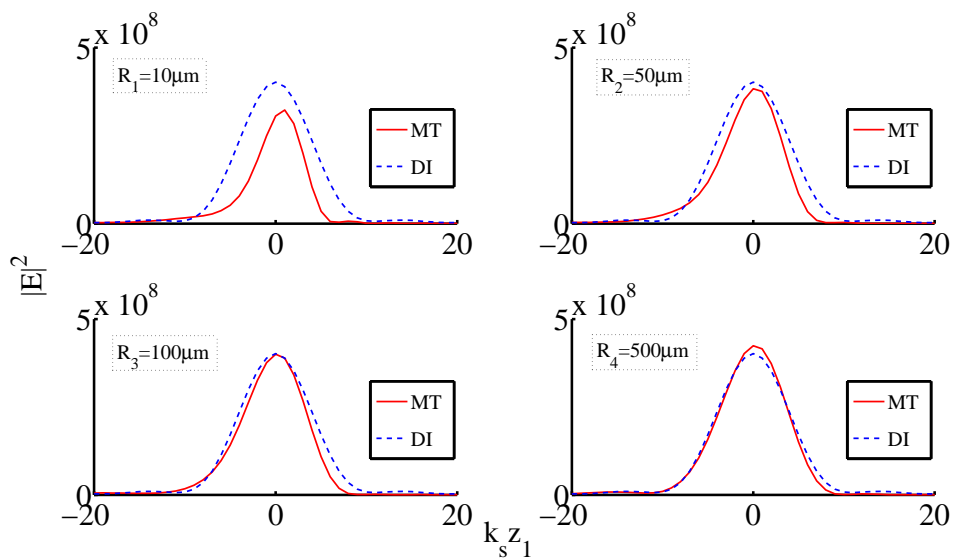
where

$$\begin{aligned}
 I_0 &= \int_0^{\alpha_m} t_p E_\alpha \sin \alpha' J_0(k_s \rho_1 \sin \alpha') e^{ik_s z_1 \cos \alpha'} \tan \alpha' \cos \alpha d\alpha, \\
 I_1 &= \int_0^{\alpha_m} t_p E_\alpha \cos \alpha' J_1(k_s \rho_1 \sin \alpha') e^{ik_s z_1 \cos \alpha'} \tan \alpha' \cos \alpha d\alpha.
 \end{aligned}$$

With  $f = 10^5 \mu\text{m}$ , we use Eqs. (5.53) and (5.54) for evaluating the focal field of the ASS with different radii of the SIL. The simulation plots are shown in Fig. 5.4. We observe that the agreement between the approximate model (DI) and the rigorous model (MT) are better for larger radii of SIL. For the longitudinal distributions, the agreement strongly depends on the radius of the SIL. This is due to the fact that the longitudinal distributions



(a) Transversal distributions



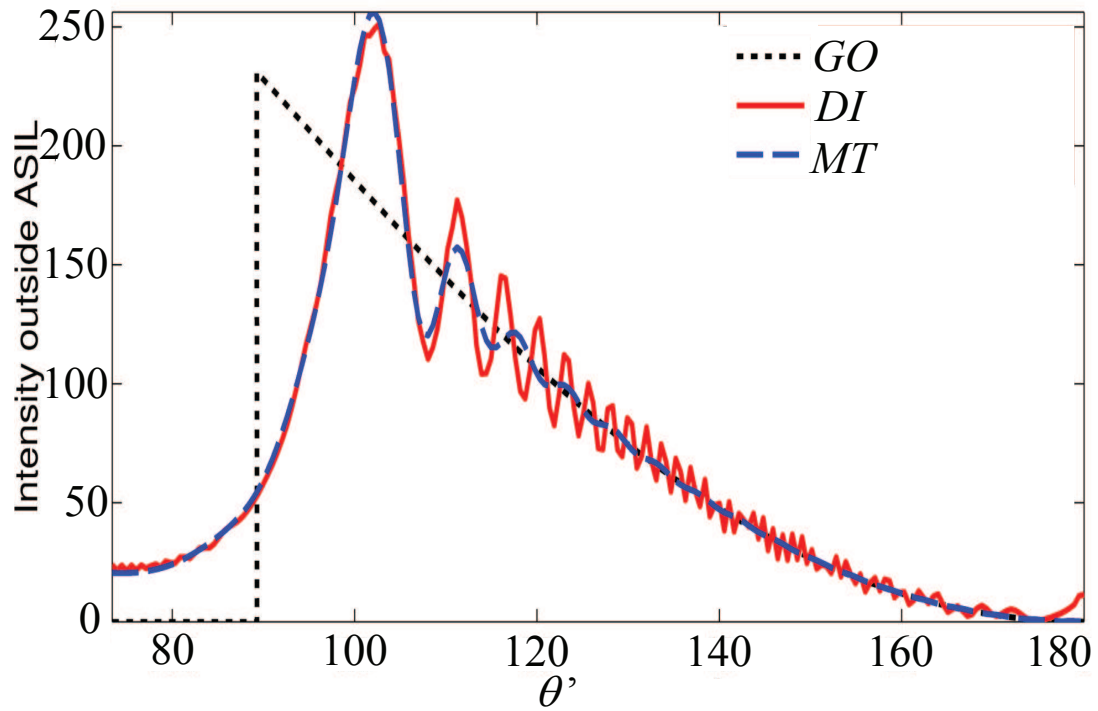
(b) Longitudinal distributions

Figure 5.4: Electric intensity distributions with different radius of ASIL and  $\alpha_m = 16^\circ$ .

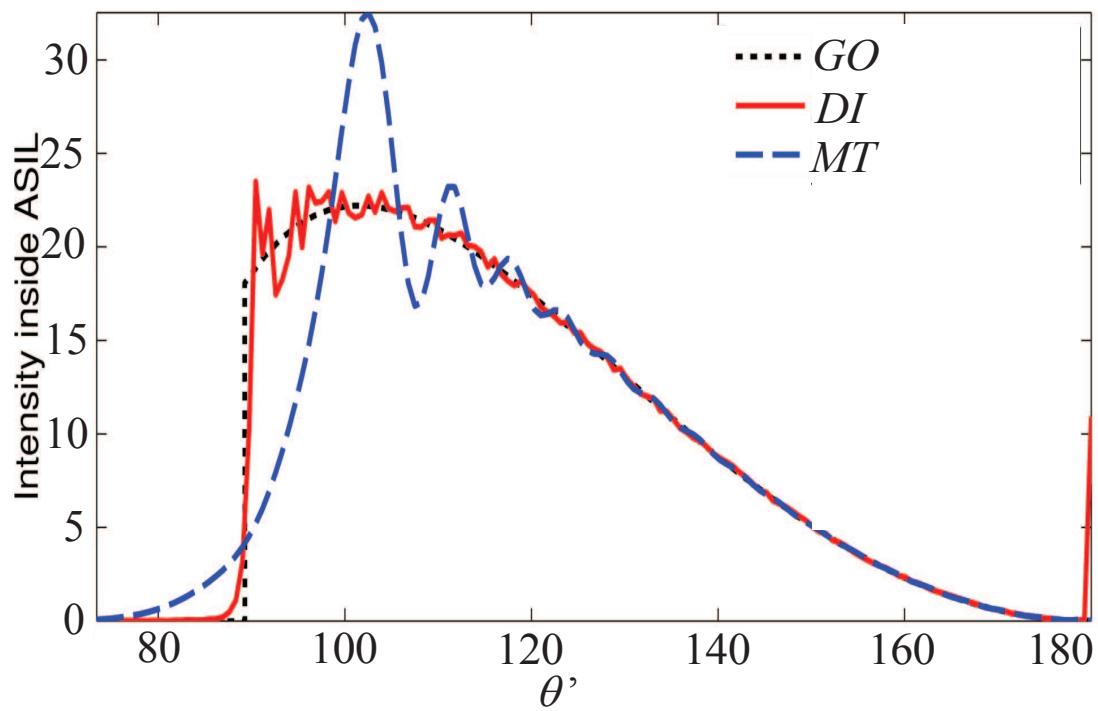
## 5. Solid Immersion Microscopy

need higher multipole terms for convergence, and hence the condition  $kr_A \gg \frac{l(l+1)}{2}$  is not well satisfied for small radii. We compare the simulation plots for the HSS (Fig. 5.3) and the ASS (Fig. 5.4) and we conclude that the approximate model for the ASS is worse than that for the HSS. This is because the NA of the incident focused beam approaching the SIL of the ASS ( $\alpha_m = 16^\circ$ ) is smaller than that of the HSS ( $\alpha_m = 60^\circ$ ), and hence more multipole terms or higher orders of the multipole terms are needed for estimating the focal field. In fact, we need to truncate the summation in Eq. (5.53) at  $l = 400$  for accurately estimating the electric field just outside the SIL. These higher order terms make the condition  $kr_A \gg \frac{l(l+1)}{2}$  not well satisfied, i.e. equation (5.27) is not good approximation and thus causes a small deviation even for a quite large-radius ( $R = 500$ ) SIL as observed in Fig. (5.4(b)). This small deviation is reduced by increasing the radius of the SIL so that the condition for the approximation in Eq. (5.27) is well satisfied. Figure 5.5 shows the electric intensity just outside the ASIL and just inside the ASIL. The plots denoted by *GO* in Figs. 5.5(a) and 5.5(b) are obtained by using Eqs. (5.25) and (5.26), respectively. The *DI* plot and *MT* plot in Fig. 5.5(a) are obtained by using Eq. (3.65) and Eq. (3.67) with  $j_l$  replaced by  $h_l^{(2)}$ , respectively. The plot denoted by *MT* is obtained by using Eq. (5.53) with  $j'_l$  replaced by  $h_l^{(2)}$ . The *DI* plot in Fig. 5.5(b) is obtained by using Eq. (5.54), i.e., this means the *DI* plot in Fig 5.5(b) is nothing else but the approximate modeling of the *GO* plot in the same Fig. 5.5(b). Intuitively, we can observe the effect of using the local plane-wave approximation, i.e., using the Fresnel transmission coefficients and the effect of the scattering coefficients. For the case of using the scattering coefficients, we observe that the shape of the electric intensity distribution does not change much across the interface. But the shape is different around the hard-edge of the beam for the case of using the Fresnel transmission coefficients. This suggests that the local plane-wave approximation is not accurate for the whole surface of the ASIL. The difference caused by using the local plane-wave approximation may be the reason of the deviation as shown in Fig. 5.4 between the approximate model and the rigorous model.

Figures 5.6 and 5.7 show the transversal electric intensity at the aplanatic point of the



(a) Electric intensity just outside the ASIL



(b) Electric intensity just inside the ASIL

Figure 5.5: Electric intensity at the spherical interface for ADW with  $f = 10\text{cm}$ ,  $R = 500\mu\text{m}$ , and  $\alpha_m = 16^\circ$ .

## 5. Solid Immersion Microscopy

ASIL with annular filters blocking the center part of the incoming beam. The incident beam is with the NA of  $\alpha_m = 16^\circ$  and the annular filters are with the blocking NAs of,  $\alpha_0 = 8^\circ$  for Fig. 5.6(a),  $\alpha_0 = 10^\circ$  for Fig. 5.6(b),  $\alpha_0 = 12^\circ$  for Fig. 5.7(a), and  $\alpha_0 = 15^\circ$  for Fig. 5.7(b). In comparison with Fig. 5.4(a), we can observe that, with larger

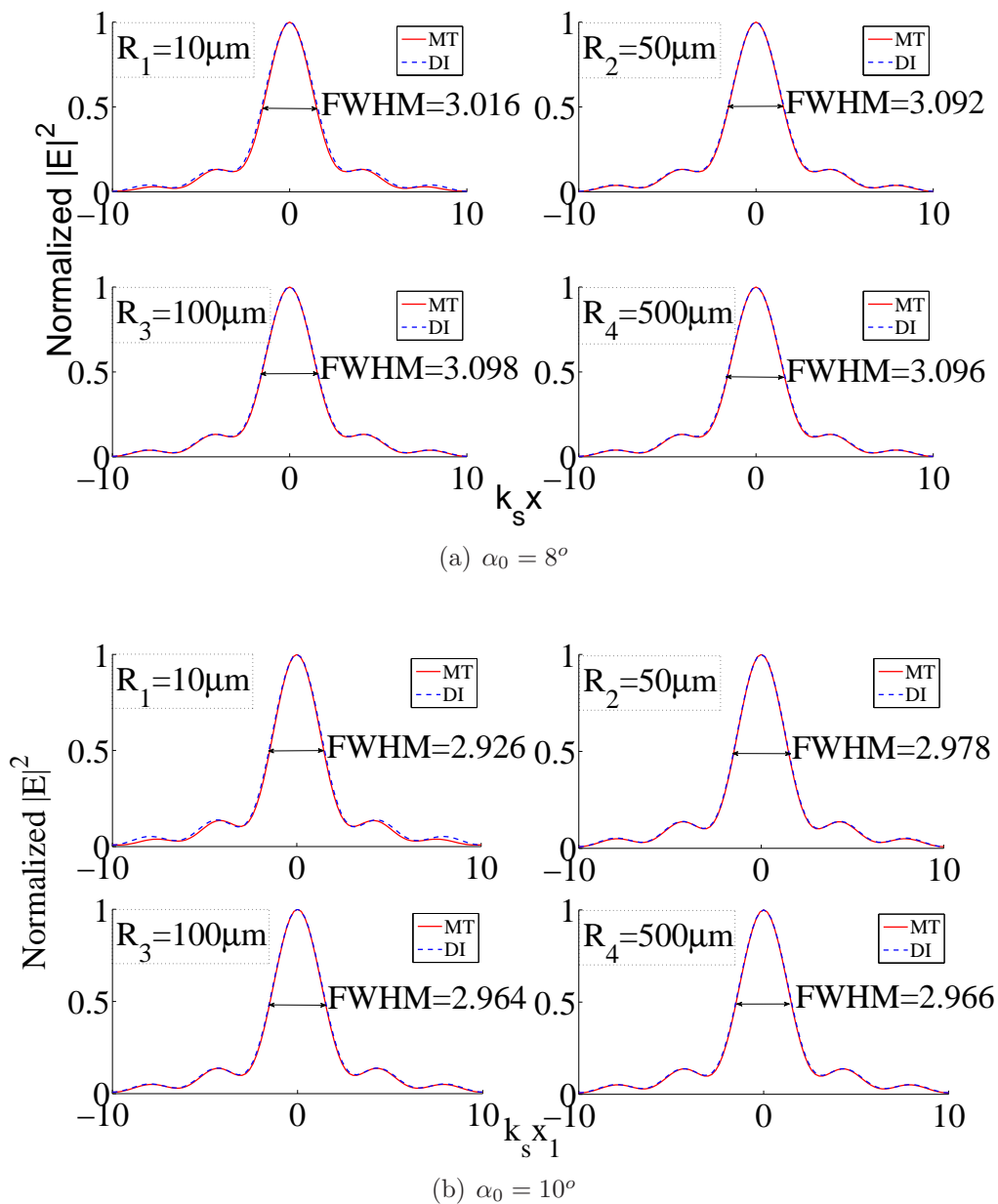
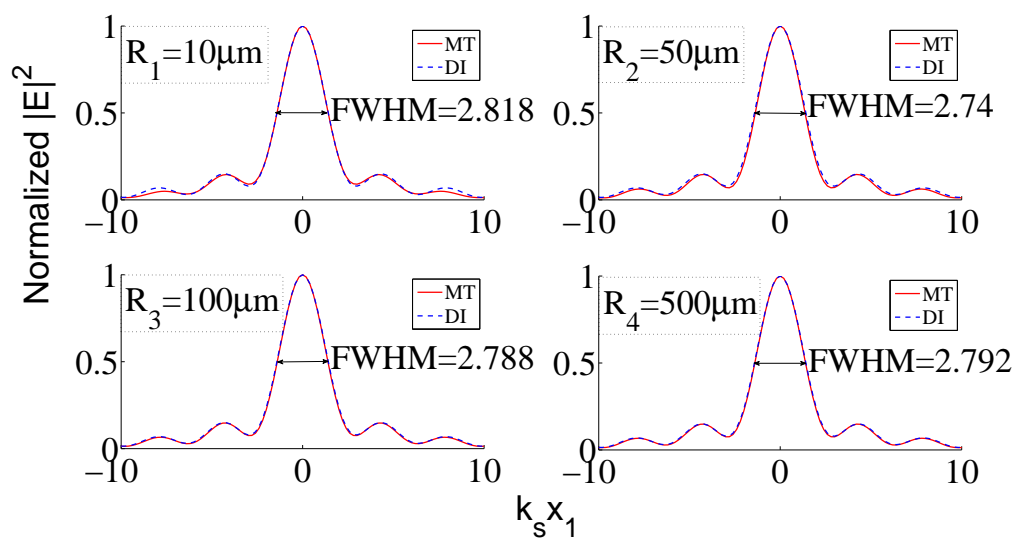
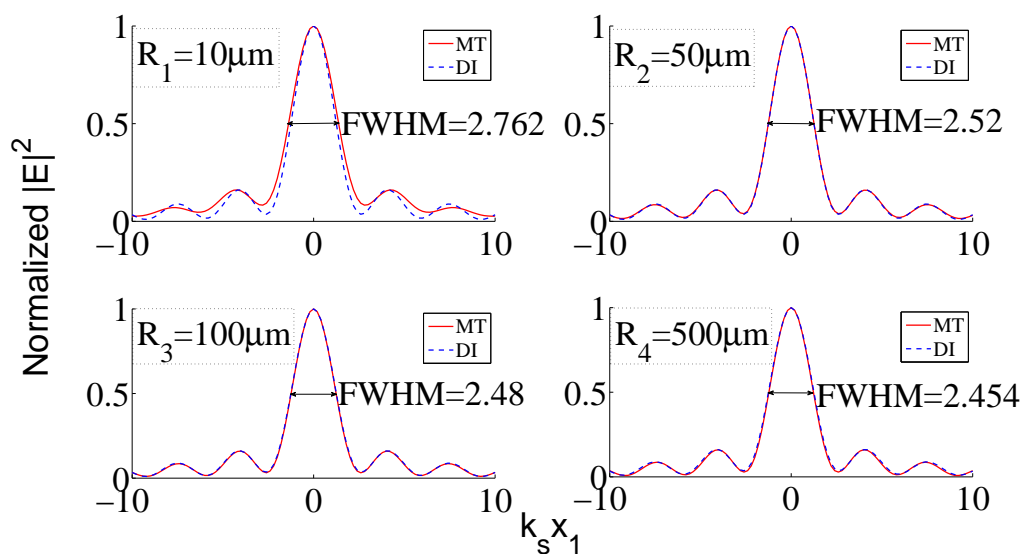


Figure 5.6: Electric intensity for ADW with  $f = 10\text{cm}$ ,  $\alpha_m = 16^\circ$ , (a)  $\alpha_0 = 8^\circ$ , and (b)  $\alpha_0 = 10^\circ$ .

annular filters, we obtain smaller full widths at half maximum (FWHM). For example, we have  $k * FWHM \simeq 3.2$  ( $FWHM \simeq 195\text{nm}$ ) without the annular filter compared to  $k * FWHM \simeq 2.5$  ( $FWHM \simeq 152\text{nm}$ ) with the annular filter  $\alpha_0 = 15^\circ$ . Though the side

(a)  $\alpha_0 = 12^\circ$ (b)  $\alpha_0 = 15^\circ$ Figure 5.7: Electric intensity for ADW with  $f = 10\text{cm}$ ,  $\alpha_m = 16^\circ$ , (a)  $\alpha_0 = 12^\circ$ , and (b)  $\alpha_0 = 15^\circ$ .

lobes become stronger with higher percentage of blocking the center part of the incident beam, they are still relative small compared to the center peak even for  $\alpha_0 = 15^\circ$ . This means we can increase the blocking ratio of the beam furthermore. The only restriction is that we face a tradeoff of the power. We we can observe from Fig. 5.8(a) in which we plot the electric intensity on the transversal plane at the aplanatic point of the ASIL for a radially-polarized beam with  $a(\alpha) = \sqrt{\cos\alpha}$  that the maximum intensity with the annular filter  $\alpha_0 = 15^\circ$  in use is  $4 \times 10^6$  compared to  $7 \times 10^7$  when the annular filter  $\alpha_0 = 8^\circ$  in use. This may be a problem in real experiments when a high power laser is not always available. Although the normalized electric intensity distributions on the transversal plane in Fig. 5.8(b) are nearly perfect using the two models, there is noticeable deviation for the absolute values of the intensities as shown in Fig. 5.8(a), especially the plots with higher blocking ratios. The higher blocking ratios mean that the contribution of the outer part near the hard edge of the incident beam is more dominant. Since the local plane-wave approximation is not a good approximation around the hard edge of the beam as shown in Fig. 5.5, the approximate model deviates more from the rigorous model with a higher blocking ratio.

For a GSS, simulation results using Eqs. (5.52) and (5.53) are shown in Fig. 5.9. We conclude that the spherical interface strongly degrades the longitudinal distribution when the focus is far from the aplanatic points. Figure 5.9(b), where longitudinal electric intensity distributions are plotted, shows that the distribution spreads along a long distance, characteristic of presence of spherical aberration. The intensity variation is also asymmetric, indicating higher orders of spherical aberration. This spread accounts for the fact that the rays converge to a large region inside the SIL, and hence the condition  $\hat{k} = -\hat{r}$  is not well satisfied for the cases of  $d = \frac{R}{2}$  and  $d = 2R$ . Consequently, models based on the ASR should not be applied for the cases of  $d = \frac{R}{2}$  and  $d = 2R$ .

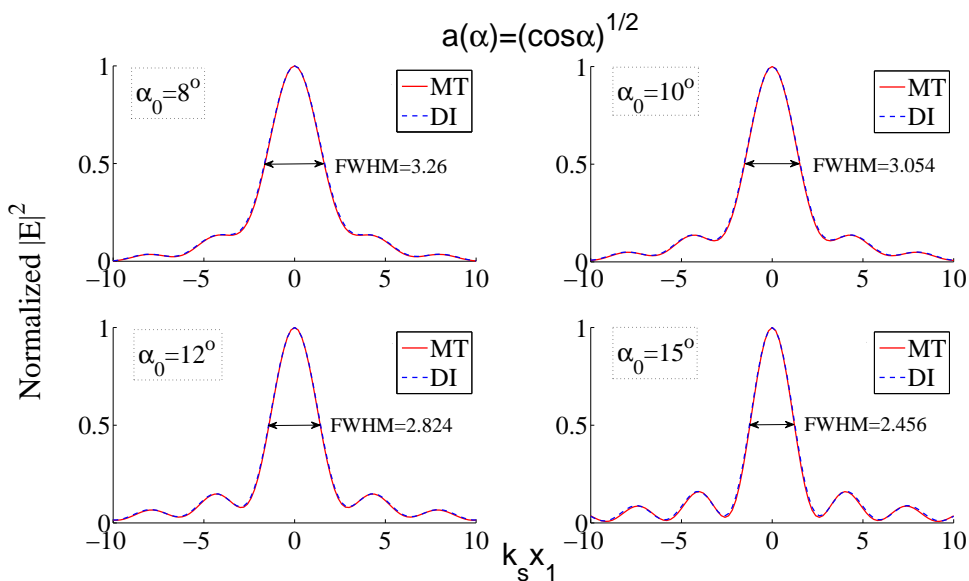
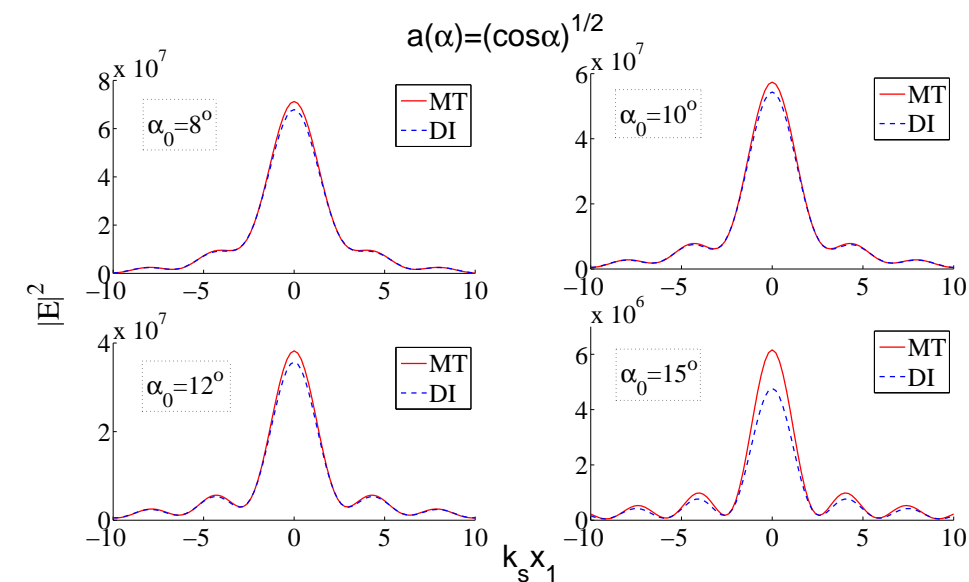
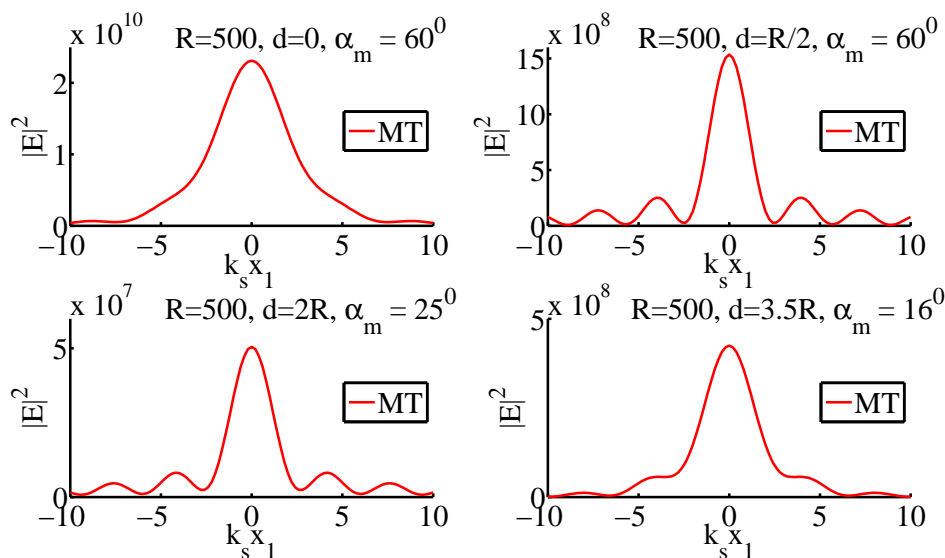
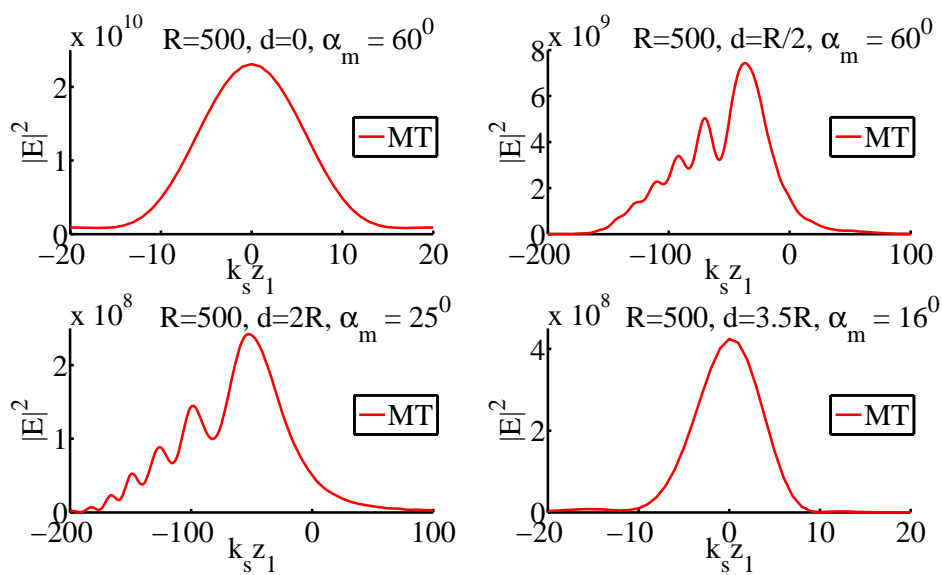


Figure 5.8: Electric intensity for ADW with  $f = 10\text{cm}$ ,  $R = 500\mu\text{m}$  and  $\alpha_m = 16^\circ$ .



(a) Transversal electric intensity distributions



(b) Longitudinal electric intensity distributions

 Figure 5.9:  $f = 10\text{cm}$ ,  $R = 500\mu\text{m}$ ,  $d_1 = 0$  (HSS),  $d_2 = \frac{R}{2}$ ,  $d_3 = 2R$ ,  $d_4 = 3.5R$  (ASS).

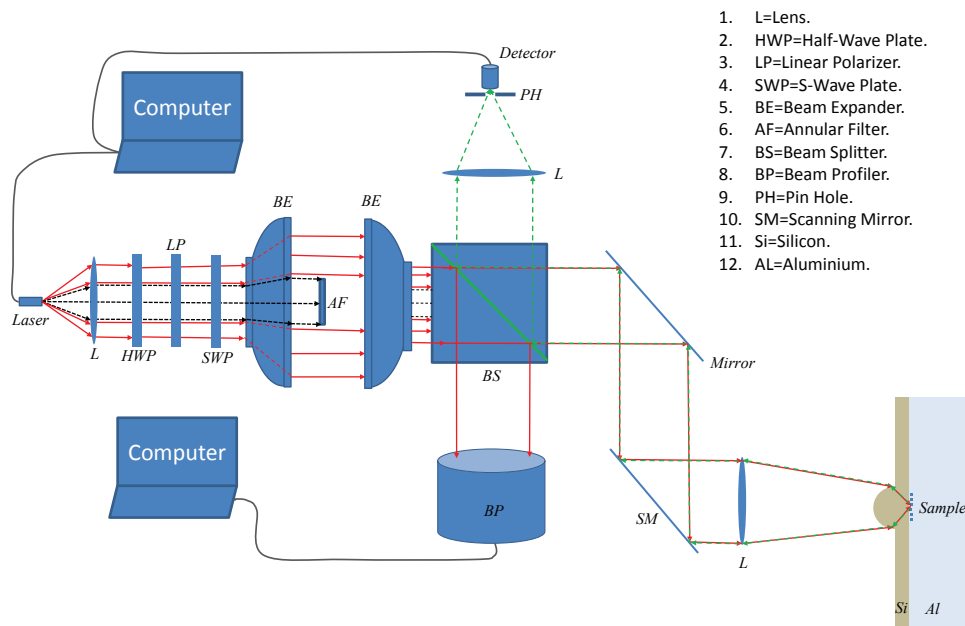


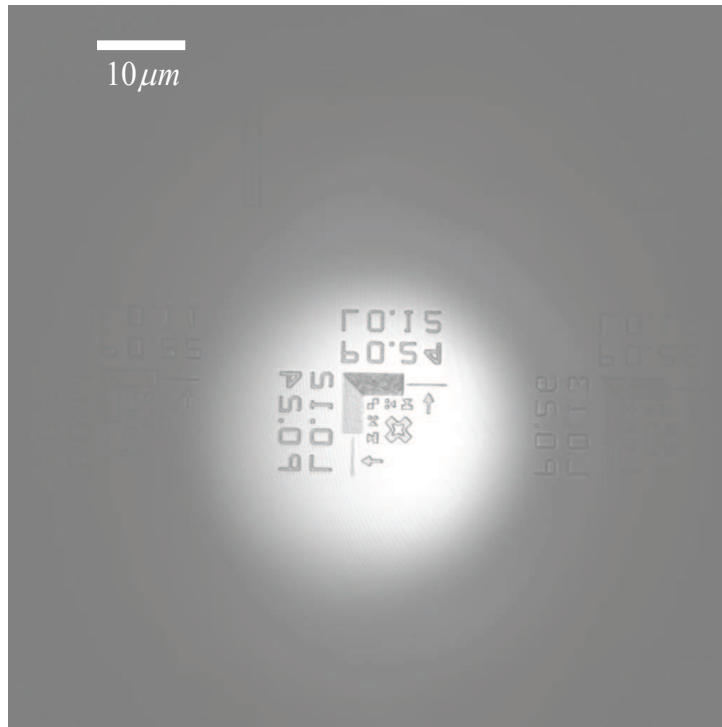
Figure 5.10: Experimental Setup.

## 5.5 Experiment

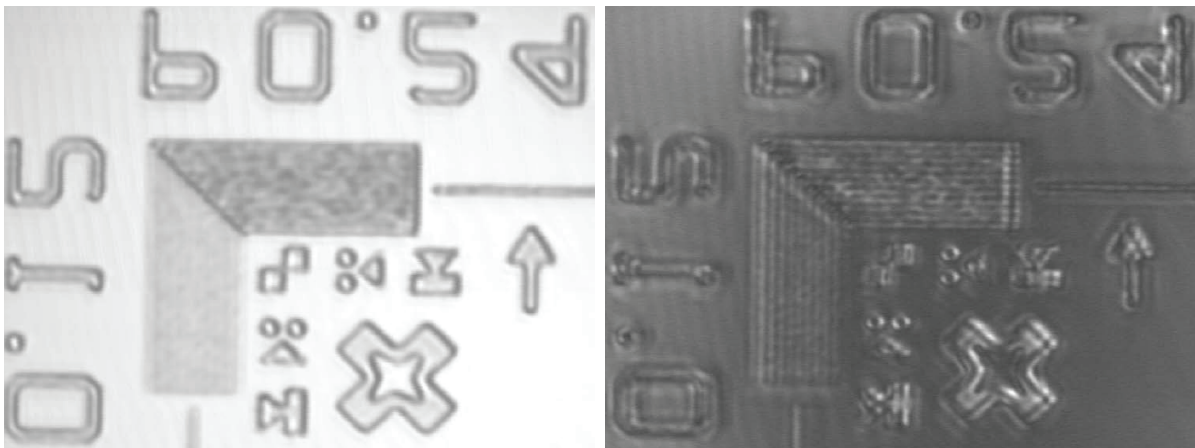
Theoretically, we have presented and studied the focusing performances of different polarizations using an aplanatic lens and an annular filter. In this section, we present and analyze experimental results. The experimental setup is shown in Fig. 5.10 which operates in a reflection mode. The laser produces a linearly-polarized Gaussian beam with a divergence angle of  $\sin \theta = 0.1$ . This diverging beam is collimated by a lens with a focal length of  $f = 15.52\text{mm}$  and the resultant collimated beam has a diameter of  $D \approx 3.1\text{mm}$ . The collimated linearly polarized beam can be manipulated to produce a circularly-polarized beam, a radially-polarized beam, a azimuthally-polarized beam, or an azimuthally-polarized beam with a vortex. More details on producing the different polarizations can be found in appendix C. This section presents the experimental results using a linearly-polarized beam, a circularly-polarized beam, a radially-polarized beam, and an azimuthally polarized beam with a vortex  $n = 1$ . In Fig. 5.10, the red lines represent the incident beam approaching the sample. After reaching to the sample, the focused beam interacts with the sample and produces induced currents in the focal region. These induced currents radiate the radiation beam indicated by the green lines in Fig.

5.10. The radiation field will be recorded by the detector. A pin hole is placed before the detector to eliminate the stray light and hence improve the image quality [174]. In this section, we use the pin hole with a diameter of  $50\mu m$  unless otherwise mentioned. The purpose of using the beam profiler in the setup of Fig. 5.10 is to assist in controlling the polarization states of the incident beam. More details on using the beam profiler are provided in appendix C. The black dotted lines in Fig. 5.10 denote the center part of the incident beam that is blocked by the annular filter. Since the smallest diameter of the available annular filters is  $4mm$ , we magnify the incident beam twice to obtain an incident beam with a diameter of  $D \approx 6.2mm$  before inserting the annular filters with diameters of  $4mm$ ,  $5mm$ , or  $6mm$  into the space just behind the first beam expander. The second beam expander is used to reduce the diameter to the original size of  $D \approx 3.1mm$ . The technical details of the optical components can be found in appendix C. We have run and studied a number of experiments using different combinations of the polarizations and the annular filters. A part of the experimental results is presented here.

Figure 5.11 shows the images of monitor lines of the Metrochip Microscope Calibration Target using the linearly-polarized beam. The direction of polarization is the horizontal direction, which we call  $x$ -direction. The  $L$  pattern comprises of 11 lines in which the width of each line is  $120nm$  and they are  $120nm$  separated from each other. The letters in Fig. 5.11(a) indicate the width and the pitch of the feature. To read the values, the letters should be rotated  $180^\circ$  around the horizontal line ( $x$ -axis). After rotating the letters in Fig. 5.11(a), we get  $P.24$  and  $L0.12$  which mean the pitch of the feature is  $240nm$  and the width of the lines is  $120nm$ . Figure 5.11(a) shows the whole area of scanning in which the bright spot marks the field of view of the SIL [81]. Figure 5.11(b) shows the region of interest without any annular filter in which we are unable to differentiate the lines of the feature. However, by introducing an annular filter with a diameter of  $4mm$  into the system to block the center part of the incident beam, we can differentiate the lines as shown in Fig. 5.11(c). We can observe that the lines along the vertical direction are easier, compared with the horizontal ones, for resolving due to the well-known fact that the electric intensity distribution in the focal region of a linear polarization is tighter in

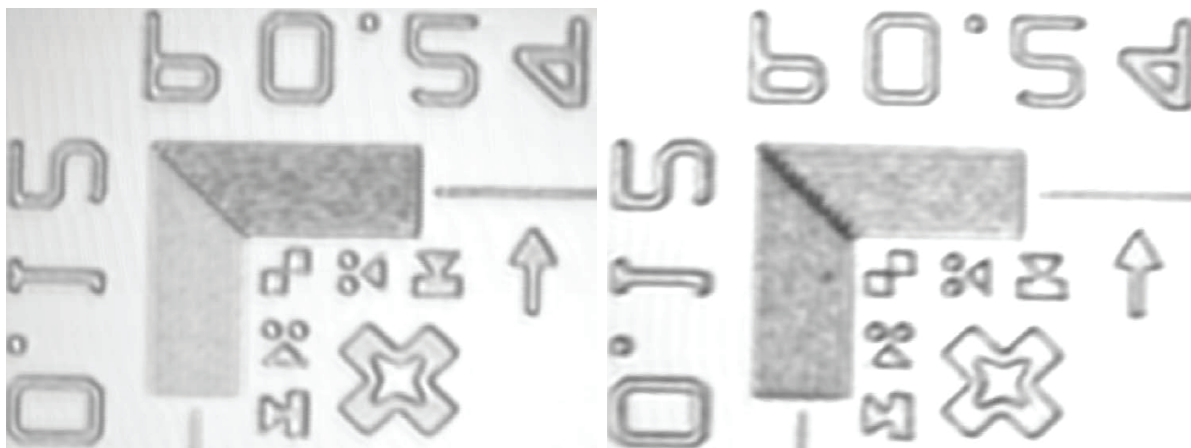


(a) No Filter, Brightness 2023, Contrast 2066, Power 10%

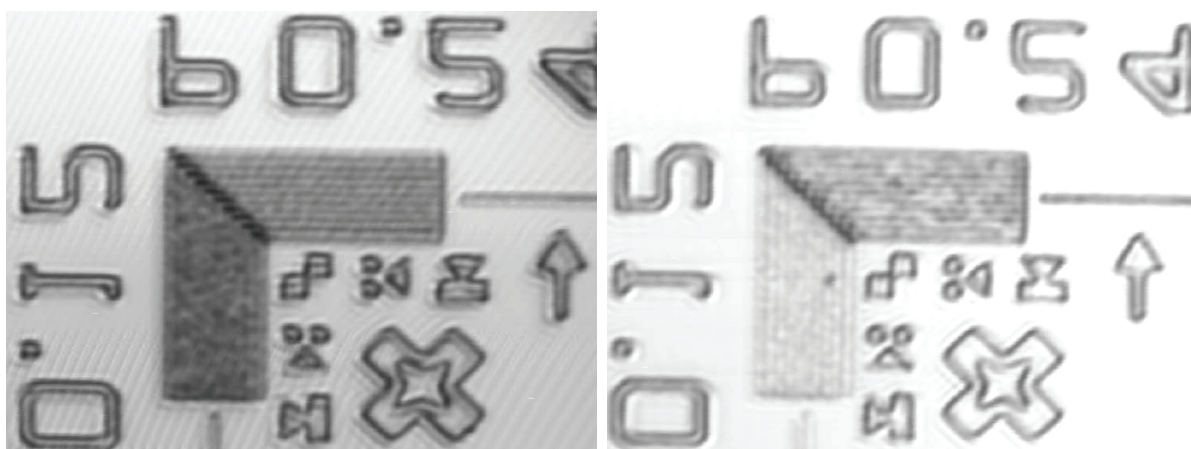


(b) No Filter, Brightness 2023, Contrast 2066, Power 10% (c) 4mm Filter, Brightness 2023, Contrast 2729, Power 80%

Figure 5.11: Imaging with linear polarization and an annular filter.



(a) Linear, Brightness 2023, Contrast 2066, Power 10%. (b) Circular, Brightness 1988, Contrast 1992, Power 4%, Pin Hole 75 micrometer.

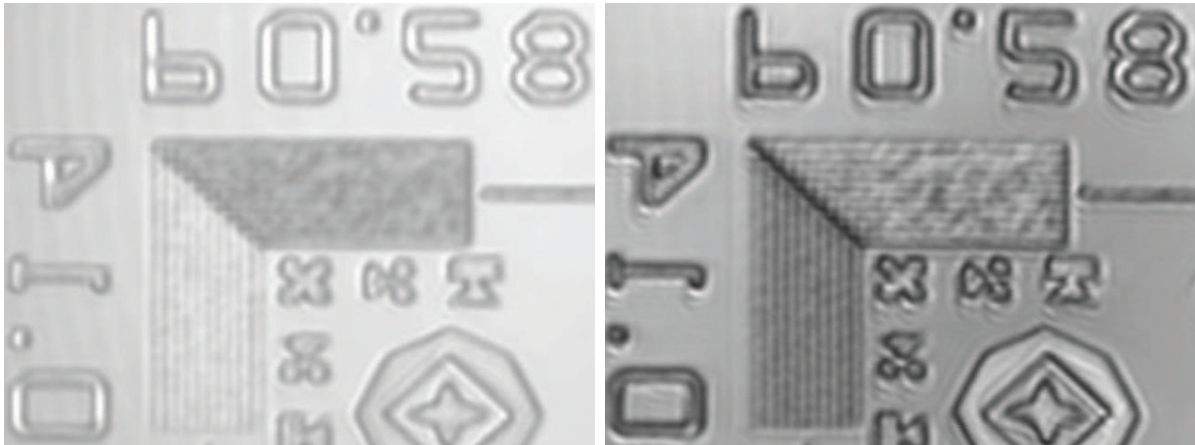


(c) Radial, Brightness 2002, Contrast 2255, Power 10%. (d) AV1, Brightness 1996, Contrast 2047, Power 4%, Pin Hole 75 micrometer.

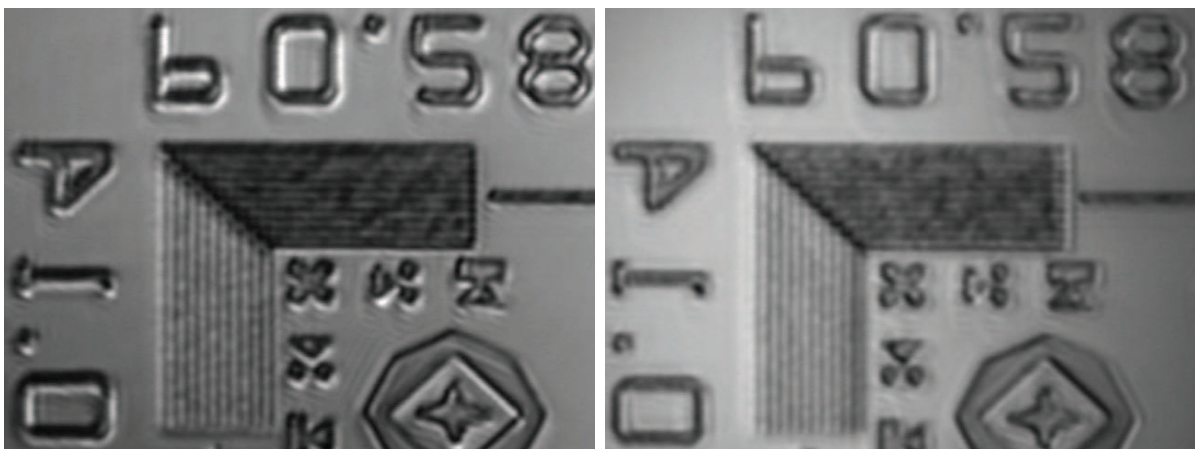
Figure 5.12: Image of the sample with pitch  $240nm$  and line  $120nm$  using different polarizations and no filter.

the perpendicular direction to the direction of the polarization as predicted in Fig. 3.13. Figure 5.12 shows the images of the same feature as in Fig. 5.11 using different polarizations without any annular filter. As expected, we are unable to resolve the lines using the linear polarization shown in Fig. 5.12(a) and the circular polarization shown in Fig. 5.12(b). Using the radial polarization shown in Fig. 5.12(c) and the azimuthal polarization with a vortex shown in Fig. 5.12(d) can improve the image quality, though it is not much improved.

Figure 5.13 shows the images of a bigger feature compared with the feature in Fig. 5.12. The line width of the feature is  $140nm$  and the pitch is  $280nm$ . The images are obtained by using the linear polarization. We can see that using the annular filters improves the

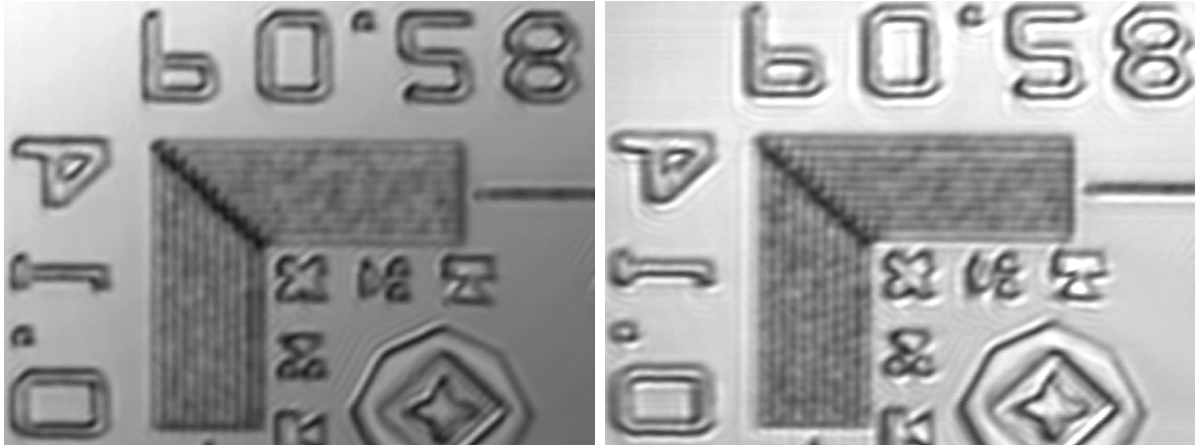


(a) No Filter, Brightness 2024, Contrast 2347, Power 8%, (b) 4mm Filter, Brightness 2020, Contrast 2720, Power 60%

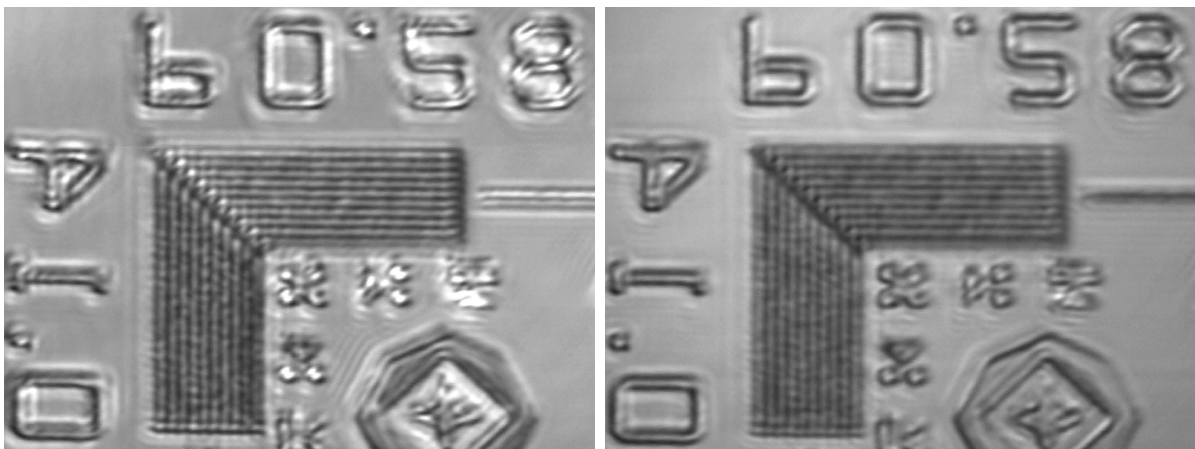


(c) 5mm Filter, Brightness 2022, Contrast 3090, Power 100%, (d) 6mm Filter, Brightness 2022, Contrast 3045, Power 100%

Figure 5.13: Imaging with linear polarization and different filters.



(a) No Filter, Brightness 2016, Contrast 2599, Power 4%, (b) 4mm Filter, Brightness 2021, Contrast 2882, Power 60%



(c) 5mm Filter, Brightness 2023, Contrast 3328, Power 100%, (d) 6mm Filter, Brightness 2023, Contrast 3328, Power 100%

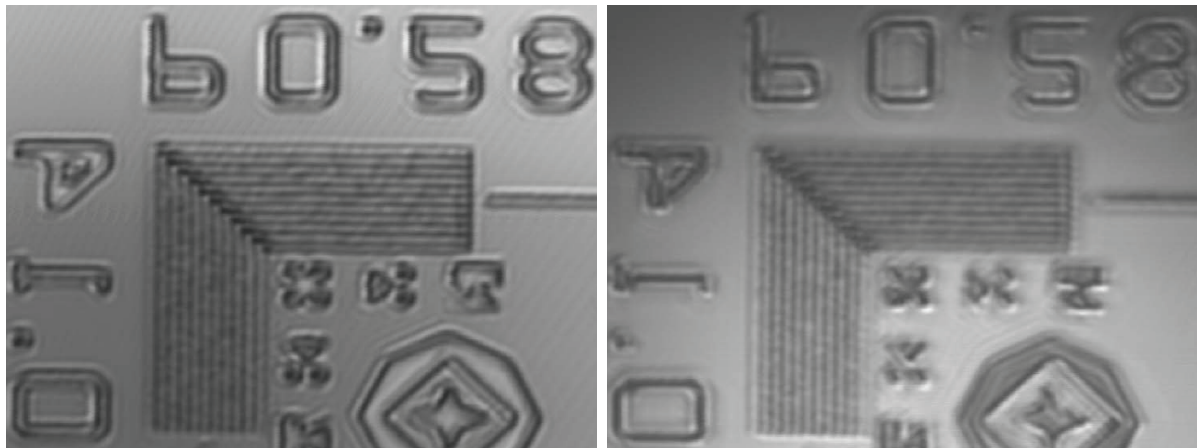
Figure 5.14: Imaging with circular polarization.

image quality significantly. The effect of linear polarization is also observed in Fig. 5.13 where the vertical lines are resolved clearer than the horizontal lines.

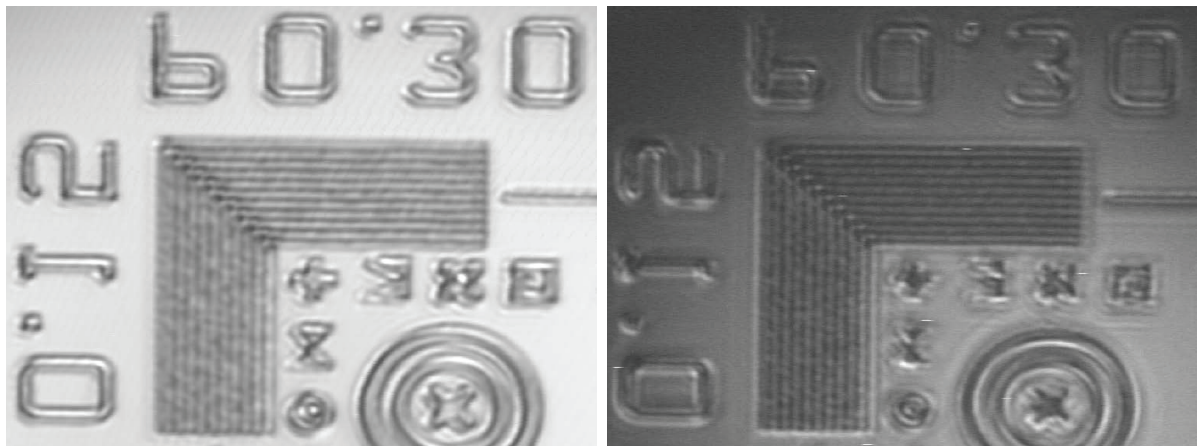
Figure 5.14 shows the images of the same feature as in Fig. 5.13 but the circular polarization is used to obtain the images. As expected for the circular polarization, both the vertical and horizontal directions are almost equally resolved. Using the annular filters improves the image quality significantly, but we need to use the incident beam with more power due to the loss of using the annular filters. For example, in Fig. 5.14(a) we use 4% of the maximum power of the beam if no filter is used but for the 5mm and 6mm filters, we need to use the maximum possible power of the incident beam. In fact, we use a laser source with a maximum power of 500 mW, however, we need from 10 mW to 20 mW only for the focused beam to get a stable image. Increasing the delivered power does not

## 5. Solid Immersion Microscopy

help to improve the image quality but increases the risk of destroying the sample due to a high energy density. Without the filters, we need only 4% of the maximum power since we use a beam splitter for splitting the incident beam into two beams, each beam with 10 mW. For the case of presence of the filters, since we block a large center part of the incident beam, we usually need to use the maximum power of the laser source. Figure 5.15 shows the images of different features using the radial polarizations. As expected, we observe that using the annular filter helps to improve the image quality. From Figs. 5.13(a), 5.14(a), and 5.15(a), we can observe that using the radial polarization leads to the best image for the same sample.



(a) No Filter, Brightness 2012, Contrast 2407, Power 8%, (b) 4mm Filter, Brightness 2021, Contrast 2747, Power 100%



(c) No Filter, Brightness 2014, Contrast 2407, Power 10%, (d) 4mm Filter, Brightness 2023, Contrast 3279, Power 20%

Figure 5.15: Imaging with radial polarization.

In fact, all of the experimental images in this thesis are obtained by manipulating different parameters such as pinhole size, focal plane, brightness, and contrast. The best

images are presented here for each particular setup. One important notice is about the exact position of the focal plane which is well-known in geometrical optics. The focus of an ASIL is shifted for the case of using high-blocking-angle annular filters. The focal shift can be explained as due to the increase percentage of the surface wave's contribution [175]. Hence, we usually need to change the position of the focal plane when we introduce an annular filter for obtaining the best image. Another important notice is that using the circular polarization and cylindrical polarization produces uniform images which mean the horizontal lines and vertical lines are resolved with the same quality. However, the linear polarization gives the best image quality for the lines in perpendicular to the polarization direction of the incident beam but the worst image quality for the lines in parallel with the polarization direction of the incident beam. These observations agree well with the simulation results for the focusing system.

# Chapter 6

## Conclusions and Further Directions

In this chapter, the contributions of the thesis are first summarized and then further directions are suggested for possible extensions. The main objective of this thesis is to study focal fields of focusing system using polarized monochromatic beams. We have presented both theoretical and experimental works.

### 6.1 Summary

The introduction chapter presents literature reviews for different topics relating to the works presented in this thesis. The author is aware that there are other topics closely related to the works presented here. However, the topics presented in the introduction chapter have motivated the author to accomplish the works. In the context of these topics, I would like to highlight the contributions of this thesis as follows.

Firstly, the two bases, plane and spherical waves, for representing electromagnetic fields are discussed in details. We derive electric fields of an incoming beam and an outgoing beam. On one hand, the outgoing beam caused by a source is usually mentioned in describing emission fields, including fields of a laser beam. On the other hand, the incoming beam caused by a sink is usually mentioned in describing absorption fields, including incoming fields of of time-reversed lasing [124] and focused fields in focusing systems. The results presented in this thesis may be helpful in time reversal analysis. We also show that for a converging field, if there is no sink at the focus, the inhomogeneous parts of the converging field and the resultant diverging field cancel each other completely such that there is no singularity at the focus. This interference is the reason of the well-

known diffraction limit in an optical system [5].

Secondly, the two approaches for evaluating the focal field of an aplanatic system are reviewed and further developed in details. The first approach based on the plane wave expansions is usually mentioned as Debye-Wolf diffraction integrals. The second approach is based on the multipole expansions. On one hand, the Debye-Wolf diffraction integrals ignore the contribution of the second kind of the critical points to the focused field and hence is not accurate in describing the focused field near to the GRS and even cause the well-known anomalous behavior on the axial axis. On the other hand, the second approach suffers from the truncation errors and hence give the small oscillation around the hard-edge of the focused beam. Since the second approach takes into account the second kind of the critical points, there is no anomalous behavior of the electric field on the axial axis. The two approaches give a perfect agreements on the field distribution around the focus where the contribution of the second kind of critical points is ignorable. For the second approach, there are two ways of deriving the multipole strengths. The two ways are presented in this thesis with detailed derivations.

Thirdly, a novel definition of the focused beam is introduced in which the incident beam approaching a scatterer includes only the converging beam. This definition gives us a clear interpretation of the scattering mechanism due to two kinds of scatterers, including solid immersion lens and sphere. The solid immersion lens has an open boundary and there is only one light-matter interaction at the spherical surface. On contrary, the sphere has a closed boundary, hence there is an infinite number of light-matter interactions at the internal surface of the sphere. To highlight this difference, we derive series of scattering coefficients to account for the infinite number of the interactions. We also consider the off-axis configurations of the scatters in which we use the addition theorems to translate the focused field for solving the boundary conditions rigorously. The interpretation helps to solve rigorously the boundary conditions at spherical interfaces and hence plays an important role in understanding the SIL modeling.

The fourth contribution is in fact the main objective of this thesis that is about studying the solid immersion microscopy in details. We present a model solving the

boundary conditions rigorously, hence we call this model, a rigorous model. This rigorous model is based on the multipole theory. We also present an approximate model based on the Debye-Wolf diffraction integrals. For a large hemispherical solid immersion lens, we prove that the rigorous model and the approximate model are in good agreements. Based on the approximate model, we discussed and pointed out some errors committed by other authors. Hence, in the theoretical aspect, this thesis provides a clear understanding about the SIL modeling. This solid immersion microscope is also studied experimentally. We propose an experimental setup for integrating the solid immersion microscope with an annular filter. We show that the image quality using different polarizations and annular filters are greatly improved in comparison with the case of no filter. We also demonstrate that we are able to resolve gratings consisting of 120-nm-wide lines, spaced 120 nm apart, using 1342 wavelength laser. These results may be important in failure analysis of integrated circuits.

## 6.2 Further Directions

The results presented in this thesis suggest some possible extensions that the author could not finish due to time constraint. These include, but are not limited to, the following directions

### 6.2.1 Theory

Regarding to the truncation of the multipole theory, the infinite summations are truncated using both the localization principle and the numerical convergence. The localization principle states that a multipole term of order  $l$  corresponds to a ray passing the origin at a distance  $(l + \frac{1}{2})\frac{\lambda}{2\pi}$  from the origin [168, 176]. This means to evaluate the field further from the origin, we need to include more multipole terms in the summations. However the localization principle is not rigorous [176] and the numerical convergence is merely a trial-error process. Hence, an analytical explanation should be derived for guiding the truncation of the summations.

The inversion of the focusing process is a topic of interest [106], i.e., given a specific

## 6. Conclusions and Further Directions

---

focal field, we derive the necessary incident beam for producing the focal field as close to the expected field as possible. As we see through this thesis that multipole strengths relate to numerical aperture, polarization, and phase of focused beams. Given a specific focal field distribution, we can use the focal plane matching method to evaluate the strengths [135] and then the formulas derived in this thesis can be used to obtain the necessary incident field on the GRS. This inversion may play an important role in designing and implementing a perfect absorber that absorb an incoming field completely.

In this thesis, we study annular filters which are the simplest filters of a general class of filters comprising binary phase mask and binary amplitude mask [117, 118]. By changing the filters, we can obtain different sets of the multipole strengths and may produce a super-oscillation phenomenon at the focus. Most of the researches on focusing system use the Debye-Wolf diffraction integrals, which ignore the contribution of the second kind of critical points. These critical points may contribute to the focused field with the number of mask layers increase. And in this aspect, the multipole theory may be superior in describing the focused field. Moreover, the super-oscillation phenomenon is usually conveniently explained and analyzed in terms of summations of harmonic functions like spherical harmonics functions [2]. Hence, the multipole theory may have an advantage on analyzing the super-oscillation phenomenon.

Recently, there are numerous researches on the wavelength-scale solid immersion lenses [170] and subwavelength-size solid immersion lens [169]. Using our rigorous model presented in this thesis, we can analyze the performances of the small solid immersion lenses. Moreover, our model for the scattering mechanism may be useful in studying and explaining the imaging theory using microlens [177, 178].

### 6.2.2 Experiment

As we show in Fig. 5.10, the annular filter is used to block the center part of the incident beam only. The filter may have interesting effects if it blocks the center parts of both the incident beam and the reflected beam, we can do this by moving the beam expanders and the annular filter to the position in between the beam splitter and the mirror. It would be

## 6. Conclusions and Further Directions

more interesting to fabricate and use the SIL as designed in Fig. 6.1. Putting the arrays of annular solid immersion lens on sample has been implemented [179]. We have mentioned that the annular filter is a simple version of the binary masks. Though the annular filter can improve the image quality significantly, the FWHM of the focal field distribution produced by using the filter is limited to around  $150nm$  for illuminating wavelength of  $1.34\mu m$ . Hence, to obtain images with even higher quality, we should implement a binary mask with more concentric annular layers using a spatial light modulator. This mask can help to focus the beam into a tighter spot [117] and hence may help to improve the image quality.

One of the most important applications of solid immersion microscope is to identify faulty locations in semiconductor failure analysis in which the size and the design of the integrated circuits are getting smaller and denser. This small scale is now down to several tens of nanometer which is a big challenge for isolating the faulty locations. Solving this challenge may need innovative ideas for pushing the imaging capacity of solid immersion technique. Unfortunately, the reflective indexes of conventional materials are limited to around 3.5 (silicon), it is thus impossible to improve the performance of the solid immersion microscopy using the conventional materials beyond some extents. Last decade, we have witnessed numerous designs and implementations of super-lenses using metamaterials for achieving super-resolution imaging. Using metamaterials which in principle have unlimited reflective indexes instead of using the conventional materials may

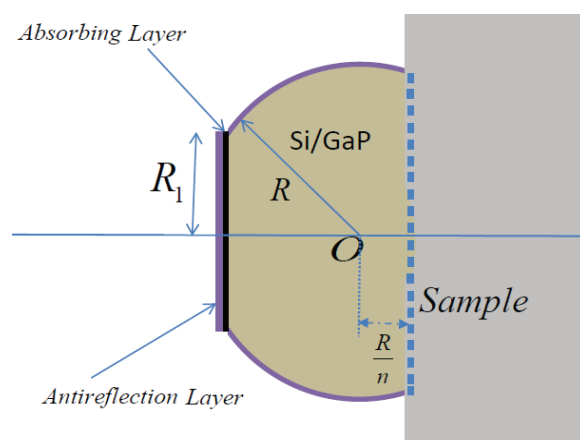


Figure 6.1: Annular solid immersion lens with radius  $R$ , reflective index  $n$ , and a blocking area  $R_1$ .

## 6. Conclusions and Further Directions

---

be worth being considered for experiment [180]. Using metamaterial faces the problem of energy loss due to the intrinsic impedance of metals, this problem makes the super-lenses less attractive. To reduce the energy loss of the super-lenses, one may consider to combine the metamaterial and a conventional material to employ the advantages of both materials [181].

# References

- [1] M. Born and E. Wolf, *Principles of Optics* (Cambridge University, Cambridge, UK, 2002). [1](#), [6](#), [15](#), [83](#)
- [2] N. I. Zheludev, “What diffraction limit?” *Nat. Mat.* **7**, 420–422 (2008). [1](#), [129](#)
- [3] R. P. Feynman, R. P. Leighton, and M. Sands, *The Feynman lectures on physics, Vol II* (Addison-Wesley, San Francisco, USA, 2006). [1](#), [16](#)
- [4] C. J. Sheppard, “High-aperture beams,” *J. Opt. Soc. Am. A* **18**, 1579–1587 (2001). [2](#), [61](#)
- [5] H. Noh, S. M. Popoff, and H. Cao, “Broadband subwavelength focusing of light using a passive sink,” *Opt. Express* **21**, 17435 (2013). [2](#), [3](#), [21](#), [127](#)
- [6] S. Heugel, A. S. Villar, M. Sondermann, U. Peschel, and G. Leuchs, “On the analogy between a single atom and an optical resonator,” *Laser Physics* **20**, 100 (2010).
- [7] A. Sentenac, P. C. Chaumet, and G. Leuchs, “Total absorption of light by a nanoparticle: an electromagnetic sink in the optical regime,” *Opt. Lett.* **38**, 818–820 (2013). [2](#), [21](#)
- [8] J. de Rosny and M. Fink, “Overcoming the diffraction limit in wave physics using a time-reversal mirror and a novel acoustic sink,” *Phys. Rev. Lett.* **89**, 124301 (2010). [2](#)
- [9] P. Lueg, “Process of silencing sound oscillations,” US Patent No 2043416 (1936). [2](#)
- [10] R. W. Hellwarth, “Generation of time-reversed wave fronts by nonlinear refraction,” *J. Opt. Soc. Am.* **67**, 1 (1977). [3](#)
- [11] Y. Urzhumov, C. Ciraci, and D. R. Smith, “Generation of time-reversed wave fronts by nonlinear refraction,” *Nat. Phys.* **9**, 393 (2013). [3](#)
- [12] A. T. M. F. G. Lerosey, J. de Rosny, “Focusing beyond the diffraction limit with

- 
- far-field time reversal,” *Science* **315**, 1120 (2007). [3](#), [22](#)
- [13] J. D. Lawson, “Some attributes of real and virtual photons,” *Contemporary Physics* **11**, 575 (1970). [3](#)
- [14] G. Leuchs and M. Sondermann, “Time reversal symmetry in optics,” *Phys. Scr.* **85**, 058101 (2012). [3](#)
- [15] S. Quabis, R. Dorn, M. Eberler, O. Glockl, and G. Leuchs, “Focusing light to a tighter spot,” *Opt. Comm.* **179**, 1–7 (2000). [3](#), [13](#), [54](#)
- [16] R. Dorn, S. Quabi, and G. Leuchs, “Sharper focus for a radially polarized light beam,” *Phys. Rev. Lett.* **91**, 233901 (2003). [3](#), [13](#), [42](#), [43](#)
- [17] E. Mudry, E. L. Moal, P. Ferrand, P. C. Chaumet, and A. Sentenac, “Isotropic diffraction-limited focusing using a single objective lens,” *Phys. Rev. Lett.* **105**, 203903 (2010). [3](#)
- [18] G. Leuchs and M. Sondermann, “Light-matter interaction in free space,” *J. Mod. Opt.* **60**, 36–42 (2013). [3](#), [4](#)
- [19] M. Sondermann, R. Maiwald, H. Konermann, N. Lindlein, U. Peschel, and G. Leuchs, “Design of a mode converter for efficient light-atom coupling in free space,” *Appl. Phys. B* **89**, 489–492 (2007). [3](#), [4](#), [5](#)
- [20] G. Zumofen, N. M. Mojarad, V. Sandoghdar, and M. Agio, “Perfect reflection of light by an oscillating dipole,” *Phys. Rev. Lett.* **101**, 180404 (2008). [4](#), [8](#)
- [21] A. Normatov, B. Spektor, Y. Leviatan, and J. Shamir, “Absorption enhancement by matching the cross-section of plasmonic nanowires to the field structure of tightly focused beams,” *Opt. Express* **19**, 8506 (2011). [4](#)
- [22] X.-W. Chen, V. Sandoghdar, and M. Agio, “Nanofocusing radially-polarized beams for high-throughput funneling of optical energy to the near field,” *Opt. Express* **18**, 10878 (2010). [5](#)
- [23] A. N. Vamivakas, M. Atatüre, J. Dreiser, S. T. Yilmaz, A. Badolato, A. K. Swan, B. B. Goldberg, A. Imamoglu, and M. S. Ünlü, “Strong extinction of a far-field laser beam by a single quantum dot,” *Nano Lett.* **7**, 2892–2896 (2007). [5](#)
- [24] M. K. Tey, Z. Chen, S. A. Aljunid, B. Chng, F. Huber, G. Maslennikov, and

- 
- C. Kurtsiefer, “Strong interaction between light and a single trapped atom without the need for a cavity,” *Nat. Phys.* **4**, 924 (2008). [8](#)
- [25] G. Wrigge, I. Gerhardt, J. Hwang, G. Zumofen, and V. Sandoghdar, “Efficient coupling of photons to a single molecule and the observation of its resonance fluorescence,” *Nat. Phys.* **4**, 6066 (2008). [5](#)
- [26] T. X. Hoang, X. Chen, and C. J. Sheppard, “Multipole theory for tight focusing of polarized light, including radially polarized and other special cases,” *J. Opt. Soc. Am. A* **29**, 32–43 (2012). [5](#), [6](#), [7](#), [8](#), [12](#), [46](#)
- [27] A. G. Curto, G. Volpe, T. H. Taminiau, M. P. Kreuzer, R. Quidant, and N. F. van Hulst, “Unidirectional emission of a quantum dot coupled to a nanoantenna,” *Science* **329**, 930 (2010). [5](#)
- [28] A. G. Curto, T. H. Taminiau, G. Volpe, M. P. Kreuzer, R. Quidant, and N. F. van Hulst, “Multipolar radiation of quantum emitters with nanowire optical antennas,” *Nat. Comm.* **4**, 1 (2013). [5](#)
- [29] L. Novotny and N. van Hulst, “Antennas for light,” *Nat. Phot.* **5**, 83 (2011). [5](#)
- [30] J. Lin, J. P. B. Mueller, Q. Wang, G. Yuan, N. Antoniou, X. Yuan, and F. Capasso, “Polarization-controlled tunable directional coupling of surface plasmon polaritons,” *Science* **340**, 331 (2013). [5](#)
- [31] E. Wolf, “Electromagnetic diffraction in optical systems. I. an integral representation of the image field,” *Proc. R. Soc. London, Ser. A* **253**, 349–357 (1959). [6](#), [8](#), [12](#), [25](#), [36](#), [42](#), [82](#), [83](#), [152](#)
- [32] B. Richards and E. Wolf, “Electromagnetic diffraction in optical systems. ii. structure of the image field in an aplanatic system,” *Proc. R. Soc. London, Ser. A* **253**, 358–379 (1959). [6](#), [11](#), [13](#), [25](#), [26](#), [27](#), [28](#), [82](#), [83](#)
- [33] G. C. Sherman and W. C. Chew, “Aperture and far-field distributions expressed by the debye integral representation of focused fields,” *J. Opt. Soc. Am.* **72**, 1076 (1981). [6](#), [52](#)
- [34] N. G. V. Kampen, “An asymptotic treatment of diffraction problems,” *Physica* **XIV**, 575 (1949). [6](#), [50](#), [52](#)

- 
- [35] G. C. Sherman, J. J. Stannnes, A. J. Devaney, and E. Lalor, “Contribution of the inhomogeneous waves in angular-spectrum representations,” *Opt. Comm.* **8**, 271 (1973). [7](#)
- [36] W. H. Carter, “Bandlimited angular spectrum approximation to a scalar dipole field,” *Opt. Comm.* **2**, 142 (1970). [7](#)
- [37] W. H. Carter, “Bandlimited angular spectrum approximation to a spherical scalar wave field,” *J. Opt. Soc. Am.* **65**, 1054 (1975). [7](#)
- [38] T. X. Hoang, X. Chen, and C. J. Sheppard, “Interpretation of the scattering mechanism for particles in a focused beam,” *Phys. Rev. A* **86**, 033817 (2012). [7](#), [12](#), [24](#)
- [39] T. X. Hoang, X. Chen, and C. J. Sheppard, “Rigorous analytical modeling of high-aperture focusing through a spherical interface,” *J. Opt. Soc. Am. A* **30**, 1426–1440 (2013). [7](#), [24](#), [88](#)
- [40] L. Brillouin, “The scattering cross section of spheres for electromagnetic waves,” *J. Appl. Phys.* **20**, 1110 (1949). [7](#)
- [41] J. A. Lock, “Interpretation of extinction in gaussian-beam scattering,” *J. Opt. Soc. Am. A* **12**, 929 (1995). [7](#)
- [42] J. A. Stratton and H. G. Houghton, “A theoretical investigation of the transmission of light through fog,” *Phys. Rev.* **38**, 159 (1931). [7](#)
- [43] S. J. V. Enk, “Atoms, dipole waves, and strongly focused light beams,” *Phys. Rev. A* **69**, 043813 (2004). [8](#), [13](#)
- [44] N. M. Mojarad, V. Sandoghdar, and M. Agio, “Plasmon spectra of nanospheres under a tightly focused beam,” *J. Opt. Soc. Am. B* **25**, 651658 (2008). [10](#), [76](#)
- [45] J. Lermé, G. Bachelier, P. Billaud, C. Bonnet, M. Broyer, E. Cottancin, S. Marhaba, and M. Pellarin, “Optical response of a single spherical particle in a tightly focused light beam: application to the spatial modulation spectroscopy technique,” *J. Opt. Soc. Am. A* **25**, 493–413 (2008).
- [46] J. Lermé, C. Bonnet, M. Broyer, E. Cottancin, S. Marhaba, and M. Pellarin, “Optical response of metal or dielectric nano-objects in strongly convergent light beams,”

- 
- Phys. Rev. B **77**, 245406 (2008).
- [47] N. M. Mojarad, G. Zumofen, V. Sandoghdar, and M. Agio, “Metal nanoparticles in strongly confined beams: transmission, reflection and absorption,” *J. Eu. Opt. Soc.* **4**, 09014 (2009). [8](#), [10](#), [76](#)
- [48] C. Sönnichsen, S. Geier, N. E. Hecker, G. von Plessen, J. Feldmann, H. Ditlbacher, B. Lamprecht, J. R. Krenn, F. R. Aussenegg, V. Z.-H. Chan, J. P. Spatz, , and M. Möller, “Spectroscopy of single metallic nanoparticles using total internal reflection microscopy,” *Appl. Phys. Lett.* **77**, 2949 (2000). [8](#)
- [49] D. Boyer, P. Tamarat, A. Maali, B. Lounis, and M. Orrit, “Photothermal imaging of nanometer-sized metal particles among scatterers,” *Science* **297**, 1160 (2002).
- [50] K. Lindfors, T. Kalkbrenner, P. Stoller, and V. Sandoghdar, “Detection and spectroscopy of gold nanoparticles using supercontinuum white light confocal microscopy,” *Phys. Rev. Lett.* **93**, 037401 (2004).
- [51] A. Arbouet, D. Christofilos, N. D. Fatti, F. Vallée, J. R. Huntzinger, L. Arnaud, P. Billaud, and M. Broyer, “Direct measurement of the single-metal-cluster optical absorption,” *Phys. Rev. Lett.* **93**, 127401 (2004).
- [52] P. Li, K. Shi, and Z. Liu, “Optical scattering spectroscopy by using tightly focused supercontinuum,” *Opt. Express* **13**, 9039–9044 (2005). [8](#)
- [53] A. J. Devaney and E. Wolf, “Multipole expansions and plane wave representations of the electromagnetic field,” *J. Math. Phys.* **15**, 234–244 (1974). [8](#), [17](#), [19](#), [36](#)
- [54] G. Gouesbet, B. Maheu, and G. Gréhan, “Light scattering from a sphere arbitrarily located in a gaussian beam, using a bromwich formulation,” *J. Opt. Soc. Am. A* **5**, 1427 (1988). [8](#)
- [55] G. Gouesbet and G. Gréhan, *Generalized Lorenz-Mie Theories* (Springer, Berlin, 2011). [61](#)
- [56] B. Maheu, G. Gouesbet, and G. Gréhan, “A concise presentation of the generalized lorenz-mie theory for arbitrary location of the scatterer in an arbitrary incident profile,” *J. Opt. (Paris)* **19**, 59 (1988). [8](#)
- [57] L. V. Lorenz, “Lysbevaegelsen i og uden for en haf plane lysbølger belyst kulge,”

- 
- Vidensk. Selk. Skr. **6**, 1 (1890). [8](#)
- [58] G. Mie, "Beiträge zur optik trüber medien, speziell kolloidaler metallösungen," Ann. Phys. **25**, 377 (1908). [8](#)
- [59] P. J. Debye, "Daselektromagnetis che feld um einen zylinder und die theorie desregenbogens," Phys. Z. **9**, 775 (1908). [8](#), [9](#)
- [60] J. A. Lock and C. L. Adler, "Debye-series analysis of the firstorder rainbow produced in scattering of a diagonally incident plane wave by a circular cylinder," J. Opt. Soc. Am. A **14**, 1316 (1997). [8](#), [9](#)
- [61] R. Li, X. Han, H. Jiang, and K. F. Ren, "Debye series of normally incident plane-wave scattering by an infinite multilayered cylinder," Appl. Opt. **45**, 6255 (2006). [8](#), [9](#)
- [62] R. Li, X. Han, and K. F. Ren, "Generalized debye series expansion of electromagnetic plane wave scattering by an infinite multilayered cylinder at oblique incidence," Phys. Rev. E **79**, 036602 (2009). [9](#)
- [63] R. Li, X. Han, and K. F. Ren, "Debye series expansion of shaped beam scattering by gi-pof," Opt. Commun. **282**, 4315 (2009). [8](#), [9](#)
- [64] B. van der Pol and H. Bremmer, "The diffraction of electromagnetic waves from an electrical point source round a finitely conducting sphere, with applications to radiotelegraphy and the theory of the rainbow," Philos. Mag. **24**, 825 (1937). [8](#)
- [65] E. A. Hovenac and J. A. Lock, "Assessing the contributions of surface waves and complex rays to far-field mie scattering by use of the debye series," J. Opt. Soc. Am. A **9**, 781 (1992). [9](#)
- [66] G. Gouesbet, "Debye series formulation for generalized lorenmie theory with the bromwich method," Part. Part. Syst. Character. **20**, 382 (2003). [8](#), [9](#), [61](#), [79](#)
- [67] B. R. Johnson, "Light scattering by a multilayer sphere," Appl. Opt. **35**, 3286 (2009). [8](#), [9](#)
- [68] J. A. Lock, "Scattering of an electromagnetic plane wave by a luneburg lens. i. ray theory," J. Opt. Soc. Am. A **25**, 2971 (2008).
- [69] J. A. Lock, "Scattering of an electromagnetic plane wave by a luneburg lens. ii.

- 
- wave theory,” J. Opt. Soc. Am. A **25**, 2980 (2008). [9](#)
- [70] J. A. Lock, “Scattering of an electromagnetic plane wave by a luneburg lens. iii. finely stratified sphere model,” J. Opt. Soc. Am. A **25**, 2991 (2008). [8](#), [9](#)
- [71] F. Xu, J. A. Lock, and C. Tropea, “Debye series for light scattering by a spheroid,” J. Opt. Soc. Am. A **27**, 671 (2009). [8](#), [9](#)
- [72] F. Xu, J. A. Lock, and G. Gouesbet, “Debye series for light scattering by a non-spherical particle,” Phys. Rev. A **81**, 043824 (2010). [8](#), [9](#)
- [73] F. Xu, J. A. Lock, G. Gouesbet, and C. Tropea, “Optical stress on the surface of a particle: I. homogeneous sphere,” Phys. Rev. A **79**, 053808 (2009). [9](#)
- [74] V. Khare and H. M. Nussenzveig, “Theory of the rainbow,” Phys. Rev. Lett. **33**, 976–980 (1974). [9](#)
- [75] P. Laven, “Simulation of rainbows, coronas and glories using mie theory and the debye series,” J. Quant. Spectrosc. Radiat. Transfer **89**, 257 (2004). [9](#)
- [76] V. Khare and H. M. Nussenzveig, “Theory of the glory,” Phys. Rev. Lett. **38**, 1279 (1977).
- [77] P. Laven, “How are glories formed?” Appl. Opt. **44**, 5675 (2005). [9](#)
- [78] J. W. T. Grandy, *Scattering of Waves from Large Spheres* (Cambridge University Press, Cambridge, 2000). [9](#), [79](#)
- [79] T. X. Hoang, X. Chen, and C. J. R. Sheppard, “Multipole theory for tight focusing of polarized light with arbitrary radiation pattern: Application to hemispherical solid immersion lens (sil) for subsurface imaging,” in “Advanced Electromagnetics Symposium,” (Paris, France, 2012). [10](#), [61](#)
- [80] S. M. Mansfield and G. S. Kino, “Solid immersion microscope,” Appl. Phys. Lett. **57**, 2615–2616 (1990). [11](#)
- [81] S. H. Goh, C. J. R. Sheppard, A. C. T. Quah, C. M. Chua, L. S. Koh, and J. C. H. Phang, “Design considerations for refractive solid immersion lens: application to subsurface integrated circuit fault localization using laser induced techniques,” Rev. Sci. Instrum. **80**, 013703 (2009). [11](#), [119](#)
- [82] Q. Wu, L. P. Ghislain, and V. B. Elings, “Imaging with solid immersion lenses,

- 
- spatial resolution, and applications,” *Proc. IEEE*. **88**, 1491–1498 (2000). [11](#), [82](#), [106](#)
- [83] E. Ramsey, N. Pleyne, D. Xiao, R. J. Warburton, and D. T. Reid, “Two-photon optical-beam-induced current solid-immersion imaging of a silicon flip chip with a resolution of 325 nm,” *Opt. Lett.* **30**, 26 (2005).
- [84] E. Ramsey, K. A. Serrels, M. J. Thomson, A. J. Waddie, M. R. Taghizaheh, R. J. Warburton, and D. T. Reid, “Three-dimensional nanoscale subsurface optical imaging of silicon circuits,” *Appl. Phys. Lett.* **90**, 131101 (2007).
- [85] K. A. Serrels, E. Ramsay, R. J. Warburton, and D. T. Reid, “Nanoscale optical microscopy in the vectorial focusing regime,” *Nat. Phot.* **2**, 311 (2008). [13](#)
- [86] F. H. Koklu, B. B. Goldberg, and M. S. Ünlü, “Dielectric interface effects in subsurface microscopy of integrated circuits,” *Opt. Commun.* **285**, 1675–1679 (2012). [11](#), [12](#)
- [87] S. B. Ippolito, B. B. Goldberg, and M. S. Ünlü, “Theoretical analysis of numerical aperture increasing lens microscopy,” *J. Appl. Phys.* **97**, 053105 (2005). [11](#)
- [88] Y. Zhang, C. Zheng, and Y. Zou, “Focal-field distribution of the solid immersion lens system with an annular filter,” *Optik* **115**, 277 (2004). [11](#)
- [89] I. Ichimura, S. Hayashi, and G. S. Kino, “High-density optical recording using a solid immersion lens,” *Appl. Opt.* **36**, 4339 (1997). [11](#), [82](#), [85](#), [106](#)
- [90] B. D. Terris, H. J. Mamin, and D. Rugar, “Near-field optical data storage,” *Appl. Phys. Lett.* **68**, 141–143 (1996). [11](#), [13](#)
- [91] Y. Zhang, X. Xu, and Y. Okuno, “Theoretical study of optical recording with a solid immersion lens illuminated by focused double-ring-shaped radially-polarized beam,” *Opt. Commun.* **282**, 4481–4485 (2009). [11](#)
- [92] L. P. Ghislain, V. B. Elings, K. B. Crozier, S. R. Manalis, S. C. Minne, K. Wilder, G. S. Kino, and C. F. Quate, “Near-field photolithography with a solid immersion lens,” *Appl. Phys. Lett.* **74**, 501–503 (1999). [11](#), [13](#)
- [93] S. H. Goh and C. J. R. Sheppard, “High aperture focusing through a spherical interface: Application to refractive solid immersion lens (rsil) for subsurface imaging,”

- 
- Opt. Comm. **282**, 1036–1041 (2009). [11](#), [12](#)
- [94] K. M. Lim, G. C. F. Lee, C. J. R. Sheppard, J. C. H. Phang, C. L. Wong, and X. Chen, “The effect of polarization on a solid immersion lens of arbitrary thickness,” *J. Opt. Soc. Am. A* **28**, 903–911 (2011). [12](#)
- [95] L. E. Helseth, “Roles of polarization, phase and amplitude in solid immersion lens systems,” *Opt. Commun.* **191**, 161 (2001). [11](#)
- [96] A. S. van de Nes, L. Billy, S. F. Pereira, and J. J. M. Braat, “Calculation of the vectorial field distribution in a stratified focal region of a high numerical aperture imaging system,” *Opt. Express* **12**, 1281–1293 (2004).
- [97] K. Huang and Y. Li, “Realization of a subwavelength focused spot without longitudinal field component in solid immersion lens-based system,” *Opt. Lett.* **36**, 3536–3538 (2011). [11](#)
- [98] L. Hu, R. Chen, K. Agarwal, C. J. R. Sheppard, J. C. H. Phang, and X. Chen, “Dyadic green’s function for aplanatic solid immersion lens based sub-surface microscopy,” *Opt. Express* **19**, 19280–19295 (2011).
- [99] R. Chen, K. Agarwal, C. J. R. Sheppard, J. C. H. Phang, and X. Chen, “Resolution of aplanatic solid immersion lens based microscopy,” *J. Opt. Soc. Am. A* **29**, 1059–1070 (2012).
- [100] R. Chen, K. Agarwal, C. J. R. Sheppard, J. C. H. Phang, and X. Chen, “Complete modeling of subsurface microscopy system based on aplanatic solid immersion lens,” *J. Opt. Soc. Am. A* **29**, 2350 (2012). [11](#), [95](#)
- [101] C. J. R. Sheppard and S. H. Goh, “Comment on ‘theoretical analysis of numerical aperture increasing lens microscopy’ [*J. appl. phys.* 97, 053105 (2005)],” *J. Appl. Phys.* **100**, 086108 (2006). [12](#), [93](#)
- [102] M. S. Ünlü, S. B. Ippolito, A. N. Vamivakas, and B. B. Goldberg, “Response to ‘comment on theoretical analysis of numerical aperture increasing lens microscopy’,” *J. Appl. Phys.* **100**, 086109 (2006). [12](#)
- [103] A. N. Vamivakas, R. D. Younger, B. B. Goldberg, A. K. S. M. S. Unlu, E. R. Behringer, and S. B. Ippolito, “A case study for optics: The solid immersion mi-

- croscopie,” *Am. J. Phys.* **76**, 758–768 (2008). [12](#), [27](#), [82](#)
- [104] P. Török, P. Varga, Z. Laczik, and G. R. Booker, “Electromagnetic diffraction of light focused through a planar interface between materials of mismatched refractive indices: an integral representation,” *J. Opt. Soc. Am. A* **12**, 325–332 (1995). [12](#)
- [105] S. S. Sherif, M. R. Foreman, and P. Török, “Eigenfunction expansion of the electric fields in the focal region of a high numerical aperture focusing system,” *Opt. Express* **16**, 3397 (2008). [12](#)
- [106] M. R. Foreman, S. S. Sherif, P. R. T. Munro, and P. Török, “Inversion of the debyewolf diffraction integral using an eigenfunction representation of the electric fields in the focal region,” *Opt. Express* **16**, 4901–4917 (2008). [12](#), [128](#)
- [107] N. Bokor and N. Davidson, “Toward a spherical spot distribution with 4 pi focusing of radially polarized light,” *Opt. Lett.* **29**, 1968–1970 (2004). [13](#)
- [108] C. J. Sheppard, “Electromagnetic field in focal region of wide-angular annular lens and mirror systems,” *IEE J. Microw. Opt. Acous.* **2**, 163–166 (1978).
- [109] C. J. Sheppard and P. Torok, “Electromagnetic field in the focal region of an electric dipole wave,” *Optik* **104**, 175–177 (1997). [49](#), [57](#)
- [110] C. J. Sheppard and P. Torok, “Efficient calculation of electromagnetic diffraction in optical systems using a multipole expansion,” *J. Mod. Opt.* **44**, 803–818 (1997). [13](#), [56](#)
- [111] L. Novotny, M. R. Beversluis, K. S. Youngworth, and T. G. Brown, “Longitudinal field modes probed by single molecules,” *Phys. Rev. Lett.* **86**, 5251–5254 (2001). [13](#)
- [112] T. Kuga, Y. Torii, N. Shiokawa, T. Hirano, Y. Shimizu, and H. Sasada, “Novel optical trap of atoms with a doughnut beam,” *Phys. Rev. Lett.* **78**, 4713–4716 (1997). [13](#)
- [113] A. A. Asatryan, C. J. Sheppard, and C. M. D. Sterke, “Vector treatment of second-harmonic generation produced by tightly focused vignetted gaussian beams,” *J. Opt. Soc. Am. B* **21**, 2206–2212 (2004). [13](#)
- [114] R. Dorn, S. Quabis, and G. Leuchs, “The focus of light-linear polarization breaks

- the rotational symmetry of the focal spot,” *J. Mod. Opt.* **50**, 1917 (2003). [13](#)
- [115] X. Hao, C. Kuang, T. Wang, and X. Liu, “Phase encoding for sharper focus of the azimuthally polarized beam,” *Opt. Lett.* **35**, 3928 (2010). [13](#), [43](#)
- [116] C. J. Sheppard and A. Choudhury, “Annular pupils, radial polarization, and super-resolution,” *Appl. Opt.* **43**, 4322–4327 (2004). [13](#)
- [117] H. Wang, L. Shi, B. Lukyanchuk, C. J. Sheppard, and C. T. Chong, “Creation of a needle of longitudinally polarized light in vacuum using binary optics,” *Nat. Phot.* **2**, 501 (2008). [13](#), [129](#), [130](#)
- [118] E. T. Rogers, J. Lindberg, T. Roy, S. Savo, J. E. Chad, M. R. Dennis, and N. I. Zheludev, “A super-oscillatory lens optical microscope for subwavelength imaging,” *Nat. Mat.* **11**, 432 (2012). [13](#), [129](#)
- [119] A. Erdélyi, “Zur theorie der kugelwellen von artur erdélyi,” *Physica* **IV**, 107–120 (1937). [17](#)
- [120] A. J. Devaney and G. C. Sherman, “Plane-wave representations for scalar wave fields,” *Siam Review* **15**, 765–786 (1973). [17](#), [19](#), [23](#)
- [121] M. Nieto-Vesperinas, *Scattering and Diffraction in Physical Optics* (World Scientific, Singapore, 2006). [19](#)
- [122] C. Brosseau, *Fundamentals of Polarized Light: A Statistical Optics Approach* (Wiley, New York, 1998). [21](#)
- [123] Y. D. Chong, L. Ge, H. Cao, and A. D. Stone, “Coherent perfect absorbers: Time-reversed lasers,” *Phys. Rev. Lett.* **105**, 053901 (2010). [21](#)
- [124] W. Wan, Y. Chong, L. Ge, H. Noh, A. D. Stone, and H. Cao, “Time-reversed lasing and interferometric control of absorption,” *Science* **331**, 889–892 (2011). [21](#), [126](#)
- [125] T. X. Hoang, X. Chen, and C. J. Sheppard, “Multipole and plane wave expansions of diverging and converging fields,” *Opt. Express* **22**, 8949–8961 (2014). [22](#)
- [126] P. Grahn, A. Shevchenko, and M. Kaivola, “Electromagnetic multipole theory for optical nanomaterials,” *New J. Phys.* **14**, 093033 (2012). [24](#)
- [127] G. Molina-Terriza, “Determination of the total angular momentum of a paraxial beam,” *Phys. Rev. A* **78**, 053819 (2008). [24](#)

- 
- [128] R. Martínez-Herrero and P. M. Mejías, “Angular momentum decomposition of non-paraxial light beams,” *Opt. Express* **18**, 7965 (2010).
- [129] X. Zambrana-Puyalto, X. Vidal, and G. Molina-Terriza, “Excitation of single multipolar modes with engineered cylindrically symmetric fields,” *Opt. Express* **20**, 24536 (2012). [24](#)
- [130] R. Borghi, “On the angular-spectrum representation of multipole wave fields,” *J. Opt. Soc. Am. A* **21**, 1805–1810 (2004). [24](#)
- [131] H. F. Arnoldus, “Angular spectrum representation of the electromagnetic multipole fields, and their reflection at a perfect conductor,” *Surf. Sci.* **590**, 101–116 (2005). [25](#)
- [132] C. J. R. Sheppard, J. Lin, and S. S. Kou, “Rayleigh-sommerfeld diffraction formula in  $k$  space,” *J. Opt. Soc. Am. A* **30**, 1180–1183 (2013). [25](#)
- [133] R. N. Bracewell, *The Fourier Transform and Its Applications* (McGraw-Hill Book Company, New York, 1965). [30](#)
- [134] J. W. Goodman, *Introduction to Fourier Optics* (McGraw-Hill Book Company, New York, 1968). [30](#)
- [135] T. Nieminen, H. Rubinsztein-Dunlop, and N. Heckenberg, “Multipole expansion of strongly focussed laser beams,” *J. Quant. Spectrosc. Radiat. Transfer* **79**, 1005–1017 (2003). [37](#), [129](#)
- [136] C. J. R. Sheppard, N. K. Balla, and S. Rehman, “Performance parameters for highly-focused electromagnetic waves,” *Opt. Commun.* **282**, 727–734 (2009). [46](#), [57](#)
- [137] W. K. H. Panofsky and M. Phillips, *Classical Electricity and Magnetism: Second Edition* (Wiley, 1962). [48](#)
- [138] C. J. R. Sheppard and E. Y. S. Yew, “Performance parameters for focusing of radial polarization,” *Opt. Lett.* **33**, 497–499 (2008). [48](#), [49](#)
- [139] C. J. R. Sheppard and K. G. Larkin, “Optimal concentration of electromagnetic radiation,” *J. mod. Optics* **41**, 1495–1505 (1994). [49](#), [56](#)
- [140] C. J. R. Sheppard and S. Saghafi, “Transverse-electric and transverse-magnetic

- 
- beam modes beyond the paraxial approximation,” *Opt. Lett.* **24**, 1543–1545 (1999). [55](#)
- [141] C. J. R. Sheppard and S. Rehman, “Highly convergent focusing of light based on rotating dipole polarization,” *App. Opt.* **50**, 4463–4467 (2011). [55](#)
- [142] J. J. Stamnes and V. Dhayalan, “Focusing of electric dipole waves,” *Pure. Appl. Opt.* **5**, 195 (1996). [57](#)
- [143] C. J. Sheppard, “Fundamentals of superresolution,” *Micron* **38**, 772 (2007). [57](#)
- [144] J. A. Kong, *Electromagnetic Wave Theory* (EMW Publishing, Cambridge, Massachusetts, USA, 2008). [61](#)
- [145] G. Gouesbet, “Rigorous justification of the localized approximation to the beam shape coefficients in generalized lorenzmie theory. ii. off-axis beams,” *J. Opt. Soc. Am. A* **11**, 2516 (1994). [61](#)
- [146] G. Gouesbet, J. A. Lock, and G. Gréhan, “Partial wave representations of laser beams for use in light scattering calculations,” *Appl. Opt.* **34**, 2133 (1995).
- [147] G. Gouesbet, “Partial wave expansions and properties of axisymmetric light beams,” *Appl. Opt.* **35**, 1543 (1996).
- [148] G. Gouesbet, “Higher-order descriptions of gaussian beams,” *J. Opt. (Paris)* **27**, 35 (1996).
- [149] A. Doicu and T. Wriedt, “Computation of the beam-shapecoefficients in the generalized lorenzmie theory by using the translational addition theorem for spherical vector wave functions,” *Appl. Opt.* **36**, 2971 (1997). [61](#)
- [150] C. C. Lu and W. C. Chew, “A multilevel algorithm for solving a boundary integral equation of wave scattering,” *Microw. Opt. Techn. Lett.* **7**, 466–470 (1994). [64](#)
- [151] J. M. Song and W. C. Chew, “Multilevel fast-multipole algorithm for solving combined field integral equations of electromagnetic scattering,” *Microw. Opt. Techn. Lett.* **10**, 14–19 (1995).
- [152] L. Greengard and V. Rokhlin, “A new version of the fast multipole method for the laplace equation in three dimensions,” *Acta. Numerica.* **6**, 229–269 (1997).
- [153] W. C. Chew, J. M. Jin, E. Michielssen, and J. M. Song, *Fast and Efficient Algo-*

- 
- rithms in Computational Electromagnetics* (Artech House, Boston, MA, 2001).
- [154] H. Cheng, W. Y. Crutchfield, Z. G. butas, L. F. Greengard, J. F. Ethridge, J. Huang, V. Rokhlin, N. Y. Arvin, and J. Zhao, “A wideband fast multipole method for the helmholtz equation in three dimensions,” *J. Comput. Phys.* **216**, 300–325 (2006). [64](#)
- [155] B. Friedman and J. Russek, “Addition theorems for spherical waves,” *Quart. Appl. Math.* **12**, 13–23 (1954). [64](#)
- [156] S. Stein, “Addition theorems for spherical wave functions,” *Quart. Appl. Math.* **19**, 15–24 (1961). [64](#)
- [157] O. R. Cruzan, “Translational addition theorems for spherical vector wave functions,” *Quart. Appl. Math.* **20**, 33–40 (1962). [64](#)
- [158] J. H. Bruning and Y. T. Lo, “Multiple scattering of em waves by spheres, part i multipole expansion and ray-optical solutions,” *IEEE Trans. Antennas Propagat.* **19**, 378–390 (1971). [65](#)
- [159] F. Borghese, P. D. Ti, G. T. Oscano, and O. I. Sindoni, “An addition theorem for vector helmholtz harmonics,” *J. Math. Phys.* **21**, 2754–2755 (1980).
- [160] B. U. Felderhof and R. B. Jones, “Addition theorems for spherical wave solutions of the vector helmholtz equation,” *J. Math. Phys.* **28**, 836–839 (1987).
- [161] R. C. Wittmann, “Spherical wave operators and the translation formulas,” *IEEE Trans. Antennas Propagat.* **36**, 1078–1087 (1988).
- [162] W. C. Chew, *Waves and Fields in Inhomogeneous Media* (IEEE Press, 1995). [65](#)
- [163] W. C. Chew, “Recurrence relations for three-dimensional scalar addition theorem,” *J. Elect. Wave. Appl.* **6**, 133–142 (1992). [65](#), [153](#), [154](#)
- [164] W. C. Chew and Y. M. Wang, “Efficient ways to compute the vector addition theorem,” *J. Elect. Wave. Appl.* **7**, 651–665 (1993). [65](#), [153](#), [155](#), [156](#)
- [165] K. T. Kim, “Efficient recursive generation of the scalar spherical multipole translation matrix,” *IEEE Trans. Antenna Propagat.* **55**, 3484–3494 (2007). [65](#)
- [166] K. T. Kim, “Symmetry relations of the translation coefficients of the scalar and vector spherical multipole fields,” *Progress In Electromagnetics Research PIER*

- 
- 48, 45–66 (2004). [65](#)
- [167] W. C. Chew, “Vector addition theorem and its diagonalization,” *Commun. Comput. Phys.* **3**, 330–341 (2008). [65](#)
- [168] H. C. van de Hulst, *Light Scattering by Small Particles* (Dover, New York, 1981). [76](#), [128](#)
- [169] M. S. Kim, T. Scharf, M. T. Haq, W. Nakagawa, and H. P. Herzig, “Subwavelength-size solid immersion lens,” *Opt. Lett.* **36**, 3930 (2011). [88](#), [129](#)
- [170] D. R. Mason, M. V. Jouravlev, and K. S. Kim, “Enhanced resolution beyond the abbe diffraction limit with wavelength-scale solid immersion lenses,” *Opt. Lett.* **35**, 2007 (2010). [129](#)
- [171] A. Vlad, I. Huynen, and S. Melinte, “Wavelength-scale lens microscopy via thermal reshaping of colloidal particles,” *Nanotechnology* **23**, 285708 (2012). [88](#)
- [172] R. Chen, K. Agarwal, C. J. R. Sheppard, J. C. H. Phang, and X. Chen, “A complete and computationally efficient numerical model of aplanatic solid immersion lens scanning microscope,” *Opt. Express* **21**, 14316 (2013). [95](#)
- [173] K. Agarwal, R. Chen, L. S. Koh, C. J. Sheppard, J. C. Phang, and X. Chen, “Experimental validation of the computational model of aplanatic solid immersion lens scanning microscope,” in “Focus On Microscopy,” (Maastricht, The Netherlands, 2013). [95](#)
- [174] R. Chen, K. Agarwal, C. J. R. Sheppard, and X. Chen, “Imaging using cylindrical vector beams in a high numerical-aperture microscopy system,” *Opt. Lett.* **38**, 3111 (2013). [119](#)
- [175] T. X. Hoang, R. Chen, K. Agarwal, C. J. Sheppard, and X. Chen, “Imaging with annular focusing through a dielectric interface,” in “Focus On Microscopy,” (Sydney, Australia, 2014). [125](#)
- [176] G. Gouesbet, G. Gréhan, and B. Maheu, “Localized interpretation to compute all the coefficients  $g_l^m$  in the generalized lorenz-mie theory,” *J. Opt. Soc. Am. A* **7**, 998 (1990). [128](#)
- [177] Y. Duan, G. Barbastathis, and B. Zhang, “Classical imaging theory of a microlens

- with super-resolution,” *Opt. Lett.* **38**, 2988 (2013). [129](#)
- [178] Z. Wang, W. Guo, L. Li, B. Lukyanchuk, A. Khan, Z. Liu, Z. Chen, and M. Hong, “Optical virtual imaging at 50 nm lateral resolution with a white-light nanoscope,” *Nat. Commun.* **2**, 218 (2011). [129](#)
- [179] Z. L. Liao, “Annular solid-immersion lenslet array super-resolution optical microscopy,” *J. Appl. Phys.* **112**, 083110 (2012). [130](#)
- [180] C. Ma and Z. Liu, “Focusing light into deep subwavelength using metamaterial immersion lenses,” *Opt. Express* **18**, 4838 (2010). [131](#)
- [181] G. Zheng, R. Zhang, S. Li, P. He, H. Zhou, and Y. Shi, “A hyperlens-embedded solid immersion lens for beam focusing beyond the diffraction limit,” *IEEE Phot. Tech. Lett.* **23**, 1234 (2011). [131](#)

# Appendix A

Let's define  $s_x = \frac{k_x}{k}$ ,  $s_y = \frac{k_y}{k}$ ,  $s_z = \frac{k_z}{k}$ ;  $u_x = \frac{x}{r}$ ,  $u_y = \frac{y}{r}$ ,  $u_z = \frac{z}{r}$ . We have:

$$k_x x + k_y y + k_z z = kr(s_x u_x + s_y u_y + s_z u_z) = kr f(s_x, s_y) \quad (1)$$

where  $f(s_x, s_y) = s_x u_x + s_y u_y + s_z u_z$  is a function of  $s_x$  and  $s_y$  only since  $s_z$  is a function of  $s_x$  and  $s_y$ . As we observe from Eq. (3.15), we need to know  $\hat{\mathbf{E}}(k_x, k_y; 0)$  to evaluate the focal field. To derive  $\hat{\mathbf{E}}(k_x, k_y; 0)$  in terms of the incident field, we will consider the field expressed by Eq. (3.15) at the far region. Substituting Eq. (1) into Eq. (3.15), we obtain the field at the far region as follows

$$\bar{E}(x_\infty, y_\infty, z_\infty) = \iint_{s_x^2 + s_y^2 \leq 1} \hat{\mathbf{E}}(ks_x, ks_y; 0) e^{ikr_\infty f(s_x, s_y)} k^2 ds_x ds_y. \quad (2)$$

It is seen that Eq. (2) has the form of

$$F(k) = \iint_D h(x, y) e^{ikg(x, y)} dx dy, \quad (3)$$

where  $h(x, y)$  and  $g(x, y)$  are assumed to be real valued, well-behaved functions of two real variables  $x$  and  $y$ .  $D$  is simply a two dimensional region with a smooth boundary  $C$ . To evaluate the integration in Eq. (3), we can apply the stationary phase method in which we assume that there is only one critical point in the region  $D$  at which the function  $g(x, y)$  is stationary. Then, the principle of the stationary phase states that for a sufficiently large value of  $k$ , the term  $e^{ikg(x, y)}$  oscillates so rapidly across the domain of integration  $D$  that the negative and positive values of the integrand around each point cancel each other except in the proximity of the critical point. This means the value of  $F(k)$  can be approximated by taking the double integrations in a small region around the

critical point only.

To continue, we find the stationary point. We assume that a point of stationary phase at  $(s_x^0, s_y^0, s_z^0)$  exists, hence we have

$$\left. \frac{\partial f(s_x, s_y)}{\partial s_x} \right|_{s_x^0, s_y^0} = 0, \quad (4)$$

$$\left. \frac{\partial f(s_x, s_y)}{\partial s_y} \right|_{s_x^0, s_y^0} = 0. \quad (5)$$

We know

$$\begin{aligned} f(s_x, s_y) &= s_x u_x + s_y u_y + s_z u_z \\ &= s_x u_x + s_y u_y + \sqrt{1 - s_x^2 - s_y^2} u_z. \end{aligned} \quad (6)$$

Substituting Eq. (6) into Eqs. (4) and (5), we obtain

$$u_x + u_z \left( -\frac{s_x^0}{s_z^0} \right) = 0, \quad (7)$$

$$u_y + u_z \left( -\frac{s_y^0}{s_z^0} \right) = 0. \quad (8)$$

Equations (7) and (8) lead to

$$\frac{s_x^0}{u_x} = \frac{s_y^0}{u_y} = \frac{s_z^0}{u_z} = b \quad (9)$$

$$\Rightarrow b^2 = \left( \frac{s_x^0}{u_x} \right)^2 = \left( \frac{s_y^0}{u_y} \right)^2 = \left( \frac{s_z^0}{u_z} \right)^2 = \frac{(s_x^0)^2 + (s_y^0)^2 + (s_z^0)^2}{u_x^2 + u_y^2 + u_z^2} = 1. \quad (10)$$

Equation (10) leads to  $b = \pm 1$ . The correct value of  $b$  should be obtained by considering the signs of  $s_z^0$  and  $u_z$ . In the region of  $z \rightarrow -\infty$ , we have  $u_z < 0$  and  $s_z^0 > 0$  since the wave is traveling toward the origin. Hence, we conclude  $b = -1$ . Equation (9) becomes

$$\frac{s_x^0}{u_x} = \frac{s_y^0}{u_y} = \frac{s_z^0}{u_z} = -1. \quad (11)$$

Equation (11) means that, for each position  $(x, y, z)$ , there exists only one corresponding stationary phase point. Moreover, the main contribution to the double integrations in Eq. (2) is due to the neighborhood of the stable point and the angular spectrum  $\hat{\mathbf{E}}(ks_x, ks_y; 0)$  in the neighborhood of the stable point is approximated to be  $\hat{\mathbf{E}}(ks_x, ks_y; 0) \approx \hat{\mathbf{E}}(ks_x^0, ks_y^0; 0)$ .

Hence, we can rewrite Eq. (2) as follows

$$\bar{E}(x_\infty, y_\infty, z_\infty) = k^2 \hat{\mathbf{E}}(ks_x^0, ks_y^0; 0) \iint_{-\infty}^{+\infty} e^{ikr_\infty f(s_x, s_y)} ds_x ds_y. \quad (12)$$

Next, we expand the function  $f(s_x, s_y)$  around the point of stationary phase in accordance to Taylor's expansion theorem. Since the first order derivation of  $f(s_x, s_y)$  at the stable point is zero and only the neighborhood of the stationary phase point contributes to the double integrations, we take into account the second order derivations of  $f(s_x, s_y)$  only. Taylor expansion of  $f(s_x, s_y)$  around  $(s_x^0, s_y^0)$  is

$$\begin{aligned} f(s_x, s_y) \approx & f(s_x^0, s_y^0) + \frac{1}{2}[f_{xx}(s_x^0, s_y^0)](s_x - s_x^0)^2 + [f_{xy}(s_x^0, s_y^0)](s_x - s_x^0)(s_y - s_y^0) \\ & + \frac{1}{2}[f_{yy}(s_x^0, s_y^0)](s_y - s_y^0)^2. \end{aligned} \quad (13)$$

From Eqs. (6) and (11), we have:

$$f_{xx}(s_x^0, s_y^0) = \left(1 + \frac{(s_x^0)^2}{(s_z^0)^2}\right), \quad (14)$$

$$f_{yy}(s_x^0, s_y^0) = \left(1 + \frac{(s_y^0)^2}{(s_z^0)^2}\right), \quad (15)$$

$$f_{xy}(s_x^0, s_y^0) = \frac{s_x^0 s_y^0}{(s_z^0)^2}. \quad (16)$$

Substituting Eq. (13) into Eq. (12) we obtain

$$\bar{E}(x_\infty, y_\infty, z_\infty) \approx k^2 \hat{\mathbf{E}}(ks_x^0, ks_y^0; 0) e^{ikr_\infty f(s_x^0, s_y^0)} \iint_{-\infty}^{+\infty} e^{\frac{ikr_\infty}{2}(f_{xx}\alpha^2 + 2f_{xy}\alpha\beta + f_{yy}\beta^2)} d\alpha d\beta, \quad (17)$$

where  $f_{xx} = f_{xx}(s_x^0, s_y^0)$ ,  $f_{yy} = f_{yy}(s_x^0, s_y^0)$ ,  $f_{xy} = f_{xy}(s_x^0, s_y^0)$ ,  $\alpha = s_x - s_x^0$ , and  $\beta = s_y - s_y^0$ . We can see that the integration in Eq. (17) is similar to a Gaussian type function. We can evaluate the integration as follows:

1. First, we consider the integration of a Gaussian type function:  $G = \int_{-\infty}^{+\infty} e^{-x^2} dx$ ,

we have:

$$\begin{aligned}
 G^2 &= \int_{-\infty}^{+\infty} e^{-x^2} dx \int_{-\infty}^{+\infty} e^{-y^2} dy \\
 &= \iint_{-\infty}^{+\infty} e^{-x^2-y^2} dx dy \\
 &= \int_0^{2\pi} \int_0^{+\infty} e^{-r^2} r dr d\phi = \pi.
 \end{aligned}$$

The calculation of  $G$  has been done by substituting Cartesian coordinates  $(x, y)$  by cylindrical coordinates  $(r, \phi)$ .

2. Second, we consider the integration  $F = \iint_{-\infty}^{+\infty} e^{-(Ax^2+Bxy+Cy^2)} dx dy$ .

$$\begin{aligned}
 F &= \int_{-\infty}^{+\infty} \left[ \int_{-\infty}^{+\infty} e^{-A(x+\frac{B}{2A}y)^2} dx \right] e^{-(C-\frac{B^2}{4A})y^2} dy \\
 &= \int_{-\infty}^{+\infty} \left[ \frac{1}{\sqrt{A}} \int_{-\infty}^{+\infty} e^{-(\sqrt{A}x+\frac{B}{2\sqrt{A}}y)^2} d(\sqrt{A}x + \frac{B}{2\sqrt{A}}y) \right] e^{-(C-\frac{B^2}{4A})y^2} dy \\
 &= \int_{-\infty}^{+\infty} \left[ \sqrt{\frac{\pi}{A}} \right] \frac{1}{\sqrt{C-\frac{B^2}{4A}}} e^{-(C-\frac{B^2}{4A})y^2} d(\sqrt{C-\frac{B^2}{4A}}y) \\
 &= \sqrt{\frac{\pi}{A}} \sqrt{\frac{\pi}{C-\frac{B^2}{4A}}}.
 \end{aligned}$$

3. Now, the integration in Eq. (17) is easily evaluated using the result of  $F$  integration

$$\text{with } A = -\frac{ikr_\infty}{2} \left( 1 + \frac{(s_x^0)^2}{(s_z^0)^2} \right), \quad B = -ikr_\infty \frac{s_x^0 s_y^0}{(s_z^0)^2}, \quad C = -\frac{ikr_\infty}{2} \left( 1 + \frac{(s_y^0)^2}{(s_z^0)^2} \right)$$

$$\Rightarrow F = \frac{2\pi s_z^0}{-ikr_\infty}. \text{ Or we have}$$

$$\iint_{-\infty}^{+\infty} e^{\frac{ikr_\infty}{2}(f_{xx}\alpha^2+2f_{xy}\alpha\beta+f_{yy}\beta^2)} d\alpha d\beta = \frac{2\pi s_z^0}{-ikr_\infty}. \quad (18)$$

Substituting Eq. (18) into Eq. (17), we obtain

$$\begin{aligned}
 \bar{E}(x_\infty, y_\infty, z_\infty) &\approx k^2 \hat{\mathbf{E}}(ks_x^0, ks_y^0; 0) e^{ikr_\infty f(s_x^0, s_y^0)} \frac{2\pi s_z^0}{-ikr_\infty}, \\
 &\approx 2\pi i k s_z^0 \frac{e^{-ikr_\infty}}{r_\infty} \hat{\mathbf{E}}(ks_x^0, ks_y^0; 0)
 \end{aligned} \quad (19)$$

where  $f(s_x^0, s_y^0) = s_x^0 u_x + s_y^0 u_y + s_z^0 u_z = -u_x^2 - u_y^2 - u_z^2 = -1$ .

The relationship in Eq. (19) can be interpreted in terms of plane wave representation or spherical wave representation [31]. To get an insightful understanding about Eq. (19), we go back to the starting point which is Eq. (3.14). Equation (3.14) expands the electric field in terms of an infinite number of plane waves. Each individual plane wave travels with the direction of  $(k_x, k_y, k_z)$  and the amplitude of  $\hat{\mathbf{E}}(k_x, k_y; 0)$ . The amplitude  $\hat{\mathbf{E}}(k_x, k_y; 0)$  can be obtained from Eq. (19). We rewrite Eq. (19) as follows:

$$\hat{\mathbf{E}}(k_x^0, k_y^0; 0) = -\frac{ir_\infty e^{ikr_\infty}}{2\pi k_z^0} \bar{E}(x_\infty, y_\infty, z_\infty). \quad (20)$$

We stop for a while to think about  $(x_\infty, y_\infty, z_\infty)$ . From Eq. (11), we obtain  $x_\infty = -\frac{k_x^0}{k} r_\infty$ ,  $y_\infty = -\frac{k_y^0}{k} r_\infty$ , and  $z_\infty = -\frac{k_z^0}{k} r_\infty$ . Noting that  $k_z^0$  is a function of  $k_x^0$  and  $k_y^0$ , we rewrite Eq. (20) as follows:

$$\hat{\mathbf{E}}(k_x^0, k_y^0; 0) = -\frac{ir_\infty e^{ikr_\infty}}{2\pi k_z^0} \bar{E}(k_x^0, k_y^0). \quad (21)$$

The physical meaning behind Eq. (21) is that, at a given point in the far region, only one individual plane wave is sufficient to describe the field. Hence, without loss of generality, Eq. (21) can be rewritten as follows:

$$\hat{\mathbf{E}}(k_x, k_y; 0) = -\frac{ir_\infty e^{ikr_\infty}}{2\pi k_z} \bar{E}(k_x, k_y). \quad (22)$$

# Appendix B

This appendix derives the translational coefficients for translating electromagnetic field among different coordinate systems. We employ the recurrence relations derived by Chew for both scalar and vector addition theorems [163, 164]. Since we use different definitions for the multipole fields, we need mathematically manipulate Chew's results to obtain the recurrence relations for our definitions. We also derive some useful expressions and discuss some symmetrical relations of the translation coefficients which help to reduce computational load in this appendix.

## Scalar addition theorem

The scalar addition theorem translates a spherical scalar multipole field  $\Psi_l^m(\bar{r}) = h_l^{(2)}(kr)Y_l^m(\theta, \phi)$  from  $O$  coordinates to  $O'$  coordinates as shown in Fig. (5.1). Let's denote  $\bar{r}'' = O\bar{O}'$ , we have  $\bar{r} = \bar{r}'' + \bar{r}'$ . Then the theorem can be described as follows:

$$\Psi_l^m(\bar{r}) = \sum_{l'=0}^{\infty} \sum_{m'=-l'}^{l'} \Psi_{l'}^{m'}(\bar{r}') \alpha_{l'm'}^{lm}, \quad (23)$$

where  $\Psi_{l'}^{m'}(\bar{r}')$  and  $\alpha_{l'm'}^{lm}$  depend on the translational vector  $\bar{r}'' = \bar{r} - \bar{r}'$ :

$$\Psi_{l'}^{m'}(\bar{r}') = \begin{cases} h_{l'}^{(2)}(kr')Y_{l'}^{m'}(\theta', \phi'), & r'' < r' \\ j_{l'}(kr')Y_{l'}^{m'}(\theta', \phi'), & r'' > r' \end{cases}$$

Applying the following differential operators to Eq. (23)

$$\begin{aligned}\frac{\partial}{\partial x} &= \sin \theta \cos \phi \frac{\partial}{\partial r} + \frac{\cos \theta \cos \phi}{r} \frac{\partial}{\partial \theta} - \frac{\sin \phi}{r \sin \theta} \frac{\partial}{\partial \phi}, \\ \frac{\partial}{\partial y} &= \sin \theta \sin \phi \frac{\partial}{\partial r} + \frac{\cos \theta \sin \phi}{r} \frac{\partial}{\partial \theta} + \frac{\cos \phi}{r \sin \theta} \frac{\partial}{\partial \phi}, \\ \frac{\partial}{\partial z} &= \cos \theta \frac{\partial}{\partial r} - \frac{\sin \theta}{r} \frac{\partial}{\partial \theta},\end{aligned}$$

$$\begin{aligned}C_{\pm} &= \frac{\partial}{\partial x} \pm i \frac{\partial}{\partial y} \\ &= e^{\pm i \phi} \left[ \sin \theta \frac{\partial}{\partial r} + \frac{\cos \theta}{r} \frac{\partial}{\partial \theta} \pm \frac{i}{r \sin \theta} \frac{\partial}{\partial \phi} \right],\end{aligned}$$

we can calculate  $\alpha_{l'm'}^{lm}$  recursively from  $\alpha_{l'm'}^{00}$  by the following equations [163]:

$$\alpha_{l'm'}^{00} = \begin{cases} (-1)^{l'+m'} \sqrt{4\pi} j_{l'}(kr'') Y_{l'}^{-m'}(\theta'', \phi''), & r'' < r' \\ (-1)^{l'+m'} \sqrt{4\pi} h_{l'}^{(2)}(kr'') Y_{l'}^{-m'}(\theta'', \phi''), & r'' > r' \end{cases}$$

$$a_{lm}^+ \alpha_{l'm'}^{l+1,m} = -a_{lm}^- \alpha_{l'm'}^{l-1,m} + a_{l'-1,m'}^+ \alpha_{l'-1,m'}^{lm} + a_{l'+1,m'}^- \alpha_{l'+1,m'}^{lm}, \quad (24)$$

$$b_{lm}^+ \alpha_{l'm'}^{l+1,m+1} = -b_{lm}^- \alpha_{l'm'}^{l-1,m+1} + b_{l'-1,m'-1}^+ \alpha_{l'-1,m'-1}^{lm} + b_{l'+1,m'-1}^- \alpha_{l'+1,m'-1}^{lm}, \quad (25)$$

where  $a_{lm}^+ = -\sqrt{\frac{(l+m+1)(l-m+1)}{(2l+1)(2l+3)}}$ ,  $a_{lm}^- = \sqrt{\frac{(l+m)(l-m)}{(2l+1)(2l-1)}}$ ,  $b_{lm}^- = \sqrt{\frac{(l-m)(l-m-1)}{(2l+1)(2l-1)}}$ , and  $b_{lm}^+ = \sqrt{\frac{(l+m+2)(l+m+1)}{(2l+1)(2l+3)}}$ .

In the case of  $m = l$ , Eq. (25) reduces to

$$b_{ll}^+ \alpha_{l'm'}^{l+1,l+1} = b_{l'-1,m'-1}^+ \alpha_{l'-1,m'-1}^{ll} + b_{l'+1,m'-1}^- \alpha_{l'+1,m'-1}^{ll} \quad (26)$$

The above equations are valid for an arbitrary translational vector  $\vec{r}''$ . Now, we apply the above formulas for our case shown in Fig. 5.1 in which the coordinate system is translated along  $-z$  direction a distance of  $d$ . We have  $r'' = d$ ,  $\theta'' = \pi$ ,  $\phi'' = 0$ . Noting

that  $\sqrt{4\pi}Y_{l'}^{-m'}(\pi, 0) = (-1)^{l'}\sqrt{2l'+1}\delta_{m'}^0$ , it follows that

$$\alpha_{l'm'}^{00} = \begin{cases} \sqrt{2l'+1}j_{l'}(kd)\delta_{m'}^0, & d < r' \\ \sqrt{2l'+1}h_{l'}^{(2)}(kd)\delta_{m'}^0, & d > r'. \end{cases}$$

Subsequently, using Eq. (26) and reduction, it can be proven that

$$\alpha_{l'm'}^{ll} = \sqrt{\frac{(2l+1)!!}{(2l)!!}} \sqrt{\frac{(l+l)!}{(l-l)!}} \frac{\alpha_{l'0}^{00}}{(kd)^l} \delta_{m'}^l. \quad (27)$$

The order  $m$  is usually fixed for polarized beams. Then Eq. (24) is recursively used to calculate the translation matrix with initial values of  $\alpha_{l'm'}^{mm}$  and  $\alpha_{l'm'}^{m+1,m}$ . Equations (27) and (24) give us:

$$\begin{aligned} \alpha_{l'm'}^{mm} &= \sqrt{\frac{(2m+1)!!}{(2m)!!}} \sqrt{\frac{(l+m)!}{(l-m)!}} \frac{\alpha_{l'0}^{00}}{(kd)^m} \delta_{m'}^m, \\ \alpha_{l'm'}^{m+1,m} &= \sqrt{\frac{(2m+3)!!}{(2m)!!}} \sqrt{\frac{(l+m)!}{(l-m)!}} \frac{\alpha_{l'0}^{00}}{(kd)^m} \left( \frac{j_{l'}(kd)}{j_{l'}(kd)} - \frac{m}{kd} \right) \delta_{m'}^m. \end{aligned} \quad (28)$$

By reduction, it is proven from Eqs. (24) and (28) that

$$\alpha_{l'm'}^{lm} = \alpha_{l'm}^{lm} \delta_{m'}^m. \quad (29)$$

Another useful property of the translational coefficients is:

$$\alpha_{l',-m'}^{l,-m} = \alpha_{l'm'}^{lm}. \quad (30)$$

## Vector addition theorem

The vector addition theorem translates vector multipole fields between different coordinates. As mentioned above, there is a difference between our definition for vector multipole fields and the definition used in [164]. Hence, we need some mathematical manipulations for deriving the translational coefficients for the definition that we used. Reference [164] defines

$$\mathbf{M}_l^m(\vec{r}) = \nabla \times [\vec{r}\Psi_l^m(\vec{r})], \quad \mathbf{N}_l^m(\vec{r}) = \frac{1}{k}\nabla \times \nabla \times [\vec{r}\Psi_l^m(\vec{r})].$$

Then the following relationships hold:

$$\mathbf{M}_l^m(\bar{r}) = -\frac{i}{k}\mathbf{M}_{lm}(\bar{r}), \quad \mathbf{N}_l^m(\bar{r}) = \frac{1}{k}\mathbf{N}_{lm}(\bar{r}) \quad (31)$$

Reference [164] expresses the vector addition theorem as follows:

$$\mathbf{M}_l^m(\bar{r}) = \sum_{l'=1}^{\infty} \sum_{m'=-l'}^{l'} [A_{l'm'}^{lm}\mathbf{M}_{l'}^{m'}(\bar{r}') + B_{l'm'}^{lm}\mathbf{N}_{l'}^{m'}(\bar{r}')]. \quad (32)$$

By noticing that  $\mathbf{N}_l^m(\bar{r}) = \frac{1}{k}\nabla \times \mathbf{M}_l^m(\bar{r})$ ,  $\mathbf{M}_l^m(\bar{r}) = \frac{1}{k}\nabla \times \mathbf{N}_l^m(\bar{r})$  and that the operator  $\nabla$  is invariant under coordinate translation, Eq. (32) leads to

$$\mathbf{N}_l^m(\bar{r}) = \sum_{l'=1}^{\infty} \sum_{m'=-l'}^{l'} [A_{l'm'}^{lm}\mathbf{N}_{l'}^{m'}(\bar{r}') + B_{l'm'}^{lm}\mathbf{M}_{l'}^{m'}(\bar{r}')], \quad (33)$$

where the translation coefficients  $A_{l'm'}^{lm}$  and  $B_{l'm'}^{lm}$  are related to  $\alpha_{l'm'}^{lm}$  as follows:

$$\begin{aligned} A_{l'm'}^{lm} &= \alpha_{l'm'}^{lm} + kr'' \sin \theta'' \frac{e^{-i\phi''}}{2(l'+1)} \sqrt{\frac{(l'-m'+2)(l'-m'+1)}{(2l'+1)(2l'+3)}} \alpha_{l'+1, m'-1}^{lm} \\ &\quad - kr'' \sin \theta'' \frac{e^{-i\phi''}}{2l'} \sqrt{\frac{(l'+m'-1)(l'+m')}{(2l'-1)(2l'+1)}} \alpha_{l'-1, m'-1}^{lm} \\ &\quad - kr'' \sin \theta'' \frac{e^{i\phi''}}{2(l'+1)} \sqrt{\frac{(l'+m'+2)(l'+m'+1)}{(2l'+1)(2l'+3)}} \alpha_{l'+1, m'+1}^{lm} \\ &\quad + kr'' \sin \theta'' \frac{e^{i\phi''}}{2l'} \sqrt{\frac{(l'-m')(l'-m'-1)}{(2l'-1)(2l'+1)}} \alpha_{l'-1, m'+1}^{lm} \\ &\quad + kr'' \cos \theta'' \frac{1}{l'+1} \sqrt{\frac{(l'+m'+1)(l'-m'+1)}{(2l'+1)(2l'+3)}} \alpha_{l'+1, m'}^{lm} \\ &\quad + kr'' \cos \theta'' \frac{1}{l'} \sqrt{\frac{(l'+m')(l'-m')}{(2l'-1)(2l'+1)}} \alpha_{l'-1, m'}^{lm}, \\ B_{l'm'}^{lm} &= kr'' \cos \theta'' \frac{im'}{l'(l'+1)} \alpha_{l'm'}^{lm} + \frac{ir'' \sin \theta''}{2l'(l'+1)} [\sqrt{(l'-m')(l'+m'+1)} e^{i\phi''} \alpha_{l', m'+1}^{lm} \\ &\quad + \sqrt{(l'+m')(l'-m'+1)} e^{-i\phi''} \alpha_{l', m'-1}^{lm}]. \end{aligned} \quad (34)$$

Substituting Eq. (31) into Eqs. (32) and (33), the vector addition theorem for our definition can be described as follows:

$$\mathbf{M}_{lm}(\bar{r}) = \sum_{l'=1}^{\infty} \sum_{m'=-l'}^{l'} [A_{l'm'}^{lm} \mathbf{M}_{l'm'}(\bar{r}') + iB_{l'm'}^{lm} \mathbf{N}_{l'm'}(\bar{r}')], \quad (35)$$

$$\mathbf{N}_{lm}(\bar{r}) = \sum_{l'=1}^{\infty} \sum_{m'=-l'}^{l'} [A_{l'm'}^{lm} \mathbf{N}_{l'm'}(\bar{r}') - iB_{l'm'}^{lm} \mathbf{M}_{l'm'}(\bar{r}')]. \quad (36)$$

Now the electric field is easily expressed in the  $O'$ -system. Substituting Eqs. (35) and (36) into Eq. (3.42), we obtain

$$\mathbf{E}(\bar{r}') = \sum_{l'=1}^{\infty} \sum_{m'=-l'}^{l'} [p_{El'}^{m'} \mathbf{N}_{l'}^{m'}(\bar{r}') + p_{Ml'}^{m'} \mathbf{M}_{l'}^{m'}(\bar{r}')], \quad (37)$$

where

$$\begin{aligned} p_{El'}^{m'} &= \sum_{l=1}^{\infty} \sum_{m=-l}^l [A_{l'm'}^{lm} p_{El}^m + iB_{l'm'}^{lm} p_{Ml}^m], \\ p_{Ml'}^{m'} &= \sum_{l=1}^{\infty} \sum_{m=-l}^l [A_{l'm'}^{lm} p_{Ml}^m - iB_{l'm'}^{lm} p_{El}^m]. \end{aligned} \quad (38)$$

The above equations are valid for an arbitrary translational vector  $\bar{r}''$ . For the translation in Fig. 5.1, the translational coefficients  $A_{l'm'}^{lm}$  and  $B_{l'm'}^{lm}$  in Eq. (34) are reduced to

$$\begin{aligned} A_{l'm'}^{lm} &= \alpha_{l'm'}^{lm} - kd \left( \frac{1}{l'+1} \sqrt{\frac{(l'+m'+1)(l'-m'+1)}{(2l'+1)(2l'+3)}} \alpha_{l'+1,m'}^{lm} + \frac{1}{l'} \sqrt{\frac{(l'+m')(l'-m')}{(2l'-1)(2l'+1)}} \alpha_{l'-1,m'}^{lm} \right) \\ B_{l'm'}^{lm} &= -kd \frac{im'}{l'(l'+1)} \alpha_{l'm'}^{lm}. \end{aligned} \quad (39)$$

Referring to the properties of  $\beta_{l'm'}^{lm}$ , some important properties of the coefficients  $A_{l'm'}^{lm}$  and  $B_{l'm'}^{lm}$  are observed:

$$A_{l'm'}^{lm} = A_{l'm}^{lm} \delta_{m'}^m, \quad B_{l'm'}^{lm} = B_{l'm}^{lm} \delta_{m'}^m, \quad A_{l',-m}^{l,-m} = A_{l'm}^{lm}, \quad B_{l',-m}^{l,-m} = -B_{l'm}^{lm}. \quad (40)$$

With Eq. (37), we have successfully translated the electric field into the coordinate system of which the origin is the center of the SIL.

# Appendix C

Our purposes are to manipulate the polarization of the incident beams and block the center part of the incident beams for obtaining tighter focal spots. Figure 5.10 shows the setup for producing a cylindrical beam. We can obtain a linear polarization by removing the S-wave plate (SWP). Our laser produces a linearly-polarized beam, however to make sure the direction of the linear polarization is the horizontal direction, it is necessary to introduce the half-wave plate (HWP) and the linear polarizer (LP) as shown in Fig. 5.10. We use the LP to allow the horizontal component of the electric field passing through and block the vertical component. The HWP is used to rotate the direction of the polarization to obtain the maximum power passing through the LP, i.e. the axis of the polarization of the beam approaching the LP is horizontal. We can read and record the maximum power passing through the LP from the beam profiler (BP). To obtain a circularly-polarized beam, we replace the SWP in Fig. 5.10 with a quarter-wave plate (QWP). We setup the QWP so that the horizontal direction makes a  $45^\circ$  with the fast and slow axes of the QWP. We can also check the accuracy of the circular polarization using the BP by placing a LP in front of the BP so that we allows only the vertical component or horizontal components to be recorded by the BP at one time. If the two values recorded by the BP are the same, we get a perfect circular polarization. Figure 5.10 is the setup for producing the cylindrical beam in which the SWP converts a linearly-polarized beam to a radial or azimuthal beam. There is an alignment mark fabricated on the SWP. This mark should be aligned parallel to incident linear polarization orientation (horizontal orientation in our setup) to get radial and perpendicular to get azimuth polarization. We can use the BP for checking the quality of the cylindrical beam by recording the beam in different directions. An azimuthally-polarized beam with a vortex is produced

by inserting a vortex phase plate into the space just before the annular filter (AF). The below table provides details of the main optical components used in our experiment.

Part Number	Description	Manufacturer	Supplier
MIL-III-1342nm-500mW	Infrared Laser at 1342nm	Changchun New Industries Optoelectronics Technology Co., Ltd.	SEMICAPS Pte Ltd.
F260FC-C	FC/PC Fiber Collimation Package	Thorlabs	LASER 21 Pte Ltd
RPC-1340-06	S-waveplate (Passive Radial Polarization Converter)	Altechna Co. Ltd.	LASER 21 Pte Ltd.
RPC-VPP-m1340	Vortex Phase Plate	RPC Photonics, Inc.	LASER 21 Pte Ltd
BE02-05-C	Galilean Beam Expander	Thorlabs	LASER 21 Pte Ltd
WPQ05M-1310	Mounted Zero-Order, Quarter-Wave Plate	Thorlabs	LASER 21 Pte Ltd
WPH05M-1064	Mounted Zero-Order, Half-Wave Plate	Thorlabs	LASER 21 Pte Ltd
632	Metrochip Microscope Calibration Target	Ted Pella Inc	Pelco International
50160911	Pupil Filter	Esteemoptics	Esteemoptics